Investigating Some Aspects of Dark Matter Indirect Detection Using Different Dark Matter Particle Physics Models

By

KAMAKSHYA PRASAD MODAK

(PHYS05201004008)

Saha Institute of Nuclear Physics, Kolkata
India

A thesis submitted to the
Board of Studies in Physical Sciences
In partial fulfillment of requirements
for the Degree of

DOCTOR OF PHILOSOPHY

of

HOMI BHABHA NATIONAL INSTITUTE

January, 2016

Homi Bhabha National Institute

Recommendations of the Viva Voce Committee

As members of the Viva Voce Committee, we certify that we have read the dissertation prepared by Kamakshya Prasad Modak entitled "Investigating Some Aspects of Dark Matter Indirect Detection Using Different Dark Matter Particle Physics Models" and recommend that it may be accepted as fulfilling the thesis requirement for the award of Degree of Doctor of Philosophy.

P Bhattacharjee — Date: 23/05/2016
Chairman - Prof. Pijushpani Bhattacharjee

Debasish Majumdar — Date: 23/05/2016
Guide / Convener - Prof. Debasish Majumdar

Kaushik Bhattacharya — Date: 23rd May 2016
Examiner - Prof. Kaushik Bhattacharya

Debades Bandyopadhyay — Date: 23.5.2016
Member 1 - Prof. Debades Bandyopadhyay

Arunansu Sil. — Date: 23/05/2016.
Member 2 - Prof. Arunansu Sil

Subhendu Rakshit — Date: 23/05/2016
Member 3 - Prof. Subhendu Rakshit

Final approval and acceptance of this thesis is contingent upon the candidate's submission of the final copies of the thesis to HBNI.

I hereby certify that I have read this thesis prepared under my direction and recommend that it may be accepted as fulfilling the thesis requirement.

Date: May the 23rd, 2016
Place: Kolkata

Debasish Majumdar
Guide

STATEMENT BY AUTHOR

This dissertation has been submitted in partial fulfillment of requirements for an advanced degree at Homi Bhabha National Institute (HBNI) and is deposited in the Library to be made available to borrowers under rules of the HBNI.

Brief quotations from this dissertation are allowable without special permission, provided that accurate acknowledgement of source is made. Requests for permission for extended quotation from or reproduction of this manuscript in whole or in part may be granted by the Competent Authority of HBNI when in his or her judgment the proposed use of the material is in the interests of scholarship. In all other instances, however, permission must be obtained from the author.

Kamakshya Prasad Modak

Kamakshya Prasad Modak

DECLARATION

I, hereby declare that the investigation presented in the thesis has been carried out by me. The work is original and has not been submitted earlier as a whole or in part for a degree / diploma at this or any other Institution / University.

Kamakshya Prasad Modak

Kamakshya Prasad Modak

List of Publications arising from the thesis

Journal

1. *"Gamma Ray and Neutrino Flux from Annihilation of Neutralino Dark Matter at Galactic Halo Region in mAMSB Model"*,
   Kamakshya Prasad Modak, Debasish Majumdar,
   Journal of Physics G: Nuclear and Particle Physics, **2013**, *40*, 075201 [arXiv:1205.1996 [hep-ph]].

2. *"A Possible Explanation of Low Energy γ-ray Excess from Galactic Centre and Fermi Bubble by a Dark Matter Model with Two Real Scalars"*,
   Kamakshya Prasad Modak, Debasish Majumdar, Subhendu Rakshit,
   Journal of Cosmology and Astroparticle Physics, **2015**, *1503*, 011 [arXiv:1312.7488 [hep-ph]].

3. *"3.5 keV X-ray Line Signal from Decay of Right-Handed Neutrino due to Transition Magnetic Moment"*,
   Kamakshya Prasad Modak,
   Journal of High Energy Physics, **2015**, *1503*, 064 [arXiv:1404.3676 [hep-ph]].

4. *"Confronting Galactic and Extragalactic γ-ray observed by Fermi-LAT with Annihilating Dark Matter in Inert Higgs Doublet Model"*,
   Kamakshya Prasad Modak, Debasish Majumdar,
   Astrophysical Journal: Supplement Series, **2015**, *219*, no. 2, 37 [arXiv:1502.05682 [hep-ph]].

Conferences

1. *"A Two Component Dark Matter Model with Real Singlet Scalars confronting GeV γ-ray Excess from Galactic Centre and Fermi Bubble"*,

Debasish Majumdar, **Kamakshya Prasad Modak**, Subhendu Rakshit,

Pramana, **2016**, *86*, no. 2, 343-351,

Proceedings, International Workshop on Unification and Cosmology after Higgs Discovery and BICEP2 (UNICOS-2014).

List of Publications not contributing to the thesis

Journal

1. *"Dragging of inertial frames inside the rotating neutron stars"*,

   Chandrachur Chakraborty, **Kamakshya Prasad Modak**, Debades Bandyopadhyay,

   Astrophysical Journal, **2014**, *790*, no. 1, 2 [arXiv:1402.6108 [astro-ph]].

2. *"Deriving super-horizon curvature perturbation from the dynamics of preheating"*,

   Arindam Mazumdar, **Kamakshya Prasad Modak**,

   Journal of Cosmology and Astroparticle Physics, **2015**, *1504*, no. 04, 053 [arXiv:1412.8522 [astro-ph]].

3. *"Constraints on variations in inflaton decay rate from modulated preheating"*,

   Arindam Mazumdar, **Kamakshya Prasad Modak**,

   Journal of Cosmology and Astroparticle Physics, **2016**, *1606*, no. 06, 030 [arXiv:1506.01469 [astro-ph.CO]].

Others

1. *"Constraining Effective Self Interactions of Fermionic Dark Matter"*,

   Kamakshya Prasad Modak,

   [arXiv:1509.00874 [hep-ph]] (in communication).

Kamakshya Prasad Modak

Kamakshya Prasad Modak

Dedicated To

My Parents

ACKNOWLEDGEMENTS

Though only my name appears on the cover of this thesis work, a great many people have contributed to its production. I owe my gratitude to all those people who have made this thesis possible and because of whom my entire period of PhD research has been one that I will cherish forever.

Firstly, I would like to express my sincere gratitude and indebtedness to my advisor Prof. Debasish Majumdar for providing his continuous support of my Ph.D study and related research, sincere help and excellent guidance during the entire period of my Ph.D. research and also for his patience, motivation and immense knowledge. He has motivated me in many ways and encouraged me a lot to pursue my own thinkings. I was introduced to several areas of Astroparticle Physics during innumerable discussions with him. His guidance and friendly nature have helped me pursuing research and finally writing of this thesis. I could not have imagined having a better advisor and mentor for my Ph.D study.

Besides my advisor, I would like to convey my sincere thanks to the rest of my thesis committee: Prof. Debades Bandyopadhyay, Prof. Pijushpani Bhattacherjee, Prof. Arunanshu Sil, Prof. Subhendu Rakshit for providing their continuous guidance and help during the entire period of my PhD research. Their insightful comments and fruitful discussions in various aspects of research work have widened my research from various perspectives. My sincere thanks also goes to Prof. Palash Baran Pal, Prof. Parthasarathi Majumdar and Prof. Ambar Ghosal for their help and various discussions throughout this period of research. Moreover, I would like to thank Prof. Parthasartahi Mitra for his help regarding HBNI registration.

I would like to thank my institute Saha Institute of Nuclear Physics (SINP), Kolkata for giving me the opportunity to pursue my research career and proving excellent academic infrastructural facilities. I am also grateful to Department of Atomic Energy (DAE, Govt. of India) for giving me the financial assistance during my entire Ph.D career. Besides, I would like to offer my sincere acknowledgement to Homi Bhabha National Institute

(HBNI) for giving me chance to register for my Ph.D.

I wish to express my warm gratitude to all of my academic collaborators from whom I have learnt a lot of interesting insights about physics. Among them I would like to thank Prof. Subhendu Rakshit for collaborating me and discussing various aspects of particle physics. Especially I wish to convey my deepest gratitude to Prof. Debades Bandyopadhyay not only for various discussions on Relativistic Astrophysics but also for his perpetual encouragement during my research life. Also I would like to thank my friend Chandrachur Chakraborty for discussing General Relativity which results a successful collaboration in a project. I have learnt a lot from uncountable discussions with him on various academic as well as non-academic issues. Last but not the least, I am grateful to Arindam Mazumdar for including me in his projects and appraising me about several areas in Cosmology via detailed discussions.

I am very much fortunate to get associated with some of the finest teachears and researchers during my whole academic career. This list includes Prof. Palash Baran Pal, Prof. Ajay Choudhury, Prof. Nirmal Bhattacharya, Biren Biswas, Ajay Ghosh and many others. Their sincere devotion and deep understanding as well as guidance have improved my knowledge and motivated me to research. I owe my deepest gratitude to Prof. Venktesh Singh, Prof. Sourov Roy, Prof. Kaushik Bhattacharya for giving me opportunities at different occasions to present my reseach works. Also I would like to express my appreciation to Biplab Das (journalist) and the Editor of *Nature India* for highlighting our research work in the international science news portal *Nature India*.

The friendships I have developed during these 5 years here in SINP have been amazing. I would like to convey my heartfelt appreciations to my friends Chandrachur Chakraborty, Uttam Basak, Kaustabh Dan, Prasanta Char, Biswarup Paul, Abhik Mukherjee, Rome Samanta, Biswajit Banejee, Anshu Chatterjee, Apurbo Kheto, Goutam Das, Kalyanmoy Chatterjee, Roopam Sinha, Kousik Bagani, Moumita Nandi, Rajeshwari Roychowdhury, Sultana Tajmili Hasnahena, Dipankar Das, Niyaz Rather, Hitesh Rahangdale, Rajni Raman, Bijoy Daga, Souvik Priyam Adhya, Amit Dutta Banik, Chowdhury Aminul Islam, Naosad Alam and many others for spending many unforgettable lovely moments during my research life.

I am quite fortunate to have wonderful human beings as my seniors during SINP days. Both academic as well as non-academic discussions with them are wonderful and fun. I am especially thankful to Pritibhajan Byakti, Srijit Bhattacharjee, Rana Nandi, Arindam Mazumdar, Sirshendu Gayen, Kallol Bera, Ankan Dutta Choudhury, Arpan Bhattacharya, Bhramar Chatterjee, Anisur Rahaman, Anirban Biswas, Mainak Chakraborty, Debabrata Adak, Palash Khan, Abhishek Majhi, Lab Saha, Parijaat Dey, Pratyay Banerjee, Soumini Chaudhury, Sustana Seth, Susmita Kundu, Satyajit Seth, Najmul Haque, Raktim Abir and many others. I would like to thank the non-teaching stuffs Pradyut Mitra, Bijoy Das, Nilanjan Biswas for their help. I also want to thank all the members (teaching, non-teaching, JRFs, SRFs, RAs of Physics and Bio-physics divisions) of SINP for maintaining a pleasant atmosphere at the institute.

Last but not the least, I express my deepest gratitude and indebtedness to my parents (Ram Chandra Modak & Subhra Modak) for their unconditional love, patience, encouragements and extending all kind of support during my whole life. I would never ever achieve this goal without them. I am grateful to them for giving me every freedom in my life and career and for constant moral and emotional support during every stage of my life. I want to convey my heartfelt regards to my Grand Father and Grand Mother for their affection and support since childhood. Besides, I am also indebted to my other family members (aunts, uncles) for their many valuable suggestions. Especially I offer my special thanks to my cousins Soumyadeep Dutta, Subhasis Rakshit, Arijit Ruj, Rakhi Rakshit for extending their love, encouragements and moral support towards every aspect of my life.

Kamakshya Prasad Modak

Kamakshya Prasad Modak

Contents

Synopsis

The overwhelming cosmological and astrophysical evidences have now established the existence of an unknown non-luminous matter present in the universe in enormous amount, namely the dark matter (DM). Experiments like Wilkinson Microwave Anisotropy Probe (WMAP), BOSS or more recently Planck measure the baryonic fraction precisely to consolidate the fact that this non-baryonic DM constitutes around $\sim 26.8\%$ of the content of the universe. The particle nature of DM candidate is still unknown. The relic density of dark matter deduced from cosmological observations mentioned above tends to suggest that most of the DM could be made of weakly interacting massive particles or WIMPs. The general wisdom is that in order to account for the relic abundance of DM, a candidate for dark matter should be massive, very weakly interacting and non-relativistic (cold dark matter or CDM) particles. This allows the structure formation on large scales. In the following analyses, we consider such weakly interacting massive particles (WIMPs) to consist of the total DM content of the universe.

Because of its nature, the detection of dark matter is very challenging experimental effort. In general there are two types of detection mechanism namely direct detection of dark matter and indirect detection of dark matter.

Direct detection DM experiments can detect DM by measuring the recoil energy of a target nucleon of detecting material in case a DM particle happens to scatter off such nucleons. Experiments like CDMS, DAMA, CoGeNT, CRESST, XENON 100, LUX present their results indicating allowed zones in the scattering cross-section – DM mass plane.

The indirect detection of dark matter involves detecting the particles (and their subsequent decays) or photons produced due to dark matter annihilations. These annihilation products can be fermions or γ photons. The dark matter particles, if trapped by the gravity of a massive body like sun or galactic centre, can annihilate there to produce these particles. Study of such photons and fermions such as neutrinos thus throw light on the nature of galactic dark matter as well as the nature of the galactic dark matter halo profile. There are generally two kinds of γ-ray emission from DM annihilation. In the first category γ is produced directly from the annihilation final state particles which is called primary emission in which final charged leptons emit gamma ray or π^0 which eventually decays to gamma ray after hadronization. The other kind is called secondary emission in which gamma rays are produced by interactions of final state particles with external medium or radiation field such as the inverse Compton effects etc. Here we consider only the first type of emission in our analyses. In our study, we have calculated the gamma ray flux from the galactic centre as also from other places in galactic dark matter halo along the line of sight around the GC. Different satellite-borne and ground-based experiments such as FERMI-LAT looking for extra terrestrial gamma signals have reported the observence of excess gamma ray signals in the direction of galactic centre in different energy regions.

Experiments such as HESS, MAGIC etc. detect very high energy gamma rays (in TeV range) from the galactic centre, which has no khown astrophysical origin. If the observed TeV gamma rays from the galactic centre are indeed due to the annihilation of dark matter at galactic centre then such dark matter mass should be $\sim$ TeV. In order to confront such TeV gamma ray, the dark matter candidate is considered to be the lightest supersymmetric particle (LSP) neutralino in the minimal anomaly mediated supersymmetry breaking (mAMSB) model where the LSP is stabilised by conservation of R-parity. In mAMSB model, the LSP neutralino that can be a possible candidate for WIMP or cold dark matter with its mass in TeV range, can annihilate to generate such gamma ray with TeV energy range. In the superconformal Anomaly Mediated Supersymmetry Breaking (AMSB) mechanism, dynamical or spontaneous breaking is supposed to take place in some 'hidden' sector (HS) and this breaking is mediated to the observable sector (OS) by gravitino mass ($m_{\frac{3}{2}}$) $\sim$ 100 TeV. Supersymmetry breaking effects in the observable sector have a gravitational origin in this framework. In ordinary gravity-mediated supersymmetry breaking model, the supersymmetry breaking is transmitted from HS to OS via tree level exchanges with gravitational coupling. But in AMSB, the HS and the OS superfields are assumed to be located in two parallel but distinct 3-branes and the supersymmetry breaking is propagated from the HS to the OS via loop generated superconformal anomaly.

An sparticle spectrum in this model is fixed by three parameters, $m_{\frac{3}{2}}$ which is gravitino mass, tanβ which is the ratio of the vacuum expectation values of the two Higgs fields (H_1^0 and H_2^0) and sign(μ), where μ is the Higgsino mass. Also another parameter, namely m_0^2 which is an universal mass-squared term required to circumvent the problem of tachyonic slepton mass terms in mAMSB model. Thus four parameters are needed to generate particle spectrum in mAMSB model. The neutralino is the lowest mass eigenstate of linear superposition of photino ($\tilde{\gamma}$), zino ($\tilde{Z}$), and the two Higgsino states ($\tilde{H}_1^0$ and $\tilde{H}_2^0$).

In this analysis, the SUSY parameter space namely m_0, $m_{\frac{3}{2}}$, tanβ and sign(μ) is initially adopted with proper incorporation of the recent LHC (ATLAS) bound on chargino mass. The relic densities for such dark matter are then computed using these SUSY parameters and they are compared with the WMAP results. The mass of the LSP neutralino in the present scenario is obtained in two regions of which one is around 1 TeV and the other is at a somewhat higher range of $\sim$ 2 TeV. The parameters, thus constrained further by the WMAP results, are then used to calculate the spin independent and spin dependent cross sections ($\sigma_{\rm scatt}$) for different neutralino masses (m_χ) (obtained using the restricted parameter space). The χ-nucleon scattering process is essential for the direct searches of dark matter. As mentioned above, we calculate χ-nucleon elastic scattering cross section $\sigma_{\rm scatt}$ for the restricted parameter space discussed earlier. The $m_\chi - \sigma_{\rm scatt}$ region, thus obtained, is found to be within the allowed limits of most of the direct detection experiment results.

We further investigate its indirect detections. Using the constrained mAMSB parameter space discussed above we calculate the gamma ray flux in the direction of the galactic centre. These studies are performed for different galactic dark matter halo profiles. We find that the gamma spectrum from galactic centre and halo produced by neutralino dark matter within the framework of the present mAMSB model, is highly energetic. The experiment like HESS, that can probe high energy gamma rays and which, being in the southern hemisphere has better visibility of the galactic centre, will be suitable to test the viability of the present dark matter candidate in mAMSB model.

The possibility of detecting neutrinos from galactic centre and halo from dark matter annihilations are also addressed with reference to ANTARES (Astronomy with a Neutrino Telescope and Abyss environmental RESearch) under sea neutrino experiment. Different flavours of neutrinos from the dark matter annihilation at galactic centre are addressed in the present analysis. The flux and detection of muon species of such neutrinos are calculated for the neutralino dark matter in mAMSB model. Given the masses of such dark matter candidates the energies of such neutrinos will also be in the range GeV to TeV. The location of the galactic centre with respect to earth is downwards. The high energetic muon neutrinos may produce muons by the charged current scattering off ice or water and may be detected by their Cerenkov lights. We calculate the fluxes of neutrinos of different flavours due to annihilations of dark matter when viewed in the direction of the galactic centre as also at the other two chosen positions in its neighbourhood. The results are shown for the four halo profiles considered. In order to estimate the detection yield of such neutrinos in a terrestrial neutrino observatory, we have chosen the ANTARES under sea detector and calculated the muon yield for muon neutrinos from galactic centre for all the four halo profiles considered. The calculations of neutrinos in case of different halo profiles also exhibit similar trend as those for the calculation of γ flux.

The signal of anomalous GeV gamma-ray excess from the galactic centre (GC) and inner galaxy region as *seen* by the satellite borne experiment Fermi-LAT from its recent data. Fermi Bubbles, a bi-lobular structure of gamma-ray emission extending 25,000 light-years upward (north) and downward (south) from the galactic centre of the Milky

Way galaxy, also exhibit an anomaly in its gamma-ray emission spectrum. While the inverse Compton Scattering (ICS) process of the cosmic ray electrons could well explain the observed gamma-ray emission (ranging from a few GeV to ~ 100 GeV) from the higher galactic latitude (b) of the lobes, the observed gamma ray spectrum by the Fermi-LAT from the lower latitudes of the Fermi Bubbles indicates a bump-like feature in the energy regime, $E_\gamma \sim 1-3$ GeV which could not be explained solely by the ICS mechanism. This bump-like features indicating gamma ray excess are also reported by Fermi-LAT collaboration for the gamma rays from the galactic centre region. An early analysis of Fermi-LAT data reveals that the gamma rays from the galactic centre region exhibit excesses (bump) in the energy range $\sim 0.3-10$ GeV. More involved and modified recent analysis including more recent data restricts the range of excess gamma to be in the energy region of $\sim 1-3$ GeV.

In the following study we have addressed this anomalous nature of gamma-spectrum from galactic centre and Fermi Bubbles. To this end, we promote the idea of multi-component Dark Matter (DM) to explain results from both direct and indirect detection experiments. In these models as contribution of each DM candidate to relic abundance is summed up to meet WMAP/Planck measurements of $\Omega_{\rm DM}$, these candidates have larger annihilation cross-sections compared to the single-component DM models. We illustrate this fact by introducing an extra scalar to the popular single real scalar DM model. Thus our viable annihilating multicomponent dark matter model consists of two real gauge singlet scalars that are stabilized by $\mathbb{Z}_2 \times \mathbb{Z}_2'$ symmetry. Theoretical aspects of the model such as the vacuum stability bounds, perturbative unitarity and triviality constraints are checked for this model. As direct detection experimental results still show some conflict, we kept our options open, discussing different scenarios with different DM mass zones. Guided by the direct detection experiments we considered three DM mass zones. The "low" zone of $7-11$ GeV is indicated by CDMS II, CoGeNT and CRESST II experiments. CRESST II also favours a "mid" zone ~ 25 GeV. As XENON 100 and LUX seem to rule out these zones, the only DM masses consistent with both XENON 100 or LUX and Planck observations belong to a “high” mass zone > 50 GeV. The advantage of dealing with this zone is that they do not give rise to unacceptable invisible branching ratio for Higgs. But a too high DM mass > 100 GeV predicts a photon flux from DM annihilations peaked at higher energies than what has been observed in the indirect detection experiments. This high DM mass zone will be probed by future XENON 1T and LUX measurements. We have computed the photon flux from the galactic centre and compared with the observed Fermi-LAT data for the chosen DM mass zones (benchmark scenarios). We then consider the γ-rays from regions of the Fermi Bubbles and confront the calculated flux with the low energy residual γ-ray excess from its the lower galactic latitudes in the light of the two singlet scalar model. For this, total extent of the Fermi Bubbles are devided in terms of the galactic latitudes, namely, $|b| = 1^\circ - 10^\circ, 10^\circ - 20^\circ, 20^\circ - 30^\circ, 30^\circ - 40^\circ, 40^\circ - 50^\circ$. Theoretical calculations are performed for photon flux for each of the zones and then compared with the Fermi-LAT observation.

From the detailed analyses, we have come to a conclusion that the proposed model can also potentially interpret the low energy ($\sim 1 - 3$ GeV) gamma ray excess from both Galactic Centre and Fermi Bubble by Fermi Gamma-ray Space Telescope (FGST). Together with the indirect detection, the different chosen zones for studing direct dark matter detection have the capability to distinguish between different DM halo profiles. There is some advantage of addressing both direct and indirect detection experiments. The allowed model parameter space is rather restricted by the direct DM detection experiments and relic density constraints as imposed by Planck. This makes indirect DM detection predictions quite sensitive to the assumed DM halo profiles. we make an interesting observation that for the low DM mass zones, one needs very flat DM halo profiles in order to confront both direct and indirect signatures of DM in this framework, whereas a much cuspy DM halo profiles are suitable for very high mass zones in this model.

Recently an evidence of X-ray line of energy 3.55 keV with more than 3σ CL has been reported from the analysis of X-ray data of 73 galaxy clusters from XMM-Newton observatory. Another group has also claimed a similar line (3.52 keV X-ray line at 4.4σ CL) from the data of X-ray spectra of Andromeda galaxy (M31) and Perseus cluster. The galaxy clusters are assumed to contain huge amount of DM. Thus the signal may have a possible origin related to DM. In order to explain the observation, we consider the dark matter model with radiative neutrino mass generation where the Standard Model is extended with three right-handed singlet neutrinos (N_1, N_2 and N_3) and one additional $\mathrm{SU}(2)_L$ doublet scalar η. One of the right-handed neutrinos (N_1), being lightest among them, is a leptophilic fermionic dark matter candidate whose stability is ensured by the imposed $\mathbb{Z}_2$ symmetry on this model. The second lightest right-handed neutrino (N_2) is assumed to be nearly degenerated with the lightest one enhancing the co-annihilation between them. The effective interaction term among the lightest, second lightest right-handed neutrinos and photon containing transition magnetic moment is responsible for the decay of heavier right-handed neutrino to the lightest one and a photon ($N_2 \to N_1+\gamma$). This radiative decay of heavier right-handed neutrino with charged scalar and leptons in internal lines could very well explain the X-ray line signal $\sim$ 3.5 keV recently claimed by XMM-Newton X-ray observatory from different galaxy clusters and Andromeda galaxy (M31). The value of the transition magnetic moment (μ_{12}) for such an observed signal is estimated to be few orders of magnitude smaller than the reach of recent DM direct direct detection experimental limits sustaining the possibility of the cold DM candidate in this model to be detected directly. The other parameters of this model, namely masses of lightest right-handed neutrino (N_1), doublet scalar (η) and phase factor (ξ) between Yukawa couplings, h_1 and h_2 are further constrained from the observed X-ray line data. A very small but non-zero value of the phase difference between Yukawa couplings, h_1 and h_2 have been predicted. Also the co-annihilation between N_1 and N_2 becomes smaller and the s-wave contribution of dark matter annihilation cross section is calculated to be reduced. Finally the analysis performed here for this model framework would be viable for any DM signal in this energy regime. In addition the DM candidate (lightest right-handed neutrino), being leptophilic and massive, can potentially explain AMS-02 positron excess.

In another thorough study we focus on the indirect detection of Dark Matter through the confrontation of unexplained galactic and extragalactic γ-ray signatures for a low mass DM model. For this, we consider a simple Higgs-portal DM model, namely, the inert Higgs doublet model (IHDM) where the Standard Model is extended with an additional complex $\mathrm{SU}(2)_L$ doublet scalar. The stability of the DM candidate in this model, i.e., the lightest neutral scalar component of the extra doublet, is ensured by imposing discrete $\mathbb{Z}_2$ symmetry. The model, in general, provides a broad range of DM mass from GeV to TeV range. In this study we only consider the lower mass range of DM in this model. The analysis of experimental data for DM relic density from PLANCK experiment and the other direct detection experimental results for the case of this IHDM gives a set of best fit values for DM mass, annihilation cross section and other model parameters. We adopt this best fit point (obtained using χ^2 minimisation) for IHDM mass from such analyses. Thus the DM mass of 63.54 GeV is our chosen benchmark point in the present study. We study the γ-ray spectrum obtained from the annihilation of this chosen DM particle in IHDM framework and interpret various types of continuum γ-ray fluxes with astrophysical origins measured by Fermi-LAT satellite.

In this study we compare our calculated γ-ray flux with the galactic centre γ-ray excess in the light of this model. For this we have employed different analysed Fermi-LAT residual γ-ray flux data for different angular regions around the galactic centre. The calculated low energetic photon spectra from the annihilation of the DM particle (for the chosen benchmark scenario) for various chosen regions surrounding the galactic centre are found to be in the same ballpark as reported by these studies. Although in some previous analyses it was argued that the photon spectra originated from different annihilation channels of dark matter particles with low masses can possibly fit the obtained data, very recent analyses have obtained the resulting best fit masses of dark matter to be much more conservative (and also somewhat higher as well). We have computed the photon spectra for our benchmark scenario in IHDM framework and have confronted with the residual photon spectra obtained for all of the above-mentioned studies. Our theoretical calculations for photon spectra in this model have been performed after suitable parametrisation of the dark matter halo parameters, region of interest surrounding the galactic centre etc.

We then consider the γ-rays from regions of the Fermi Bubbles and compare the low energy residual γ-ray excess from its the lower galactic latitudes in the light of the IHDM framework. Theoretical calculations are performed for photon flux from annihilating IHDM dark matter of chosen mass for five zones covering the total extent of the Fermi Bubbles. These zones are divided in terms of the galactic latitudes $|b| = 1^\circ - 10^\circ, 10^\circ - 20^\circ, 20^\circ - 30^\circ, 30^\circ - 40^\circ, 40^\circ - 50^\circ$. The calculated results are then compared with the Fermi-LAT observation. However the observation hints much prominent signature of bumpy features in the residual photon flux only in the regions with $|b| = 1^\circ - 10^\circ, 10^\circ - 20^\circ, 20^\circ - 30^\circ$. The annihilating low mass DM in IHDM is also found to yield similar nature of photon spectra from Fermi Bubbles.

We also address the prospects of the continuum γ-ray signal which may come from DM-dominated dwarf spheroidal galaxies (dSphs) in case they originate from dark matter annihilation. We then compare the γ-ray flux that can be obtained from the IHDM dark matter (for the chosen benchmark scenario). For this we choose 18 Milky Way dSphs whose J-factor can be estimated from measurements. The uncertainties in the measurement of J-factor for different dSphs are also incorporated in our calculations. The calculated photon spectra for IHDM benchmark point are seen to obey the allowed limits for observed spectra of continuum γ-ray.

After addressing the issues regarding indirect DM searches with γ-ray signals from various galactic cases, we finally confront the extragalactic γ-ray signal with that from the annihilation of low mass DM (considered in this study) in IHDM scenario. We calculate the extragalactic γ-ray flux for different extragalactic parametrisations and compare with the observed extragalactic gamma ray background by EGRET and Fermi-LAT. For this we consider several possible classes of non-DM astrophysical sources which may yield γ-ray signal embedded in the extragalactic background. Although there are too many uncertainties involved in modelling of such astrophysical sources and other parameters for extragalactic flux calculation, we have shown that the considered low mass DM in IHDM can generate photon flux within the observed flux limit.

From the detailed study of various galactic and extragalactic γ-ray searches for probing the indirect signatures of DM in light of IHDM, we can conclude that the low mass DM in the IHDM framework is still a viable candidate to be probed in future γ-ray searches. Although we have performed the thorough analysis considering only a single Higgs-portal model, the analysis is valid for any simple Higgs-portal DM model such as singlet scalar DM model, singlet fermion DM, inert Higgs triplet model etc. with DM mass in the same ballpark as in our study.

List of Figures

List of Tables

Chapter 1

Introduction to Dark Matter

1.1 Brief Introduction

Dark Matter represents an unknown, non-luminous form of matter whose presence is inferred only via gravitational effects on galaxies and stars. The presence of dark matter is now well established by various cosmological and astrophysical evidences. Observations suggests that around $\sim 26.8\%$ of the total content of the Universe is constituted by this invisible form matter. The existence of dark matter was initially addressed by Oort in 1932 [17] in order to account for the vertical motion of the stars in the Milky Way. Few years later, Babcock (1939) [18] reported the measurements of the rotation curve for Andromeda galaxy via optical spectroscopy, suggesting radial increment of the mass-to-luminosity ratio. Later Swiss Physicist Fritz Zwicky [19] introduced the presence of dark matter from the study of velocity distribution of galaxies in the Coma galaxy cluster since the presence of luminous mass only in the cluster does not solely account for the dynamics of the whole cluster. Few years later, from the observation of the Virgo cluster [20], Smith in 1936 had come to similar conclusion but lack of understanding of various astrophysical details had prevented to confirm the fact.

1.2 Evidences for Dark Matter

Various astrophysical observations suggest the existence of dark matter. In this section we want to summarize the evidence from observations on galactic scales up to cosmological scales. All evidences are based on the gravitational effect of dark matter. By now, no significant evidence for dark matter has been found on microscopic scales.

- **Motion of the Galaxies (Coma and Virgo Cluster)**

  Although there is a huge difference in scale between an individual galaxy and a cluster of galaxy, the relation between the kinetic energy and gravitational potential energy plays a common role for the search of dark matter in galactic and galaxy cluster scales. Evidence for the existence of dark matter in galaxies as well as clusters dates from the 1930s. The Swiss astronomer Fritz Zwicky used the velocity dispersion of galaxies in clusters as determined from Doppler shifts to estimate their dynamical mass [19, 21]. He has applied the virial theorem for the system of galaxies in the Coma cluster. The virial theorem thus gives a simple relationship between the average kinetic energy and average gravitational potential energy of bodies in a gravitationally bound system. Alternatively if Hamiltonian of a system of interacting non-relativistic particles is

$$H = \sum_{i}^{n} \frac{p_i^2}{2m_i} + V(r_i) \ , \tag{1.1}$$

  then the virial theorem states that

$$\left\langle \frac{p_i^2}{2m_i} \right\rangle = \left\langle \frac{\partial V(r_i)}{\partial r_i} . r_i \right\rangle \ , \tag{1.2}$$

where the average $\langle .. \rangle$ is over time and 'i' denotes the particle index for a system of n point particles. In the above r_i, v_i, p_i and m_i are the position, velocity, momentum vectors and mass, respectively, for the i-th particle and F_i is the net force which may be both internal and external in nature, impinging on the i-th particle. $V(r_i)$ denotes potential energy of i-th particle situated at position r_i. This reduces to the following relation

$$U + 2T = 0 \ , \tag{1.3}$$

where U is the potential energy of the system and T denotes the kinetic energy.

For a spherically symmetric distribution of galaxies (a self gravitating system), the total potential energy can be given as

$$U = \frac{3}{5}\frac{GM^2}{R} \ , \tag{1.4}$$

where R is the radius of the cluster and M is the total mass of the cluster. By measuring the redshift, we can only measure velocities parallel to the line of sight ($v_{\rm par}$). If we assume velocities are distributed isotropically, the average velocity, $\langle v^2 \rangle = \langle v^2_{\rm par} \rangle$. Thus, the total kinetic energy of the cluster can be written as

$$T = \frac{3}{2} M \langle v^2_{\rm par} \rangle \ , \tag{1.5}$$

Combining Eqs.1.4 and 1.5 by the virial theorem, we get

$$2 \times \frac{3}{2} M \langle v^2_{\rm par} \rangle = \frac{3}{5}\frac{GM^2}{R} \tag{1.6}$$

$$M = \frac{5R\langle v^2_{\rm par} \rangle}{G} \tag{1.7}$$

The value of $\sqrt{\langle v^2_{\rm par} \rangle}$ is replaced by the root mean square velocity of the galaxy as

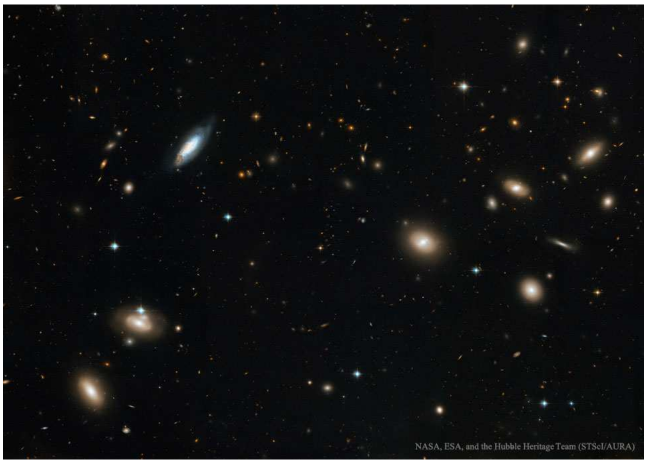

(a)

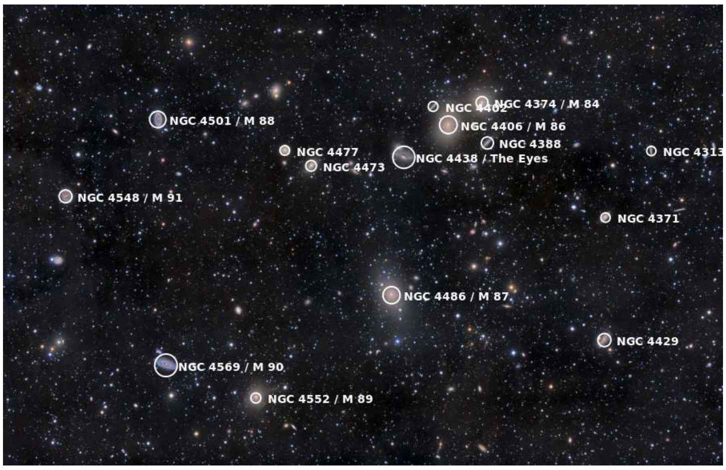

(b)

Figure 1.1: *Galaxy Clusters. Panel (a): inside the Coma Cluster of galaxies. Image Credit: NASA, ESA, Hubble Heritage (STScI/AURA); Acknowledgment: D. Carter (LJMU) et al. and the Coma HST ACS Treasury Team. Panel (b): Virgo Cluster of galaxies. Image Credit & Copyright: Rogelio Bernal Andreo.*

calculated from the known radial velocities of the seven galaxies in Coma cluster by Zwicky. In order to determine their velocities Zwicky used the measurements of the Doppler shift of the spectra of all the galaxies in the cluster. From Eq. 1.7, the dynamical mass of the cluster can be estimated to be $\sim 1.9 \times 10^{13}$ $M_\odot$. On the other hand, from the observation of galaxies, Zwicky has estimated the total visible mass (mass calculated from the light emitted by the cluster) of $\sim 8.0 \times 10^{11}$ $M_\odot$ (nearly $\sim$ 400 times smaller than the dynamical mass) by considering reasonable assumptions on the distribution of star population in the galaxies [19, 21]. Since Zwicky's time, more mass has been discovered in the Coma cluster in the form of hot X-ray emitting gas between and within the galaxies [22, 23]. In recent time it can be estimated to be $((1.0 \pm 0.2)h^{-1} + (5.48 + 0.98)h^{-\frac{5}{2}}) \times 10^{13}$ $M_\odot$ [24] which gives $\sim 1.6 \times 10^{14}$ $M_\odot$ after using the value of Hubble parameter (in terms of 100 km s^{-1} Mpc^{-1}) $h = 0.673 \pm 0.012$. Later Sinclair Smith performed a similar analysis on the measurement of mass in Virgo cluster [20] which is irregular in shape and contains numerous elliptical and lenticular galaxies. The diffuse, irregular, random distribution and motion of the stars in the elliptical galaxy affect the collective average motion of such galaxies inside a cluster like Virgo. Smith also came to the similar conclusions as drawn by Zwicky. Therefore it can be inferred that a huge amount of invisible mass is present in the galaxy cluster. The picture of two popular galaxy clusters for the search of dark matter, namely, Coma Cluster and Virgo Cluster are shown in Fig. 1.1 as an example.

Similarly the Tully-Fisher relation in spiral galaxies can also be explained by the virial theorem and the presence of dark matter within those galaxies [25]. The Tully-Fisher relation states the empirical relation between the luminosity (L) of the spiral galaxies and the maximum rotational velocity ($V_{\rm max}$) of the stars of those galaxies and can be written as [26]

$$L \propto V_{\rm max}^{\beta}, \ \ \beta = 3 - 4 \ . \tag{1.8}$$

On the other hand, virial theorem relates the total galactic mass and the maximum rotation velocity. Therefore the connection between the visible mass and dark matter is manifested in Tully-Fisher relation for spiral galaxies. The alternative for the analogues of Tully-Fisher relation for non-rotationally-supported galaxies like elliptical galaxies is the Faber-Jackson relation [27].

- **Flattening of Rotation Curves of Spiral Galaxies**

The most convincing evidence for the existence of DM in the galaxy comes from the study of rotation curves of the spiral galaxies. The components of spiral galaxy consists of flat, rotating disc containing newly formed stars and interstellar matter, a central buldge of old stars with supermassive black hole at its centre and a near-spherical halo of stars. Also the spiral arms of such galaxies containing stars extend from the centre to the disc. The rotation curve (or velocity curve) of a galaxy is simply the variation in the orbital circular velocity of stars or gas clouds at different distances from the centre. In order to perform the analysis of the rotation curves of the galaxies, the dependence of rotational velocity ($v(r)$) of a star within the galaxy as a function of radial distance (r) of the star from the centre of the galaxy is investigated. The velocities of the neutral hydrogen as a function of distance can be measured by the Doppler shift of the emission lines (hydrogen alpha in the optical, neutral hydrogen 21 cm in the radio). Assuming a spherical symmetry of the dark matter halo and applying Newtonian dynamics (law of circular motion) to the circular motion of a star, the following relation can be written as a balance between the gravitational and centrifugal force fields

$$\frac{mv(r)^2}{r} = G\frac{M(r)m}{r^2} \quad , \tag{1.9}$$

where $M(r)$ is the contained mass of the galaxy inside radius r surrounding the centre of the galaxy and m is the mass of the star. For an average density of the central bulge of the galaxy ρ, $M(r)$ can be written as

$$M(r) = \frac{4}{3}\pi r^3 \rho \quad . \tag{1.10}$$

Combining the above two equations (Eqs. 1.9 and 1.10), it can be inferred that the

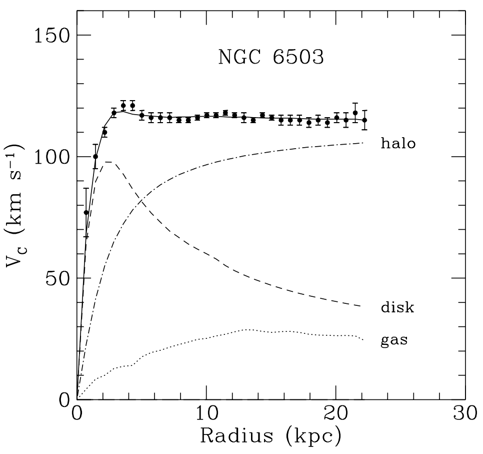

(a)

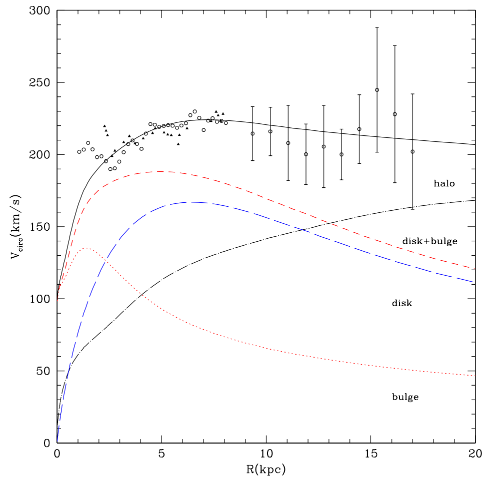

(b)

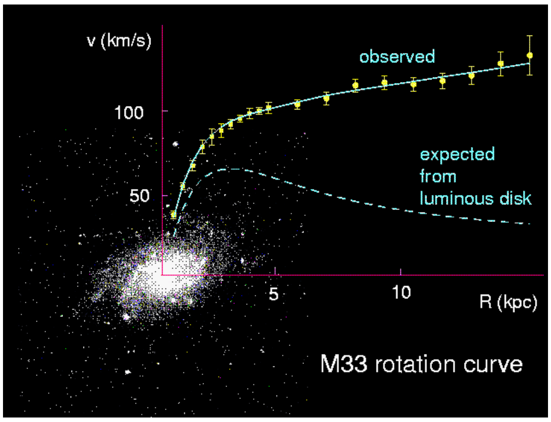

(c)

Figure 1.2: *Examples of galactic rotation curves for different galaxies. Panel (a): the rotation curve for spiral galaxy NGC 6503 (from Refs. [1, 2]). Panel (b): the rotation curve of Milky Way (from Ref. [3]). Panel (c): observed rotation curve of dwarf spiral galaxy M33 (from Ref. [4]). The points in each plot are the measured circular velocities at different radial distances for each galaxy. The dotted and dashed lines in these plots denote theoretical expected contributions of different components of the galaxy. The fitted curves that pass through the data points are also shown in these plots.*

circular velocity $v(r)$ of a star is proportional to r, i.e.,

$$v(r) \propto r \quad . \tag{1.11}$$

On the other hand, for a star outside the central bulge region (the central buldge of a spiral galaxy contains the most of the mass of a galaxy) the circular velocity also follows Eq. 1.9 but $M(r)$ is replaced by the total mass of the galaxy $M_{\rm gal}$ which can be taken to be constant. Hence in this case the velocity $v(r)$ of a star is inversely proportional to $\sqrt{r}$, i.e.,

$$v(r) \propto \frac{1}{\sqrt{r}} \ . \tag{1.12}$$

Therefore the circular velocity of a star in a spiral galaxy should exhibit increasing behaviour with r in the central buldge region up to the distance $r_\odot$ from the centre of the galaxy, where $r_{\rm gal}$ is the radius of the central bulge region of the galaxy. However it should theoretically show Keplerian decline as $\frac{1}{\sqrt{r}}$ (Eq. 1.12) for the regions outside the central bulge. But the observational results for rotation curve for several spiral galaxies indicate $v(r) \sim$ constant up to a very large radius r in those regions. Thus from Eq. 1.9 we obtain

$$M(r) \sim r \ . \tag{1.13}$$

This indicates the presence of huge unseen mass beyond the reaches of the visible mass of the galaxy. The interpretation of such anomalous rotation curves of spiral galaxies as an evidence of dark matter halos was probably first proposed by Freeman [28] who noticed that the expected Keplerian decline was not present in NGC 300 and M33 galaxies. Later Vera C. Rubin and collaborators [29–31] and Bosma [32, 33] had carried out an extensive study, after which the existence of dark matter in spiral galaxies was widely accepted. They measured the velocity of hydrogen gas clouds in and near the Andromeda galaxy and noticed deviations of the orbital velocities (anomalous) of the hydrogen gas outside the visible edge of the galaxy from that predicted by the virial theorem. Van Albada et al. [34] analyzed the rotation curve of NGC 3198 spiral galaxy and the distribution of its hypothetical dark matter, concluding that this galaxy has a 'dark' halo. Few examples of galactic rotation curves are shown in Fig. 1.2.

- **Cosmic Microwave Background**

The most precise measurement of the amount of dark matter comes from the observation of the cosmic microwave background (CMB). The CMB is an echo of the decoupling of the photons from matter in the early Universe. This effect was first predicted by Gamow in 1948 [35, 36] and accidentally discovered by Penzias and Wilson 1965 [37, 38].

The CMB, a faint glow in microwave radiation, appears as an almost perfectly uniform background which fills the whole Universe. The CMB which is simply the leftover heat of the Big Bang was released as thermal radiation when the Universe became cool enough to become transparent to light and other electromagnetic radiation, about 380,000 years after the Big Bang. At this time, the Universe was filled with a hot, ionized gas. At the time when the CMB was initially emitted/created, it was not in the form of mostly visible and ultraviolet light. But over the past few billion years, due to the expansion of the Universe this radiation has been redshifted toward longer and longer wavelengths, until today it appears in the microwave band. The CMB peaks at a wavelength of about 2 mm with a nearly perfect blackbody spectrum corresponding to a temperature of 2.73 K. Although the CMB is extremely uniform, there are slight polarizations and variations in temperature throughout. These very faint features offer important glimpses into the physics of the early Universe. This almost perfectly uniform gas has very tiny deviations ($\sim$ 1 part in 10^5) from its homogeneity. The small changes in the intensity of the CMB across the sky (deviations of only 1 part in 10^5) give us a map of the early Universe [39, 40].

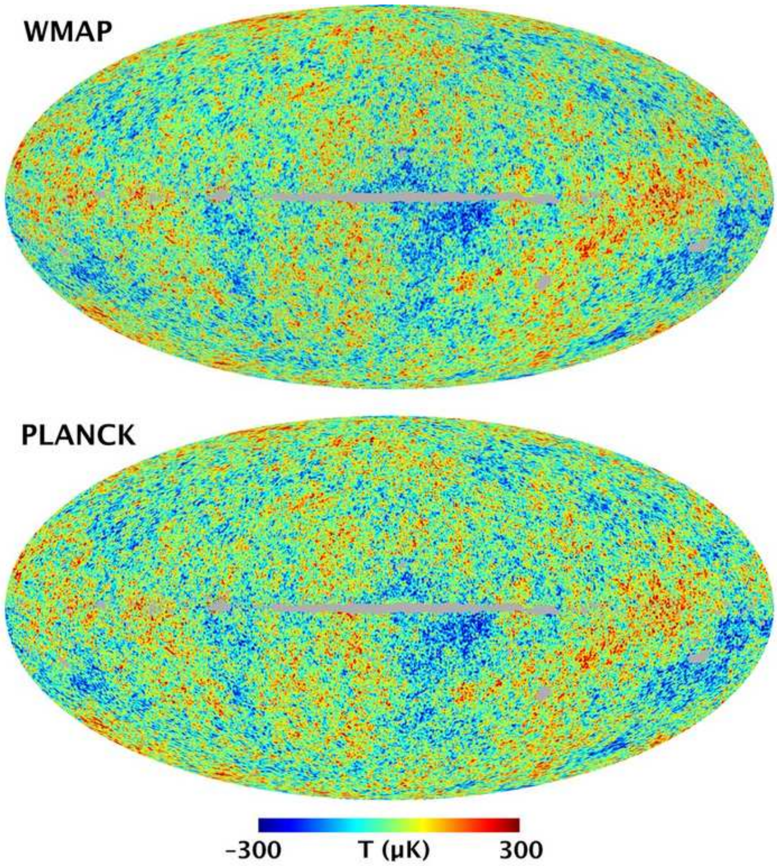

Figure 1.3: *The detailed, all-sky picture of the very early universe from both WMAP and Planck data. This image shows a temperature fluctuations in a range of* $\pm 300\ \mu K$ *around* $2.73\ K$*. The top image is the WMAP nine-year W-band CMB map and the bottom image is the Planck SMICA CMB map. Figure courtesy: WMAP Science Team.*

The observed temperature anisotropies in the sky can be expanded in terms of spherical harmonics

$$\frac{\delta T}{T}(\theta, \phi) = \sum_{l=2}^{\infty} \sum_{m=-l}^{l} a_{lm} Y_{lm}(\theta, \phi) \tag{1.14}$$

We can calculate exactly the variance of $a_{lm} Y_{lm}$ through

$$C_l \equiv \left\langle |a_{lm}|^2 \right\rangle \equiv \frac{1}{2l+1} \sum_{m=-l}^{l} |a_{lm}|^2. \tag{1.15}$$

Then, we can plot C_l as a function of l (in practice the quantity $l(l+1)C_l/2\pi$ is plotted against l) and fit a cosmological model to this data. The anisotropy in the spectrum of CMB is measured by the satellite-borne experiments such as Wilkinson Microwave Anisotropy Probe (WMAP) [41] and Planck [42]. In Fig. 1.3 the detailed all-sky maps of the observed temperature anisotropies from these observations are shown. Moreover, a typical CMB power temperature spectrum (obtained by WMAP) is shown in Fig. 1.4. By studying this spectrum, very important information regarding the evolution and composition of the Universe is obtained.

Most of the cosmological information from the CMB can be found by studying its power spectrum, a plot of the amount of fluctuation in the CMB temperature spectrum at different angular scales on the sky. The shape of this power spectrum is precisely determined by oscillations in the hot gas of the early Universe. Also the resonant frequencies and amplitudes of these oscillations are determined by its composition. Since the physics of hot gases is very well understood, the properties of the oscillating gas can be computed by studying the positions and relative sizes of these peaks. The position of the first peak, for example, provides valuable information about the curvature of the Universe while the ratio of heights between the first and second peaks denotes how much of the matter content is baryonic (ordinary matter). In practice, there are many variables that can affect all parts of the power spectrum and detailed numerical simulations are mostly required in order to get a more clear picture.

The physics of CMB provides the information on dark matter content of the Universe in the following way. Before the formation of the neutral hydrogen, the matter was supposed to be distributed almost uniformly in space although there can be small variations occurred in the density of both normal matter and dark matter due to the quantum mechanical fluctuations. Due to the influence of gravity, the matter content (normal matter as well as dark matter) are pulled toward the centre of each fluctuation. While the dark matter continued to move inward, the normal matter fell in only until the pressure of photons pushed it back. This caused the

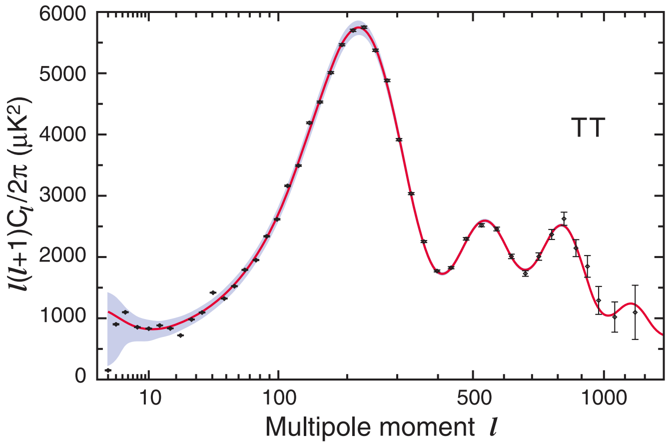

Figure 1.4: *The nine-year temperature power spectrum from WMAP. The WMAP data are shown in black with error bars. The best fit model is denoted by the red curve. the grey shaded region represents the smoothed binned cosmic variance curve. The results are shown as a function of multipole moment of the spectral functions that are used to quantify the angular size of the fluctuations observed by WMAP. Figure courtesy: WMAP Science Team.*

normal matter to flow outward until the gravitational pressure overcame the photon pressure. As a result the matter began to fall in once again. Each fluctuation had the certain frequency that depended on its size. Such fluctuation, in turn, influenced the temperature of the normal matter. The temperature heated up when the matter fell in and similarly it cooled off when the matter flowed out. The dark matter which being predominantly non-baryonic in nature does not interact with photons and therefore remained unaffected by this oscillating effect.

When the neutral hydrogen was formed, the temperature of the regions into which the matter had fallen increased than those of their surroundings. On the other hand, the regions from which the matter had streamed out became cooler. The temperature of the matter in different regions of the sky and the photons in thermal equilibrium with it should essentially reflect the distribution of dark matter in the initial density fluctuations as well as the oscillating normal matter.

- **Bullet Cluster**

The observation of Bullet Cluster such as galaxy clusters 1E0657-56, 1E0657-558 etc. [5, 43] provides one of the most promising evidences for dark matter [44]. The bullet cluster essentially consists of two colliding clusters of galaxies. The name "bullet" is stemmed from the fact that during the collision process the smaller subcluster passes through the core of the larger subcluster in the process of energetic explosion between the clusters and it looks like an event of passing through of focussed bullet. The main components of the clusters, namely, the visible mass (gas, galaxies, stars etc.) and the dark matter behave differently. The stars in the process of collision remain unaffected other than gravitational effects while the hot gas of the clusters, seen by X-ray telescope, are affected mostly by electromagnetic interactions because of their baryonic nature. On the other hand, the putative dark matter components of the clusters remain unaffected and can be measured by gravitational lensing (therefore, the bullet cluster is possibly the most popular example of a dark matter lens). Thus it provides a potential evidence for the existence of dark matter against various other propositions (e.g. Modified Newtonian Dynamics or MOND [45, 46]) as applied to the case of large galactic clusters.

Moreover, the spatial offset of the centre of the total mass of the cluster from that of baryonic mass peaks of the cluster (with statistical significance of 8σ CL) cannot be solely interpreted with altered form of gravitational force. In many propositions without the dark matter (such as MOND) the effect of lensing would supposedly follow the baryonic matter (such as X-ray gas). However, the lensing effect becomes strongest in two separated regions near (possibly coincident with) the visible galaxies. This eventually provides support for the idea that most of the mass content in the cluster pair is in the form of two regions of dark matter, which bypassed the gas regions during the collision. This also accords with predictions of dark matter particles to be only weakly interacting in nature other than the gravitationally interacting.

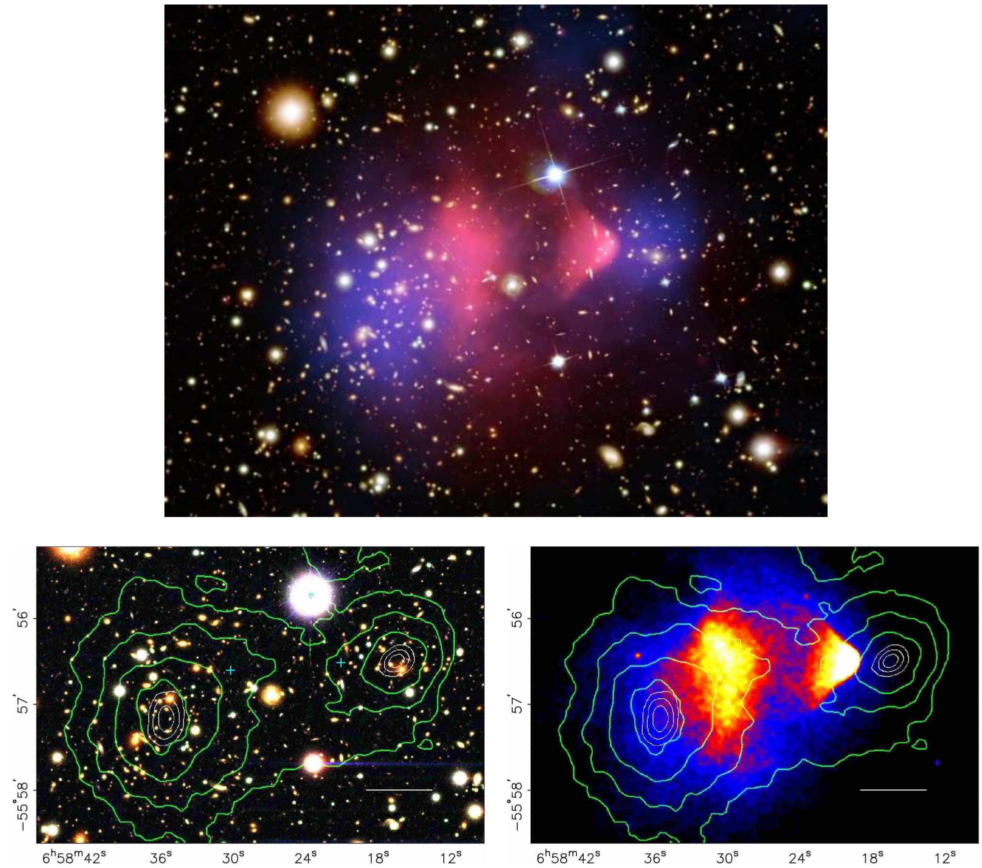

Figure 1.5: *Example of direct evidence for dark matter: Bullet Cluster. Top Panel: The Bullet Cluster 1E 0657-56. The red features in this figure represents X-ray emission from hot, intra-cluster gas. The gas cloud at the right appears to be distorted into the shape of a bullet from the collision. The blue features in this figure exhibit a reconstruction of the total mass from measurements of gravitational lensing in the region. Bottom Panels: the mass reconstruction of the Bullet Cluster 1E 0657-56 from Ref. [5]. The total mass of the two colliding clusters (mass density contours in green) as measured by gravitational lensing with VLT and Hubble satellite substantially differs from the visible matter (red and yellow), observed in optical wavelengths (left panel) and X-rays (right panel) by the CHANDRA satellite. Credit: X–ray: NASA/CXC/CfA/ M.Markevitch et al. [6]; Lensing Map: NASA/STScI; ESO WFI; Magellan/U.Arizona/ D.Clowe et al. [5]; Optical: NASA/STScI; Magellan/U.Arizona/D.Clowe et al. [5].*

The popular example of bullet cluster (1E 0657-56) is shown in Fig. 1.5. This astrophysical object is in fact two colliding clusters. In the plot (the top panel of Fig. 1.5) the mass estimated from the lensing map (in blue) exhibit large amounts of dark matter which does not appear in the map from the X-ray emission from hot, intra-cluster gas (in pink). The distribution of the two components (normal matter and dark matter) also gives crucial information on the properties of the dark matter. The dark matter halos have passed straight through both the gas clouds and each other and therefore appear to be undisturbed after such collision unlike the gas clouds. This hints that it is effectively collisionless (non-ineracting) in nature. The plots in the bottom panel of Fig. 1.5 show the deviations of total mass of the clusters (measured via gravitational lensing) from those observed in optical (left plot) and X-ray (right plot) wavelengths.

- **Gravitational Lensing**

According to the theory of General Relativity, the presence of any mass can cause the space in its vicinity to curve. This curved space then defines the geodesic. The result of such curved geodesics is the bending of light rays around any massive bodies [47]. Therefore, the light rays coming from the background objects can be lensed by the mass of the foreground objects as they pass through the gravitational field of the foreground objects. As a result, those light rays are bent towards a distant observer. Therefore, the observer who is situated in the foreground of such a lensing massive body may visualise multiple images (or distorted images) of the object which is located in the background of the gravitating mass at some appropriate distance. The gravitating mass present in between the observer and the distant object, thus acts as a lens to the light rays that are coming from the distant background object. Since such bending of space due to the gravitational mass lenses the divergent light rays from the background object, it may produce multiple images of the background object or the brightness of the background object increases. The observation of 'Twin Quasar' ('Twin QSO') SBS 0957+561 was the first identified gravitationally lensed object [48]. Therefore, this phenomena of gravitational lensing provides a very clean and powerful tool to probe the distribution mass present in the foreground

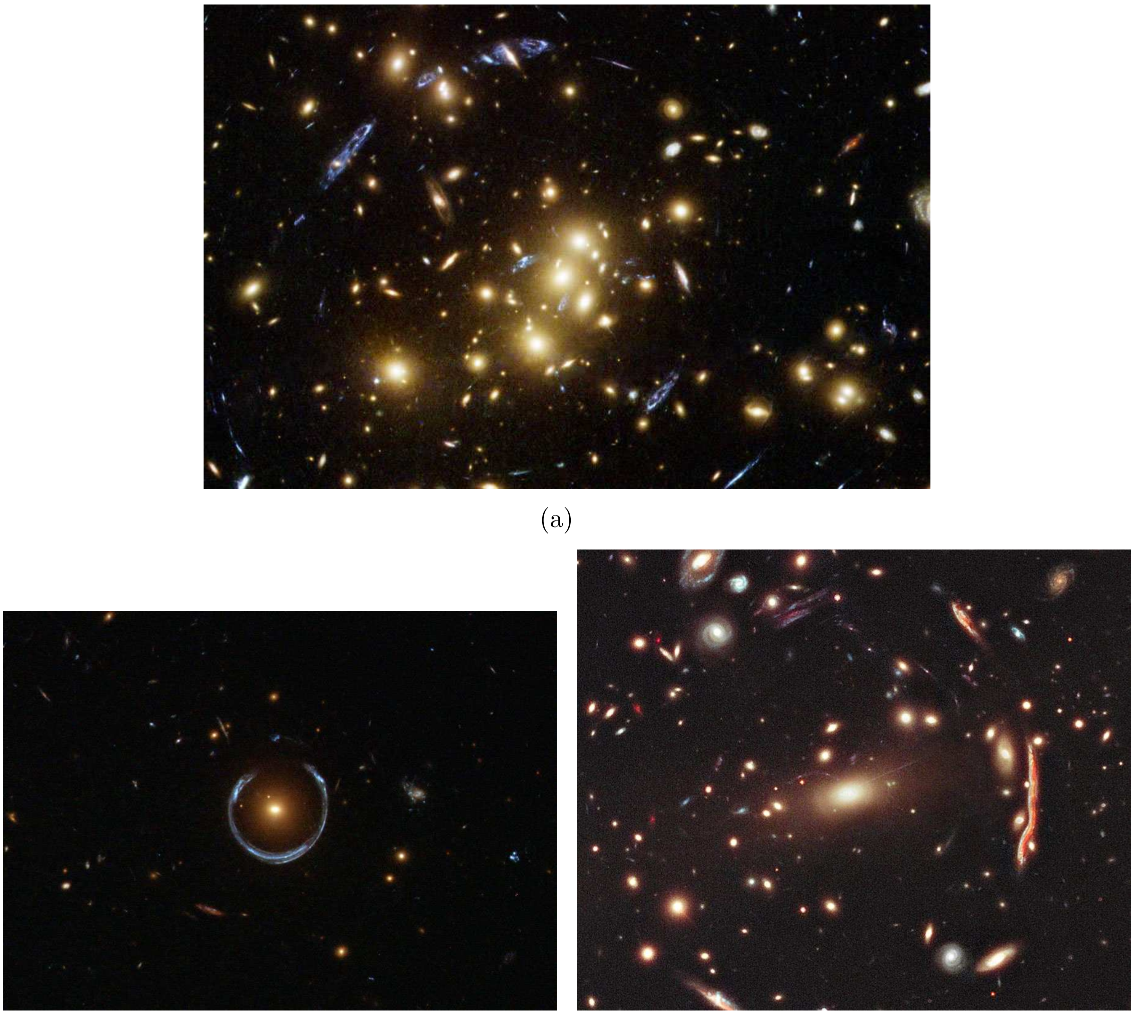

(a)

(b) (c)

Figure 1.6: *Examples of strong gravitational lensing. Panel (a): The dark matter enriched galaxy cluster CL0024+1654 acts as a lens and as a result many blue images of a distant galaxy appear. Credit: NASA, ESA, H. Lee & H. Ford (Johns Hopkins U.) [7]. Panel (b): 'the Cosmic Horseshoe'. The Luminous Red Galaxy LRG 3-757 acts as a lens to the distant blue galaxy. Due to the precise alignment an almost complete ringlike shape (horseshoe) appears. Credit: ESA/Hubble & NASA. Panel (c): the cluster MACS J1206.2-0847 lensing the image of a yellow-red background galaxy into the huge arc (right portion). Credit: NASA, ESA, M. Postman (STScI) & the CLASH Team.*

object [49, 50].

There are three classes of gravitational lensing, namely, strong gravitational lensing, weak gravitational lensing and microlensing. When the deflection of light is caused by the effect of very strong gravitational field of the massive objects present between the distant object and the observer, the effect of lensing is very strong enough to produce noticeable effects such as multiple images, arcs and the Einstein-Chwolson ring. When the distant object, lensing mass and the observer are exactly aligned, the Einstein-Chwolson ring appears to the observer as an effect of strong lensing. In other words, the distant object is situated exactly behind a symmetric massive lensing body from the view of the observer in such situation. The angular size (the Einstein radius) of such ring is given by

$$\theta_{EC} = \sqrt{\frac{4GM}{c^2}\frac{d_{LO}}{d_L d_O}} \ , \tag{1.16}$$

where G, M, c are the gravitational constant, mass of the lensing body and the velocity of light respectively. In the above, d_{LO}, d_L and d_O denote the angular diameter distances measured from the observer between the lens and the objects, to the lens and to the object respectively. When the object, lens and the observer are not aligned, i.e., when the asymmetry among their positions is partially broken, arcs or multiple images of the object can be observed. In both cases mass distributions of the lensing mass can be reconstructed using the observed deflections. Comparison of the mass obtained using gravitational lensing with that inferred from luminosity gives a mismatch and hence hints the presence of dark matter in those sites. Examples of such strong gravitational lensing are given in Fig. 1.6. On the other hand, weak gravitational lensing occurs when the light rays from the distant object pass through the gravitational field which is not strong to produce effects as in strong lensing case but strong enough to make slight deflections. Since most of such observed lensing phenomena belong to weak gravitational regime, the technique for measuring mass via 'weak gravitational lensing' is applied there. Since the distortion for a single background object is much smaller compared to the strong lensing

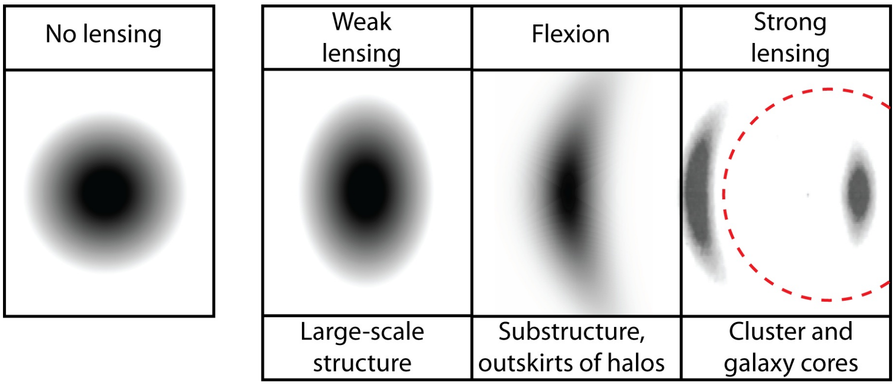

Figure 1.7: *The different regimes of gravitational lensing image distortion. The effect of lensing due to the passage of massive galaxies or clusters of galaxies results several distortions of the image of the circular source (in black and grey shadow) appeared to the observer (from Ref. [8])*

case, the foreground mass can be detected by considering a systematic alignment of background sources around the lensing mass and analysing such large number of background sources to obtain coherent distortion in a statistical fashion. The coherent shear distortion produced by the presence of mass along such line of sights can be measured averaging over large numbers of distant galaxies (background objects). This shear distortion can be used to reconstruct the mass distribution, particularly the background distribution of dark matter in this region [8] without requiring any assumption of their dynamical state. Another physical effect, namely, microlensing caused by the gravitational lensing is used to probe lensing mass via observations. Unlike the cases of strong and weak lensing where the lenses are generally galaxies and galaxy clusters and therefore the mass of the lens is large enough to produce resolvable deflections of light rays at the telescope, the mass is too low for the case of microlensing and usually of the planet or star scale. Hence deflection of light in case of microlensing is hard to detect. But the apparent brightness of the object which changes as the lensing mass pass by the object can be detected and thus the lensing mass can be measured [51–53]. The various possible types of distortions caused due to gravitational lensing effects are shown in Fig. 1.7.

- **The Large Scale Structure of the Universe**

The Universe, on large scales, shows an abundance of structures. The galaxies are assembled to form clusters which are part of superclusters. Moreover, the arrangements of such superclusters form large-scale sheets, filaments and voids (shown in Fig. 1.8). This cosmic scaffolding has been probed by large-scale surveys like 2dF-GRS (the 2-degree Field Galaxy Redshift Survey) [54, 55] and SDSS (the Sloan Digital Sky Survey) [56]. This interesting pattern of such galactic superstructure is expected to reflect the formation of gravitational clustering of matter since the epoch of Big Bang. Dark matter, if present during the structure formation, should, therefore, highly influence such large-scale structure formation in the Universe.

Large-scale cosmological N-body simulations such as Millenium, NFW, Aquarius, Vialactea, Vialactea-II etc. reveal that the observed large-scale structure of luminous baryonic matter could only have been constructed in the presence of a substantial amount of dark matter [57–60]. Moreover, in order to produce the structures in accordance with the observed ones, the most of dark matter must be cold and non-dissipative. The term 'cold' in this context signifies that the dark matter particles must have a very non-relativistic motion and have a very short free-streaming length (less than the size of a gas cloud undergoing gravitational collapse). Furthermore, dark matter is cold in the sense that the dark matter particles can gravitationally accumulate on small scales and therefore seed for the formation of galaxies. Also, its non-dissipative nature prevents it from cooling and collapsing with the visible matter, which would eventually form larger and more abundant galactic disks than observed. However, hot (highly relativistic) and warm (in between relativistic and non-relativistic) dark matter could still be a fraction of the total dark matter content, though magnitude of such fraction critically relies on the its warmness.

The amount and the pattern of the structures in the Universe as well as the the

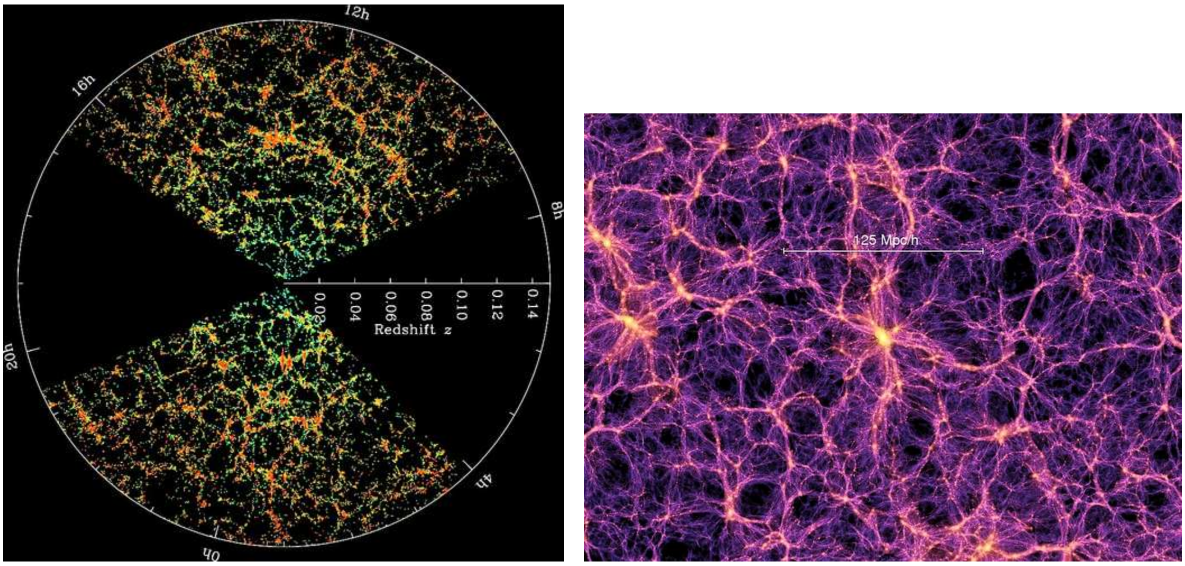

(a) (b)

Figure 1.8: *Large scale structures of the Universe are shown. Panel (a): the 3-dimensional map of the distribution of galaxies from the SDSS with the earth at the centre of the plot. Credit: M. Blanton and the Sloan Digital Sky Survey. The radius of the circle is at distance of very high redshift (2 billion light-year). Each point in this plot denotes a galaxy that contains about 100 billion stars. The colour of each point (galaxy) represents the ages of the stars within the galaxy. The red zones denote clustered points representing galaxies made of older stars. Panel (b): the distribution of dark matter at large scale in the Universe obtained in the Millennium simulation. From the Millennium Simulation Project webpage.*

total mass contained within those structures can be well estimated by the large-scale galaxy surveys [55, 56, 61]. The mean baryonic density in the Universe determines the characteristic size of density perturbations of the baryonic matter. These baryonic density perturbations can sustain till matter-radiation equality condition holds and then collapse to yield structures such as galaxies and clusters [62]. The perturbations which are smaller in size are erased by radiative and neutrino damping and those with larger size fragment. Since dark matter interact gravitationally with the baryonic matter, the power spectrum of the perturbations that ultimately sustain to produce galaxies is altered by the presence of such dark matter which enhances the gravitational clustering. This results the power spectrum of the large-scale galaxy structure to depend strongly on the total matter content in the Universe and rather weakly on the baryonic matter fraction. Recent surveys measure the total matter (sum total of dark matter and visible matter) density of $\Omega_{\rm m} \equiv \rho_{\rm m}/\rho_{\rm c} \approx 0.29$ [61], where $\rho_{\rm c}$ denotes the critical density of the Universe. surveys indicate a total matter (i.e. dark plus luminous matter) density of $\Omega_{\rm m} \equiv \rho_{\rm m}/\rho_{\rm c} \approx 0.29$ [61], where $\rho_{\rm c}$ is the critical density required to close the Universe.

- **Big Bang Nucleosynthesis**

According to the popular cosmological model (the Big Bang Cosmology), the very early Universe was in an extremely hot and dense state. The protons and neutrons were bounded or fused in the primordial fireball to form the light elements as the temperature of the Universe cooled off to become the order of an MeV. However, the Universe was so hot during the first second after the Big Bang that atomic nuclei could not form. Therefore, the space is contained only with a very hot soup of protons, neutrons, electrons, photons and many short-lived particles. At this epoch, sometimes, a proton and a neutron collided and bounded together to form a nucleus of deuterium (a heavy isotope of hydrogen). But high-energy photons at such high temperatures instantly broke such bound state [63].

At the subsequent stages of the Universe when its temperature was lowered, these high-energy photons became rare enough to make deuterium nuclei to survive. Moreover, these deuterium nuclei could keep bounding to other protons and neutrons to form the nuclei of helium-3, helium-4, lithium, and beryllium. This process of element-formation at the early Universe is termed as "nucleosynthesis". The abundances of the formed light elements strongly depend only on the nuclear reaction rates and the baryon-to-photon ratio (η) at the time. Therefore, various laboratory-based measurements and theoretically-calculated nuclear reaction rates (such as NACRE [64]) can be utilised in order to estimate the primordial abundances of the

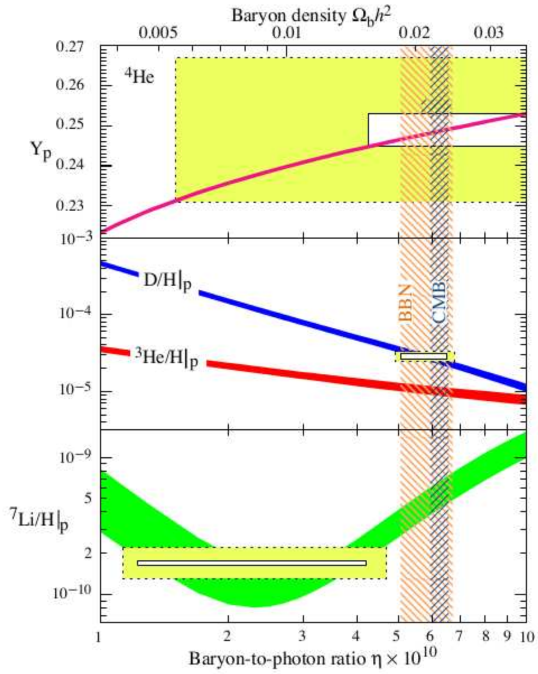

Figure 1.9: *The prediction of abundances of lighter elements ^{4}He, D, ^{3}He, ^{7}Li from the standard model of Big Bang Nucleosynthesis (BBN). The bands in the plot represent abundance values at 95% CL for different baryon-to-photon ratios (η). The boxes in this plot denote the observed abundances of those elements. The BBN concordance range and the cosmic baryon density (CMB) are shown by vertical boxes. From Ref. [9].*

elements as a function of η [65–67], as shown in Fig. 1.9. The baryon-to-photon ratio η is proportional to $\Omega_b h^2$ and therefore completely equivalent to $\Omega_b h^2$, where Ω_b is the baryon density of the Universe and h is the dimensionless Hubble parameter (the Hubble constant in the units of $100\,\mathrm{km\,s^{-1}\,Mpc^{-1}}$) measured as $h = 0.72 \pm 0.08$ [68]. Therefore, the primordial value of Ω_b can be measured by Big Bang Nucleosynthesis (BBN) using the observations of the true primordial abundances of the elements and precise measurement of h. However, the primordial abundances of the light isotopes are difficult to estimate and this requires direct observations of extremely unevolved systems.

As the Universe expands, however, the density of protons and neutrons decreases and the process of nucleosynthesis slows down. Neutrons are unstable (with a lifetime of about 15 minutes) unless they are bound up inside a nucleus. After a few minutes, therefore, the free neutrons will be unavailable and nucleosynthesis will stop. There is only a small window of time in which nucleosynthesis can take place, and the relationship between the expansion rate of the Universe (related to the total matter density) and the density of protons and neutrons (the baryonic matter density) determines how much of each of these light elements are formed in the early Universe.

The universal abundances of D, ^{3}He, ^{4}He, ^{7}Li (also ^{6}Li) fixed at three minutes after the Big Bang are predicted by the theory of BBN [69]. The abundances of those elements measured at much later epochs after the beginning of stellar nucleosynthesis, are different from BBN prediction since the process of stellar nucleosynthesis alter the abundances of such light elements from their primordial values. Also heavy elements and metals such as C, N, O and Fe are produced in this process in the stellar sites. Therefore, astrophysical sites with low metallicities are ideal places to observe in order to precisely determine the primordial abundances of such light elements. However, systematic uncertainties are often involved in such measurements.

The presence of deuterium (D) in high-redshift, low-metallicity quasar absorption systems is revealed by high-resolution spectra from its isotope-shifted Lyman-α absorption. Since there is no astrophysical sources of deuterium, any detection would therefore gives lower limit of D/H ratio and thus upper limit of η. Since deuterium is simply wiped out inside stellar interiors and it is not yielded substantially by other different processes, the abundance of D therefore steadily decreases with time. The absorption lines in very old hydrogen clouds illuminated from behind by high-redshift quasars are observed and subsequently extrapolated backwards towards the era of nucleosynthesis in order to obtain the D/H ratio.

On the other hand, ^{3}He is produced and destroyed inside stellar interiors, the interstellar medium as well as in the atmosphere of Earth. Since ^{3}He is observed at the Solar system and high-metallicity (Galactic H II regions) regions in Milky Way Galaxy, the estimation of the primordial abundance of ^{3}He is very difficult to predict precisely. Therefore, the observations of emission lines from the Galactic H II regions or protosolar nebula can provide the so far best upper limits on the primordial abundance of ^{3}He. In addition, models for stellar nucleosynthesis of ^{3}He are not well understood. Hence ^{3}He is not considered as proper cosmological probe.

^{4}He is substantially produced in the process of hydrogen fusion via *pp*-chain in stars and can be observed in the clouds of ionized hydrogen (H II regions). Therefore stellar ^{4}He abundance is much more than BBN production. The data on ^4He and CNO in those observational sites the small stellar contribution to helium is positively correlated with metal production. The extrapolation of such measurement to zero metallicity provides primordial ^{4}He abundance.

Primordial abundance of lithium (Li) plays a major role in the physics of BBN and gives hint the new physics. The extremely metal-poor stars in the spheroid (Pop II stars) of Milky Way Galaxy with metallicity of the order of 10^{-4} or 10^{-5} times solar value are good targets for the observation of ^{7}Li in absorption in the atmospheres of such low metallicity stars. Stellar determination of Li abundances typically consists of contributions from both lithium isotopes ^{6}Li and ^{7}Li. The abundance of ^{7}Li shows a plateau nature with decreasing metallicity [70]. The abundance of another lithium isotope ^{6}Li is confirmed in those stars [71] but in very small amount compared to ^{7}Li. However, the presence of ^{6}Li can be deduced/menifested only from the precise measurements of the isotopic and thermal broadening of spectral lines. The three-dimensional effects of convection related to those lines and the deviation from local thermodynamic equilibrium (LTE) on those line shapes are considered. The indication of ^{6}Li plateau (analogous to the observed ^{7}Li plateau) hints the major primordial abundance of ^{7}Li. Apart from those lighter elements discussed above, the heavier elements are not considered since precise observational measurements can hardly be done from their primordial abundances.

According to the prediction obtained from nucleosynthesis data, the baryonic matter makes up 0.04 of the critical cosmological density ($\Omega_{\rm b} \approx 0.04$) with baryon-to-photon ratio $\eta \approx 6 \times 10^{-10}$ [72]. Such baryon density can be estimated much consistently from the measured abundances of D and the He isotopes. Although for the case of lithium isotopes, the corresponding prediction for Li abundances shows discrepancy with the observational result. ^{7}Li is found to be under-abundant relative to the BBN prediction. Moreover, ^{6}Li is not expected to have been yielded in BBN at all. The lithium isotopes are exposed to various stellar processes in stellar layers as well as in the interstellar medium. Also the stellar measurements are difficult since they involve precise determination of several quantities such as the fine points of detailed convective line shapes in stars and the input atomic data required for isotopic shifts and non-LTE calculations etc. The most interesting resolution of the lithium problem may involve non-standard BBN caused by particle physics beyond the Standard Model including some choices of dark matter models [73].

The presence of dark matter is therefore indisputably inferred together by the independent measurements of $\Omega_{\rm m}$ from large-scale structure formation and $\Omega_{\rm b}$ from BBN. Since all the luminous matter should be part of baryonic matter content of the Universe, the difference between the measured quantities $\Omega_{\rm m}(\approx 0.29)$ and $\Omega_{\rm b}(\approx 0.04)$ implies that the leftover matter ($\Omega_{\rm leftover} \approx 0.25$) must be in the form of dark matter in the Universe. Furthermore, from the above information it can be concluded that the dark matter particles must be predominantly non-baryonic in nature. Therefore, essentially they do not interact electromagnetically and are dissipationless. It may also be noted in this context that a small portion of dark matter may be baryonic in nature (discussed afterwards in this chapter). In this thesis work, we consider dark matter particles to be the dominant, non-baryonic component.

- **X-ray Observation**

Another possible method to probe the dark matter in the galaxies and galaxy clusters is to probe the gravitational potential of a galaxy via the X-ray observations from those sites. Furthermore the density distribution of the galaxy can also be inferred from such observation. In order to make a theoretical estimate of such technique, let us consider a thin shell of hot X-ray emitting gas outside the galaxy which consists of stars, gas and dark matter. The gravitational force field due to mass (mass of gas, stars, dark matter) enclosed by the shell will try to pull such shell of hot gas inward. On the other hand, the pressure gradient of the gas shell, if the pressure decreases outward, will try to push the shell outward. This two forces make a balance in hydrostatic equilibrium condition and hence the gravitational mass of the galaxy can be inferred via the estimation of pressure gradient from X-ray observations. The difference between the gravitational mass and the visible mass of the galaxy therefore suggests the evidence for dark matter [74].

If we consider the elliptical galaxy to be spherically symmetric for simplicity. The gravitational force on the shell of hot gas at radius r (of width dr) due to the enclosed mass is

$$F_g(r) = \frac{GM(< r)M_s}{r^2}\,, \tag{1.17}$$

where $M_s = 4\pi r^2 \rho_{\rm gas}(r) dr$ is the mass of the hot gas shell. In the above, $M(< r)$ is the total mass enclosed inside the shell of radius r (consisting of stars, gas and dark matter; $M = M_\star + M_{\rm gas} + M_{\rm DM}$), and dr is the thickness of the shell. Since the pressure force on a surface is pressure times the surface area of the shell, the net outward force is the difference between the outward and inward pressure forces.

Expanding the pressure in a Taylor series, such force is given by

$$F_p(r) = 4\pi r^2 (p(r) - p(r + dr)) = -4\pi r^2 \frac{dp}{dr}\, dr\,, \tag{1.18}$$

where $p(r)$ is the pressure in the hot gas and $4\pi r^2$ is the surface area of the shell of width dr. In hydrostatic equilibrium, the two forces in Eq. 1.17 and Eq. 1.18 balance and therefore

$$\frac{GM(< r)}{r^2} 4\pi r^2 \rho_{\rm gas}(r) dr = -4\pi r^2 \frac{dp}{dr} dr\,, \tag{1.19}$$

and hence

$$\frac{GM(< r)}{r^2} = -\frac{1}{\rho_{\rm gas}(r)} \frac{dp}{dr}\,, \tag{1.20}$$

Alternatively the above equation can be written in terms of the gravitational potential Φ

$$\nabla\Phi = -\nabla p / \rho_{\rm gas}\,. \tag{1.21}$$

The above equation is similar to hydrostatic equilibrium in stars.

Now the temperature of the hot gas $T_{\rm gas}(r)$ can be determined by modelling the X-ray spectrum as function of position. Also since the X-ray intensity is $\propto \rho_{\rm gas}^2 T_{\rm gas}^{1/2}$, the radial gas density $\rho_{\rm gas}(r)$ can be estimated. The pressure is $\propto \rho_{\rm gas} T_{\rm gas}$ and can be written as

$$p = \frac{\mathrm{k_B}\, T_{\rm gas}}{\mu\, m_{\rm H}}\, \rho_{\rm gas}\,. \tag{1.22}$$

where μ is the mean or average molecular weight (chosen to be 0.6) and $m_{\rm H}$ is the mass of hydrogen atom. Substituting the expression for p from Eq. 1.22 in Eq. 1.20 we get,

$$GM(<r) = -\frac{\mathrm{k_B}T}{\mu\, m_\mathrm{p}} r^2 \left(\frac{d\ln\rho_\mathrm{gas}}{dr} + \frac{d\ln T_\mathrm{gas}}{dr} \right), \tag{1.23}$$

$$= -\frac{\mathrm{k_B}T}{\mu\, m_\mathrm{p}} r \left(\frac{d\ln\rho_\mathrm{gas}}{d\ln r} + \frac{d\ln T_\mathrm{gas}}{d\ln r} \right). \tag{1.24}$$

From the above expression the gravitational potential can be reconstructed and hence the mass distribution can also be determined. We can also obtain an approximate expression for the density profile if the temperature T_gas remains approximately constant. If we take T constant then the rhs of Eq. 1.20 becomes $-\frac{\mathrm{k_B}\, T_\mathrm{gas}}{\mu\, m_\mathrm{p}} d\ln(\rho_\mathrm{gas})/dr$ and hence

$$GM(<r) = -\frac{\mathrm{k_B}T_\mathrm{gas}}{\mu\, m_\mathrm{p}} r^2 \frac{d\ln\rho_\mathrm{gas}}{dr}. \tag{1.25}$$

Since $dM(<r)/dr = 4\pi\, r^2\, \rho_\mathrm{tot}$ where ρ_tot denotes the total mass density due to stars, gas and dark matter, the derivative of both sides of Eq. 1.25 with respect to r gives

$$G4\pi r^2 \rho_\mathrm{tot} = -\frac{\mathrm{k_B}T_\mathrm{gas}}{\mu\, m_\mathrm{p}} \frac{d}{dr}(r^2 \frac{d\ln\rho_\mathrm{gas}}{dr}), \tag{1.26}$$

Now with the assumption of the gas density and total mass density being proportional, $\rho_\mathrm{gas} \propto \rho_\mathrm{tot}$, a solution of the form $\rho_\mathrm{tot} = \rho_0\, (r_0/r)^\beta$ for the above equation will give $\beta = 2$ in which case

$$\rho_\mathrm{tot}(r) = \frac{\mathrm{k_B}\, T_\mathrm{gas}}{2\pi\, G\mu m_\mathrm{p}}\, r^{-2}. \tag{1.27}$$

Therefore a measurement of T can constrain the total mass density ρ_tot. On the other hand, the stellar mass density ($\rho_\star$) can be estimated from the luminosity and the gas density ($\rho_{\rm gas}$) from the X-ray emissivity. Hence the density of dark matter can also be determined by the relation $\rho_{\rm DM} = \rho_{\rm tot} - \rho_{\star} - \rho_{\rm gas}$. More detailed modelling of this type confirms that elliptical galaxies also have most of their mass in the form of dark matter.

The method of hydrostatic equilibrium condition which has advantages over the optical determination of mass has been used to determine the total gravitational mass and density distribution of the galaxy. However, the most X-ray observations of clusters do not have very good spectral resolution and give precise measurement of density rather than the temperature. The most successful application of hydrostatic method has been with M87 galaxy in the virgo cluster [75,76]. The X-ray observation at that site are consistent with a total mass of

$$M(r) = (3-6) \times 10^{13} M_{\odot} \frac{r}{300\rm kpc} \,. \tag{1.28}$$

At a very large radii $r > 100$ kpc, the total mass-to-light ratio, $\frac{M}{L_B}_{tot} > 150 \frac{M_{\odot}}{L_{\odot}}$ and a local value $\frac{M}{L_B}_{loc} > 500 \frac{M_{\odot}}{L_{\odot}}$ [76]. This implies the huge presence of dark matter in the region around M87 galaxy. Although whether the dark matter halo is centered around M87 galaxy or there is a distributed dark matter halo of the entire cluster remained unclear.

The hydrostatic method has been widely implemented for estimation of the mass of other clusters such as Coma and Perseus. The total mass of Coma cluster as derived by Hughes (1989) [77] lies to be within 5 Mpc as $2 \times 10^{15} M_{\odot}$ and the mass-to-light ratio, $\frac{M}{L_B}_{tot} \sim 165 \frac{M_{\odot}}{L_{\odot}}$. But the estimated values have high uncertainty due to lack of spectral and spatial resolutions.

- **Lyman Alpha Forest**

Lyman alpha system is an useful cosmological tool to probe various information of physical Cosmology. It can be used to unravel some properties of Dark Matter. Lyman alpha lines arise when an electron of hydrogen atom makes a transition from the higher energetic state to the ground state and thus the hydrogen atom emits some emission lines. Conversely, when a hydrogen atom is exposed to an electromagnetic radiation of proper energy, the electron of the atom is excited or boosted from the ground state energy level to the higher energetic state. In this case, the energy of the electromagnetic wave is absorbed by the atom. Hence the wavelength of such absorbed energy will be missing from the energy spectra and it appears to be an absorption line to an observer. Since the intergalactic medium contains large amount of neutral hydrogen, the series of similar absorption lines that represents the excitation of ground state hydrogen atoms are known as Lyman alpha system. The system of absorption lines appears as a 'forest' of lines since each line gets redshifted towards larger wavelength by a different amount in proportion to the distance of the absorbing gas cloud from the observer. This is illustrated in Fig. 1.10. The Lyman-alpha forest was first discovered in 1970 by astronomer Roger Lynds in an observation of the quasar 4C 05.34 [78] by observation of unusually large number of absorption lines in its spectrum. Although initially the forest was thought to be originated from physical interactions within QSOs (Quasi Stellar Object), later it was confirmed to be due to the absorption of interstellar gas distribution in superclusters.

If there exist a lot of neutral hydrogen atoms in their ground state, they will certainly absorb more radiation. Therefore if one looks at the intensity of the received spectra as a function of wavelength, there will be dip in the intensity at certain wavelength (e.g. ~ 1215.67 Angstrom in the UV region) that undergoes the absorption. This depends on the amount of neutral hydrogen present in its ground state. The amount of light absorbed (also known as the 'optical depth') is thus proportional to the probability (or cross section) that the hydrogen will absorb the photon

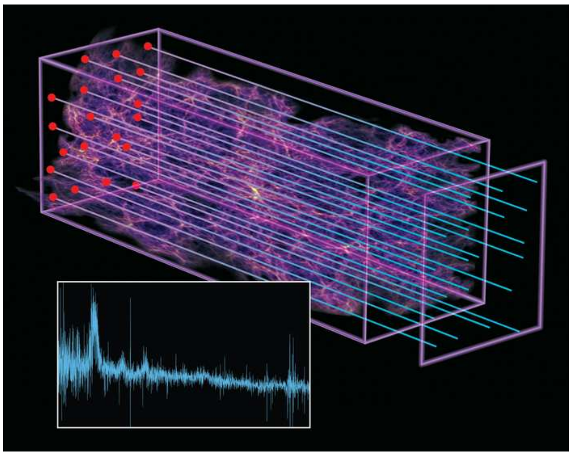

Figure 1.10: *Lyman Alpha Forest. Light rays from distant quasars (red dots) get partially absorbed as they pass through clouds of intergalactic hydrogen gas. A 'forest' of hydrogen absorption lines in the spectrum of an individual quasar (figure in box), collected by the spectrograph of telescope, traces denser clumps of gas along the line of sight. By reconstructing of three-dimensional map of such invisible gas, the large-scale structure of the early Universe as well as the nature of dark matter can be probed. Illustration Credit: Zosia Rostomian, Lawrence Berkeley National Laboratory; Nic Ross, BOSS Lyman-alpha team, Berkeley Lab; and Springel et al., Virgo Consortium and Max Planck Institute for Astrophysics.*

times the number of hydrogen atoms along the path of photon propagation. Generally such Lyman alpha forest is observed in the spectra of distant high-luminous quasi stellar radio objects or quasars. Quasars (or QSO) which belong to a class of the active galactic nuclei are very high energetic objects located at very high redshifts and emit electromagnetic radiations including X-rays, UV, optical, radio and gamma energies. The emitted light when travels to a distant observer (at earth) passes through the intergalactic medium containing neutral hydrogen and gets absorbed at certain wavelength. Since the Universe is expanding, the QSO-emitted photons suffer redshifts to somewhat higher wavelengths on arriving at the observer. Needless to mention that the hydrogen-absorbed wavelengths (or the Lyman alpha absorption lines) are also redshifted. Hence a distant observer would observe such Lyman alpha absorption line at a shifted wavelength from that which corresponds to the absorbed wavelength at the particular site of intergalactic medium at earlier time. Thus the Lyman alpha forest contains information of the neutral hydrogen content of the intergalactic medium. From the known value of expansion rate of the Universe (Hubble parameter), one can trace back the positions of region of intervening hydrogen in the intergalactic medium between us and the quasar using the absorption map. Therefore the absorptions at different positions of interstellar medium leave their signatures at different redshifted absorption-line.

Before the advent of dark matter proposition, it was thought that the absorption systems which were supposed to be discrete, pressure-confined gas clouds in thermal, hydrostatic and ionisation equilibria were confined by the pressure of hotter and more tenuous intercloud medium and float in intergalactic space. But the model fails to reproduce the observed large range in column densities and evolution of absorption systems with redshifts. Also it lacks to confront the observational evidence of CMB by COBE (Cosmic Background Explorer) satellite which discards the scenario of hot intercloud medium. Now since the dark matter in the cosmological scale interacts gravitationally with the interstellar matter, the interstellar gas forms large scale structures (flattened or filamentary structures) by the influence of such putative cold dark matter. This cosmic web of interstellar gas can be traced by analyzing the Lyman alpha forest. The gravitational collapse of dark matter can trap baryonic matter considerably. The structure formation mechanism invoked by cold dark matter scenario generates collapsed cold dark matter halos in a large amount. But the masses of individual halos are so small that they are unable to form galaxies or stars. The intergalactic gas, on the other hand, tends to accrete on such small dark matter halos or filaments but is resisted by its thermal gas pressure and eventually form a stable gaseous configuration which can only be envisaged in absorption spectra. The cosmological hydro-simulations (N-body simulations) based on hierarchical structure formation models has subsequently confirmed the cosmic web-like structures that give rise to the Lyman alpha forest. In addition, the scenario of hot dark matter is also discarded from the observation of the forest.

1.3 Nature of Dark Matter

Depending on different production mechanisms, the dark matter candidates differ among themselves in respect of the order of velocities of their particles. Therefore, on the basis of the velocities of dark matter particles at the time of freeze out, the class of dark matter candidates can be broadly divided [79] as

- **Hot Dark Matter (HDM)**

  Hot dark matter (HDM) particles are supposed to move at relativistic velocities during the era of galaxy formation or structure formation. A dark matter candidate is termed as *hot* if the velocity of such dark matter particle is relativistic at the time of freeze out. Quantitatively the factor x_f which is defined by the ratio $\frac{m}{T_f}$ with m and T_f being the mass and freeze out temperature of the dark matter is respectively $\lesssim 3$ [80]. The hot dark matter particles tend to damp the primordial density fluctuations below their free-streaming length similar to Silk damping effect which happens during the recombination era due to the free-streaming of photons. One potential candidate for such HDM is the massive neutrinos (the Standard Model neutrinos but with non-zero mass) with a mass in the eV range (should be less than 100 eV). Hot DM particles have a cosmological number density roughly comparable to that of the microwave background photons implying an upper bound to their mass of a few tens of eV. This implies that the free streaming of these relativistic particles destroys any fluctuations smaller than the supercluster scale, $\sim 10^{15} M_{\odot}$. Therefore, the free-streaming length of such HDM particles (neutrinos) is nearly about supercluster scale. Moreover, HDM predicts top-down hierarchy in structure formation whereby the small scale structure are formed in the fragmentation of larger structures, in contrast to the observations (some galaxies older than superclusters has been observed). The possibility of such neutrinos being HDM candidate is yet to be ruled out by the current observational limits on neutrino mass and the very low interaction cross-section for these relic neutrinos hinders their detection. Although it has been concluded in modern N-body simulations that such neutrinos cannot solely account for the observed large scale structure formation of the Universe, since the density fluctuations in the early Universe needs to be sustained in order to form such structures (galaxy, galaxy clusters etc.). Strong constraints on HDM has been imposed from the observation of Lyman α forest and also from WMAP or Planck observations.

- **Cold Dark Matter (CDM)**

Cold dark matter particles are *cold* in the sense that these dark matter particles are non-relativistic during structure formation and permits formation of small scale clumping. In CDM scenario, the dark matter particles are freezed out at a temperature much greater than the mass of dark matter particles and hence non-relativistic at the time of freeze out. The factor x_f is therefore $\gg 3$ [80]. The free streaming of such CDM particles is of no great cosmological importance. These type of particles are much favoured by simulations of large scale structure formation (N-body simulations) since CDM can well account for the observed large scale structures such as cluster abundance and galaxy-galaxy correlation functions. The CDM particles are mainly categorised mainly into two different scenarios of elementary particles: heavy thermal remnants of some annihilation process such as supersymmetric neutralinos and a cold Bose condensate such as axions. Out of these possibilities, the popular candidates for CDM are Weakly Interacting Massive Particles (or WIMPs) which bear strong motivation in extensions of the Standard Model and will be studied throughout this thesis in the context of several particle physics models for cold dark matter. In spite of its huge success, this type of dark matter (CDM) suffers several discrepancies between numerical predictions and the observations [81] such as 'missing satellite' problem [82], 'core-vs-cusp' problem [83], 'too-big-to-fail' problem [84]. These problems can be alleviated by considering alternatives to CDM paradigm like warm dark matter or the dark matter including self-interactions.

- **Warm Dark Matter (WDM)**

Warm dark matter particles are in between the above two categories (CDM and HDM) in nature and hence are called *warm*. The factor x_f is therefore ~ 3 [80]. The WDM particles cause structure formation to form bottom-up from above their free-streaming scale and top-down below their free streaming scale. These type of dark matter particles interact much more weakly than neutrinos. WDM particles decouple at temperature $T \gg T_{\rm QCD}$ and do not get heated by the subsequent annihilation of hadronic species. As a result, the number density and mass of warm dark matter particles are respectively lower and higher (by $\sim \mathcal{O}(10)$) than those of hot dark matter particles. Therefore the fluctuations corresponding to very large galaxy halos ($\sim 10^{11} M_{sun}$) could then survive free streaming. Also the cutoff in the power spectrum $P(k)$ at large k as obtained in the scenario of WDM implies the formation of small DM halos. Some examples of this type of dark matter include very light gravitinos (where local supersymmetry broken at $\sim 10^6$ GeV) and sterile neutrinos. Strong upper bounds on the thermal velocity or the free-streaming length of the particles can be obtained from high redshift quasar spectra by SDSS observations of the Lyman α forest [85] are taken into account. This in turn implies lower bound on warm DM mass [86].

The simplest alternative to either pure HDM or pure CDM is "mixed" Dark Matter which is just some combination of HDM and CDM proposed in order to confront observation. Additionally, there are proposals such as primordial black holes, topological defects and modifications of Newtonian gravity on large scales which have not been experimentally ruled out.

The candidates for dark matter can also be classified based on the nature of their constituents into two types namely

- **Baryonic Dark Matter**

  If a dark matter candidate is baryonic in nature then such candidates for dark matter are dark matter are termed as *baryonic dark matter*. The particles like neutrinos, neutrons, black holes, jupitar like objects can potentially be the constituents of such type of dark matter. Galactic dark halos may be the most natural place for dark baryons since galactic rotation curve indicates presence of dark matter halo in the galactic region. The detected microlensing events at Large Magellanic Cloud (LMC) may also possibly hint that there may exist some baryonic DM in our Galaxy [51–53]. The density of visible matter of the Universe can be written as [87]

$$\rho_v = \sum \int dL \ \phi(L) L \Upsilon_v \quad . \tag{1.29}$$

  The above integration is carried over the luminosity L and the summation denotes contributions from different galaxy types and hot gas in clusters and groups of galaxies. For each system the corresponding luminosity function $\phi(L)$ and mass-to-light ratio $\Upsilon_v = M_v/L$ are considered. On the other hand, Big Bang nucleosynthesis (BBN) helps us understand the formation and production of light elements in the Universe. The relative amount of such light elements can be estimated from the baryon number density. The primordial abundances of such elements restrict the present density of baryons ρ_B. The ratio between the lower limit of baryon density ρ_B and the visible matter density ρ_v is large implying that a bulk of baryons is missing from measurement and may behave as baryonic dark matter [88]. However, since the precise value of lower bound of baryonic matter depends strongly on the abundances of Deuterium and Helium, the systematics involved in such measurements of abundances yield huge uncertainty in obtaining baryonic dark matter density. Also the X-ray data possibly indicates large baryonic gas density within clusters and groups of galaxies further restricting baryonic dark matter density [24]. The two main promising candidates for the baryonic dark matter are diffuse baryonic gas and dark stars (white dwarfs, neutron stars, black holes or objects with mass around or below the hydrogen-burning limit) [88, 89]. Since at the time of cluster formation, most of the baryons are supposed to take gaseous form [1], such diffuse gas may contain those dark baryons. However, such cold and warm diffuse gaseous baryons bound to galaxy groups are too cool to be visible or even detectable. Since such diffuse gaseous baryons have not been detected yet, there exists strong proposition of another possible candidate called MACHOs (MAssive Compact Halo Objects) which include small brown and black dwarf stars, cold unattached planets, comet-like lumps of frozen hydrogen, tiny black holes, possibly even mini dark galaxies.

- **Non-Baryonic Dark Matter**

  Most of the dark matter is supposed to be non-baryonic in nature and hence termed non-baryonic dark matter. Observations like supernova measurements of the expansion of the Universe, CMB measurements of the degree of spatial flatness of the Universe and measurements of the amount of matter in the structures of galaxies obtained through big galaxy redshift surveys precisely measure the total matter (Ω_m) and energy (Ω_Λ) contents of the Universe. On the other hand, the baryonic density (Ω_b) in the Universe can be obtained using the measurements of primordial nucleosynthesis and CMB spectrum. Since the calculated baryon density (Ω_b) is

[1] This is because mean gas density at cluster formation time was equal to baryon density.

much smaller than the total mass content (Ω_m), the difference ($\Omega_m - \Omega_b$) must be attributed to the non-baryonic dark content in the Universe [90]. Recent observation of Planck satellite measures the presence of such non-baryonic dark matter as $\sim 26.8\%$ of the total energy budget of the Universe [42]. Such non-baryonic dark matter has very weak interaction with the Standard Model particles and therefore the detectability of such form is rather hard in nature. Since they are supposed to be the relics of the Big Bang, these particles therefore should have mass in order to satisfy the observed dark matter density of the Universe. Moreover, the mass of such non-baryonic dark matter particles are also unknown. The candidates for such non-baryonic dark matter are mostly exotic in nature and an extension of the Standard Model for particle physics is required in most cases. The plausible candidates for non-baryonic dark matter in literature include supersymmetric particles, Kaluza Klein dark matter in extra dimension or other scalars or fermions in theories beyond the Standard Model [90]. Some of these candidates are neutralinos, gravitinos, sneutrinos, axions, WIMPZILLAs, solitons (B-balls and Q-balls) etc. In this thesis work, we have only considered candidates for dark matter which are non-baryonic.

Dark matter particles can be produced in the early Universe both via thermally and non-thermally. Thermal production of dark matter relies on the fact that the DM particles are produced via the mechanism of collision of cosmic plasma at the radiation dominated epoch. Therefore the non-thermal dark matter, on the other hand, have a different origin of production when the energy spectrum of the generated DM is different from a thermal distribution, i.e., via non-thermal production mechanism. The DM produced from the out-of-equilibrium decay of heavy unstable particles or from bosonic coherent motion or from some production mechanisms which do not respect thermal equilibrium.

- **Thermal Dark Matter**

Thermal production of dark matter relics is defined by the mechanism in which they are produced from particles in thermal equilibrium in such a way that their resultant energy spectrum is the same as that of the particles in the thermal equilibrium. In the early Universe the dark matter particles were continuously generated from the annihilation of Standard Model (SM) particles and simultaneously would annihilate into SM particles. The production and annihilation of DM-antiDM pairs in particle-antiparticle collisions are given by

$$\chi\bar{\chi} \leftrightarrow e^+e^-, \mu^+\mu^-, q\bar{q}, W^+W^-, ZZ, HH, \ldots. \tag{1.30}$$

Both the rate of forward and backward interactions were same at that epoch. They were thus in chemical and thermal equilibrium with the rest of the universal soup. But with the expansion of the Universe when the situation so arose that the interaction rate between a pair of dark matter particles fell short of the expansion rate of the Universe a dark matter particle would not find another of its species to interact with and thus they became "frozen" or decoupled from the plasma of the Universe to become relic particles. The measurement of the relic density of dark matter by PLANCK satellite-borne experiment suggests that the dark matter is likely to be massive and weakly interacting in nature. Hence the dark matter particles are often termed as Weakly Interacting Massive Particles or WIMPs in short. This process of generation of dark matter is the thermal process of dark matter production and is also known as thermal dark matter. We denote $\chi(\bar{\chi})$, $m_\chi(m_{\bar{\chi}})$ and n_χ $(n_{\bar{\chi}})$ to be the dark matter particle (antiparticle), the mass and the number density of such DM particles (antiparticles) respectively. In the very early Universe when the temperature (T) is much high ($T \gg m_\chi$), then the DM number density n_χ simply follows its equilibrium value, namely $n_\chi^{\rm eq}$. Alternatively, since the temperature of the Universe at this epoch was much higher compared to the mass of the DM particles, the number density of DM particles would behave like photons at that time and therefore, $n_\chi \sim T^3$. [2] At such high temperature when $T \gg m_\chi$, the colliding particle-antiparticle pairs in hot plasma of the Universe had sufficient energy to produce the WIMP pairs efficiently. The reverse process where the WIMP pairs produced the SM particles by WIMP pair-annihilation also existed and was effectively in equilibrium with the the forward reaction whereby the WIMP pairs are generated. At equilibrium the common production rate for both the forward and reverse processes (production and annihilation rates of WIMPs) at such epoch was given by

$$\Gamma_{\rm ann} = \langle \sigma_{\rm ann} v \rangle n_{\rm eq}, \tag{1.31}$$

where $\sigma_{\rm ann}$ is the WIMP annihilation cross section, $n_{\rm eq}$ is the WIMP number density in chemical equilibrium, v is the relative velocity of the annihilating WIMPs and the angle bracket $\langle ... \rangle$ denotes the average over the WIMP thermal distribution. As the Universe began to expand, the temperature of the Universe therefore decreased. When the temperature of the Universe's plasma decreased to become smaller than the mass of the WIMP ($T < m_\chi$), n_χ fell out exponentially with the decreasing temperature as the Boltzmann factor, $exp(-m_\chi/T)$. So, the equilibrium WIMP number density can be expressed as

$$n_\chi^{\rm eq} = g \left(\frac{m_\chi T}{2\pi} \right)^{\frac{3}{2}} e^{-\frac{m_\chi}{T}} \tag{1.32}$$

where g is effective number of degrees of freedom at that epoch. But both the annihilation and production processes remained in equilibrium at that time. Since the particles followed the Boltzmann distribution, the kinetic energy of the colliding particle-antiparticle pairs required to generate the WIMP pair production lies in

[2] Since for such high temperature ($T \gg m_\chi$), the number density n_χ can approximately be written as $\int \frac{8\pi}{(hc)^3} \frac{E^2 dE}{exp\left(-\frac{E}{k_B T}\right)}$ where h, c and k_B are the Planck constant, the speed of light in vacuum and the Boltzmann factor respectively. The integration thus reduces to $n_\chi \sim T^3$.

the tail of the Boltzmann distribution. At the same time, due to the expansion of the Universe, the number density of WIMPs n_χ decreased. This further caused the production and annihilation rates of WIMPs to fall since both are proportional to n_χ. Finally when the annihilation rate of WIMPs, $\Gamma_{\rm ann}$ became smaller than the expansion rate of the Universe H, the chemical decoupling occurred and the further production of WIMPs ceased. Alternatively, when the mean free path of collisions for the production of WIMP pairs became longer than the Hubble radius at some particular time of expansion of the Universe, such decoupling of WIMPs took place and the number of WIMPs in a comoving volume remained approximately constant (actually the number density of WIMPs after such decoupling fell off/decreased with increasing volume). The particular temperature at which such decoupling happened is called freeze-out temperature. The relic density of DM (Ω_χ) after the freeze-out would depend inversely on the annihilation cross-section ($\Omega_\chi \sim \frac{1}{\langle \sigma_{\rm ann} v \rangle}$).

Boltzmann Equation for Thermal WIMPs

The evolution of number density of a DM particle created at the early stage of the Universe is governed by the Boltzmann equation. The variation of comoving number density of a WIMP with the temperature of the Universe can be found by solving the Boltzmann equation. The Boltzmann equation is actually some continuity relation which describes the process. In the generalised version of the Boltzmann equation can be written as [80]

$$\mathcal{L}[f(x^\mu, p^\mu)] = \mathcal{C}[f(x^\mu, p^\mu)]\,, \tag{1.33}$$

where $f(x^\mu, p^\mu)$ is the phase-space dependent quantity. In this case, it is the phase-space density distribution function of the species. p^μ represents the four-momentum of the species at some space-time point x^μ. In the above $\mathcal{L}[f(x^\mu, p^\mu)]$ denotes the Liouville operator which describes the evolution of a phase-space volume. $\mathcal{C}[f(x^\mu, p^\mu)]$ in the r.h.s. of Eq. 1.33 is the collision operator which describes all possible processes that results in production or destruction of distribution function $f(x^\mu, p^\mu)$. In other words, it represents the number of particles produced or lost per unit phase space volume and per unit time in the course of collision with other particles or any other processes.

The general relativistic form of the Liouville operator can be written as

$$\mathcal{L}_{\rm GR} = p^\alpha \frac{\partial}{\partial x^\alpha} - \Gamma^\alpha_{\beta\gamma} p^\beta p^\gamma \frac{\partial}{\partial p^\alpha}\,, \tag{1.34}$$

where $\Gamma^\alpha_{\beta\gamma}$ are Christoffel symbols. Since in FRW cosmology the phase space distribution function is both homogeneous and isotropic in nature, the distribution function f of the species is only dependent on p^0 and x^0 components which are simply its energy E and time t respectively and hence $f \equiv f(E,t)$. The first term in Eq. 1.34 becomes the temporal term. All values of the second term disappear except for $\alpha = 0$. Now, since $\Gamma^0_{0i} = \Gamma^0_{i0} = \Gamma^0_{00} = 0$ and $\Gamma^0_{ij} = \delta_{ij} a\dot{a}$ and $p^i p^i = g^{ij} p_j p^i = \frac{p^2}{a^2}$, the form of Liouville operator therefore reduces to

$$\mathcal{L}[f] = E\frac{\partial f}{\partial t} - Hp^2 \frac{\partial f}{\partial E}\,, \tag{1.35}$$

where $H = \frac{\dot{a}}{a}$ denotes the Hubble expansion rate. After substituting Eq. 1.35 in Eq. 1.33 and then multiplying both sides of the equation $\frac{d^3p}{(2\pi)^3 E}$, the equation is then integrated over the entire phase space as

$$\int \frac{\partial f}{\partial t} \frac{d^3p}{(2\pi)^3 E} - H \int \frac{p^2}{E} \frac{\partial f}{\partial E} \frac{d^3p}{(2\pi)^3} = \int \frac{\mathcal{C}[f]}{E} \frac{d^3p}{(2\pi)^3}\,. \tag{1.36}$$

The second term can be rewritten as

$$H \int \frac{p^2}{E} \frac{\partial f}{\partial E} \frac{d^3p}{(2\pi)^3} = \frac{H}{(2\pi)^3} \int p \frac{\partial f}{\partial p} d^3p \,, \tag{1.37}$$

using the relations $E = \sqrt{p^2 + m^2}$ and $\frac{\partial f}{\partial E} = \frac{\partial f}{\partial p}\frac{\partial p}{\partial E} = \frac{E}{p}\frac{\partial f}{\partial p}$. The integration by parts of the term leads to following

$$\frac{H}{(2\pi)^3} \int_0^\infty p \frac{\partial f}{\partial p} d^3p = \frac{4\pi H}{(2\pi)^3} \int_0^\infty p^3 \frac{\partial f}{\partial p} dp = \frac{4\pi H}{(2\pi)^3} \left([p^3 f]_0^\infty - 3 \int_0^\infty p^2 f dp \right) , \tag{1.38}$$

where the term in the square bracket vanishes. Since the number density of the species χ can be given as

$$n_\chi(t) = \frac{g}{(2\pi)^3} \int f(E,t) d^3p \,, \tag{1.39}$$

Eq. 1.36 can be rewritten in terms of number density $n(t)$ as

$$\frac{dn_\chi(t)}{dt} + 3Hn_\chi(t) = g \int \frac{\mathcal{C}[f]}{E} \frac{d^3p}{(2\pi)^3} \,. \tag{1.40}$$

For simplicity, if we consider the process of the following form

$$\chi + a + b + \ldots \longrightarrow \alpha + \beta + \gamma + \ldots \,, \tag{1.41}$$

where χ is the DM candidate, the collision term on the r.h.s of Eq. 1.40 can be expressed as

$$
\begin{aligned}
g\int\frac{\mathcal{C}[f]}{E}\frac{d^3p}{(2\pi)^3} &= -\int\Pi_\chi\int\Pi_a\int\Pi_b...\int\Pi_\alpha\int\Pi_\beta\int\Pi_\gamma... \\
&\times(2\pi)^4\delta^4(p_\chi+p_a+p_b+...-p_\alpha-p_\beta-p_\gamma+...) \\
&\times[|\mathcal{M}|^2_{\chi+a+b+...\longrightarrow\alpha+\beta+\gamma+...}f_\chi f_a f_b(1\pm f_\alpha)(1\pm f_\beta)(1\pm f_\gamma)... \\
&-|\mathcal{M}|^2_{\alpha+\beta+\gamma+...\longrightarrow\chi+a+b+...}f_\alpha f_\beta f_\gamma(1\pm f_\chi)(1\pm f_a)(1\pm f_b)...], \qquad (1.42)
\end{aligned}
$$

where δ^4 is the four-momentum Dirac delta function and $\mathcal{M}$ denotes the corresponding matrix element for a certain interaction process. In the above p_i and f_i are the momentum and distribution function of the i-th particle species. The factor Π_i is the phase-space factor for the i-th particle species, defined as

$$
\Pi_i = \frac{g_i}{(2\pi)^3}\frac{d^3p_i}{2E_i}\,. \qquad (1.43)
$$

In Eq. 1.42, the sign $+$ (or $-$) within the factors $(1\pm f_i)$ is for bosonic (or fermionic) particle i.

In order to proceed further, a set of well-motivated and valid assumptions are considered:

- (a) The interaction is assumed to be reversible. This gives the following relation between the matrix elements of the processes as

$$
|\mathcal{M}|^2_{\chi+a+b+...\longrightarrow\alpha+\beta+\gamma+...} = |\mathcal{M}|^2_{\alpha+\beta+\gamma+...\longrightarrow\chi+a+b+...} \qquad (1.44)
$$

- (b) The condition of kinetic equilibrium among the species are considered. In fact, the scattering is supposed to occur so rapidly that the distributions of the different species are considered either Fermi-Dirac (FD) or Bose-Einstein (BE) in nature. The assumption is indeed a valid one since it holds true for most of the cases. Therefore, the only uncertainty on the distributions of the particle species comes from their respective chemical potentials $\mu(t)$.

– (c) The assumption that there is no degenerate matter as well as BE condensates present in the process is also considered. In the absence of these two factors the blocking and stimulated emission factors in Eq. 1.42 may be ignored and thus $(1 \pm f_i) \equiv 1$ Also since the interaction process is supposed to occur at a temperature well below $E - \mu$, the FD or BE nature of the distribution of the species becomes indistinguishable. Therefore, the Maxwell-Boltzmann (MB) statistics can be applied for all the species.

Hence, under these assumptions, Eqs. 1.40 and 1.42 can be rewritten as

$$\begin{aligned}\frac{dn_\chi}{dt} + 3Hn_\chi = g\int \frac{\mathcal{C}[f]}{E}\frac{d^3p}{(2\pi)^3} &= -\int \Pi_\chi \int \Pi_a \int \Pi_b ... \int \Pi_\alpha \int \Pi_\beta \int \Pi_\gamma ... \\ &\times (2\pi)^4 \delta^4 (p_\chi + p_a + p_b + ... - p_\alpha - p_\beta - p_\gamma + ...) \\ &\times |\mathcal{M}|^2 [f_\chi f_a f_b ... - f_\alpha f_\beta f_\gamma ...] \,. \end{aligned} \tag{1.45}$$

The number density n_i of a species i can, therefore, be given by

$$n_i = g_i \; e^{\mu_i/T} \int \frac{d^3p_i}{(2\pi)^3} e^{-\frac{E_i}{T}} \tag{1.46}$$

where g_i denotes the degeneracy of the species. Also the number density at equilibrium is defined as

$$n_i^{\rm eq} = g_i \int \frac{d^3p_i}{(2\pi)^3} e^{-\frac{E_i}{T}} \tag{1.47}$$

Now, if the DM particle χ interacts with its antiparticle $\bar{\chi}$ and produce the daughter SM particle-antiparticle pair, X and $\bar{X}$, i.e.,

$$\chi + \bar{\chi} \longrightarrow X + \bar{X} \,, \tag{1.48}$$

the annihilation cross section will be given as,

$$\sigma_{ann} = \frac{g_\chi g_{\bar{\chi}}}{4E_\chi E_{\bar{\chi}} v}(2\pi)^4 \delta^4(p_\chi + p_{\bar{\chi}} - p_X - p_{\bar{X}})|\mathcal{M}|^2 \,. \tag{1.49}$$

In the above the velocity v appearing in the annihilation cross-section is the Moller velocity which is defined as

$$v_{\rm Mol} = \left[|\vec{v}_1 - \vec{v}_2|^2 - |\vec{v}_1 \times \vec{v}_2|^2\right]^{1/2} \,. \tag{1.50}$$

Also from the argument of energy conservation one obtains,

$$E_\chi + E_{\bar{\chi}} = E_X + E_{\bar{X}} \,. \tag{1.51}$$

If the produced daughter particles maintain equilibrium, then their equilibrium distribution functions will be $f^{\rm eq}_{X,\bar{X}} = exp(-E_{X,\bar{X}}/T)$. Thus it follows that

$$f_\chi f_{\bar{\chi}} = exp(-(E_\chi + E_{\bar{\chi}})/T) = exp(-(E_X + E_{\bar{X}})/T) = f^{\rm eq}_\chi f^{\rm eq}_{\bar{\chi}}. \tag{1.52}$$

Therefore, by putting the above relations, the Boltzmann equation (Eq. 1.45) for the evolution of DM particle χ can be recasted in terms of the annihilation cross section as,

$$\frac{dn_\chi}{dt} + 3Hn_\chi = -\int \frac{d^3p_1}{(2\pi)^3} \int \frac{d^3p_2}{(2\pi)^3} \sigma_{ann} v [f_\chi f_{\bar{\chi}} - f^{\rm eq}_\chi f^{\rm eq}_{\bar{\chi}}] \,, \tag{1.53}$$

$$= -\langle \sigma_{ann} v \rangle [n_\chi n_{\bar{\chi}} - n^{\rm eq}_\chi n^{\rm eq}_{\bar{\chi}}] \,. \tag{1.54}$$

In the above the expression, $\langle \sigma_{ann} v \rangle$ which is namely the thermally averaged cross section times relative velocity is given by

$$\begin{aligned} \langle \sigma_{ann} v \rangle &= \frac{(2\pi)^4}{n_\chi^{\rm eq} n_{\bar{\chi}}^{\rm eq}} \int \Pi_\chi \int \Pi_{\bar{\chi}} \int \Pi_X \int \Pi_{\bar{X}} \\ &\times \delta^4(p_\chi + p_{\bar{\chi}} - p_X - p_{\bar{X}}) |\mathcal{M}|^2 exp\left(-\frac{E_\chi}{T}\right) exp\left(-\frac{E_{\bar{\chi}}}{T}\right) . \quad (1.55) \end{aligned}$$

The thermally averaged cross section times relative velocity $\langle \sigma v \rangle$ can also be written in the following form [91]

$$\langle \sigma v \rangle = \frac{1}{8m^4 T K_2^2(\frac{m}{T})} \int_{4m^2}^{\infty} ds\, K_1\left(\frac{\sqrt{s}}{T}\right) \sqrt{s}(s - 4M_S^2)\ \sigma(s)\ , \quad (1.56)$$

For the case when the dark matter particle χ is same as its own antiparticle, the above equation becomes,

$$\frac{dn_\chi}{dt} + 3Hn_\chi = \langle \sigma v \rangle \left[(n_\chi^{\rm eq})^2 - n_\chi^2\right] . \quad (1.57)$$

Therefore it is obvious that the contribution from the expansion of the Universe comes from the second term on the left hand side of Eq. 1.57 while the right hand side of the equation takes care of the change in number density due to annihilations and reverse annihilations. It should also be noted in this context that in case the dark matter particle χ and the dark matter anti-particle $\bar{\chi}$ are different and follow a particle-antiparticle relation, a factor of 1/2 should appear in front of the cross-section in Eq. 1.57. This is because the density of the annihilating dark matter particles will be half the one of majorana-like particles. In the thesis work we will study the cases where particle and its antiparticle of a dark matter species are identical. In order to compute the relic abundance for a dark matter species Eq.(1.57) should, in principle, be solved. Some reliable numerical codes such as `micrOMEGAs` [92–100] or `DarkSUSY` [101–104], have been developed for solving the Boltzmann equation with a very high level of accuracy to the whole process. Further advancements such as implementation of coannihilation channels, coupled Boltzmann equations have also been studied in the context of thermal DM scenario. The law of entropy conservation in the Universe is given by,

$$\frac{ds}{dt} = -3Hs\,. \tag{1.58}$$

In the above t is time, s denotes the entropy density, In order to compute the current relic density of WIMPs, the rate equation for the WIMP number density n_χ (Eq. 1.57) and the law of entropy conservation (Eq. 1.58) are required to be combined. Also, it is useful to define dimensionless quantities, namely, Y and x for further proceeding to study the evolution of the WIMP number density. The quantity $Y = n/s$ which is defined as the ratio between the number density of WIMPs and the entropy density represents the comoving number density of the WIMPs. Another quantity $x = m_\chi/T$ which is the ratio between the mass of WIMP (m_χ) and the photon temperature T gives the measure of time. Using the dimensionless quantities the Eqs. (1.57) and (1.58) are thus combined into a single one given by,

$$\frac{dY}{dx} = \frac{1}{3H}\frac{ds}{dx}\,\langle\sigma v\rangle\,(Y^2 - Y_{eq}^2)\,, \tag{1.59}$$

where Y_{eq} is the equilibrium value of Y when $n = n_{eq}$.

In FRW cosmology the Hubble parameter can be determined, according to the Friedman equation, by the mass-energy density ρ as

$$H = \frac{1}{M_{Pl}}\sqrt{\frac{8\pi}{3}\rho} = \sqrt{\frac{8\pi G}{3}\rho} \tag{1.60}$$

where $M_{Pl} = 1.22 \times 10^{19}$ GeV denotes the Planck mass. In the above G is the gravitational constant and ρ is the energy density of the Universe. The energy and

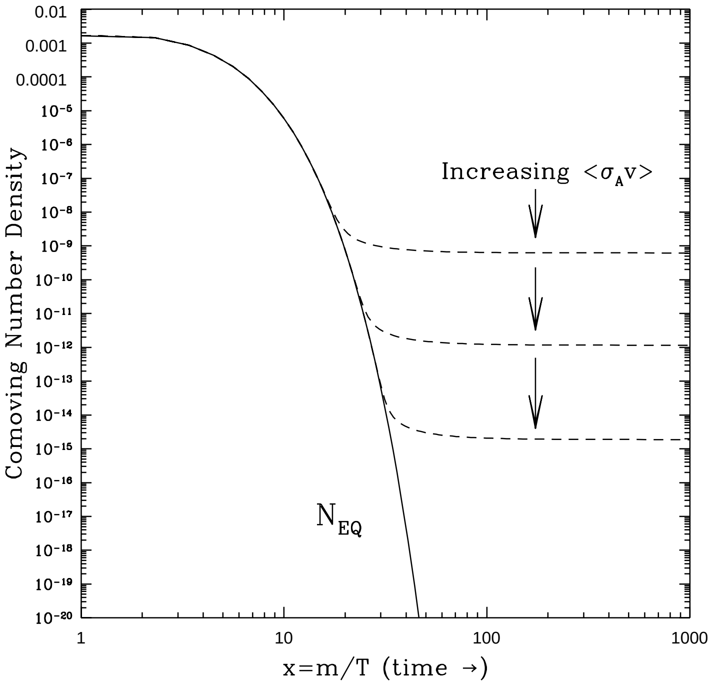

Figure 1.11: *The thermal evolution of the Comoving number density of WIMP (thermal relic particle) in the early Universe during the epoch of WIMP chemical decoupling. The dashed curves in this plot indicate the expected abundance. The solid curve denotes the equilibrium abundance of the WIMP (from Ref. [2]).*

entropy densities are related to the photon temperature of the Universe (T) through the following equations

$$\rho = \frac{\pi^2}{30} g_{\rm eff}(T) T^4, \tag{1.61}$$

$$s = \frac{2\pi^2}{45} h_{\rm eff}(T) T^3, \tag{1.62}$$

where $g_{\rm eff}(T)$ and $h_{\rm eff}(T)$ denote the effective degrees of freedom for the energy density and entropy density respectively. These two quantities ($g_{\rm eff}(T)$ and $h_{\rm eff}(T)$) represent respectively the contributions to the energy and entropy densities from the relativistic degrees of freedom present in the Universe at the temperature T.

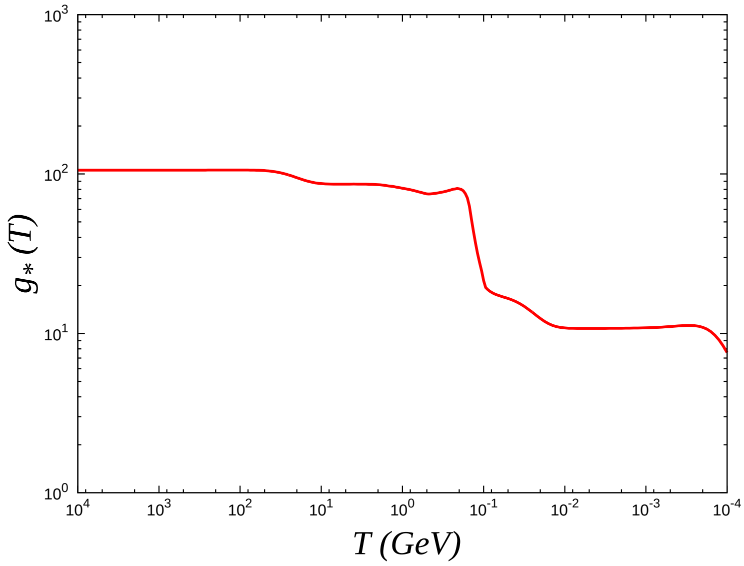

Figure 1.12: *The temperature evolution of the number of relativistic degrees of freedom (g_*) for the Standard Model.*

The expressions for $g_{\rm eff}(T)$ and $h_{\rm eff}(T)$ are given by

$$g_{\rm eff}(T) = \sum_{\rm bosons(b)} g_b \left(\frac{T_b}{T}\right)^4 + \frac{7}{8} \sum_{\rm fermions(f)} g_f \left(\frac{T_f}{T}\right)^4 , \tag{1.63}$$

$$h_{\rm eff}(T) = \sum_{\rm bosons(b)} g_b \left(\frac{T_b}{T}\right)^3 + \frac{7}{8} \sum_{\rm fermions(f)} g_f \left(\frac{T_f}{T}\right)^3 . \tag{1.64}$$

where g_b and g_f denote the respective internal degrees of freedom of relativistic bosonic and fermionic species present in the Universe at temperature T. In the above T_b and T_f represent the temperature of a bososnic and fermionic species respectively. Therefore $g_{\rm eff}(T)$ and $h_{\rm eff}(T)$ for a relativistic species present in the Universe must be same if it remains in thermodynamic equilibrium with the temperature of the Universe ($T_{b,f} = T$). When such relativistic species are decoupled from the thermal photon, the values of $g_{\rm eff}(T)$ as well as $h_{\rm eff}(T)$ will thus be changed. Numerical computations of $g_{\rm eff}(T)$ and $h_{\rm eff}(T)$ involving the QCD effects can be obtained in Ref. [105]. Substituting Eqs. 1.60-1.62 in Eq. 1.59, the following equation for the evolution of Y can be arrived,

$$\frac{dY}{dx} = -\left(\frac{45}{\pi M_P^2}\right)^{-1/2} \frac{g_*^{1/2} m}{x^2} \langle \sigma v \rangle \left(Y^2 - Y_{eq}^2\right), \tag{1.65}$$

where the relativistic degrees of freedom parameter $g_*^{1/2}$ is defined as

$$g_*^{1/2} = \frac{h_{\rm eff}}{g_{\rm eff}^{1/2}} \left(1 + \frac{1}{3} \frac{T}{h_{\rm eff}} \frac{dh_{\rm eff}}{dT}\right). \tag{1.66}$$

The variations of the quantity $g_*(T)$ for SM particles, which depends on both $g_{\rm eff}(T)$ and $h_{\rm eff}(T)$, with temperature T in the range 10^{-4} GeV to 10^4 GeV are shown in Fig. 1.12. This single equation is thereafter numerically solved with the initial condition $Y = Y_{eq}$ at $x \simeq 1$ in order to obtain the present comoving number density of WIMP Y_0. The expression for the equilibrium value of comoving number density (Y_{eq}) is written as [91],

$$\begin{aligned} Y_{eq} = \frac{n_{eq}}{s} &= \frac{\frac{g}{(2\pi)^3}\int exp\left(-\frac{E}{T}\right) d^3p}{\frac{2\pi^2}{45} h_{\rm eff}(T) T^3} \\ &= \frac{45g}{4\pi^4} \frac{x^2 K_2(x)}{h_{\rm eff}(\frac{m}{x})} \quad , (x \gg 3) \qquad (1.67) \\ &= \frac{45g'}{2\pi^4} \frac{\zeta(3)}{h_{\rm eff}(\frac{m}{x})} \quad , (x \ll 3) \qquad (1.68) \end{aligned}$$

where g is the internal degrees of freedom of a DM species and m is its mass. In the above $K_n(x)$ denotes the modified Bessel function of order n. In Eq. 1.68 the value of Riemann Zeta $\zeta(3)$ is 1.20206. In the above the values of g' are $g' = g$ (for bosons) and $g' = \frac{3}{4}g$ (for fermions). After solving Eq. 1.66 for Y, the WIMP relic density can then be calculated using the following relation,

$$\Omega_\chi h^2 = \frac{\rho_\chi^0 h^2}{\rho_c^0} = \frac{m_\chi s_0 Y_0 h^2}{\rho_c^0} = 2.755 \times 10^8\, Y_0 m_\chi/\text{GeV}\,, \tag{1.69}$$

where ρ_c^0 and s_0 denote the present critical density and entropy density respectively. In order to obtain the numerical value in Eq. (1.69), the value of the present background radiation temperature is chosen to be $T_0 = 2.726\,\mathrm{K}$ and $h_{\rm eff}(T_0) = 3.91$ corresponding to photons and three species of neutrinos.

The numerical solution of Eq. (1.65) has been illustrated in Fig. 1.11. In Fig. 1.11 it is found that at very high temperatures Y closely follows its equilibrium value Y_{eq}. At very high temperature the annihilation rate of WIMPs (Γ) was sufficiently high so that thermal as well as chemical equilibrium with the plasma was maintained. This is because the relation $\Gamma = n_\chi \langle \sigma_{\rm ann} v \rangle \gtrsim H$ is satisfied at such temperatures. WIMP annihilation is then balanced by the rate of WIMP-creating inverse processes, driving Y_χ to $Y_\chi^{\rm eq}$. But with the decrement of the temperature from such high value, Y_{eq} becomes exponentially suppressed and Y began to deviate from its equilibrium value. As the Universe expands further and its temperature falls, the number density of WIMPs decreases, reducing the WIMP annihilation rate until it is smaller than the Hubble expansion rate. The processes of WIMP annihilation and creation can then no longer maintain chemical equilibrium. As a result the WIMPs decouple chemically from the thermal bath and the WIMP number density is said to "freeze out". The temperature at which the process of freeze-out happens, T_f is roughly given as

$$\Gamma(T_f) = n_\chi(T_f) \langle \sigma_{\rm ann} v \rangle (T_f) \sim H(T_f)\,. \tag{1.70}$$

At the freeze out temperature (T_f), when the WIMP annihilation rate is nearly of the order of the Hubble expansion rate, WIMP production becomes negligible and the WIMP abundance per comoving volume reaches its final value. Assuming that the freeze-out occurs during the radiation-dominated era during which $H \equiv$

$1.66 g_*^{1/2} T^2/M_{Pl}$, the above condition can be expressed as

$$g \left(\frac{mT_f}{2\pi}\right)^{\frac{3}{2}} exp\left(\frac{-m}{T_f}\right) \langle\sigma_{\rm ann} v\rangle(T_f) = 1.66 g_*^{1/2} \frac{T^2}{M_{Pl}} \,. \tag{1.71}$$

In the standard cosmological scenario, the typical value of freeze out temperature of cold dark matter turns out to be $T_f \simeq m_\chi/20$ or alternatively $x_f = \frac{m_\chi}{T_f} \simeq 20$. This corresponds to a typical WIMP speed at freeze-out of $v_f = (3T_f/2m_\chi)^{1/2} \simeq 0.27c$. It may be mentioned in this context that the nature of different types of dark matter particles can be distinguished according to the values of their freeze-out temperatures: hot dark matter (HDM) with $x_f \ll 3$, cold dark matter with $x_f \gg 3$ and intermediate warm dark matter (WDM) with $x_f \sim 3$.

Another important feature that Fig. 1.11 illustrates is that smaller annihilation cross sections lead to larger relic densities, i.e., the weakest interacting particle has dominating abundance. This also can be easily understood from the fact that WIMPs with stronger interactions remain in chemical equilibrium for a longer time and hence decouple when the Universe is colder. Hence the density of such WIMPs is further suppressed by a smaller Boltzmann factor. This simply establishes a the inverse relation between $\Omega_\chi h^2$ and $\langle\sigma_{\rm ann} v\rangle$. From the Boltzmann equation it also follows that the freeze out temperature plays an important role in determining the WIMP relic density. In general, however, the freeze out temperature depends not only on the mass and interactions of the WIMP but also, through the Hubble parameter and the content of the Universe. In this thesis work we consider such thermally produced dark matter.

- **Non-thermal Dark Matter**

When DM particles are produced in a non-thermal production mechanism, then such DM is termed *non-thermal* dark matter [106]. For non-thermal DM, the energy spectrum of the generated DM is different from that of thermal distribution. In this scenario, the DM can be produced from bosonic coherent motion of oscillating (pseudo)scalar fields. Another mechanism for production of non-thermal DM is via decays of heavy particles which are already out-of-equilibrium. Gravitational effects can also play important role in the formation of non-thermal DM. For example, the non-thermal DM candidates like primordial black holes (PBH) and super-heavy particles such as Wimpzillas are produced from gravitational effects.

The bosonic coherent motion such as the axion field oscillation, which is possibly required to produce cold dark matter, requires very light boson which can originate from Goldstone bosons as a result of feebly breaking of the corresponding global symmetries. In case of axion, the boson should have lifetime larger than the age of the Universe. The principle of bosonic coherent motion is discussed in the following. The equation of motion for a bosonic field, ϕ in the expanding Universe can be written as

$$\ddot{\phi} + 3H(T)\dot{\phi} + \frac{\partial V(\phi)}{\partial \phi} = 0. \tag{1.72}$$

where $H(T)$ denotes the Hubble term and $V(\phi)$ is the potential energy term. For small values of ϕ, the potential energy term can be given by

$$V(\phi) \simeq \frac{1}{2} m^2(T) \phi^2 \tag{1.73}$$

The temperature dependent boson mass term $m(T)$ introduced in the potential becomes very large at a sufficiently high temperature. For the case when the potential is zero, the solution of ϕ is almost constant. But when the potential term becomes comparable to the Hubble term, Eq. 1.72 takes the form of the equation of a damped harmonic oscillator where the Hubble term acts as the friction term of this equation and hence the solutions become oscillatory in nature. The solution of $\phi(t)$ is therefore termed as bosonic coherent motion. Such mechanism is applied universally in the case of axions, inflatons, moduli, saxions, Affleck-Dine fields etc. in the early Universe.

Heavy unstable particles produced in the early Universe can decay and produce thermal DM in the form of thermal population if they decay while remaining in thermal equilibrium. These heavy particles can also decay and produce DM as a non-thermal population if they decay out-of-equilibrium and do not respect thermal equilibrium. These heavy particles can be yielded either thermally, such as WIMPs, or non-thermally such as the inflaton, moduli or curvaton etc. Non-thermal productions from particle decay have been considered in various models for DM. These include production of neutralinos from axinos, saxions, gravitinos and inflatons; axinos from NLSP binos or staus; gravitinos from the decays of bino, stau, sneutrino and also from Q-ball; KK-gravitons from the decay of KK U(1) hypercharge gauge bosons or in the string compactification. The decay of inflaton, as in the standard inflationary scenario, produced many relativistic particles or 'radiations'. Subsequently with the expansion of the Universe, some of these 'radiations' get decoupled (or frozen-out) from the thermal plasma of the Universe. These frozen-out particles, if unstable, may further decay to yield such non-thermal DM. If the produced non-thermal DM particles are non-interacting at the time of such decay of heavy particles, the abundance of such DM is related (directly proportional) to that of the decaying parent particle. The DM particles produced from the decay can possess a different evolution depending on their properties at the time of production-via-decay, i.e., based on the relation between the temperature of radiation at the time of heavy particle decay and the temperature of freeze-out of such produced DM particles.

Alternative mechanisms for the production of non-thermal DM include gravitational mechanism. Production of superheavy DM such as WIMPZILLAs can be taken as example. The accelerated expansion of the Universe can create such DM particles similar to the mechanisms of Hawking radiation (radiation around a black hole) and Unruh radiation (radiation in accelerated reference frame). Apart from gravitational mechanism such massive relics might have other variety of production mechanisms such as during preheating, during reheating, in bubble collision. The WIMPZILLAs can be produced in the process of transition between inflation and a matter or radiation-dominated Universe due to the non-adiabatic expansion by classical gravitational effects. These supermassive relics can also be produced during reheating after inflation. The produced DM particles (WIMPZILLAs) should be very heavy (their mass $M_{\rm wz}$ is much larger than the reheating temperature and $\equiv 10^{13}$ GeV) in order to have the right relic density in the present Universe. These DM particles are stable with lifetime greater than the age of the Universe.

Other non-thermal DM particles include Pseudo Nambu-Goldstone boson such as Majorons, familons, branons, dilatons etc. Other candidates include Q-balls, mirror-matter DM, fuzzy CDM, Charged Massive Particles (CHAMPs), heavy fourth generation neutrinos, Chaplygin gas, Strongly interacting dark matter (SIMPs), Dynamical dark matter (DDM) etc. [106]

1.4 Detection of Dark Matter

There are heightened ongoing efforts worldwide aimed to detect DM particles. Besides the gravitational evidence which is by and large only evidence for the presence of dark matter, there are primarily three different methods of confirming the existence of DM in the Universe and distinguishing between the various models about its nature. These are 1) direct detection of DM, 2) indirect detection of DM through the detection of annihilation products and 3) search for the signature of DM at colliders. The direct detection of

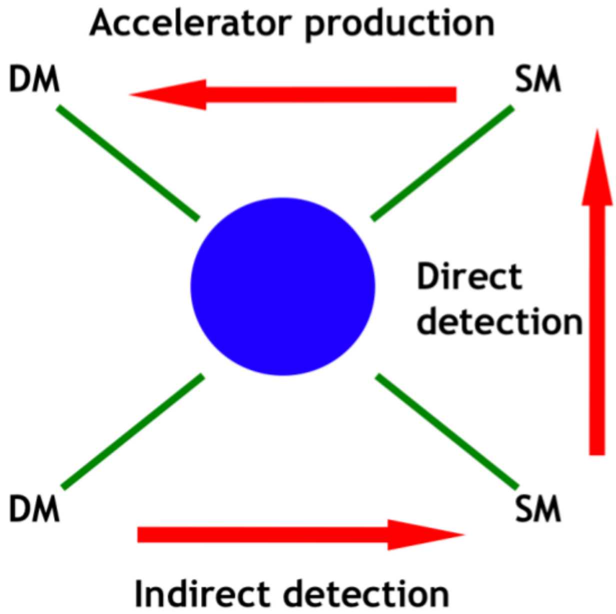

Figure 1.13: *Schematic diagram illustrating different ideas for the detection of dark matter particles. Different types of search can broadly be envisaged depending on the direction of the time axis (red arrow).*

DM relies on the possible scattering of a DM particle off a target nucleus in earth-based laboratory experiments. The indirect detection searches for DM are, on the other hand, involve in the annihilation products of DM. Finally, The DM particles can also be, in principle, generated at the colliders via the collision of SM particles. In order to detect DM particles, the collider should operate at a much higher energy scale than the mass of DM. Presently the LHC has reached upto $\sim$ TeV scale of energy. These three detection processes are shown schematically in Fig. 1.13. These three methods may also possibly shed light on the nature of DM particles. [3]

- **Direct Detection**

  The observational evidence of DM is so far only via gravitational interaction. The WIMP may also, in principle, elastically scatter off the detector nuclei. This idea is

[3]Apart from these three kinds of DM searches, one may also look at the astrophysical laboratories such as Neutron Stars for studying dark matter physics via precise measurements related to thermalisation etc. of such stars.

similar to that of Drukier and Stodolsky [107] proposed to detect neutrinos directly by exploiting their elastic scattering with the detector nuclei. Therefore if one can detect any signature of such scattering of nuclei, this may be the possible direct detection of DM. The galactic rotation curves suggests that the DM is supposed to form an extended halo around galaxies such that our solar system, moving through this halo, is exposed to an apparent flux of DM particles. Therefore, if a DM particle makes an impact on the terrestrial DM detector, the nuclei of the detector material will be scattered off and will get recoiled by the DM particle. The recoil would, however, generate energies of only a few keV since the interaction strength is very weak. The WIMPs can be directly detected if one can measure the energy deposition made by such recoiling nucleus. The direct detection experiments, therefore, must be performed in a very low background environment, very low intrinsic and external radiological background, and should be installed/located in very deep underground sites shielded from cosmic rays in order to precisely measure such low recoil energy of the nucleus due to possible WIMP impact. The recoiled nucleus deposit their energy in the detector to yield scintillator light, phonon excitation, ionization, etc. Also the rate of collision with the target material is significantly low. Many advanced technologies for the detection of DM are being developed to overcome the two main difficulties in DM detection, namely, the very small detectable signatures ($\sim$ a few keV) and the rarity of the collisions ($\sim$ a few per year per kg of target mass). Different measurement techniques are adopted by different direct detection experiments in order to measure the nuclear recoil energies. Some experiments use the physical processes such as scintillation, phonon or ionization as their measurement techniques. These experiments usually choose Ge, Si or NaI as detector materials On the other hand, detectors such as TPC (Time Projection Chamber) use some other process as measurement techniques. For example, TPC detectors consider the process of the drifting of ionized charges, produced by recoil nucleus of the detector material (usually noble liquids like xenon, argon and neon), yield the track from which the direction of recoil can eventually be traced. Enormous efforts are given worldwide in order to probe direct dark matter signal. Some of the ongoing experiments for the search of such elusive dark matter include DAMA (NaI) [108–110], CDMS (^{73}Ge) [111, 112], PICASSO (CS_2) [113, 114], XENON [115–119], COUPP [120], LUX (use xenon) [121], CLEAN (use liquid argon and neon as scintilator) and DEAP (use argon) [122] etc. Limits on scattering cross sections for different mass of dark matter particles (without considering any particle physics model for dark matter) can be obtained from these searches.

Since the direct detection of dark matter is based on the interaction of dark matter with nucleus of a detector, the signal of direct detection precisely depends on the type of interaction (scalar, vector, axial-vector etc.) between the dark matter and detector nucleus. The dark matter-nucleus scattering cross sections can be classified into two types, namely, spin-dependent and spin-independent depending on the spin state of detector nucleus. Hence the direct detection is also of these two types. The target nucleus, with zero ground state spin gives rise to spin independent interaction and scalar type of interaction between dark matter and nucleus is responsible for this. On the other hand, the axial-vector type of interaction between them causes spin-dependent interactions [4] which happen for the the case of nuclei with unpaired nucleon that gives rise to non-zero ground state spin. Some experiments to search for the spin independent interactions include Edelweiss [123], DAMA/NaI, CDMS SuperCDMS [124], Xenon10 [115,116], Xenon100 [117–119], Zeplin [125,126], KIMS [127–129], CoGeNT [130]. These detectors use detectors made of heavy nuclei (Ge or Xe) to probe scalar interactions. On the other hand, experiments such as NAIAD [131], SIMPLE [132], PICASSO [114], Tokyo/NaF [133] use light nuclei in order to look for spin-dependent signals. Also since the direct detection of dark matter may

[4] Since spin is an angular momentum and hence an axial-vector

depend on the diurnal and annular motion of the earth, this causes a small variation in the signal rate. There are attempts and claims (eg., DAMA) as well in detecting signals originating from such daily and annular variations.

- **Indirect Detection**

  DM particles, in principle, can be trapped by the strong gravity of massive objects such as Solar core, galactic centre etc. Inside a massive body a dark matter particle may loose its velocity. Due to such process, if its velocity falls below its velocity of escape from that gravitating body, the dark matter particle is trapped inside such bodies. If accumulated in considerable amount in those sites. These trapped DM can undergo pair annihilation inside those objects to yield known SM particles. The annihilation products yield different known particles including (anti)protons, electrons, positrons, neutrinos, gamma rays, and a few others whose flux can be measured for indirect DM searches [134–136]. These annihilation products should be in large amount especially in regions where the local DM densities are much higher than they are in our galactic neighborhood such as galactic centre, dwarf galaxy etc. But the main disadvantages associated with the DM indirect search are the usual astrophysical backgrounds and the statistical fluctuations. The indirect detection of DM will be discussed elaborately in the following chapters.

- **Collider Searches**

  Complementary to the above searches, collider searches have mainly focussed on the particle nature of DM [137–139]. DM, if produced at the collider, may escape the collider undetected but its signature may be traced in the form of missing energy. This, in fact, is a convenient collider search technique for DM. Although there are other alternative proposals for the DM search at colliders. Collider searches for DM have their own advantages as well as weaknesses. While both direct and indirect signals become less sensitive as the DM particle becomes lighter due to the available smaller interaction energy, the colliders, on the other hand, may be able to yield such light DM and do not suffer from threshold effect for light DM search. However, for the case of very heavy DM particles, the colliders require sufficiently high energy to generate such DM and suffer from the parton distribution function suppression, while direct and indirect searches work better in those regimes of DM mass. There are other uncertainties associated with the collider search for DM such as the basic understanding of signals caused by 'true' DM or some imposter unstable particle.

Chapter 2

Indirect Detection of Dark Matter

2.1 Brief Introduction

The indirect searches for dark matter are primarily based on detecting excesses in fluxes of cosmic rays with respect to their expected astrophysical backgrounds [134–136]. Substantial amount of stable Standard Model particles may be produced as end products from the annihilation or decay of dark matter in the massive astrophysical regions such as galactic centre or the solar core. Such SM particles after being produced in those sites would propagate through space and eventually reach a detector. Promising targets for the study of indirect detection of dark matter are usually the most massive regions such as the inner halo of our galaxy, the Galactic Centre, solar core etc. [140] However, often the most complicated astrophysical uncertainties in some regions usually make hard correctly estimate the astrophysical background. The SM particles that are usually studied in order to get information of dark matter are photons, neutrinos and stable antiparticles such as positrons and anti-protons (and possibly, anti-deuteron) [141]. We discuss here briefly about the prospects of detection and studies of such dark matter annihilation products at various detectors.

- **Photons**

  After creation from the process of annihilation of the DM particles, the photons propagate freely in the galaxy without suffering any deflections due to interstellar magnetic field. Also since their attenuation over the large galactic distance scales is very small, their energy spectra measured at a terrestrial detector closely mimic that produced in the process of DM annihilation. The above two reasons, therefore, make photons potential annihilation signal for DM. They deliver precise angular information of the position of the source and the energy spectrum of DM annihilation products. A lot of experiments (both satellite-borne and earth-based) are involved in search for the gamma rays originating both from Milky Way and beyond (both galactic and extragalactic). Such ongoing and proposed experiments include EGRET, HESS, FERMI-LAT, MAGIC, CTA etc. In the rest of the thesis, I shall mainly focus on the gamma ray from various particle physics models for DM. The main difficulty in search for DM-originated gamma ray is the large astrophysical background which is also difficult to estimate.

- **Neutrino**

  Neutrinos also provide substantial information regarding their sources since their energy as well as direction remain completely unaltered during the propagation through matter and in space. The high energy cosmic neutrinos, in practice, mostly do not suffer any hindrance in propagation while propagating through space. After being produced from DM annihilation at massive astrophysical sites, the neutrinos, unlike other DM annihilation products, can escape from such dense objects without being trapped. However, the detection of neutrino is very challenging due to its weak interactions. The produced neutrino fluxes (expected high energy neutrinos) can be measured indirectly via the detection of charged particles such as muons produced by a neutrino interaction in the surroundings (water, rocks, etc) of the detector. Neutrinos as a result of interaction with the rock in the surroundings of the detectors generate charged particles (e.g. muons) that emit Cherenkov radiation when traveling through the detector. From such radiation it can be possible to understand the energy and direction of the charged particles and therefore to partially reconstruct the original energy and direction of the parent neutrino. The major background for this search are atmospheric muons. the experiments only focus on the upgoing tracks. The present and proposed neutrino telescopes devoted to the search for the DM-generated/induced neutrinos include ANTARES, ICECUBE, SUPER-Kamiokande etc.

- **Positrons**

  The search for positrons or antimatters, in general, in cosmic space for probing DM may have the advantage over other searches that the galaxies comprise less number of positron (or antimatter) sources. Positrons diffuse in the galaxy after losing their energy due to the mechanisms like synchrotron emission, ionization, Coulomb scattering, bremsstrahlung and inverse Compton scattering. Therefore, the nearby regions of the galaxy contributes more in the positron flux. The only information that can be precisely extracted from the positron flux is with its energy spectrum. In order to reduce the cosmic ray induced positron flux background in the atmosphere, the detectors are installed at high altitude or in cosmic space for the measurement of DM-induced positron flux. Since solar magnetic field affects the measurement in positron flux, the solar modulation effect should be included below few GeV. Satellite-based or balloon-based experiments for the search of positrons include PAMELA, AMS, HESS etc.

- **(Anti)Proton**

The search for antiprotons has generated considerable interest for the detection of DM. The energy loss for the flux of antiprotons produced in the process of DM annihilation is smaller than that of positron and is primarily due to scattering on matter. Therefore the distant reaches of the galaxy can contribute to the antiproton flux measured at Earth and this entails more astrophysical uncertainties due to the DM halo profile. Similar to the case of positron, DM-induced antiprotons also suffers solar modulation effect below few GeV energy and only provide information only via energy spectrum. Experiments such as BESS, GAPS etc. are devoted in search of DM-induced antiproton signals in cosmic space.

2.2 Formalism of Indirect Detection of DM via Neutral Particles

The strong gravitational potential at the massive astrophysical sites such as galactic centre, dwarf galaxy can have a high DM density. These DM particles can undergo self annihilation to produce γ, lepton pairs (such as neutrinos) etc. Unlike the case of DM accumulation by gravitational capture of WIMPs from the galactic halo, the expected gamma-ray or neutrino fluxes from DM annihilation do not depend on the capture process (inside those massive bodies) but the estimated DM halo density profile. In order to estimate such fluxes for both photons and neutrinos coming from the annihilation (or decay) of DM, the astrophysical models of density distribution of DM halo as well as relevant particle physics inputs such as cross-section (or decay width) should be taken into account. Therefore the DM annihilation rate is heavily influenced by the uncertainties arising from our limited astrophysical knowledge and poor statistics.

In order to derive the annihilation rate of WIMP, the nature of WIMP should be

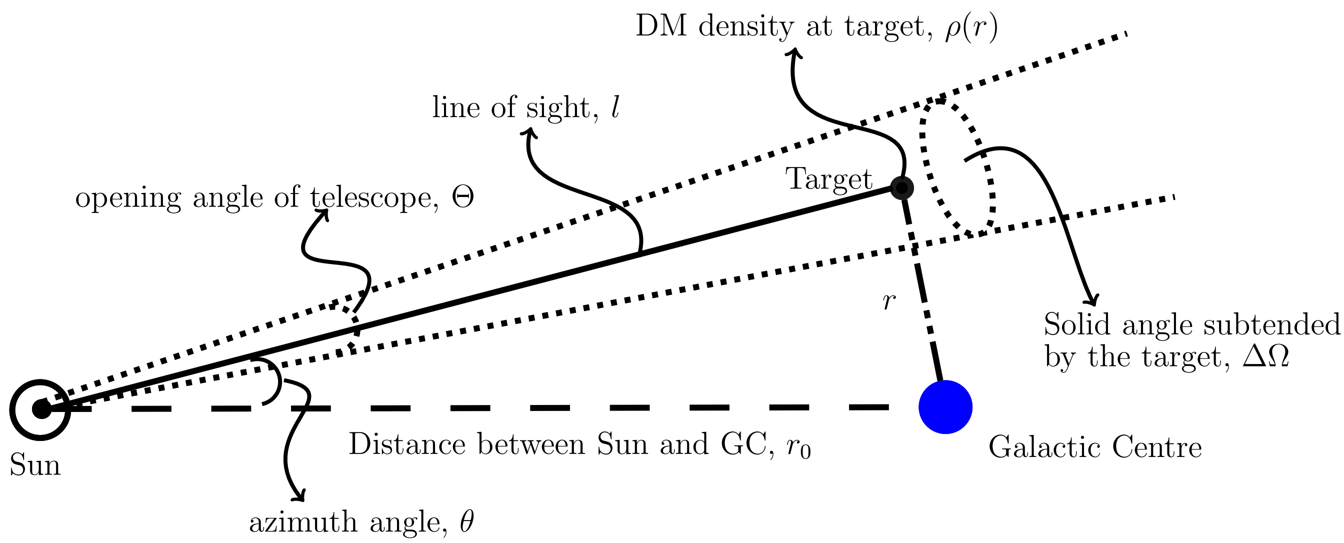

Figure 2.1: *The schematic representation of the indirect detection of dark matter in the Galactic halo.*

taken into account, i.e., whether it is self-conjugate or not. Let m_χ ($m_{\bar{\chi}}$) be the mass of DM particle χ (anti-DM particle $\bar{\chi}$) and ρ_χ ($\rho_{\bar{\chi}}$) be the density of DM (anti-DM). If the thermally averaged cross-section for DM annihilation channel i is $\langle \sigma v \rangle_i$, then the DM annihilation rate per annihilating DM or anti-DM particle is given by

$$\sum_i^{\text{channels}} \frac{\rho_\chi}{m_\chi}.\langle \sigma v \rangle_i \quad \text{or} \quad \sum_i^{\text{channels}} \frac{\rho_{\bar{\chi}}}{m_{\bar{\chi}}}.\langle \sigma v \rangle_i \,, \tag{2.1}$$

where the summation is performed over all annihilation channels. Now, in the interaction volume V, there exist $\frac{\rho V}{m_\chi}$ DM particles χ and $\frac{\rho V}{m_{\bar{\chi}}}$ anti-DM particles $\bar{\chi}$. Therefore, the number of possible pairs of DM-antiDM particles ($\chi\bar{\chi}$) per unit of the interaction volume is given by

$$\frac{\rho_\chi V}{m_\chi}.\frac{\rho_{\bar{\chi}} V}{m_{\bar{\chi}}}.\frac{1}{V} \,. \tag{2.2}$$

The total rate of annihilation in the interaction volume V is given by the product of the annihilation rate per DM (anti-DM) particle and the number of DM-antiDM pairs of particles in V., i.e.,

$$\left(\sum_{i}^{\text{channels}} \frac{\rho_\chi}{m_\chi}.\langle\sigma v\rangle_i\right).\left(\frac{\rho_{\bar{\chi}}V}{m_{\bar{\chi}}}\right) \tag{2.3}$$

Assuming there is no particle-antiparticle asymmetry in the DM sector, we have $\rho_\chi = \rho_{\bar{\chi}} = \rho/2(say)$ and $m_\chi = m_{\bar{\chi}} = m(say)$. Therefore, number of annihilations occurred in the infinitesimal interaction volume dV is

$$\Gamma_{\chi\bar{\chi}} = \frac{\rho^2}{4m^2}dV \sum_{i}^{\text{channels}} \langle\sigma v\rangle_i \tag{2.4}$$

In case where the DM is self-conjugate, i.e., its own antiparticle, the possible number of annihilating pairs of DM particles is enhanced by a factor of 2 compared to the non-self-conjugate DM case. The rate of annihilation is therefore given by

$$\Gamma_{\chi\chi} = \frac{\rho^2}{2m^2}dV \sum_{i}^{\text{channels}} \langle\sigma v\rangle_i \tag{2.5}$$

Now, the infinitesimal interaction volume dV is given by $\ell^2 d\Omega d\ell$, where ℓ is the distance at which that volume element is located from the observer and $d\Omega$ is the infinitesimal solid angle subtended by the volume element at the observer. Therefore the differential flux of photons or neutrinos at a distance ℓ from the observer is given by,

$$\frac{d\Phi_{\gamma,\nu}}{dE_{\gamma,\nu}} = \frac{1}{4\pi\ell^2}\frac{\langle\sigma_{\rm ann}v\rangle\rho^2}{2\alpha m^2}\sum_{i}^{\text{channels}} \mathcal{B}_i\frac{dN^i}{dE}\ell^2 d\ell d\Omega\,, \tag{2.6}$$

where the differential energy spectrum of photon or neutrino produced per single annihilation in the channel with final state i is $\frac{dN^i}{dE}$ which determines the spectral shape of the signal and $\mathcal{B}_i$ denotes the the branching fraction to different annihilation channels i. In the above $\langle\sigma_{\rm ann}v\rangle$ is the the total annihilation cross-section averaged over the DM velocity distribution. The value of $\alpha = 1$ or 2 depends on self-conjugating DM or non-self-conjugating DM scenario respectively. It is, therefore, automatically comes from such simple stoichiometry that the DM annihilation rate, being proportional to the product of initial densities of the DM particles, is also proportional to the square of the DM density. The differential flux of gamma-ray or neutrino due to DM annihilation in galactic halo in angular direction that produce a solid angle $d\Omega$ is given by [142]

$$\frac{d\Phi_{\gamma,\nu}}{d\Omega\ dE_{\gamma,\nu}} = \frac{1}{8\pi\alpha m^2}\langle\sigma_{\rm ann}v\rangle \sum_i^{\rm channels} \mathcal{B}_i \frac{dN^i}{dE} \int_{l.o.s} d\ell \ \ \rho[r(\ell,\theta)]^2 \ . \tag{2.7}$$

It should be mentioned in this context that in case of DM decay, the rate of decay is given by

$$\mathcal{D}_\chi = \frac{\rho}{\alpha m} dV \sum_i^{\rm channels} \Gamma_i \, , \tag{2.8}$$

where Γ_i is the decay width of DM for the decay channel i. Similarly, the differential flux of photons or neutrinos for the case of decaying DM from a target in the galactic halo at a distance ℓ from the observer in angular direction with a solid angle $d\Omega$ is given by

$$\frac{d\Phi_{\gamma,\nu}}{d\Omega\ dE_{\gamma,\nu}} = \frac{1}{4\pi\alpha m}\Gamma_{\rm dec} \sum_i^{\rm channels} \mathcal{B}_i \frac{dN^i}{dE} \int_{l.o.s} d\ell \ \ \rho[r(\ell,\theta)] \ , \tag{2.9}$$

where $\Gamma_{\rm dec}$ is the total decay width of DM. From Eq. 2.9 it is obvious that for the case of DM decay the flux of indirect DM signal is proportional to single power of density $\rho(r)$ unlike the annihilating DM scenario.

In the above (Eqs.2.7 and 2.9) r denotes the distance between the target location and the centre of the DM halo and can be written as

$$r = \sqrt{r_\odot^2 + \ell^2 - 2r_\odot \ell \cos\theta} \, , \tag{2.10}$$

where ℓ is the line of sight distance and θ is the aperture angle (or azimuth angle) between the direction of the line of sight and the axis connecting the observer to the centre of the object. In the above $r_\odot \sim 8.5$ kpc denotes the distance between the observer (located at solar system) and the centre of the DM halo. It may be noted in this context that the limits of integration for the line of sight variable ℓ in Eq. 2.7 should are from the position of observer to that of the target source. Now, the maximum limit of ℓ ($\ell_{\rm max}$) should, in principle, be any point of the Universe from which light rays can come to the observer. However, the contributions from extragalactic dark matter to the flux are not considered in this formalism since the galactic halo profiles take care of only the galactic contribution. Therefore the value of $\ell_{\rm max}$ is finite and depends on the maximum radius of the galaxy. If the maximum radius of Milky Way galaxy is r_{MW}, then $\ell_{\rm max}$ can be obtained using Eq. 2.10 and is given by

$$\ell_{\rm max} = \sqrt{r_{MW}^2 - r_\odot^2 \sin^2\theta} + r_\odot \cos\theta\,. \tag{2.11}$$

Moreover, any instrumental observation, in practice, cannot be performed with observations only along a 1-dimensional line of sight. Instead, the flux on the earth (or on a satellite) should therefore be calculated within a cone centered around any angle Θ_0 (say). Therefore, if a telescope operates with an opening angle 2Θ (or the angle subtended by the target at the eye of the observer is 2Θ) centered around Θ_0 [1], the corresponding solid angle will then be given by $\Delta\Omega = 2\pi(1 - \cos\Theta)$. The angle of the cone is, however, bound from below by the angular resolution of the detector which is simply defined as the minimal angular separation required between two points in the sky to be properly distinguished by the detector. The basic schematic representation for the above discussion is elaborately shown in Fig. 2.1.

[1]The half-angle of the cone is chosen to be Θ.

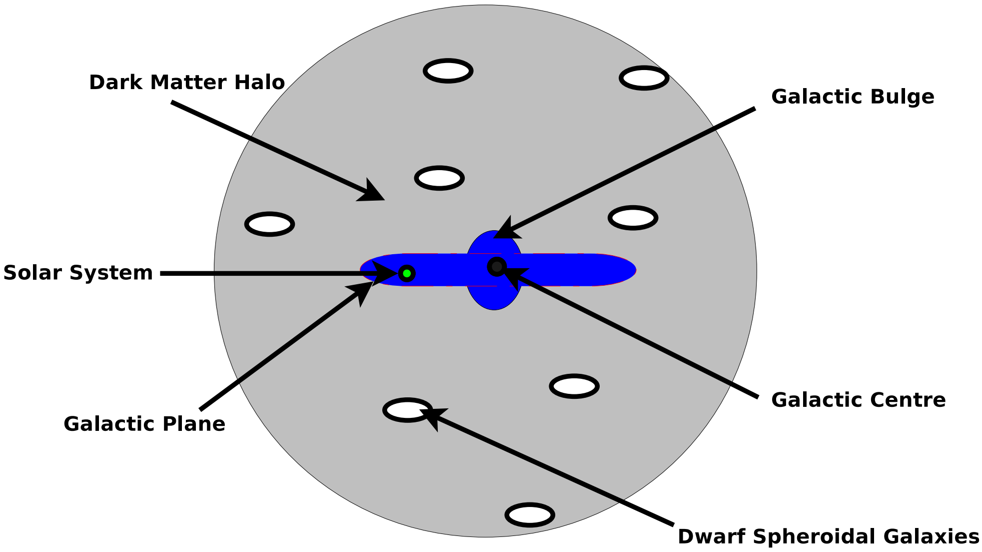

Figure 2.2: *The schematic representation of Galactic dark matter halo. The grey shaded region represents the DM halo.*

2.3 Dark Matter Halo Density Profiles

The dark matter halo profile can precisely give information about the mass density ($\rho(r)$) of dark matter particles as a function of position from the centre of the halo distribution. Since the dark matter halo (schematically shown in Fig. 2.2) is supposed to be distributed around the galaxies or the galaxy clusters, the centres of such halo are generally chosen to be the centres of the galaxies or the centre of galaxy clusters where the mass densities of dark matter are rich. In general, the halo distribution is not spherically symmetric in nature and hence the dark matter density distribution depends on both radial distance r and azimuthal angle θ from the chosen halo centre. Numerical simulations also give hints of this fact. The isodensity surfaces within the halo form triaxial ellipsoids [143]. Apart from few efforts such as stellar tidal streams [144] and proposed GAIA space mission for the measurements of a huge number of galactic stars [145], there is so far no precise observational determinations of halo shapes. Therefore, in most cases the dark matter halo distributions are considered to be spherically symmetric and the density distribution of dark matter solely depends on r. Until now there is no preferred unique dark matter halo profile that can address and handle all of the astrophysical issues very well. Also, there is not very well known astrophysical behaviour of dark matter in the galactic disk and in galactic halo of our Milky Way galaxy. In Milky Way the nature of dark matter density is investigated in regions such as Galactic Centre, Galactic halo as well as in solar neighbourhood using the observed astrophysical data and numerical simulation. Since the universal density profile of dark matter is not well established, some parametrisations for such halo distribution of dark matter is adopted in literature. One of the popularly chosen parametrised dark matter halo profile is based on spherically symmetric profile. In this formulation the dark matter density at a radial distance r from Galactic Centre is given by

$$\rho(r) = \frac{\rho_s}{\left(\kappa + \left(\frac{r}{r_s}\right)^{\gamma}\right)\left(1 + \left(\frac{r}{r_s}\right)^{\alpha}\right)^{\frac{\beta-\gamma}{\alpha}}} \,, \tag{2.12}$$

where α, β, γ and κ are the different parameters that represent some particular halo profile listed in Table 2.1. The form of such generalised halo profile is also known as generalised (α, β, γ) Hernquist profile [146–148]. In the above the other two parameters, namely, ρ_s and r_s are called the scale density and the scale radius respectively. The values of ρ_s and r_s are chosen simply by the astrophysical observational data of the Milky Way rather than from numerical simulations. These two quantities are estimated from the value of dark matter mass density at the solar location and the total dark matter mass contained within a few tens of kpc. The local dark matter halo density at solar location $(\rho(r_\odot))$ is taken to be 0.3 GeV/cm^3 as canonical value [2] and $r_\odot$ is the distance of the sun to the Galactic Centre ($\sim$ 8.5 kpc). From the kinematic surveys of stars in SDSS data, the mass of dark matter contained in $\sim$ 60 kpc is estimated to be $\sim 4.7 \times 10^{11}\ M_\odot$ [149]. It can be seen in Eq. 2.12 that the density distribution $\rho(r) \propto r^{-\gamma}$ for radial distance

[2] Although $\rho(r_\odot)$ ranges from $\sim 0.2 - 0.8$ GeV/cm^3 in various literatures

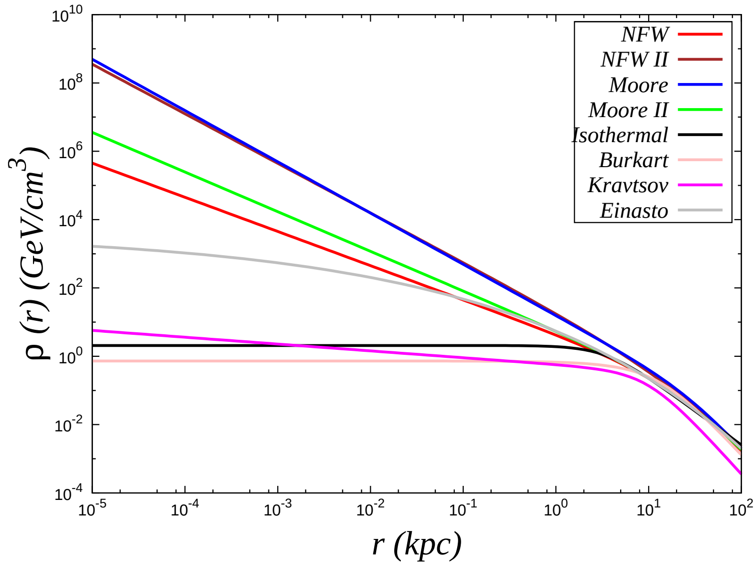

Figure 2.3: *Different Galactic dark matter halo density profiles, $\rho(r)$ as a distance r from the the Galactic Centre.*

$r \ll r_s$ while for very large r ($r \gg r_s$), $\rho(r) \propto r^{-\beta}$. On the other hand, the parameter α characterises the sharpness of the change in logarithmic slope of the profile.

Table 2.1: Values of parameters for some of popular dark matter halo profiles

Halo Model	α	β	γ	κ	r_s (kpc)	ρ_s (GeV/cm^3)
Navarro, Frenk, White (NFW) [150,151]	1	3	1	0	20	0.259
NFW with adiabetic compression [152]	0.8	2.7	1.45	0	20	0.257
Moore [153]	1.5	3.0	1.5	0	20	0.256
Moore II [154]	1.0	3.0	1.16	0	30.28	0.108
Isothermal [155]	2	2	0	0	3.5	2.069
Burkart [156]	2	3	1	1	12.67	0.729
Kravtsov [157]	2	3	0.2	0	10	0.361

Using the corresponding values of parameters α, β, γ and κ from Table 2.1, one obtains different forms of DM density ρ as a function of radial distance r from the Galactic Centre as

$$\begin{aligned}
\text{NFW}: \quad \rho_{\rm NFW}(r) &= \rho_s \frac{r_s}{r}\left(1+\frac{r}{r_s}\right)^{-2} \\
\text{NFW II}: \quad \rho_{\rm NFW\ II}(r) &= \rho_s \left(\frac{r_s}{r}\right)^{1.45}\left(1+\left(\frac{r}{r_s}\right)^{0.8}\right)^{-1.5625} \\
\text{Moore}: \quad \rho_{\rm Moo}(r) &= \rho_s \left(\frac{r_s}{r}\right)^{1.5}\left(1+\left(\frac{r}{r_s}\right)^{1.5}\right)^{-1} \\
\text{Moore II}: \quad \rho_{\rm Moo\ II}(r) &= \rho_s \left(\frac{r_s}{r}\right)^{1.16}\left(1+\frac{r}{r_s}\right)^{-1.84} \\
\text{Isothermal}: \quad \rho_{\rm Iso}(r) &= \frac{\rho_s}{1+(r/r_s)^2} \\
\text{Burkert}: \quad \rho_{\rm Bur}(r) &= \frac{\rho_s}{(1+r/r_s)(1+(r/r_s)^2)} \\
\text{Kravtsov}: \quad \rho_{\rm Kra}(r) &= \rho_s \left(\frac{r_s}{r}\right)^{0.2}\left(1+\left(\frac{r}{r_s}\right)^{2}\right)^{-1.4}
\end{aligned} \tag{2.13}$$

However, a different kind of parametric form is adopted in case of Einasto halo profile [158–160] which can be written as,

$$\text{Einasto}: \quad \rho_{\rm Ein}(r) = \rho_s \exp\left\{-\frac{2}{\tilde{\alpha}}\left[\left(\frac{r}{r_s}\right)^{\tilde{\alpha}} - 1\right]\right\} \tag{2.14}$$

where $\tilde{\alpha}$ is a parameter of the halo profile usually chosen to be 0.17 and the scale radius r_s is 20 kpc. Therefore, the value of scale density ρ_s comes out to be 0.061 GeV/cm^3 after normalisation of the halo profile to give DM density of 0.3 GeV/cm^3 at the solar location. It may be noted in this context that for a particular halo profile the values of the some parameters may differ from those listed in table 2.1 due to any change in the factors chosen for normalisation such as $\rho_\odot$ and the DM mass content in a galaxy etc.

There are, however, some motivations for considering the above mentioned halo profiles (Eq. 2.13 and Eq. 2.13). The Navarro, Frenk and White (NFW) [150] profile is motivated by cosmological N-body simulations performed in 1996 and often used as benchmark halo profile. At very small radial distance r from the Galactic Centre, i.e., near the central region of our galaxy, the NFW density profile behaves as r^{-1}. In other words, it shows cuspy nature at this region. The Einasto profile [159, 160], on the other hand, do not converge to some power law at the galactic centre region and is rather flat in comparison to NFW profile at kpc scale. Also it appears to show a better fit to the numerical simulations like the Aquarius Project simulation [59] with a completely different parametrisation of halo profile. The shape parameter of the Einasto profile, $\tilde{\alpha}$ can take different values depending on different physics of the halo profile. Numerical DM simulations which include the effects of the existence of baryons have consistently indicated modified halo profiles which are steeper at the central region than that predicted by the DM-only simulations [152, 161]. The steeper density profile with $\tilde{\alpha} = 0.11$ can be obtained if baryons are added in addition to the dark matter in the numerical simulations [162]. In this thesis work we, however, adopt the canonical value of shape parameter $\tilde{\alpha} = 0.17$ for the Einasto profile for our calculations. On the other hand, if the initial density distribution is considered to be of NFW type, numerical simulations predict the more spiky profile than NFW (termed NFW II here) after imposing the effect of baryons in the analysis. This effect called 'adiabetic compression' is due to the collapse of dark matter adiabetically in the Galactic Centre region in the presence of baryonic matter. The observations of galactic rotation curves, on the other hand, support flat or cored halo profiles such as Burkart halo profile [156], truncated Isothermal halo profile[3] [1, 155], Kravtsov halo profile [157] etc. contrary to that predicted in numerical simulations. Furthermore, profiles steeper than the NFW halo profile such as Moore profile [153,154] are also studied in literature as well. The models like NFW and Moore profiles share a common feature that the DM densities for these models rise significantly towards the inner regions of the galaxy forming some kind of cusp. The density distributions of the above halo profiles are shown in Fig. 2.3 It appears from Fig. 2.3 that all the halo profiles mostly differ each other in the inner portion of the galactic halo. The difference is quite prominent in the vicinity of Galactic

[3]The profile is termed *isothermal* since the profile closely resembles the Boltzmann distribution. It is also called the 'canonical' density profile due to its simple parametric form.

Centre. At very large distance from the centre of the galaxy ($\sim$ a few kpc or beyond), the profiles are found to follow very similar distribution in nature. Therefore, the signals coming from the dark matter annihilation at the regions near the Galactic Centre will be much sensitive to the choice of the halo profiles than those at the local (solar) environment or at very distant regions from the Galactic Centre. In this context it is worth mentioning that the effect of dark matter clumping can significantly contribute to the dark matter signals from halo regions. Due to the presence of the dark matter clumping, the average of the squared density distribution of dark matter, $\langle \rho^2(r) \rangle$ which controls the flux for the dark matter signals gets substantially modified.

2.4 Astrophysical J-factor

The J-factor is defined as the integration of the intervening dark matter along the direction of line of sight, i.e., the direction along which the line of sight variable ℓ varies [163]. The above integration is distinguished by angular direction and thus the J-factor depends on θ, the angle between the direction of the line of sight and the line joining/connecting the Earth to the Galactic Center. Since the dark matter halo distribution $\rho(r)$ is assumed to be spherically symmetric, the $J(\theta)$ is therefore invariant under rotations around the axis that connects the observer (at earth) and the Galactic Centre. Therefore, the J-factor depends on the spatial distribution of dark matter as well as on the beam size. The form of J-factor precisely depends on the production mechanism of Standard Model particles from dark matter sector. In case of dark matter annihilation to the SM particles, the J-factor can be written as,

$$J_{ann} = \int_{\text{l.o.s.}} d\ell \, [\rho(r(\ell, \theta))]^2 \qquad (\text{annihilation})\,. \tag{2.15}$$

On the other hand, when the dark matter particles decay to produce the SM particles, the J-factor (also called D-factor for decaying dark matter) takes the form

$$J_{dec} = \int_{\rm l.o.s.} d\ell \, [\rho(r(\ell,\theta))] \qquad ({\rm decay})\,. \tag{2.16}$$

Therefore the dimensions of J_{ann} (for the case of dark matter annihilation) and J_{dec} (for the case of dark matter decay) as obtained from the above two equations are GeV^2/cm^5 and GeV/cm^2 respectively. Often in many cases, the J-factors are used as a dimensionless quantities. In those cases, the J-factors are weighted by proper powers of $r_\odot$ and $\rho_\odot$ in order to make them dimensionless. Therefore, the dimensionless J-factors for both the cases (dark matter annihilation and decay) are given by

$$\begin{aligned} J_{ann} &= \int_{\rm l.o.s.} \frac{d\ell}{r_\odot} \left(\frac{\rho(r(\ell,\theta))}{\rho_\odot}\right)^2 \qquad ({\rm annihilation})\,, &(2.17)\\ J_{dec} &= \int_{\rm l.o.s.} \frac{d\ell}{r_\odot} \left(\frac{\rho(r(\ell,\theta))}{\rho_\odot}\right) \qquad ({\rm decay})\,. &(2.18)\end{aligned}$$

Also in cases where the integrated flux of dark matter signal over a region subtended by some solid angle $\delta\Omega$ (specified by the observation window or resolution of the telescope) are required, the J-factor in the flux equation are replaced by the average J-factor ($\bar{J}(\Delta\Omega)$) for the region. The average J-factor is defined as the average of the J-factor over the solid angle $\delta\Omega$ and is simply written as

$$\bar{J}(\Delta\Omega) = \left(\int_{\Delta\Omega} J \, d\Omega\right) / \Delta\Omega\,. \tag{2.19}$$

Needless to mention in this context that the value of J-factor for a particular chosen region will depend on the choice of dark matter halo profile. For example, the values of J-factor for the regions around the Galactic Centre will be much higher for the case of cuspy halo profiles than those obtained for cored halo profiles. If one looks for the flux from the region which is an annuli $\theta_{\rm min} < \theta < \theta_{\rm max}$ (or a disk if $\theta_{\rm min}$ becomes zero) centered around the Galactic Centre in galactic (r, θ) coordinate, the form of the average J-factor can be given by

$$\bar{J} = \frac{2\pi}{\Delta\Omega} \int d\theta \, \sin\theta \, J(\theta), \quad \Delta\Omega = 2\pi \int_{\theta_{\rm min}}^{\theta_{\rm max}} d\theta \, \sin\theta. \quad (\text{disk or annulus})\,. \tag{2.20}$$

Similarly, the expression for the average J-factor for a $(b \times l)$ region specified in the galactic (b, l) coordinate can be written as

$$\bar{J} = \frac{4}{\Delta\Omega} \int\!\!\int db\, dl \, \cos b \, J(\theta(b, l)), \quad \Delta\Omega = 4 \int_{b_{\rm min}}^{b_{\rm max}} \int_{l_{\rm min}}^{l_{\rm max}} db\, dl \, \cos b. \quad . \tag{2.21}$$

In the above $b_{\rm min}, l_{\rm min}, b_{\rm max}, l_{\rm max}$ are the minimum and maximum values of galactic latitude b and galactic longitude l respectively for the considered region in the galactic halo.

2.5 Targets for Indirect Dark Matter Searches

The gamma-ray flux from the annihilation of DM at any particular region in the Universe strongly depends on the density distribution along the line of sight of the dark matter particles (so-called J-factor). In general, the DM densities are not very well constrained from the prediction of numerical simulations, mainly in the innermost regions. Numerical simulations predict very cuspy nature of DM halo due to the collapse of cold DM near central regions of massive bodies. This, in turn, favourably enhances the indirect detection of DM due to $\rho_{\rm DM}^2$ dependency. On the other hand, the evidence of galaxy rotation curves imply constant density cores. Also other complicated effects such as the formation of substructure in the DM distribution play significant role in determining the strength of indirect detection. The substructure which is unresolved in cold DM N-body simulations at very low mass level (below $\sim 10^5 M_\odot$) may, in principle, significantly boost the annihilation signal over that yielded in case of normal DM distribution. There are

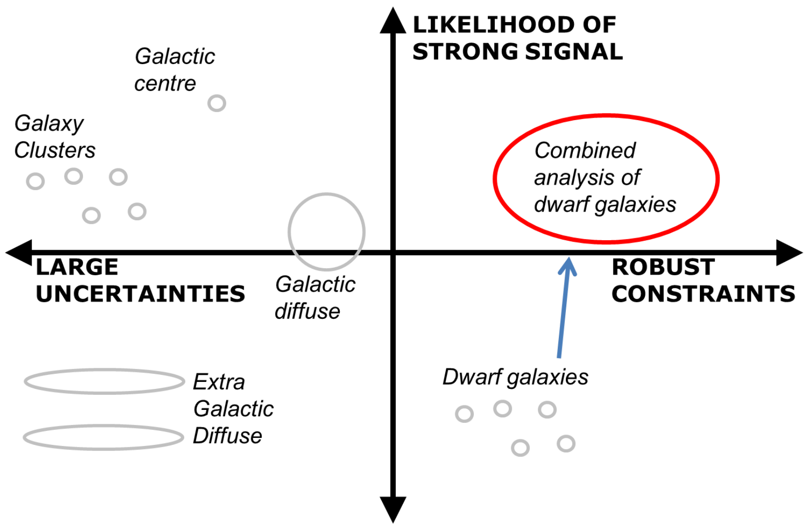

Figure 2.4: *Illustration of the relative benefits and drawbacks of different targets for gamma-ray (and neutrino) detection of WIMPs (from Ref. [10]).*

other effects which include the dominance of baryonic matter at the inner parts of the gravitational potential in objects such as Milky Way which, in turn, may alter the inner DM halo profile due to the infall of baryons. Therefore DM halo profile becomes steep through adiabatic contraction or flat through the repeated star burst due to baryonic infall. Therefore the indirect detection of DM using gamma rays entails huge uncertainty due to the choice of DM halo profile. The uncertainties are different for different targets for DM indirect detection as shown in Fig. 2.4. The potential targets for the indirect detection of DM and the prospects of detections from such targets are discussed below.

- **Galactic Centre**

  The Galactic Centre (GC) shown in Fig. 2.5 is considered to be the best suitable location for the indirect search for DM. The GC which is located approximately 8.5 kpc from Earth in the constellation Sagittarius, contains massive astrophysical objects (perhaps a supermassive black hole at the centre of the Milky Way) and hence its gravity is very strong. Therefore the DM particles, in principle, can be

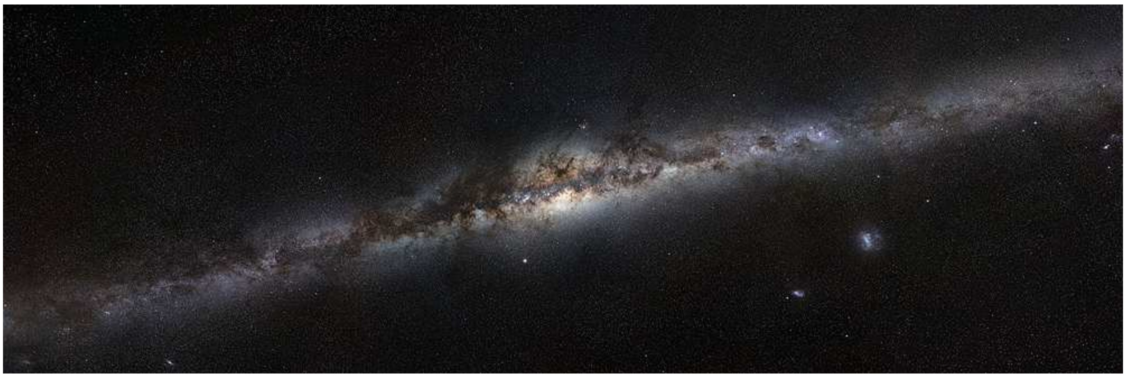

Figure 2.5: *The centre of the Milky Way galaxy (Galactic Centre) viewed edge on. Credit and Copyright: Serge Brunier*

trapped by the strong gravity of such massive object when the escape velocity of the DM particles cannot overcome such gravity. By this mechanism, the DM particles are accumulated in considerable amount and the GC may become rich in DM. The concentration of DM is therefore expected to be very high at GC region due to the large gravity in this region. The DM particles at this site indeed can yield gamma rays on pair annihilation as explained earlier. Therefore any observed excess of gamma ray signal from direction of the GC region indicate their presence when such excess cannot be explained by other known astrophysical processes that may occur in that site. However, the situation is complicated by the fact that a multitude of other astrophysical sources of gamma rays present in this region may also contribute to the observed gamma ray and therefore the true identification of the DM source region as a region of γ-emission, is hindered. The presence of a highly structured and extremely bright diffuse gamma-ray background which stems from the interaction of the cosmic rays with dense molecular material in the inner galactic region further adds complications for the detection of GeV gamma rays originated from DM annihilation. Such astrophysical gamma-ray foregrounds are considered to be several orders of magnitude larger than the expected gamma-ray signal produced from DM annihilation. Therefore the very central part of GC is masked out while performing the analysis. Since the gamma-ray distribution can be well resolved due to the proximity of GC from the solar system, the severe uncertainty in determining the limits of DM annihilation cross section comes from the choice of DM halo profile. In addition, the modelling of astrophysical foreground would also make the obtained limits to be more robust.

Different satellite-borne and ground-based experiments looking for extra terrestrial gamma signals have reported the observance of excess gamma ray signals in the direction of GC in different energy regions. At TeV energies, the HESS (The High Energy Stereoscopic System) [164–166] experiment had reported the gamma rays from the GC which cannot be suitably explained by other astrophysical propositions. If such observed TeV gamma rays from the GC are expected due to the annihilation of DM at GC then the mass of DM is also expected to be in the TeV range. Recently, analysis of the data from the satellite-borne gamma ray experiment Fermi Large Area Telescope (Fermi-LAT) reveals an excess of gamma ray flux from the direction of the GC above the galactic diffuse emission with spatially extended gamma ray distribution features. This excess is found to be in the gamma energy region of around 1-3 GeV [167, 168]. The evidence of the Galactic center excess was first found in the EGRET data [169] and eventually it was interpreted as an effect due to the annihilation of DM particles [170]. There are propositions such as millisecond pulsar population [171, 172], central supermassive black hole [168, 173], annihilating DM [168, 174–179] in order to explain such excess. We shall address such GC γ-ray excess in the framework of annihilating DM particles in particle physics models in this thesis.

- **Galaxy Clusters**

The Galaxy Clusters which are very distant and largest massive objects in the universe are considered to be one of the potential targets for the study of DM indirect

Figure 2.6: *Galaxy Cluster A2199 containing several thousands of galaxies. The motion of the galaxies suggests enormous amount of dark matter in this cluster. Credit: 1.2-m Telescope, Whipple Obs., Harvard CfA*

detection. The unresolved DM substructure may significantly alter the boost factor of the gamma ray signal from the annihilation of DM in these sites. The galaxy clusters contain a large number of astrophysical gamma ray sources like Active Galactic Nuclei (AGN) and radio galaxies which complicate the study of indirect detection of DM. Moreover, these objects can possibly yield cosmic rays which subsequently produce gamma rays via interaction with hadrons (and producing pions). Different observational results for gamma-rays from various clusters have put stringent limits on continuum gamma-ray flux from those objects. For example, limits for the Coma cluster has been produced by VERITAS experiment whereas the MAGIC telescope set limits for the Perseus cluster and the HESS for the Fornax cluster. However, such limits are relaxed upto several orders if conservative assumptions are imposed on the so-called boost factors. [4] One of the well known galaxy clusters (A2199) is shown in Fig. 2.6. Some other popular clusters are shown in Fig. 1.1. Very recently, there is an interesting evidence of a weak unidentified line with energy 3.55 keV

[4]The boost factor is defined as the ratio of integrated contributions to flux due to effects such as substructures etc. within a DM halo to the flux only due to a main host DM halo.

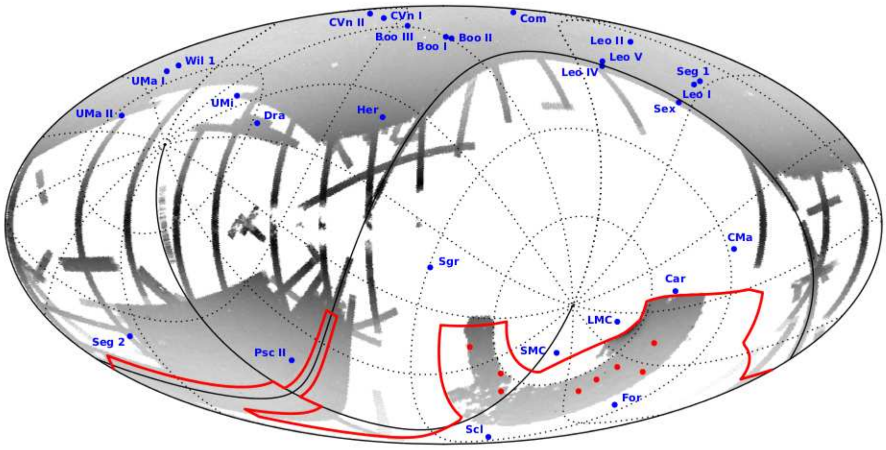

Figure 2.7: *The locations of Milky Way dwarf galaxies (in blue and red dots) in Galactic coordinates (Mollweide projection) (from Ref. [11]). The blue dots in this figure denote very well known satellite galaxies and the red ones are for the newly discovered dwarf galaxy candidates.*

(more than 3σ CL) in the X-ray spectrum from the analysis of X-ray data of XMM-Newton observatory for observed 73 galaxy clusters. Since the galaxy clusters are supposed to contain huge amount of DM, this 3.55 keV X-ray line is thought to be originated from DM in those sites.

- **Dwarf Spheroidal Galaxies**

One of the most promising targets for the search of dark matter via indirect detection is the dwarf spheroidal galaxies (dSphs) of the Milky Way. The dSphs are considered to be promising for the study of DM phenomenology because of their proximity, low astrophysical background and huge amount of DM content.

A dwarf spheroidal galaxy is a low-luminosity (less than absolute visual magnitude -14, more precisely with an absolute visual magnitude between -8 and -13) dwarf elliptical galaxy of very low surface brightness which lacks a nucleus. Typically it has an effective radius of $\sim 200-1000$ parsecs. Although it was assumed to be large and low-density globular clusters, recent studies have suggested that dSphs have a very complex stellar population than that observed in globulars. The dSphs exhibit the evidence of star formation over much extended periods with no proper sign of recent star formation and detectable interstellar matter. The stellar populations of the dSphs consist of two components; the old metal-poor population which is very much similar to that of globular clusters and the intermediate-age population with the age range of 1 to 10 billion years. The dwarf spheroidals in the Local Group (satellite galaxies of the Milky Way Galaxy and companions of the Andromeda Galaxy) have masses $\sim 10 - 100$ million times $M_{\rm sun}$. The features of dwarf spheroidal galaxies include that they are of very low luminosities, an old stellar population, very large separations between the luminous objects and are virtually devoid of almost any gas and dust. The last two above-mentioned points make dwarf spheroidal galaxies such suitable environments for the study of X-ray. The old stellar population discussed above is very crucial for the study of X-ray binary since an evolved stellar population is required in order to even have compact objects like neutron stars, white dwarfs or black holes. The ages of population in dwarf galaxies, on average, have been reported to be older than 2.5 Gyr.

Dwarf spheroidal galaxies also contain a large amount of dark matter. This has been inferred from the studies of mass-to-luminosity ratios of dSphs galaxies which are found to be much larger than what can be accounted for by the luminous matter in the galaxy. The mass-to-luminosity ratios of dSphs are higher than those of globular clusters, also indicating the presence of a large amount of dark matter in dSphs galaxies. Recently the Sloan Digital Sky Survey, Dark Energy Survey, Panoramic Survey Telescope and Rapid Response System have discovered many faint galaxies to be the possible candidates for dwarf galaxy with much precision shown in Fig 2.7.

From the analysis of Fermi-LAT gamma-ray data for various dSphs, one can estimate the limits on DM annihilation at those objects. These limits are very interesting for

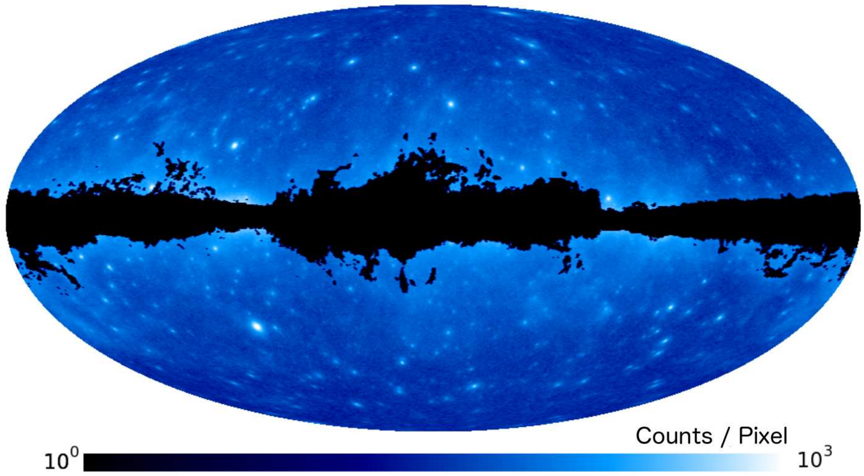

Figure 2.8: *The map in Galactic coordinates (Mollweide projection) showing the integrated count of photons for the diffuse gamma-ray background measured by Fermi-LAT detector above the energy above 100 MeV (from Ref. [12]).*

DM study in the sense that the parameter space for very low mass thermal WIMPs are very tightly constrained.

- **Isotropic Diffuse Emission (Extragalactic)**

A very faint diffuse isotropic signal of gamma ray coming from all direction of the sky has been measured by the Fermi-LAT telescope. Such gamma-ray signal termed as diffuse isotropic gamma-ray background (DIGRB) spans in the energy range from $\sim$ 200 MeV to $\sim$ 100 GeV. They seem to follow a power law with index $\sim$ 2.4. The sky-map of integrated photon count for DIGRB as measured by Fermi-LAT [12] is shown in Fig. 2.8 for clarity. The DIGRB is supposed to contain contributions of various extragalactic unresolved sources. However, since from the analysis of Fermi-LAT data it has been inferred that such unresolved sources possibly contribute mostly up to some fraction of the total DIGRB emission, the DIGRB emission is therefore expected to contain substantial contributions of other interesting astrophysical events. Therefore the signature of DM may also possibly be embedded in the DIGRB emission. One can obtain conservative limits of DM annihilation from the analysis of the DIGRB when the total DIGRB emission is assumed to be originated from DM rather considering other source contributions. Such limits can be further improved if the contributions from the source populations are considered. It is obvious that such limits may be further tightened if the source contributions are chosen conservatively. But so far the ground based observatories have not managed to provide competitive measures of DIGRB due to their constrained field of view and the undesired background of electron-shower. On the other hand, satellite borne experiments like Fermi-LAT have measured the DIGRB with better precision up to very high energy. Details of the limit obtained from such observation in the framework of DM will be addressed later in this thesis.

Chapter 3

Particle Physics Models for Dark Matter

The precise particle candidate for Dark Matter still remains an unresolved issue. Since the DM particles constitute almost about five-sixth of the total mass content of the universe, it can be estimated that these DM particles are stable or almost stable, i.e., the lifetime of such particles are greater than the age of the universe. Also from the observations it is supposed that these particles should be very weakly interacting in nature and electromagnetically neutral. Moreover, the Standard Model of particle physics within its basic framework does not contain any viable fundamental candidate for DM. Therefore, in order to investigate the particle nature of DM, the theories or models beyond the known Standard Model should be invoked. These are the main recipes in building particle physics models for DM and studying its phenomenology. Therefore, there exist a plethora of particle physics models which have been proposed for explaining the Dark Matter in the universe and studied in literature. They include along with models motivated by theory of Supersymmetry (SUSY) [180, 181], extra dimensional model (EDM) [182–185], axion dark matter (ADM) as the solution of the strong CP problem via the Peccei-Quinn mechanism [186–190], various simple extensions of Standard Model [191–198] whose DM phenomenologies are explored at length. In this chapter we shall discuss the models for DM which are studied and explored thoroughly in order to confront different indirect DM searches.

3.1 Minimal Anomaly Mediated Supersymmetry Breaking (mAMSB) Model

The theory of Supersymmetry (SUSY) provides a solution to hierarchy problem and unification of gauge coupling constants via renornalisation group evolution (RGE). R-parity conserving SUSY also provides very naturally the lightest supersymmetric particles (LSP) to be a possible candidate for DM. In the present work, we consider neutralino to be the LSP and hence the candidate for dark matter.

In SUSY models, R-parity defined by $R = (-1)^{3B+L+2S}$ where B, L and S denotes the baryon number, lepton number and spin respectively, allows only an even number of supersymmetric partner particles to interact on a fundamental interaction vertex. This stabilises the lightest supersymmetric particle (LSP), which becomes the cold dark matter candidate. Minimal Supersymmetric Standard model (MSSM) with softly broken Supersymmetry is one of the main candidates for DM in physics beyond the Standard Model. Supersymmetry, if it exists, must be broken spontaneously. Dynamical or spontaneous breaking of Supersymmetry at high scale leads to the soft Supersymmetry breaking terms appearing in MSSM as low energy remnants. This dynamical or spontaneous breaking is supposed to take place in some 'hidden' sector (HS) and this breaking is mediated to the observable sector (OS). This is schematically shown in Fig. 3.1. This mediation mechanism leads to many interesting theories including gravity-mediation (SUGRA) with

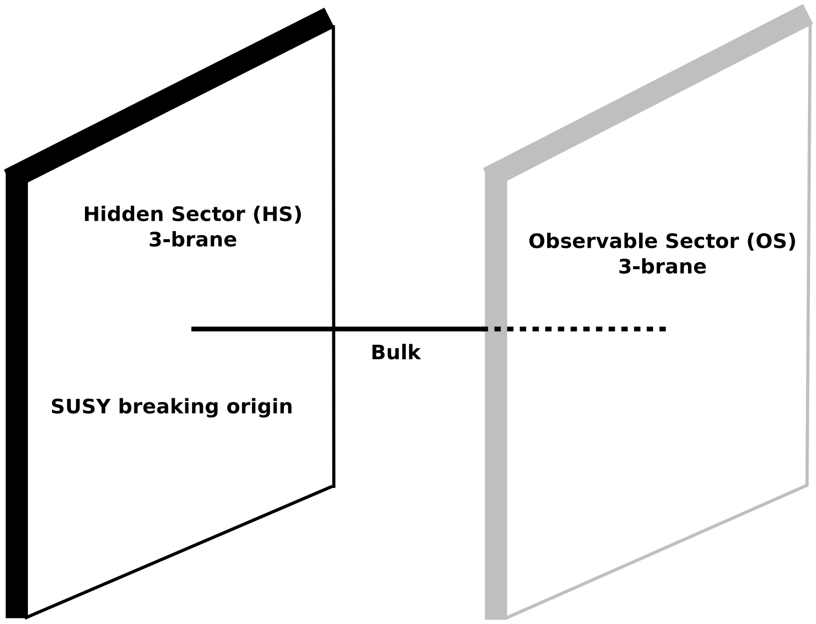

Figure 3.1: *Schematic representation of the hidden and observable 3-branes in the bulk.*

gravitino mass ($m_{\frac{3}{2}}$) ($\sim$ 1TeV), Gauge mediation (GMSB) with $m_{\frac{3}{2}} < 1$ TeV, anomaly mediation with $m_{\frac{3}{2}} \sim 100$ TeV. The superconformal Anomaly Mediated Supersymmetry Breaking (AMSB) mechanism is one of the most well-known and attractive set-ups for Supersymmetry breaking since,

(a) the soft Supersymmetry (SUSY) breaking terms are completely calculable in terms of just one free parameter (the gravitino mass, $m_{3/2}$),

(b) the soft terms are real and flavor invariant, thus solving the SUSY flavor and CP problems,

(c) the soft terms are actually renormalization group invariant and can be calculated at any convenient choice of scale,

(d) the scale of the gravitino mass is too high to affect the Big Bang nucleosynthesis (BBN) bound and cosmological gravitino problem which was the main problem in SUGRA model.

Supersymmetry breaking effects in the observable sector are of gravitational origin in this framework. In ordinary gravity-mediated Supersymmetry breaking model, the Supersymmetry breaking is transmitted from HS to OS via tree level exchanges with gravitational coupling. But in AMSB, the HS and the OS superfields are assumed to be located in two parallel but distinct 3-branes and the 3-branes are separated by bulk distance which is of the order of compactification radius, r_c. Thus any tree level exchange with mass higher than the inverse of r_c is exponentially suppressed. So, the Supersymmetry breaking is propagated from the HS to the OS via loop generated superconformal anomaly. The soft SUSY breaking terms related to gauginos and sleptons are calculated to be,

$$M_i = \frac{\beta_g}{g_i} m_{\frac{3}{2}} \ , \tag{3.1}$$

$$m^2_{\mathrm{Q}} = -\frac{1}{4}\left(\frac{\partial\gamma}{\partial g}\beta_g + \frac{\partial\gamma}{\partial y}\gamma_y\right) m^2_{\frac{3}{2}} \ , \tag{3.2}$$

$$A_y = -\frac{\beta_y}{y} m_{\frac{3}{2}} \ , \tag{3.3}$$

where M_i is the gaugino mass term, m_Q is slepton mass and A_y is the trilinear parameter. In the above γ is the anomalous dimension and β is the beta function in this theory. γ and β are defined as,

$$\gamma \equiv \frac{dlnZ}{dln\mu}, \ \ \beta_g \equiv \frac{dg}{dln\mu}, \ \ \beta_y \equiv \frac{dy}{dln\mu} \ , \tag{3.4}$$

where Z is the renormalization constant for the gauge coupling, μ is the Higgsino mass. In the abobe β_g and β_y are, respectively, the gauge coupling and Yukawa coupling β-functions, and their corresponding anomalous dimensions are denoted by γ. Another feature of AMSB is that slepton mass-squared terms are negative giving to tachyonic mass states as given in Eq. 3.2. This problem is addressed by adding an universal mass-squared term m_0^2 to all the squared scalar masses in the minimal extension to this theory, namely, minimal anomaly mediated Supersymmetry breaking (mAMSB) model [199,200].

An sparticle spectrum in this model is fixed by three parameters, namely, the gravitino mass $m_{\frac{3}{2}}$, $\tan\beta$ which is the ratio of the vacuum expectation values of the two Higgs fields (H_1^0 and H_2^0) and sign(μ), where μ is the Higgsino mass. Also, an universal mass squared term (m_0^2) is needed to make all sparticles positive. So, ultimately, with m_0, four parameters are needed to generate spectrum in mAMSB. Therefore, we can generate various LSP neutralino masses out of these four parameters in this model. This neutralino is the lowest mass eigenstate of linear superposition of the photino ($\tilde{\gamma}$), zino ($\tilde{Z}$), and the two Higgsino states ($\tilde{H_1^0}$ and $\tilde{H_2^0}$) [201], written as,

$$\chi = a_1\tilde{\gamma} + a_2\tilde{Z} + a_3\tilde{H_1^0} + a_4\tilde{H_2^0} \ . \tag{3.5}$$

This state can be obtained by diagonalising the neutralino mass matrix, which is given by,

$$M = \begin{pmatrix} M_1 & 0 & -m_z\cos\beta\sin\theta_w & m_z\sin\beta\sin\theta_w \\ 0 & M_2 & m_z\cos\beta\cos\theta_w & -m_z\sin\beta\cos\theta_w \\ -m_z\cos\beta\sin\theta_w & m_z\cos\beta\cos\theta_w & 0 & -\mu \\ m_z\sin\beta\sin\theta_w & -m_z\sin\beta\cos\theta_w & -\mu & o \end{pmatrix}$$

in the basis $\begin{pmatrix} \tilde{\gamma} & \tilde{Z} & \tilde{H_1^0} & \tilde{H_2^0} \end{pmatrix}$.

Here β is the ratio of vacuum expectation values between the two Higgs doublets, m_z is the mass of the Z_0, θ_w is the weak mixing angle and the quantities M_1, M_2, μ are the U(1) and SU(2) gaugino and Higgsino mass parameters, respectively

In addition there are phenomenological bounds on the parameter space and they are listed below.

1. A lower limit on $m_{\frac{3}{2}}$ originating from the lower bound of $m_{\chi^\pm}^{min} = 86$ GeV on

charginos causing direct search at the CERN-LEP. Recently an improved analysis has been performed by the ATLAS collaboration [202] and a new constraint on the chargino mass to $\sim$ 118 GeV is given.

2. For a certain $m_{\frac{3}{2}}$, there is a lower bound on m_0 below which $\tilde{\tau}$ is LSP or sleptons are observables.

3. For some choices of SUSY parameters, unbounded from below (UFB) directions of scalar potential are obtained and that parameter space region is not allowed.

3.2 Two Real Scalar Singlet Model

We propose a particle dark matter model in this thesis, where two real scalar singlets (S and S') are added to the standard model gauge group. We also impose the condition that both of these real scalars are stabilised separately by discrete Z_2 symmetry and thus can be viable candidates for dark matter. If both of the scalars, S and S' follow a common $\mathbb{Z}_2$ symmetry (the potential is $\mathbb{Z}_2$ symmetric for S and S' simultaneously), then the lighter of the real scalars can be a viable dark matte candidate.

On the other hand, if a discreet Z_2 symmetry is imposed on one of the singlets (say, S) and another $\mathbb{Z}_2$ ($\mathbb{Z}'_2$) is imposed on the other one (S'), then, in principle, both of these scalars are stabilised by their respective $\mathbb{Z}_2$ symmetries and hence they both simultaneously contribute as two dark matter candidates in a single theoretical framework.

The general form of the potential that appears in the Lagrangian of our model is given by,

$$
\begin{aligned}
V(H,S,S') \;=\;& \frac{m^2}{2}H^\dagger H + \frac{\lambda}{4}(H^\dagger H)^2 + \frac{\delta_1}{2}H^\dagger H S + \frac{\delta_2}{2}H^\dagger H S^2 + \frac{\delta_1 m}{2\lambda}S \\
&+\frac{k_2}{2}S^2 + \frac{k_3}{3}S^3 + \frac{k_4}{4}S^4 + \frac{\delta_1'}{2}H^\dagger H S' + \frac{\delta_2'}{2}H^\dagger H S'^2 \\
&+\frac{\delta_1' m}{2\lambda}S' + \frac{k_2'}{2}S'^2 + \frac{k_3'}{3}S'^3 + \frac{k_4'}{4}S'^4 \\
&+\frac{\delta^{pp}}{2}H^\dagger H S'S + \frac{k_2^{pp}}{2}SS' + \frac{1}{3}(k_3^a S^2 S' + k_3^b S S'^2) \\
&+\frac{1}{4}(k_4^a S^2 S'^2 + K_4^b S^3 S' + K_4^c S S'^3)\ ,
\end{aligned}
\tag{3.6}
$$

where H is the ordinary (SM) Higgs doublet and δ's are the respective couplings between the singlets and the Higgs. The k's denote the different self coupling terms between these singlets.

3.2.1 Lagrangian invariant under common $\mathbb{Z}_2$ symmetry on S, S'

The stability of both the SM singlets, S and S', are ensured by $\mathbb{Z}_2$ symmetry, i.e., each of them is Z_2 odd particle simultaneously. In this scenario, we have,

$$
\delta_1 = k_3 = \delta_1' = k_3' = k_3^a = k_3^b = 0\ . \tag{3.7}
$$

In other words, the Lagrangian respects the $\mathbb{Z}_2$ symmetry on the matrix, $\begin{pmatrix} S \\ S' \end{pmatrix}$

$$
\begin{pmatrix} S \\ S' \end{pmatrix} \rightarrow \begin{pmatrix} -S \\ -S' \end{pmatrix}, \tag{3.8}
$$

and hence the potential reduces to the following form,

$$
\begin{aligned}
V(H,S,S') \;=\;& \frac{m^2}{2}H^\dagger H + \frac{\lambda}{4}(H^\dagger H)^2 + \frac{\delta_2}{2}H^\dagger H S^2 \\
&+\frac{k_2}{2}S^2 + \frac{k_4}{4}S^4 + \frac{\delta_2'}{2}H^\dagger H S'^2 \\
&+\frac{k_2'}{2}S'^2 + \frac{k_4'}{4}S'^4 \\
&+\frac{\delta^{pp}}{2}H^\dagger H S' S + \frac{k_2^{pp}}{2}SS' \\
&+\frac{1}{4}(k_4^a S^2 S'^2 + K_4^b S^3 S' + K_4^c S S'^3)\ .
\end{aligned}
\tag{3.9}
$$

Now, the vacuum expectation value (VEV) of the Higgs field is $\frac{v}{\sqrt{2}}$ with v=246 GeV. After the spontaneous symmetry breaking in SM sector, both the physical Higgs field and the real scalar singlets in this theory acquire masses.

The mass-matrix in the basis $\begin{pmatrix} S & S' \end{pmatrix}$ can be expressed as,

$$
\begin{aligned}
M_{SS'} \;\equiv\;& \begin{pmatrix} k_2 + \delta_2 v^2/2 & \delta_2'' v^2/4 + k_2''/2 \\ \delta_2^{pp} v^2/4 + k_2''/2 & k_2' + \delta_2' v^2/2 \end{pmatrix} \\
\equiv\;& \begin{pmatrix} M_{11} & M_{12} \\ M_{12} & M_{22} \end{pmatrix}
\end{aligned}
\tag{3.10}
$$

Due to the off-diagonal terms of the mass-matrix $M_{SS'}$, the mass matrix is needed to be diagonalised. The diagonalisation of the mass matrix of S and S' gives the physical mass eigenstates as,

$$
\begin{pmatrix} S_1 \\ S_2 \end{pmatrix} = D(\theta) \begin{pmatrix} S \\ S' \end{pmatrix} , \tag{3.11}
$$

where $D(\theta)$ is the corresponding rotation matrix with the rotation angle, θ and is given by,

$$D(\theta) \equiv \begin{pmatrix} \cos\theta & \sin\theta \\ -\sin\theta & \cos\theta \end{pmatrix} . \tag{3.12}$$

The rotation angle (θ) between the two bases is dependent on the parameters of the mass-matrix elements and can be written as,

$$\tan 2\theta = \frac{2M_{12}}{M_{11} - M_{22}} = \frac{\delta_2''v^2/2 + k_2''}{(k_2 - k_2') + (\delta_2 - \delta_2')v^2/2} \tag{3.13}$$

The masses of the scalars (S_1 and S_2) after the mass-matrix diagonalisation takes the following forms,

$$M_{S_1} = (\cos\theta)^2 M_{11} + (\sin\theta)^2 M_{22} + 2\cos\theta\sin\theta M_{12} \tag{3.14}$$

$$M_{S_2} = (\cos\theta)^2 M_{22} + (\sin\theta)^2 M_{11} - 2\cos\theta\sin\theta M_{12} \ , \tag{3.15}$$

and are dependent on the six parameters, k_2, k_2', k_2'', δ_2, δ_2' and δ_2''. The candidate with lower mass is considered to be the dark matter as the scalar with higher mass can always decay to the other cannot be considered as a stable dark matter candidate.

3.2.2 Lagrangian invariant under $\mathbb{Z}_2 \times \mathbb{Z}_2'$ symmetry

On the other hand, if we restrict $\mathbb{Z}_2$ symmetry on S and $\mathbb{Z}_2'$ symmetry on S', i.e., one of the scalars is stabilised by Z_2 symmetry and the remaining one by another similar $\mathbb{Z}_2$ ($\mathbb{Z}_2'$ here) symmetry. Thus the Lagrangian is invariant under transformations of two different bases,

$$S \to -S \text{ and } \mathrm{S}' \to -\mathrm{S}' \ . \tag{3.16}$$

The potential is much more constrained and the following terms vanish,

$$\delta'' = k_2'' = k_4^b = k_4^c = 0 \ . \tag{3.17}$$

The above criteria reduce the expression for the potential and it is given by,

$$\begin{aligned} V(H,S,S') &= \frac{m^2}{2}H^\dagger H + \frac{\lambda}{4}(H^\dagger H)^2 + \frac{\delta_2}{2}H^\dagger H S^2 \\ &+\frac{k_2}{2}S^2 + \frac{k_4}{4}S^4 + \frac{\delta_2'}{2}H^\dagger H S'^2 \\ &+\frac{k_2'}{2}S'^2 + \frac{k_4'}{4}S'^4 + \frac{1}{4}k_4^a S^2 S'^2 \ . \end{aligned} \tag{3.18}$$

Now after spontaneous symmetry breaking in the SM sector, the respective masses of the two scalar fields, S and S' are,

$$M_S = k_2 + \frac{\delta_2 v^2}{2} \tag{3.19}$$

$$M_{S'} = k_2' + \frac{\delta_2' v^2}{2} \ , \tag{3.20}$$

where v is the VEV of the SM Higgs doublet. The four parameters determining the masses of the scalars are k_2, k_2', δ_2 and δ_2'.

One interesting feature of this $\mathbb{Z}_2 \times \mathbb{Z}_2'$ symmetric Lagrangian for this model is that both the scalar fields S and S' can be simultaneously considered as stable dark matter particles. We thus invoke the idea of next to minimal scalar singlet model as a perfect scenario of multicomponent dark matter. The scalar fields S and S' are stable as long as both the Z_2 and $\mathbb{Z}_2'$ symmetries are unbroken and appear to be the candidates for cold dark matter in the Universe.

3.3 Inert Higgs Doublet Model (IHDM)

The Inert Higgs Doublet Model is one of the simplest extensions of Standard Model (SM) Higgs sector where an additional complex scalar doublet, Φ is considered other than the SM Higgs doublet, H_1. The additional doublet, Φ is odd under $\mathbb{Z}_2$ symmetry while the SM fields are even under this symmetry. Thus the additional doublet Φ is *inert* since its component fields do not couple singly to SM particles. Moreover, the tree-level couplings of this inert doublet Φ with the fermionic fields is also forbidden by the requirement of renormalisablity of the model. Since the imposed $\mathbb{Z}_2$ symmetry is not spontaneously broken as assumed in the model, Φ does not acquire any vacuum expectation value (VEV). These ensure that the lightest component of the inert doublet Φ is stable. The neutral scalar of Φ, being lighter than the charged one, provides a potential DM candidate. The imposition of $\mathbb{Z}_2$ symmetry also forbids the non-diagonal terms of the mass matrix such as $-\mu_{12}^2(H^\dagger\Phi + \text{h.c.})$ where H denotes the usual SM Higgs doublet. The most general tree-level scalar potential of IHDM consistent with imposed $\mathbb{Z}_2$ symmetry can be written as,

$$V_0 \;=\; \mu_1^2|H|^2 + \mu_2^2|\Phi|^2 + \lambda_1|H|^4 + \lambda_2|\Phi|^4 + \lambda_3|H|^2|\Phi|^2 + \lambda_4|H^\dagger\Phi|^2 + \frac{\lambda_5}{2}\Big[(H^\dagger\Phi)^2 + \text{h.c.}\Big]\;, \tag{3.21}$$

where μ_is and λ_is denote various coupling parameters. After electroweak symmetry breaking (EWSB), the two doublets H and Φ can be expanded as,

$$H \;=\; \begin{pmatrix} G^+ \\ \frac{1}{\sqrt{2}}\left(v + h^0 + \mathrm{i}G^0\right) \end{pmatrix}, \qquad \Phi \;=\; \begin{pmatrix} H^+ \\ \frac{1}{\sqrt{2}}\left(H^0 + \mathrm{i}A^0\right) \end{pmatrix}, \tag{3.22}$$

where $G^\pm$ and G^0 are charged and neutral Goldstone bosons respectively [1]. In the above, v and h^0 are the VEV ($\sqrt{2}\langle\, 0|\; H \;|\, 0\,\rangle \simeq 246$ GeV) and the Higgs boson respectively. The

[1]which will be "eaten" up by $W^\pm$ and h^0 bosons to acquire masses.

components of the inert doublet, Φ consists of a pair of charged scalars, $H^{\pm}$, a neutral CP-even scalar H^0 and a pseudo-scalar A^0.

After electroweak gauge symmetry breaking, the SM Higgs doublet generate VEV, $\langle H \rangle = v/\sqrt{2}$ whereas the other doublet Φ does not acquire any VEV ($\langle \Phi \rangle = 0$) as mentioned earlier. With the unbroken $\mathbb{Z}_2$ symmetry the model has a CP-even neutral scalar H^0, a CP-odd neutral scalar A^0, and a pair of charged scalars $H^{\pm}$. Since the $\mathbb{Z}_2$ symmetry excludes the couplings of fermions with H^0, A^0, $H^{\pm}$, the decay of the latter particles to fermions are thus prevented. This ensures the stability of lightest neutral scalar (H^0 or A^0) and hence the lightest among these two can serve as a possible DM candidate. Either H^0 or A^0 is chosen as the lightest inert particle or LIP and is the candidate for dark matter in the present model. Initially the model contains 8 parameters, namely λ_i, μ_i, v out of which two parameters (v, μ_1) are fixed from the gauge boson (Z) mass and observed SM Higgs boson mass respectively. Thus we are left with only a set of six independent parameters, namely

$$\{\lambda_1, \quad \lambda_2, \quad \lambda_3, \quad \lambda_4, \quad \lambda_5, \quad \mu_2\} \,. \tag{3.23}$$

After spontaneous symmetry breaking, the different mass terms can be written from Eq. 3.21 as (in terms of the above six parameters (Eq. 3.23))

$$M^2_{h^0} = -2\mu_1^2 = 2\lambda_1 v^2 \,, \tag{3.24}$$

$$M^2_{H^0} = \mu_2^2 + \frac{1}{2}(\lambda_3 + \lambda_4 + \lambda_5)v^2 = \mu_2^2 + \lambda_L v^2 \,, \tag{3.25}$$

$$M^2_{A^0} = \mu_2^2 + \frac{1}{2}(\lambda_3 + \lambda_4 - \lambda_5)v^2 = \mu_2^2 + \lambda_S v^2 \,, \tag{3.26}$$

$$M^2_{H^{\pm}} = \mu_2^2 + \frac{1}{2}\lambda_3 v^2 \,. \tag{3.27}$$

In the above,

$$\lambda_L = \frac{1}{2}(\lambda_3 + \lambda_4 + \lambda_5)\,, \tag{3.28}$$

$$\lambda_S = \frac{1}{2}(\lambda_3 + \lambda_4 - \lambda_5)\,. \tag{3.29}$$

With these, we have a modified set of six parameters as

$$\{M_{h^0},\quad M_{H^0},\quad M_{A^0},\quad M_{H^\pm},\quad \lambda_L,\quad \lambda_2\}\,, \tag{3.30}$$

The parameters λ_L and λ_S denote the coupling strength for $H^0H^0h^0$ (if H^0 is considered to be the lightest inert particle or LIP) and $A^0A^0h^0$ (if A^0 is the LIP) respectively. The self-quartic coupling λ_2 does not have any viable contribution as far as the tree-level processes are concerned.

3.4 Radiative Neutrino Mass Model with Three Right Handed Singlet Neutrinos and One Doublet

We consider the model proposed by Ma [203] which is the extension of Standard Model with three gauge singlet right-handed neutrinos N_1, N_2, N_3 and extra $\mathrm{SU}(2)_L$ doublet scalar η. The fields can be written as,

$$N_1,\quad N_2,\quad N_3,\quad \eta = \begin{pmatrix} \eta^+ \\ \eta^0 \end{pmatrix}. \tag{3.31}$$

The doublet scalar η is assumed to obtain no vacuum expectation value and hence inert. An additional discrete $\mathbb{Z}_2$ symmetry is imposed on the model. The stability of the cold DM candidate in this model is guaranteed by this symmetry. In addition, the tree-level

Dirac masses of neutrinos are forbidden for this additional $\mathbb{Z}_2$ symmetry. SM gauge group and $\mathbb{Z}_2$ charges of the particles are shown in Tab. 3.1.

Particle	$N_k\,(k=1,2,3)$	η
$(SU(2)_L, U(1)_Y)$	$(\mathbf{1},0)$	$(\mathbf{2},1/2)$
$\mathbb{Z}_2$	odd (-)	odd (-)

Table 3.1: Additional fields under SM gauge group and $\mathbb{Z}_2$ symmetry

The Lagrangian for the right-handed neutrinos, N_k $(k = 1, 2, 3)$ invariant under both SM gauge symmetry and $\mathbb{Z}_2$ symmetry can be written as,

$$\mathcal{L}_N = \overline{N_i} i \partial\!\!\!/ P_R N_i + (D_\mu \eta)^\dagger (D^\mu \eta) - \frac{M_i}{2} \overline{N_i{}^c} P_R N_i + h_{\alpha i} \overline{\ell_\alpha} \eta^\dagger P_R N_i + \text{h.c.}, \tag{3.32}$$

where $h_{\alpha k}$, ℓ_α and M_k represent Yukawa couplings, lepton doublet and the mass of the right-handed neutrino of type k (N_k) respectively. Here M_ks are chosen to be real without any loss of generality. The invariant scalar potential containing the Higgs doublet Φ and the additional SU$(2)_L$ doublet η is given by,

$$\begin{aligned}\mathcal{V}(\phi,\eta) = \;& m_\phi^2 \phi^\dagger \phi + m_\eta^2 \eta^\dagger \eta + \frac{\lambda_1}{2}\left(\phi^\dagger\phi\right)^2 + \frac{\lambda_2}{2}\left(\eta^\dagger\eta\right)^2 \\ & + \lambda_3 \left(\phi^\dagger\phi\right)\left(\eta^\dagger\eta\right) + \lambda_4 \left(\phi^\dagger\eta\right)\left(\eta^\dagger\phi\right) + \frac{\lambda_5}{2}\left(\phi^\dagger\eta\right)^2 + \text{h.c.}\,. \end{aligned} \tag{3.33}$$

The tree-level Dirac mass terms for neutrinos can not be generated since the vacuum expectation value of the doublet η $(\langle\eta\rangle)$ is chosen be zero. After electroweak symmetry breaking SM Higgs doublet obtains vacuum expectation value, $v = 246$ GeV and the Majorana masses of neutrinos are generated radiatively via one-loop diagrams with η^0 and N_k in internal lines. The model could explain both the possibilities that the scalar (η^0) and the fermion (N_k) may be candidates for DM. But we choose the mass of one of the three right-handed neutrinos (N_1) to be lightest among the particles added to SM and hence it is a stable candidate of DM. From the forth term of the Lagrangian in Eq. 3.32

it is clear that the right-handed neutrino interacts only with the SM lepton doublet and hence leptophilic.

In the following chapters we shall discuss, in detail, the bounds on such model coming from theoretical, experimental as well as observational data. We shall mainly focus on the indirect detection of dark matter via the signature of gamma rays originating from the dark matter candidates in the above discussed models. In order to put constraints on the parameters of those dark matter models, we confront our calculated results in the frameworks of those dark matter models with those obtained from various observations.

Chapter 4

Gamma Ray and Neutrino Flux from Annihilation of Neutralino Dark Matter at Galactic Halo Region in mAMSB Model

In this chapter we consider the lightest supersymmetric particle (LSP), neutralino in minimal anomaly mediated supersymmetry breaking model (mAMSB) to be a possible candidate for weakly interacting massive particles (WIMP) or cold dark matter and investigate its direct and indirect detections. The theoretically allowed supersymmetric parametric space for such a model along with the recent bounds from LHC is constrained by the WMAP results for relic densities. The spin independent and spin dependent scattering cross sections for dark matter off nucleon are thus constrained from the WMAP results. They are found to be within the allowed regions of different ongoing direct detection experiments. The annihilation of such dark matter candidates at the galactic centre produce different standard model particles such as gamma rays, neutrinos etc. In this work, we calculate the possible fluxes of these γ-rays and neutrinos coming from the direction of the galactic centre (and its neighbourhood) at terrestrial or satellite borne detectors. The calcutated γ-ray flux is compared with the observational results of HESS experiment. The neutrino flux of different flavours from the galactic centre and at different locations away from the galactic centre produced by WIMP annihilation in this model are also obtained for four types of galactic dark matter halo profiles. The detection prospects of such ν_μ coming from the direction of the galactic centre at the ANTARES under sea detector are discussed in terms of muon signal yield from these muon neutrinos. Both the gamma and neutrino signals are estimated for four different dark matter halo profiles.

4.1 Introduction

The dark matter candidate in the present chapter is considered to be the lightest supersymmetric particle (LSP) neutralino in the minimal anomaly mediated supersymmetry breaking model [199, 200] where the LSP is stabilised by conservation of R-parity. In the superconformal Anomaly Mediated Supersymmetry Breaking (AMSB) mechanism, dynamical or spontaneous breaking is supposed to take place in some 'hidden' sector (HS) and this breaking is mediated to the observable sector (OS) by gravitino mass ($m_{\frac{3}{2}}$) $\sim$ 100 TeV. Supersymmetry breaking effects in the observable sector have a gravitational origin in this framework. In ordinary gravity-mediated supersymmetry breaking model, the supersymmetry breaking is transmitted from HS to OS via tree level exchanges with gravitational coupling. But in AMSB, the HS and the OS superfields are assumed to be located in two parallel but distinct 3-branes and the 3-branes are separated by bulk distance which is of the order of compactification radius, r_c. Thus any tree level exchange with mass higher than the inverse of r_c is exponentially suppressed. So, the supersymmetry breaking is propagated from the HS to the OS via loop generated superconformal anomaly.

In AMSB model, the slepton mass-squared terms are negative giving to tachyonic states. The problem is circumvented by adding an universal mass-squared term m_0^2 to all the squared scalar masses in the minimal extension to this theory, namely, minimal anomaly mediated supersymmetry breaking (mAMSB) model [199, 200]. An sparticle spectrum in this model is fixed by three parameters, $m_{\frac{3}{2}}$ which is gravitino mass, tanβ which is the ratio of the vacuum expectation values of the two Higgs fields (H_1^0 and H_2^0) and sign(μ), where μ is the Higgsino mass. Thus four parameters are needed to generate spectrum in mAMSB. The neutralino is the lowest mass eigenstate of linear superposition of photino ($\tilde{\gamma}$), zino ($\tilde{Z}$), and the two Higgsino states ($\tilde{H}_1^0$ and $\tilde{H}_2^0$) [201], written as,

$$\chi = a_1\tilde{\gamma} + a_2\tilde{Z} + a_3\tilde{H}_1^0 + a_4\tilde{H}_2^0 \ . \tag{4.1}$$

in the basis $\begin{pmatrix} \tilde{\gamma} & \tilde{Z} & \tilde{H}_1^0 & \tilde{H}_2^0 \end{pmatrix}$.

The ATLAS collaboration [202] has recently performed an improved analysis and give a new constraint on the chargino mass to $\sim$ 118 GeV. This new constraint differs from the previous LEP2 bound. In this work, the SUSY parameter space namely m_0, $m_{\frac{3}{2}}$, tanβ and sign(μ) is initially adopted from Datta *et al.* [204] but with proper incorporation of the recent LHC (ATLAS) bound on chargino mass [202] mentioned above. The relic densities for such dark matter are then computed using these SUSY parameters and they are compared with the WMAP results. The parameters, thus constrained further by the WMAP results, are then used to calculate the spin independent and spin dependent cross sections ($\sigma_{\rm scatt}$) for different neutralino masses (m_χ) (obtained using the restricted parameter space). The χ-nucleon scattering process is essential for the direct searches of dark matter. As mentioned above, we calculate χ-nucleon elastic scattering cross section $\sigma_{\rm scatt}$ for the restricted parameter space discussed earlier. The $m_\chi - \sigma_{\rm scatt}$ region, thus obtained, is found to be within the allowed limits of most of the direct detection experiment results.

Using the constrained mAMSB parameter space discussed above we calculate the gamma ray flux in the direction of the galactic centre. These studies are performed for different galactic dark matter halo profiles. We find that the gamma spectrum from galactic centre and halo produced by neutralino dark matter within the framework of the present mAMSB model, is highly energetic. Different satellite-borne and ground-based experiments looking for extra terrestrial gamma signals have reported the observence of excess gamma ray signals in the direction of galactic centre in different energy regions. If the observed TeV gamma rays from the galactic centre are indeed due to the annihilation of dark matter at galactic centre then such dark matter mass should be $\sim$ TeV. The HESS (The High Energy Stereoscopic System) [164–166] experiment had reported the gamma rays from the galactic centre with energies in $\sim$ TeV range. In minimal anomaly mediated supersymmetry breaking (mAMSB) model [199,200], the lightest supersymmetric particle (LSP) neutralino that can be a candidate for dark matter has its mass in TeV range. The calculated γ-ray flux is found to be within the experimental search limit of high energy gamma ray search experiments such as HESS. The experiment like HESS, that can probe high energy gamma rays and which, being in the southern hemisphere has better visibility of the galactic centre, will be suitable to test the viability of the present dark matter candidate in mAMSB model. The possibility of detecting neutrinos from galactic centre and halo from dark matter annihilations are also addressed with reference to ANTARES (Astronomy with a Neutrino Telescope and Abyss environmental RESearch) [205] under sea neutrino experiment.

In a recent work Vásquez *et al.* [206] has given a detailed analysis of the allowed parameter space for a neutralino dark matter in the framework of NMSSM model. In their case the dark matter (neutralino) mass was within the range of $\sim$ 80 GeV and hence the energies of the gamma rays from such dark matter annihilations can be probed by FermiLAT [173, 207] experiment. In the present calculation, we instead consider the neutralino dark matter in mAMSB model mentioned above. Some of the earlier works on dark matter phenomenology in AMSB model include Baer *et al.* [208], Moroi *et al.* [209], Ullio [210] etc. In Refs. [208] and [210] the γ flux from the galactic centre are discussed and although neutrinos from the neutralino annihilations are mentioned in Ref. [208] but they have not discussed elaborately. Moreover, only two halo models are considered for their analysis. In an another earlier work ([211]), a neutralino dark matter in AMSB model is studied to obtain the region in scalar cross section ($\sigma_{\rm scatt}$ - m_χ) parameter space. But in this case WMAP limit has not been taken into account. In Ref. [212], the γ signal from galactic centre region due to dark matter annihilation is addressed mainly for the case of FERMI (formerly GLAST) satellite-borne experiment. Ref. [213] discusses the the γ-flux from galactic centre region, originated by dark matter annihilations. The authors made the analysis with different particle dark matter candidates with reference to MSSM, Kaluza-Klein extra dimensional model etc. for different halo profiles and taking into account the Fermi-LAT experiment. But the neutrinos as dark matter annihilation products are not addressed. In another work by Allahverdi et al [214] considered MSSM and $U(1)_{B-L}$ extened MSSM model for dark matter candidate and calculated γ and neutrino fluxes from galactic and extra-galactic origins by annihilating dark matter. But they have considered only one dark matter halo profile namely NFW halo profile and they have not shown the neutrinos flux for different neutrino flavours. Moreover, no detailed comparison of their results with high energy neutrino or gamma search experiments is shown. There are also other earlier works like [215, 216] where dark matter annihilations in galaxy are addressed.

In this chapter we use the mAMSB framework for the neutralino DM candidate and study both the possible γ-ray and neutrino flux that an experiment will probe in the direction of galactic centre. We perform this study for four dark matter halo profiles. The γ-ray results are compared with HESS experiment and for neutrinos, we estimate the possible signal in ANTARES under sea detector.

The present chapter is organised as follows. In Sec. 4.2 we discuss the calculation of relic densities of mAMSB neutralinos for the parameter space. The relic densities are then compared with the WMAP results. The parameter space thus constrained further by WMAP is then used to calculate the spin dependent and spin independent scattering cross sections. They are compared with the existing direct detection experiment limits. These are discussed in Sec. 4.3. In Sec. 4.4 the indirect detection of the mAMSB dark matter from their annihilations at galactic centre and halo are discussed. To this end the gamma signals and neutrino signals are addressed.

4.2 Calculation of Relic Abundance in mAMSB Model

In order to calculate the relic abundance of the LSP, χ, one needs to consider annihilation of N supersymmetric particles with masses m_i (i=1,2,..,N) and internal degrees of freedom g_i respectively. The relic abundance is obtained by numerically solving the Boltzmann's equation,

$$\frac{dn}{dt} + 3Hn = -\langle \sigma v \rangle (n^2 - n_{\rm eq}^2) \ , \tag{4.2}$$

where n is the total number density of all the supersymmetric particles n_i

$$n = \Sigma_i n_i \ \ ,$$

and $n_{\rm eq}$ is the value of n when the particles for dark matter candidate were in chemical equilibrium. At this epoch the temperature T of the universe was greater than T_f ($T > T_f$), the freeze out temperature of the particle considered. At a temperature below the freeze-out temperature T_f, the particles falls out of chemical and thermal equilibrium and their co-moving number density becomes fixed or "frozen". In Eq. 4.2, H denotes the Hubble parameter and $\langle \sigma v \rangle$ is the thermal average of the product of annihilation cross section and the relative velocity of the two annihilating particles.

$$\langle \sigma v \rangle = \sum_{i,j} \langle \sigma_{ij} v_{ij} \rangle \frac{n_{\rm eq}^{(i)} n_{\rm eq}^{(j)}}{n_{\rm eq}^2} \ , \tag{4.3}$$

with

$$v_{ij} = \frac{\sqrt{(p_i.p_j)^2 - m_i^2 m_j^2}}{E_i E_j} \ .$$

In the above, (p_i, p_j) and (E_i, E_j) are the momenta and energies respectively for the ith and jth particles. Defining the abundance, $Y = n/s$ [217] where s is the total entropy density of the universe, and with the dimensionless quantity $x = m_\chi/T$, with m_χ being the mass of LSP, Eq. 4.2 can be written in the form

$$\frac{dY}{dx} = \frac{1}{3H} \frac{ds}{dx} \langle \sigma v \rangle (Y^2 - Y_{eq}^2) \, . \tag{4.4}$$

In Eq. 4.4, $Y_{\rm eq}$ is the value of Y when $n = n_{\rm eq}$. With Hubble parameter $H = \sqrt{\frac{8}{3}\pi G \rho}$, G being the gravitational constant, the total energy density (ρ) and the total entropy density (s) of the universe are given by [217]

$$\rho = g_{eff}(T) \frac{\pi^2}{30} T^4 \tag{4.5}$$

$$\text{and} \quad s = h_{eff}(T) \frac{2\pi^2}{45} T^3 \ . \tag{4.6}$$

In Eqs. 4.5 and 4.6 g_{eff}, h_{eff} are the effective degrees of freedom for the energy and entropy densities respectively. Substituting Eqs. 4.5, Eqs. 4.6 and the expression for H in Eq. 4.4, one obtains the evolution equation of Y as

$$\frac{dY}{dx} = -\left(\frac{45}{\pi}G\right)^{-1/2} \frac{g_*^{1/2} m_\chi}{x^2} \langle\sigma v\rangle (Y^2 - Y_{eq}^2) \ , \tag{4.7}$$

where $g_*^{1/2}$ is defined as [217]

$$g_*^{1/2} = \frac{h_{eff}}{g_{eff}^{1/2}} \left(1 + \frac{1}{3}\frac{T}{h_{eff}}\frac{dh_{eff}}{dT}\right) . \tag{4.8}$$

The expression for Y_{eq} is given by [217]

$$Y_{eq}(T) = \frac{45}{4\pi^4 h_{eff}(T)} \sum_i g_i \frac{m_i^2}{T^2} K_2\left(\frac{m_i}{T}\right) \ , \tag{4.9}$$

where we sum over all supersymmetric particles denoted by i with mass m_i and internal degrees of freedom g_i. $K_2(x)$ is the modified bessel function of the second kind of order 2. The thermally-averaged cross section, $\langle\sigma v\rangle$ must include all channels by which χ can interact, including coannihilation with other particles, in which the number densities of both species are important.

Integrating Eq. 5.51 from $x = x_0 = m/T_0$ to $x = x_f = m/T_f$, where T_0 is the present photon temperature (2.726^o K) we obtain Y_0 (value of Y at $T = T_0$) which is needed to compute the relic density. Eq. 5.51 is solved numerically with the following approximations,

- 1. At small x (high T), the abundance of lightest SUSY particles (LSP) are almost in equilibrium and the temperature variation of the deviation from equilibrium abundance is negligible, i.e., $Y \approx Y_{eq}$ and $\frac{Y-Y_{eq}}{T} \approx 0$. Thus, the evolution equation reduces to,

$$\frac{dln(Y_{eq})}{dx} = -\left(\frac{45}{\pi}G\right)^{-1/2}\frac{g_*^{1/2}m_\chi}{x^2}\langle\sigma v\rangle Y_{eq}\delta(\delta+2) \ , \tag{4.10}$$

where δ is some small constant coming from the definition of freeze-out temperature T_f.

- 2. At temperature below T_f, equilibrium abundance, Y_{eq} falls much below Y, as seen from Eq. 5.51 and can be neglected in the abundance evolution equation. Thus, Y_0 is obtained from the relation,

$$\frac{1}{Y_0} = \frac{1}{Y_f} - m_\chi\left(\frac{45}{\pi}G\right)^{-1/2}\int_{x_f}^{x_0}\frac{g_*^{1/2}(x)}{x^2}\langle\sigma v\rangle dx \tag{4.11}$$

The relic density of LSP, in the units of critical density, $\rho_{cr} = 3H^2/8\pi G$, can be expressed as

$$\Omega_\chi = \frac{m_\chi n}{\rho_{cr}} = \frac{m_\chi s_0 Y_0}{\rho_{cr}} \ , \tag{4.12}$$

where s_0 is the present entropy density evaluated at T_0. Finally, knowing Y_0, we can compute the relic density of the dark matter candidate, from the relation [217],

$$\Omega_\chi h^2 = 2.755\times 10^8\frac{m_\chi}{\text{GeV}}Y_0 \ . \tag{4.13}$$

In the above h is the Hubble constant in 100 Km sec^{-1}Mpc^{-1} unit. The WMAP survey combining with recent observations of large–scale structure provides the constraints on the dark matter density $\Omega_{DM}h^2$ as

$$0.099 < \Omega_{DM}h^2 < 0.123 \ . \tag{4.14}$$

where Ω_{DM} is the ratio of dark matter density to the critical density $\rho_c = 1.88h^2 \times 10^{-29}\text{gcm}^{-3}$.

In the present work we calculate the relic densities for the dark matter candidate neutralino in mAMSB model and compare our results with the WMAP bound. The allowed parameter space in the present SUSY model is thus extracted by WMAP results.

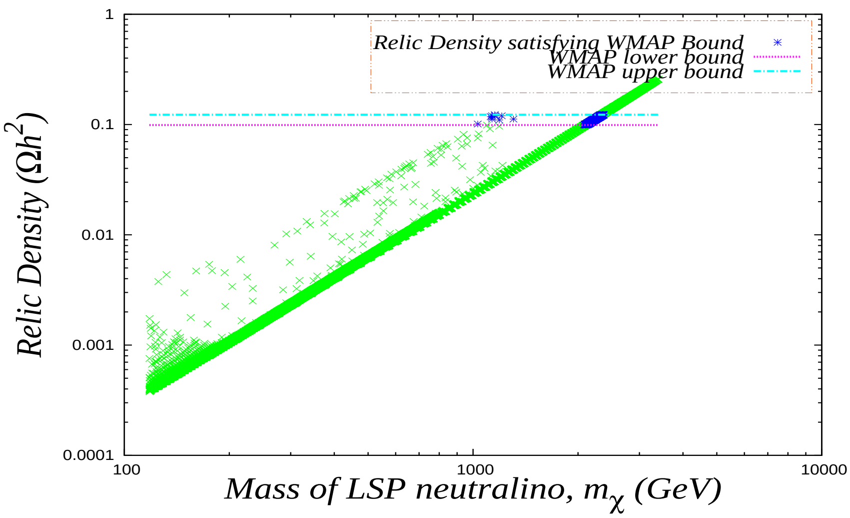

Figure 4.1: *Scatter plot of mass of the LSP neutralino (m_χ) vs. relic density (Ωh^2) in mAMSB model. The cyan and pink line represents the WMAP upper and lower bounds on dark matter relic density respectively and the blue dotted zones corresponds to the mass range satisfying the WMAP limits.*

As mentioned earlier, the parameter space of the mAMSB model is defined by the four parameters, namely $m_{3/2}$, m_0, $\tan\beta$ and sign(μ). The whole parameter space defined by the above parameters and constrained by the allowed region of $m_0 - m_{3/2}$ (see earlier) is used to calculate the relic density Ω_χ (or $\Omega_\chi h^2$) and the results are then compared with the WMAP results.

The relic density in the present formalism of SUSY model is computed using the code `micrOMEGAs` [218]. We thus obtain the relic density for the scanned SUSY parameter space discussed above. We find that the generated LSP neutralinos span very large range of mass. Each generated LSP neutralino mass gives rise to different annihilation cross section due to their annihilations to different standard model particles and also co-annihilation processes. We mention here that the LSP neutralino is found to be wino dominated with the other components like bino or higgsino have very negligible contribution. The mass scales for other sparticles are above the LSP neutralino mass scale. For example for an LSP of mass ~ 2 TeV, the sneutrinos mass is ~ 14 TeV and for squark the mass scale is ~ 18 TeV; the NLSP mass is ~ 7 TeV.

In Fig. 4.1, the variation of relic densities for different LSP neutralino masses are shown. The scatter plots in Fig. 4.1 correspond to the allowed parameter space. The WMAP bound is superimposed on this scatter plot in Fig. 4.1 and the regions of agreement of the present calculational results with WMAP data are identified by blue coloured area in Fig. 4.1. From Fig. 4.1, we obtain two different neutralino mass regions satisfying the WMAP bound. One region is around 1 TeV and the other region is at a somewhat higher range of ~ 2 TeV.

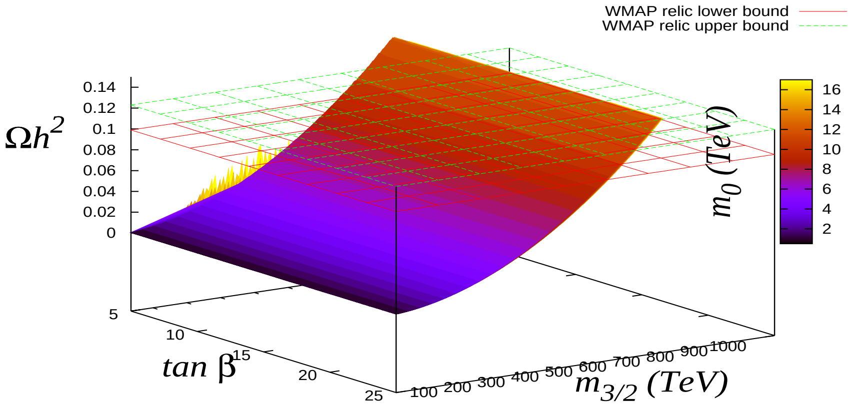

Figure 4.2: *Constraints on SUSY parameter space from WMAP limits in present SUSY model. The gaugino mass parameter m_0 are shown by the colour index where m_0 varies from blue coloured region to yellow region as its mass increases.*

In order to elaborate how the WMAP bound constrains the SUSY parameter space in the present mAMSB model, we make a 3-D colour coded plot in Fig. 4.2, where the variation of relic density Ωh^2 with the simultaneous variations of all three SUSY parameters namely $m_{3/2}$, $\tan\beta$ and m_0 are furnished. In Fig. 4.2, the parameters $m_{3/2}$

and $\tan\beta$ are plotted along X and Y axes respectively while the variation of gaugino mass m_0 is shown in colour coded display whereby the colour reference deep blue denotes the lower value of m_0 and increases towards the yellow zone in the plot. The corresponding variation of Ωh^2 is shown along Z axis. The WMAP limits are shown in Fig. 4.2 by two meshes separated by the WMAP limit along Ωh^2 axis. One observes from Fig. 2 that a very small region of the $m_{3/2} - m_0 - \tan\beta$ parameter space is allowed by WMAP. Thus WMAP limit further constraints the $m_{3/2} - m_0$ parameter limits. From Fig. 4.2 it is also clear that only higher values of m_0 ($\sim 10 - 12$ TeV), and $m_{3/2}$ ($\sim 650 - 700$) TeV could satisfy the WMAP limits. We have not obtained any other parameter space in $m_0 - m_{3/2}$ plane that satisfy WMAP limits.

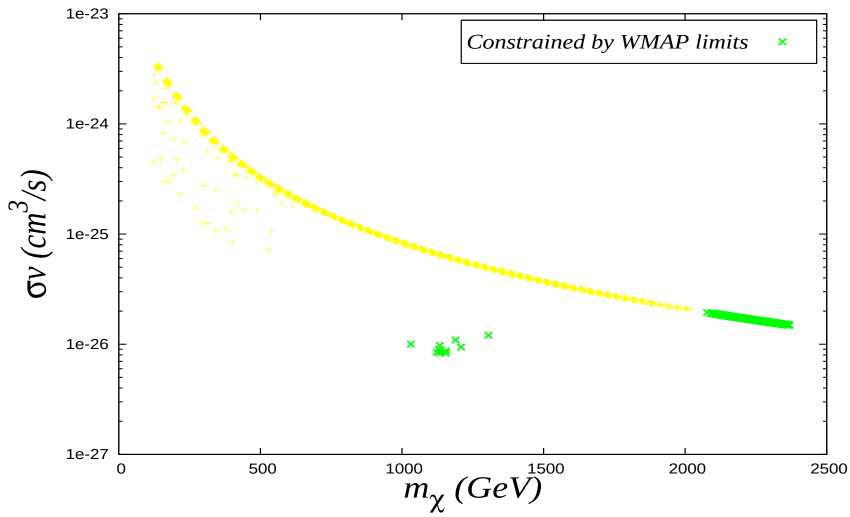

Figure 4.3: *Plot showing the variation (in yellow) of annihilation cross section times relative velocity of annihilating neutralinos (σv) with the mass of the LSP neutralino (m_χ) in mAMSB model. The green zones are the WMAP allowed regions.*

In Fig. 4.3, we show how the annihilation cross sections vary with the neutralino dark matter mass (m_χ) in the present model. The WMAP allowed mass region is also shown by green colour. The σv for the allowed zones (marked green) are seen to be around the value $\sim 10^{-26}$ cm^{3}sec^{-1}.

The variations of freezeout temperatures (T_f) of LSP neutralino for the mass range

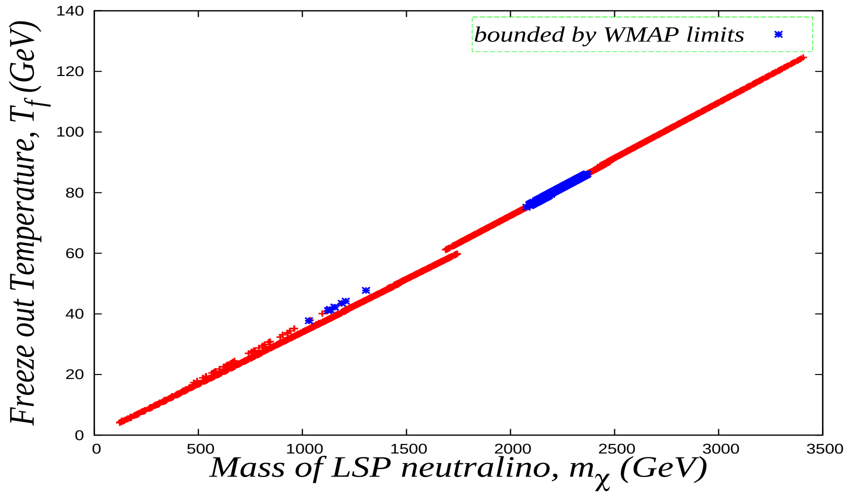

Figure 4.4: *Plot showing the variation (in red) of freezeout temperature (T_f) with the mass of the mAMSB LSP neutralino (m_χ). The blue dotted zones are constrained by WMAP limits on dark matter relic.*

obtained using the SUSY parameter space discussed earlier, are shown in the scatter plot of Fig. 4.4. The neutralinos that satisfy WMAP relic density results are shown as blue in Fig. 4.4. As in Fig. 1, in this case also one observes two such regions, one is around $T_f \sim 80 - 86$ GeV (more populated) and the other (fewer candidates) is at a lower region of around $T_f \sim 40$ GeV.

4.3 Direct Detection of Dark Matter in mAMSB Model

The direct detection of dark matter is based on the principle that the WIMP scatters off the target nucleus of the material of the detector causing the nucleus to recoil. The signal generated by the nuclear recoil (generally $\sim$ keV) is measured for direct detection. In the direct detection experiments, attempts are made to give a bound in the $m_\chi - \sigma_{\rm scatt}$ space (m_χ being the mass of the dark matter and $\sigma_{\rm scatt}$ is the dark matter-nucleus or dark matter-nucleon scattering cross sections). Different techniques are adopted by different direct detection experiments in order to measure the nuclear recoil energies.

Some experiments that use Ge, Si or NaI as detector materials use scintillation, phonon or ionization techniques. In another class of detectors like Time Projection Chamber (TPC) detectors, the drifting of ionized charges, produced by recoil nucleon of the detector material (generally noble liquids are chosen), produce the track from which the direction of recoil can also be measured. Some of the ongoing direct detection experiments include DAMA (NaI) [108–110], CDMS (^{73}Ge) [111, 112], PICASSO (CS_2) [113, 114], XENON [115–119], COUPP [120], LUX [219], CLEAN and DEAP [122] etc. They give different limits on scattering cross sections for different dark matter mass.

The dark matter-nucleus scattering cross sections can be of two types namely axial-vector (spin-dependent) or scalar (spin-independent). The target nucleus, with zero ground state spin gives rise to spin independent interaction. On the other hand, spin-dependent interactions are for the nuclei with unpaired nucleon that gives rise to non-zero ground state spin. The experiments such as Edelweiss [123], DAMA/NaI , CDMS Super-CDMS [124], Xenon10 [115, 116], Xenon100 [117–119], Zeplin [125, 126], KIMS [127–129], CoGeNT [130] are using detectors made of heavy nuclei (Ge or Xe) to search scalar interactions. On the other hand, NAIAD [131], SIMPLE [132], PICASSO [114], Tokyo/NaF [133] are using light nuclei to detect spin-dependent case.

The interaction Lagrangian for spin independent elastic scattering of Majorana fermionic WIMP off nucleon N in non-relativistic limit is given by [220],

$$L_{SI} = \lambda_N \bar{\psi}_\chi \psi_\chi \bar{\psi}_N \psi_N \ , \tag{4.15}$$

where λ_N is the WIMP-nucleon coupling. Other notations have their usual significance. The interaction Lagrangian for spin-dependent case is given by [220],

$$L_{SD} = \epsilon_N \bar{\psi}_\chi \gamma_\mu \gamma_5 \psi_\chi \bar{\psi}_N \gamma^\mu \gamma_5 \psi_N \ , \tag{4.16}$$

where ϵ_N denotes the coupling. The spin-dependent and spin-independent cross sections for scattering of dark matter particle (χ) with nucleon (N) are respectively given in compact forms as,

$$\sigma^{\rm SD} = \frac{4m_\chi^2 M_N^2}{\pi(m_\chi + M_N)^2} \times 3|A^{\rm SD}|^2 \ , \tag{4.17}$$

$$\sigma^{\rm SI} = \frac{4m_\chi^2 M_N^2}{\pi(m_\chi + M_N)^2} \times |A^{\rm SI}|^2 \ , \tag{4.18}$$

where m_χ, M_N are the dark matter particle mass and nucleon mass respectively. In the above, $A^{\rm SI}$ and $A^{\rm SD}$ are the relevant matrix elements that depend on the quark contents of the target nucleon (N) for χ-N scattering. It may be noted that there is a factor of 3 appearing in Eq. 4.17. This is because of the nuclear angular momentum function ($\frac{J+1}{J}$) with nuclear angular momentum at its ground state $J = \frac{1}{2}$, which appears in the expression of spin dependent cross section.

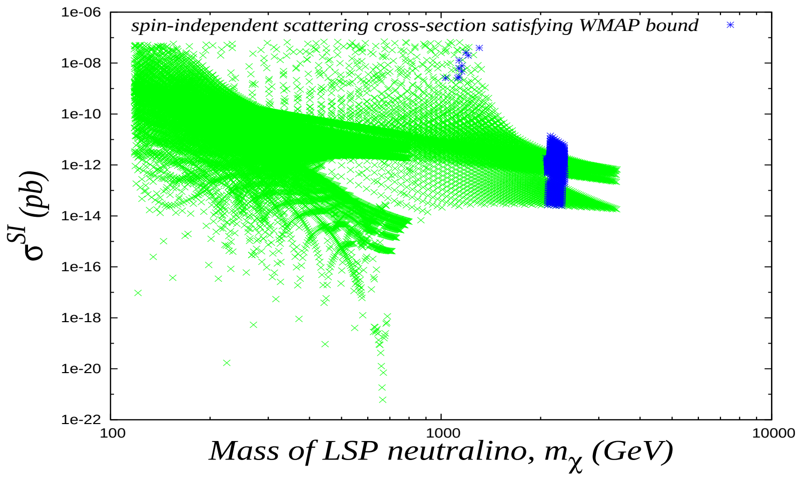

Figure 4.5: *The plot showing the variation of Spin Independent scattering cross section (σ^{SI}) with for Mass of the LSP neutralino (m_χ) for the allowed SUSY parameter space. The blue zones are the LSP neutralinos which satisfy the WMAP relic.*

We have computed both spin-independent and spin-dependent scattering cross sections of neutralino dark matter for a wide range of mass in this model respecting the allowed $m_0 - m_{3/2}$ bound. As the nucleon consists of both protons and neutrons, the WIMPs can be scattered off both nucleons. The contribution of loop diagrams along with the tree level diagrams have also been included for calculations of scattering amplitudes for both SI and SD cases of $\chi - \mathrm{N}$ scattering. These scattering cross sections for different neutralino masses are computed using `micrOMEGAs` [218] computer code. The results for both SI and SD cases are shown in Fig. 4.5 and Fig. 4.6 respectively as scattered plots for scattering with protons.

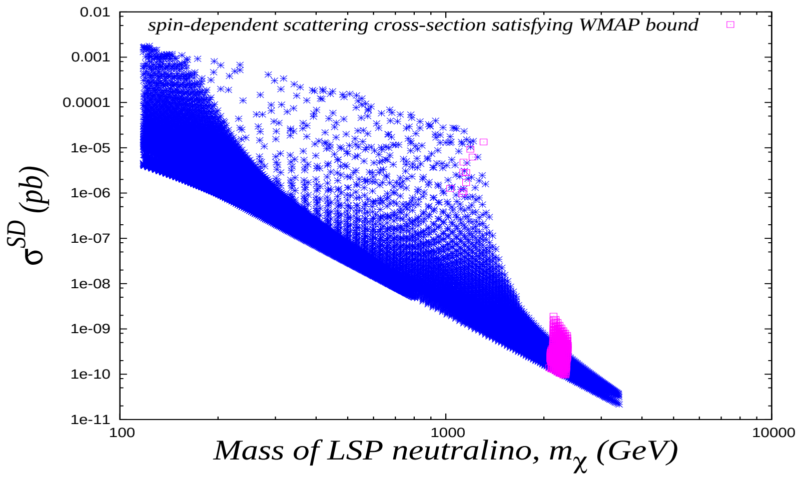

Figure 4.6: *The variation of Spin Dependent scattering cross section (σ^{SD}) with mass of the LSP neutralino (m_χ) allowed parameter space is shown in this plot. WMAP relic satisfied two zones are shown in pink.*

The green scattered plots in Fig. 4.5 give the spin independent scattering cross section σ^{SI} for various neutralino masses m_χ generated in the present AMSB model with the bound on parameter space. The blue scattered plots in Fig. 4.6, on the other hand, are for the spin dependent case. The mass region(s) in this model that satisfy the WMAP results for relic density are superimposed over these two figures in order to constrain the $m_\chi - \sigma^{\mathrm{SI/SD}}$ space obtained from Figs. 4.5, 4.6. The blue patches in Fig. 4.5 and the pink patches in Fig. 4.6 represent the mass regions that satisfy WMAP results. Clearly, there are two different zones allowed by the WMAP limits as expected from the discussions in Sect. 2. For the WMAP allowed lower mass region (around 1 TeV), the SI cross section (Fig. 4.5) extends between $\sim 10^{-9}$– $\sim 10^{-7}$ pb. The WMAP allowed higher mass region (around 2 TeV) which spans larger region in $m_\chi - \sigma^{\mathrm{SI}}$ space than the WMAP allowed lower mass region, is confined within SI cross section limit $\sim 10^{-11}- \sim 10^{-14}$ pb in Fig. 4.5. The pink regions in Fig. 4.6 signify the WMAP allowed region. Here, the value of SD scattering cross section is coming to be higher than that of SI as it is expected from the theoretical perspective.

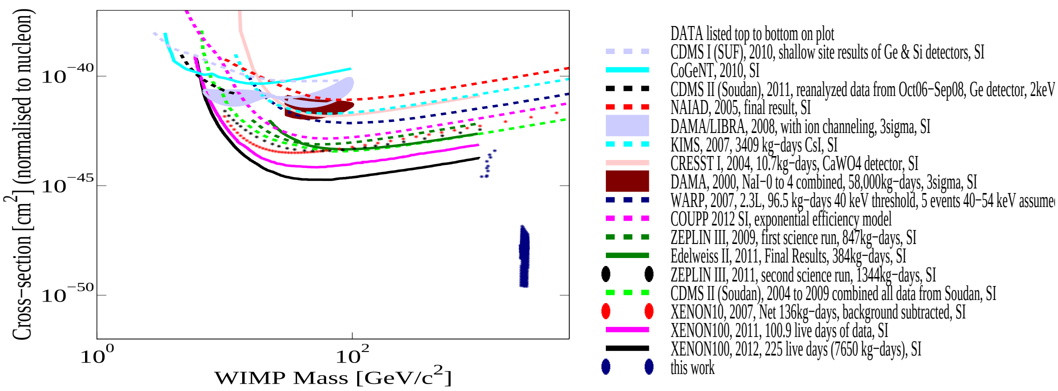

Figure 4.7: *Limits on spin independent scattering cross sections set by various experiments and comparison with our results in mAMSB model. Our calculated results that follow the WMAP limits are shown by two distinct blue patches in this figure and they are found to be within these experimental bounds.*

Similarly, in Fig. 4.6 the WMAP allowed lower mass region (around 1 TeV) constrain the spin dependent cross section $\sigma^{\rm SD}$ limits in the range $\sim 10^{-6}- \sim 10^{-5}$ pb and for the region of around 2 TeV $\sigma^{\rm SD}$ lies between $\sim 10^{-10}$ to $\sim 10^{-9}$ pb. We mentioned in passing that we obtained similar nature for WIMP-*neutron* elastic scattering.

Figs. 4.7 and 4.8 show respectively various upper limits in dark matter mass - SI or SD scattering cross section ($m_\chi - \sigma^{\rm SI\,or\,SD}$) plane set by different ongoing direct detection experiments. The WMAP-allowed regions from the present model for neutralino dark matter are superimposed on them for comparison. The experimental limits are obtained from the compilation given in DM Limit Plotter. The names of the different experiments are furnished as legends in the figures. It is obvious from Figs. 4.7 and 4.8 that the allowed parameter space for the considered AMSB model is within the allowed limits of the experimental bounds.

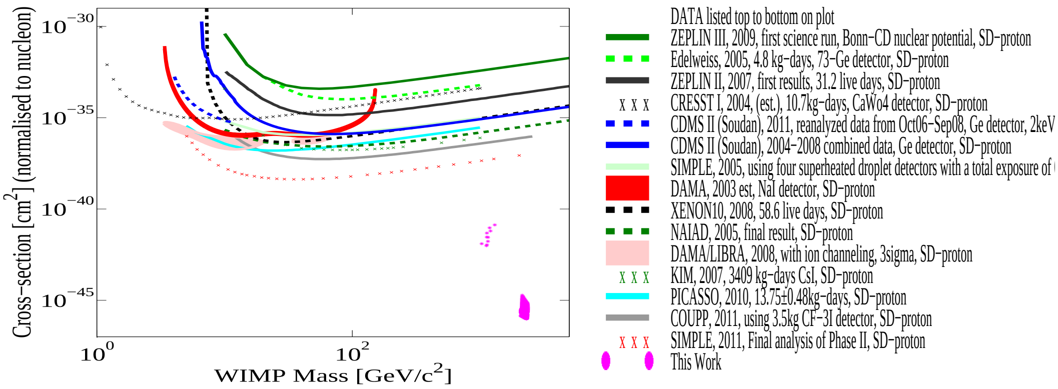

Figure 4.8: *Limits on spin dependent scattering cross sections set by various experiments and comparison with our calculated results. The pink zones are the satisfying WMAP bounds and they are few orders below the upper bounds of these experimental data.*

4.4 Indirect Detection of Dark Matter in mAMSB Model

Weakly interacting dark matter in our galaxy can be trapped inside massive heavenly bodies like galactic centre or the sun due to the gravity of these bodies. The dark matter particles, in course of their passage through such massive bodies undergo elastic scattering off the nuclei present there as a result of which their velocity deplete. If their velocities fall below their escape velocities from such massive objects, the dark matter particles are trapped. These trapped dark matter particle (χ) may undergo the process of pair-annihilation producing primarily b, c and t quarks, τ leptons, gauge bosons, etc. ($\chi\chi \rightarrow q\bar{q}, l^+l^-, \nu\bar{\nu}, ZZ, W^+W^-, ...$). The annihilation products depend on the mass and composition of the dark matter. Neutrinos and antineutrinos can be produced by the decay of primary annihilation products or through direct annihilation.

The main principle of indirect detection of dark matter is to detect and measure the fluxes of standard model particles produced from the annihilation of dark matter trapped by the gravitation of massive heavenly bodies. Recently many new results from indirect DM searches have been released. An interpretation of these excesses related to astrophysical processes from any galactic or extragalactic sources is still not very clear. The products from the annihilation of dark matter particles in massive bodies such as in galactic centre may explain such excess signals.

There are a lot of satellite borne experiments that look for gamma rays or antimatters in cosmos. Some terrestrial experiments are also suited for looking at cosmic gamma rays, neutrinos etc. Such experiments include PAMELA [221, 222] that confirms an excess in positron fraction in agreement with earlier indications by HEAT [223] and AMS01 [224]. Other satellite borne experiments like FERMI [225] and ATIC [226] report an excess in total electron and positron spectrum at energies of several hundreds of GeV's, much higher than that of PAMELA search. The cosmic gamma rays from the galactic sources and from galactic centre are measured in a wide range of energies by INTEGRAL ($< \sim$1 MeV) [227], EGRET [228], FERMI [229], HESS [164–166], MAGIC [230], Whipple/Veritas [231], CANGAROO ($> \sim$100 GeV) [232] etc.

In this work we mainly focus on the gamma ray and neutrinos from dark matter annihilations in the direction at and around galactic centre (GC). The GC region has higher dark matter density and hence a promising site for the study of indirect detection of dark matter. Although GC seems to be the most obvious target, it is also one of the most difficult areas to work with because of the complex and poorly-understood backgrounds [167, 233], for signals from around GC and uncertain dark matter profile [234–236].

The galactic gravitational potential leads to a higher dark matter density at the centre of Milky Way. The expected flux from the galactic centre depends on the distribution of dark matter in the galaxy. The dark matter density profile $\rho(r)$ is assumed to be spherically symmetric. The differential flux of the outgoing particle of type i is given by

$$I^i(E,\theta) = \frac{d\Phi_i}{dE} = \sum_j \frac{\sigma_j \upsilon}{8\pi\alpha m_\chi^2}\frac{dN_j^i}{dE}(E)J(\theta,\Delta\Omega) \tag{4.19}$$

where the factor, α is 1 or 2 depending on whether the assumed WIMPs are self-conjugated or not respectively. In the above 'j' denotes a particular annihilation channel. It is also to be mentioned that the effect of this factor, α on the above differential flux is much less significant in comparison to the dark matter density fluctuations in the innermost regions of Milky Way. Here we consider α to be unity as the neutralinos from the mAMSB model (the dark matter candidate chosen in the present work) are self-conjugated. In Eq. 4.19, σ is the annihilation cross section of dark matter and υ denotes the relative velocity of the dark matter particles. The quantity $\frac{dN^i}{dE}(E)$ in Eq. 4.19 is the energy spectrum of particle i and $J(\theta,\Delta\Omega)$ is given by,

$$J(\theta,\Delta\Omega) = \int_{\Delta\Omega} d\Omega \int_{\text{line of sight}} \langle\rho^2(r(\tilde{r},\theta))\rangle d\tilde{r} \; . \tag{4.20}$$

With θ being the angle subtended by the line of sight of an observer on the earth (along the length $\tilde{r}$) on $R_\odot$ − the distance between GC and the terrestrial observer (in solar system). The source to observer distance $\tilde{r}$ can be calulated as

$$\tilde{r} \;\; = \;\; \sqrt{(r^2 + R_\odot^2 - 2rR_\odot cos\theta)} \; , \tag{4.21}$$

In the above, the target region is considered to be at a distance r from GC (at the GC, $r = 0$). Here we also mention that the GC is assumed to be coincident with the halo centre). The solar system's position in the halo from the GC is given by $R_\odot = 8.0$ kpc. In Eq. 4.20, $\Delta\Omega$ is the solid angle over which the observation is to be made and $\rho(r)$ is the dark matter density at a distance r from GC. Clearly the integration on the RHS of Eq. 4.20 is along the line of sight. Thus the astrophysical factor J in Eq. 4.19 has only a θ dependence (along with $\Delta\Omega$) and thus the differential flux I_γ can be expressed in terms of the angle θ corresponding to different positions of the source in galactic halo with respect to GC.

The dark matter density $\rho(r)$ is related to the spherically symmetric halo profile of galactic dark matter by the equation

$$\rho(r) \;\; = \;\; \rho_0 F_{\rm halo}(r) \; , \tag{4.22}$$

where ρ_0 is the dark matter density at the galactic centre assumed to be 0.3 GeV/cm^3 and $F_{\rm halo}(r)$ is the halo profile of the galactic dark matter which can be expressed in a parametric form,

$$F_{\rm halo}(r) \;\; = \;\; \left[\frac{R_\odot}{r}\right]^\gamma \left[\frac{1+\left[\frac{R_\odot}{a}\right]^\alpha}{1+\left[\frac{r}{a}\right]^\alpha}\right]^{\frac{\beta-\gamma}{\alpha}} \; . \tag{4.23}$$

In the above, a is a scale parameter and the other parameters α, β, γ take different values for different halo models which follow the above parametric form for $F_{\rm halo}$. For example, for NFW halo profile [151], $\alpha = 1$, $\beta = 3$, $\gamma = 1$ and $a = 20$ kpc, whereas the parameter set $\alpha = 2$, $\beta = 2$, $\gamma = 0$ and $a = 4$ kpc represents isothermal profile with core [155]. Again for the Moore profile [153, 154] we have, $\alpha = 1.5$, $\beta = 3$, $\gamma = 1.5$ and $a = 28$ kpc. In Einasto halo profile [158] however, a different kind of parametric form is adopted which is given by,

$$F_{\rm halo}^{Ein}(r) = exp\left[\frac{-2}{\tilde{\alpha}}\left(\left(\frac{r}{R_\odot}\right)^{\tilde{\alpha}} - 1\right)\right] \; , \tag{4.24}$$

where $\tilde{\alpha}$ is the parameter. In this work $\tilde{\alpha} = 0.17$ is adopted. In what follows the four profiles are referred to as NFW, Isothermal, Moore and Einasto respectively. The galactic halo densities for these four halo models are shown in Fig. 4.9. In the present work we show the gamma ray and neutrino flux from galactic centre region for each of the four

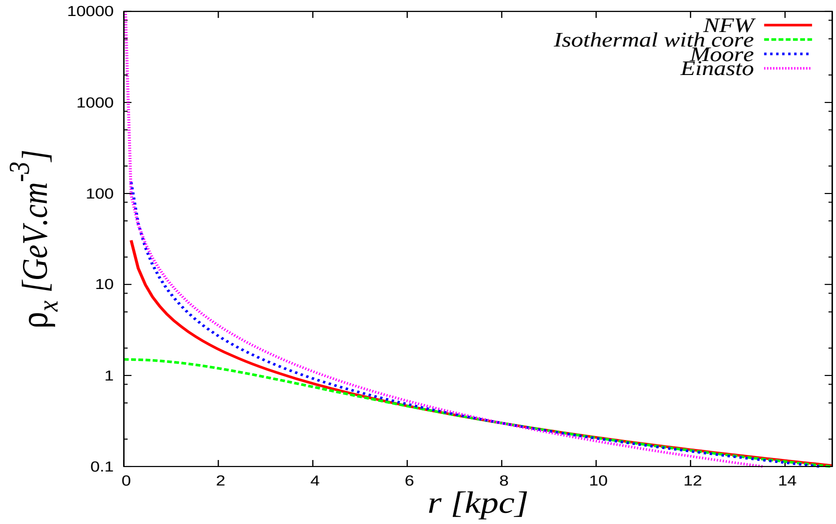

Figure 4.9: *The variation of galactic halo density with radial distance for various halo models and the cuspy or flat nature of the considered halo profiles are shown.*

halo profiles mentioned above.

4.4.1 Gamma Ray Flux Results

There are generally two kinds of γ-ray emission from DM annihilation. In the first category γ is produced directly from the annihilation final state particles which is called primary emission in which final charged leptons emit gamma ray or π^0 which eventually decays to gamma ray after hadronization. The other kind is called secondary emission in which gamma rays are produced by interactions of final state particles with external medium or radiation field such as the inverse Compton effects etc. Here we consider only the first type of emission for which the relation (4.19) holds. Here we calculate the gamma ray flux from the galactic centre as also from other places in galactic dark matter halo along the line of sight around the GC. As discussed in the previous section, the targets away from the galactic centre are characterised by changing only the angle θ. This angle θ in fact denotes the angle of sight from the observer with respect to the line of sight when the observer is looking directly at the galactic centre. The polarisation effect of final state gauge bosons ($W^{\pm}$ and Z) and also the photon radiation effect which strongly affect the gamma ray spectra are also taken into account in the present work. The γ-flux is computed using `micrOMEGAs` code. The calculations are made for each the four halo profiles, referred to as NFW, Isothermal, Moore and Einasto and the results are furnished in the four figures namely Figs. 4.10a - 4.10d respectively.

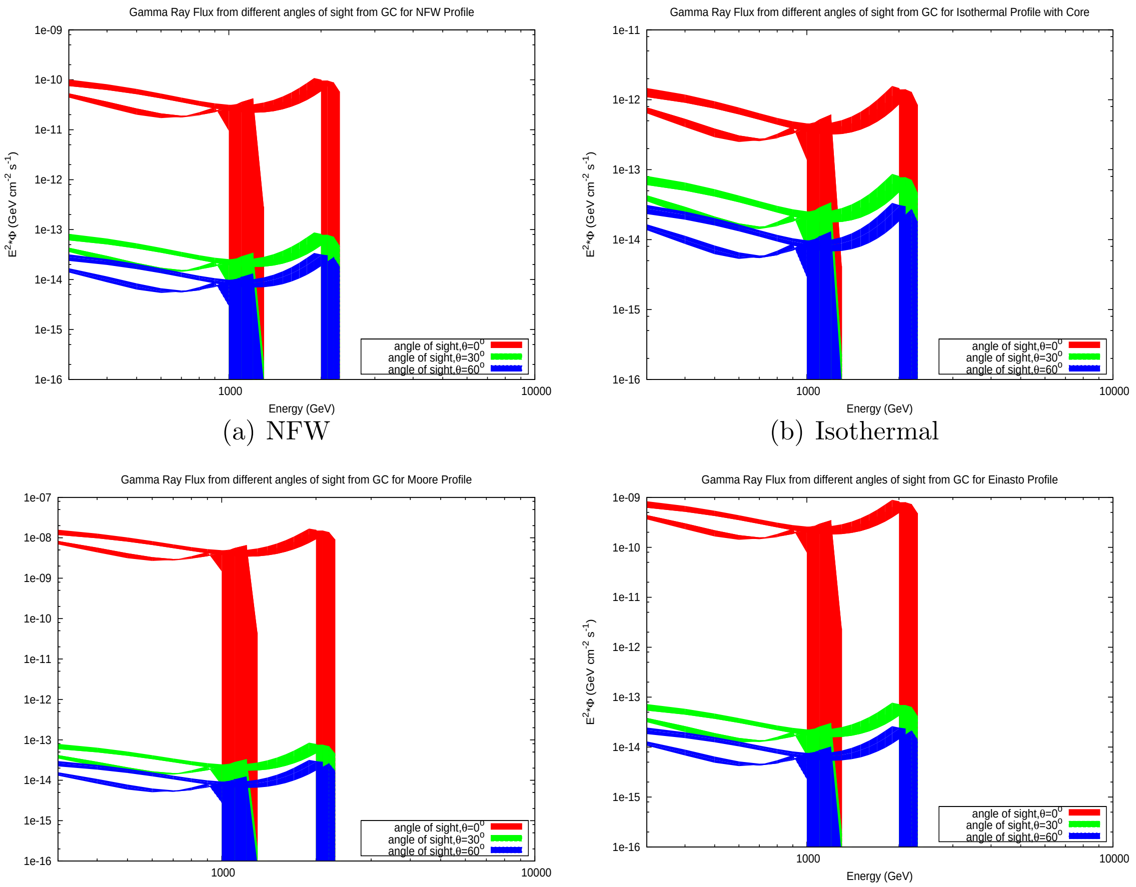

(a) NFW

(b) Isothermal

(c) Moore

(d) Einesto

Figure 4.10: *Plot showing the variation of gamma ray flux with energies from the annihilation of dark matter for different galactic DM halo models and for different angles of sight, θ. The red lines describe the flux observed at $\theta = 0^o$, i.e., from the galactic centre and the green and blue coloured regions are for the observations at $\theta = 30^o$ and 60^o respectively. The subfigures are for different commonly used dark matter halo profiles implemented in this work, a) NFW profile b) Isothermal profile with core c) Moore profile d) Einasto profile*

In Figs. 4.10a - 4.10d, we plot the quantity $E^2 \times \frac{d\Phi}{dE}$ for different values E, the energy of the emitted γ rays from dark matter annihilations. We show the results for the cases when $\theta = 0$ (galactic centre), $\theta = 30^o$ and $\theta = 60^o$ and are shown as red, green and blue regions respectively. One notices in Figs. 4.10a - 4.10d that γ flux for any particular value of the angle θ are given as a pair of plots designated by the specific colour code (red, blue or green), assumed for the results corresponding to that particular θ. This is due to the fact that the WMAP data constrain the supersymmetric parameter space considered in this work, in two distinct zones as shown in Figs. 4.1, 4.2 and each of the plots in every such pair of γ flux in Figs. 4.10a - 4.10d correspond to each of the WMAP allowed regions for the present AMSB model for cold dark matter candidates. It is clear from Figs. 4.10a - 4.10d that calculations with different halo profiles yield different results for γ flux. It is also to be noted that the flux in the direction of the galactic centre ($\theta = 0$) is larger than the flux from other directions (corresponding to different values of $\theta \neq 0$) for each of the four halo models considered.

The γ fluxes are found to be almost of the similar order for the cases when $\theta = 30^o$ and $\theta = 60^o$ in each of the Figs. 4.10a - 4.10d. This reflects the fact that the DM halo profiles are almost flat in those regions. The Einasto profile has a finite (zero) central slope. On the other hand, we choose the NFW profile to be cuspy halo profile, although in many variants of the NFW profile, they become flat for very small radial distances. As it is not yet known which model provides the best description of the central densities of simulated dark-matter halos, we have taken these known models into account.

The γ-flux thus obtained for different halo models are compared with the observational results of The High Energy Stereoscopic System (HESS) experiment. Located in Namibia, the HESS experiment is designed to investigate high energy cosmic gamma rays (~ 100 GeV - TeV energy ranges) and it can also investigate the γ-rays in its observable energy range which can be due to the annihilation of cold dark matter particles. The results are given in Fig. 4.11 and Fig. 4.12. In each of the figures, the calculated flux are shown by two diferent regions corresponding to WMAP constrained two zones of dark matter mass in the present mAMSB model (discussed earlier). It has been argued by Prada *et al.* in Ref. [152] (and also in Ref. [237]) that due to the infall of baryons at the galactic centre, the expected γ signal from dark matter annihilation at galactic centre will be boosted in case the dark matter consists of supersymmetric particles. In fact, considering neutralino in minimal supergravity (mSUGRA) model as the candidate for dark matter and with the NFW dark matter halo profile, they have demonstrated that the said boost can be of the order of 1000. In Fig. 4.11a, the γ flux from the galactic centre as calculated from the annihilation of neutralino dark matter in present mAMSB model assuming the NFW profile, is compared with the HESS results. The solid angle at which the HESS experiment looks at the galactic centre is $\sim 10^{-5}$ sr, a value which is also adopted in the present calculations to obtain the results shown in Fig. 4.11 and Fig. 4.12. It is evident from Fig. 4.11a that the γ-flux obtained from the present calculations is much less than the HESS results for the energy range given by the model with WMAP constraints. In Fig. 4.11b we show a representative plot where the calculated γ-flux is multiplied ("boosted") by a factor of 1000 and then compared with the HESS results. Fig. 4.11b shows that the "boosted" flux is in the similar ball park of HESS results which seems to satisfy the claim made in Ref. [152]. In Figs. 4.12a, 4.12b and 4.12c, we show similar comparisons with HESS results for calculations made with Einasto, Moore and isothermal halo profiles respectively. One observes from Fig. 4.12 that both for isothermal and Einasto profiles, the calculated fluxes are below the HESS results while for Moore profile, they are comparable with HESS results. Both NFW and Moore profiles are cuspy in nature and they essentially differ by the values of the parameters α, β, γ. On the other hand both the Einasto and isothermal profiles are non-cuspy in nature while the latter is a flat halo profile. One needs to increase the calculated flux by a factor $\sim 10^2$ for the former case while the calculated flux for the isothermal profile needs a boost of $\sim 10^5$ to be in the regime of HESS observational results.

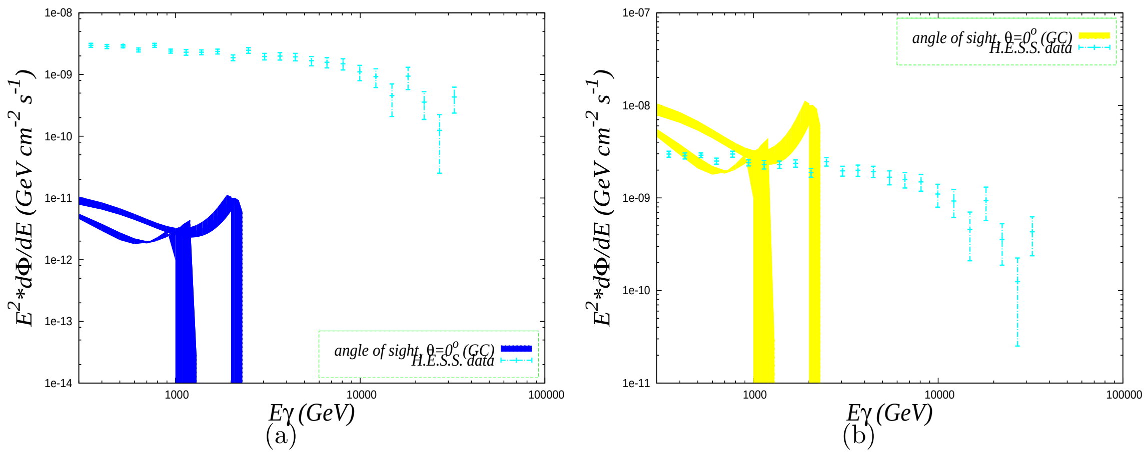

Figure 4.11: *Plot of energy vs.* γ *flux for dark matter annihilation at the galactic centre and comparison with the HESS experimental data for NFW profile a) without baryonic compression and b) with the baryonic compression and* $\sim 10^3$ *flux enhancement*

4.4.2 Neutrino Flux Results

As discussed earlier, neutrinos can also be produced by the annihilation of two neutralinos – the present dark matter candidate. These trapped dark matter at the galactic centre produces primarily b, c, t quarks, τ leptons, gauge bosons, etc. through the process of pair-annihilations. The neutrinos can be obtained from the decay or pair annihilation of the primary products. The neutrinos can also be produced directly from the annihilation of two mAMSB neutralinos ($\chi\tilde{\chi} \rightarrow \nu\bar{\nu}$) mediated by Z, sneutrino ($\tilde{\nu}$) etc. In this work we investigate the muon neutrino (ν_μ) flux from the galactic centre due to the annihilation of such neutralinos in the present mAMSB model and its possible detection prospect at an earthbound detector. Searches for neutralino annihilation into neutrinos is subject to extensive experimental investigations in view of the neutrino telescopes like IceCube, Baikal, NESTOR, ANTARES [205]. The calculation of flux of neutrinos coming from GC are similar to that of gamma rays as both are electromagnetically neutral particles. So, they are not affected by the irregularities of galactic magnetic fields or any magnetic turbulences. Also, they do not suffer any energy loss from inverse compton effect or from

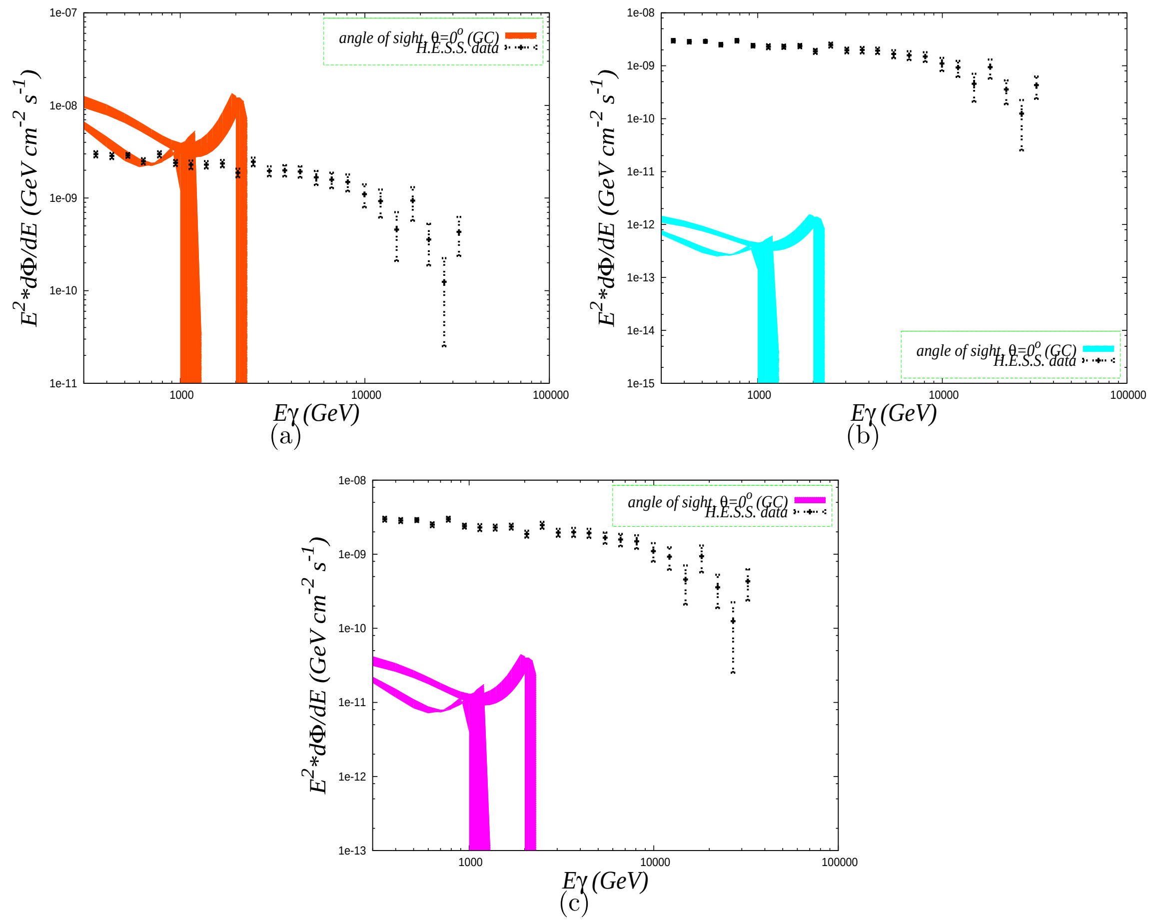

Figure 4.12: *Plot of energy vs. γ flux from DM annihilation at the GC and comparison with the HESS experimental data for a) Moore profile, b) Isothermal profile with core and c) Einasto profile*

synchrotron radiation. For the present case we calcuate the possible muon (μ) signal from these neutrinos at ANTARES neutrino telescope [205] installed in the sea-bed off France coast.

We use `micrOMEGAs` computer code to calculate the neutrino flux in the direction of the galactic centre for all the four halo models considered. The neutrino flux for the halo models can be obtained using similar equations (Eqs. 4.19 - 4.23) that is used for obtaining γ-flux. The ν-flux for each of the three flavours namely ν_e, ν_μ and ν_τ are calculated separately for three values of the angle θ (Eq. 4.19 and discussions earlier)

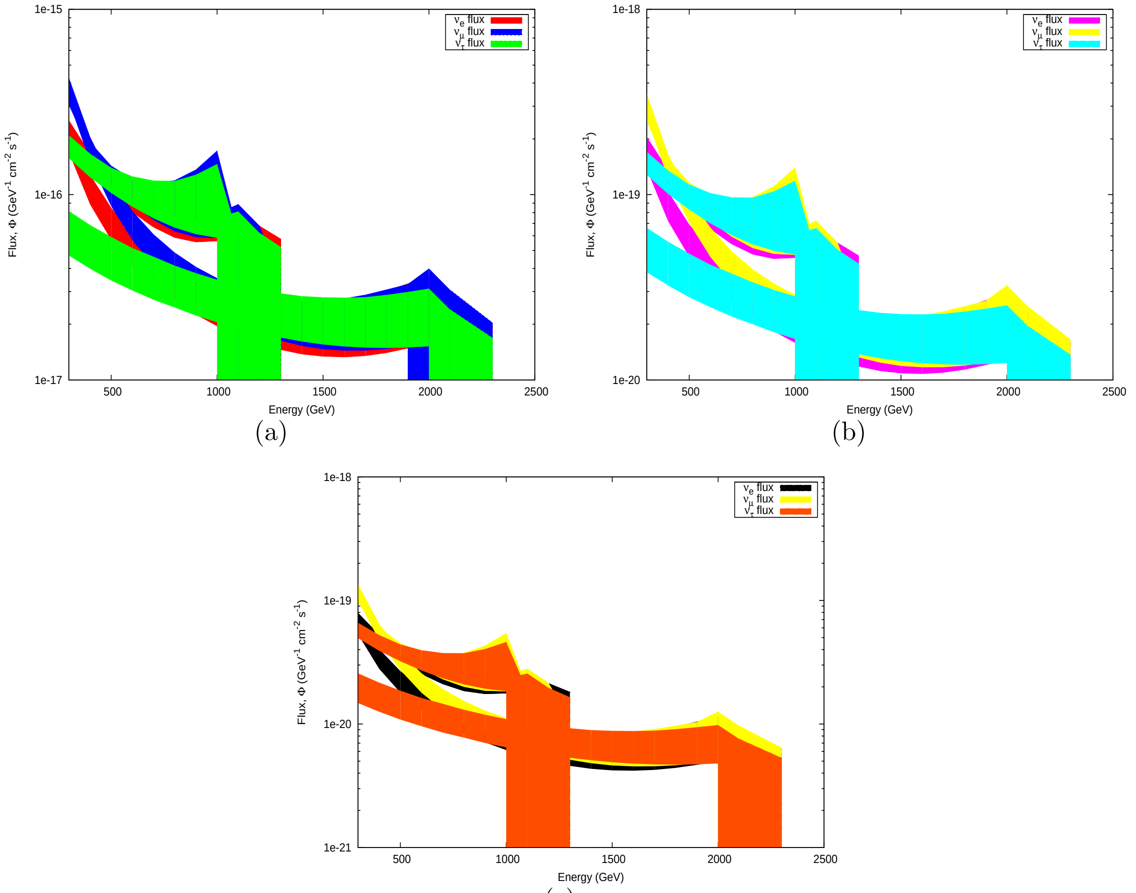

(a) (b) (c)

Figure 4.13: *Neutrino flux of three flavours (ν_e, ν_μ and ν_τ) for different energies for a) angle of sight, $\theta = 0^o$ b) angle of sight, $\theta = 30^o$ and c) angle of sight, $\theta = 60^o$ from the galactic centre respectively.*

namely $\theta = 0^o$, $\theta = 30^o$, $\theta = 60^o$. The results are furnished in Figs. 4.13 - 4.16. In Fig. 4.13, we give results only for NFW profile for the two allowed regions of dark matter mass around 1 TeV and around 2 TeV. We have done similar calculations for other three profiles namely Einasto, Isothermal and Moore halo profiles. As seen from Fig. 4.13, the big overlap regions of the plots for the two allowed mass zones reduce their clarity and readability. Therefore in Figs. 4.14 - 4.16, we plot the neutrino fluxes for energies upto 1000 GeV for the two allowed dark matter mass regions discussed earlier.

The three figures namely Fig. 4.14, Fig. 4.15 and Fig. 4.16 correspond to $\theta = 0^o$, 30^o

and 60^o respectively. In these figures the ν_e flux , the ν_μ flux and the ν_τ flux are shown respectively by red, blue and green colours in Fig. 4.14, pink, yellow and turquiose colour labels in Fig. 4.15 and black, yellow and orange colours in Fig. 4.16 respectively. The two flux regions for each of the neutrino flavours are for the two different allowed dark matter mass zones in this model obtained from WMAP results. The ν flux for different dark matter profiles considered here, exhibit similar trends as for the case of γ flux in the sense that the flux is more for Moore profile and gradually decreases for Einasto, NFW and isothermal profiles.

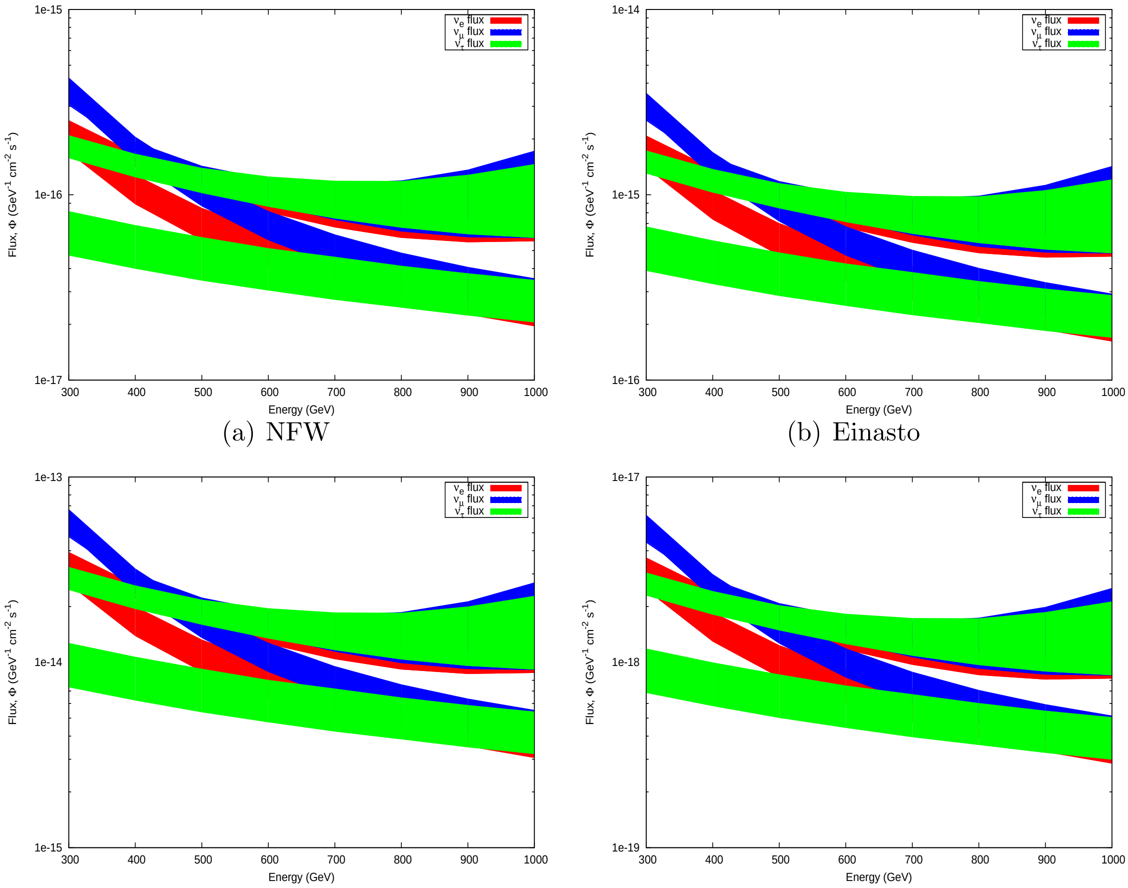

(a) NFW (b) Einasto

(c) Moore (d) Isothermal

Figure 4.14: *neutrino flux for three flavours (ν_e, ν_μ and ν_τ) for different energies from the annihilation of dark matter at from the galactic centre. The red, blue and green patches describe the fluxes corresponding to ν_e, ν_μ and ν_τ respectively*

The neutrinos, while reaching the earth from the galactic centre will undergo flavour

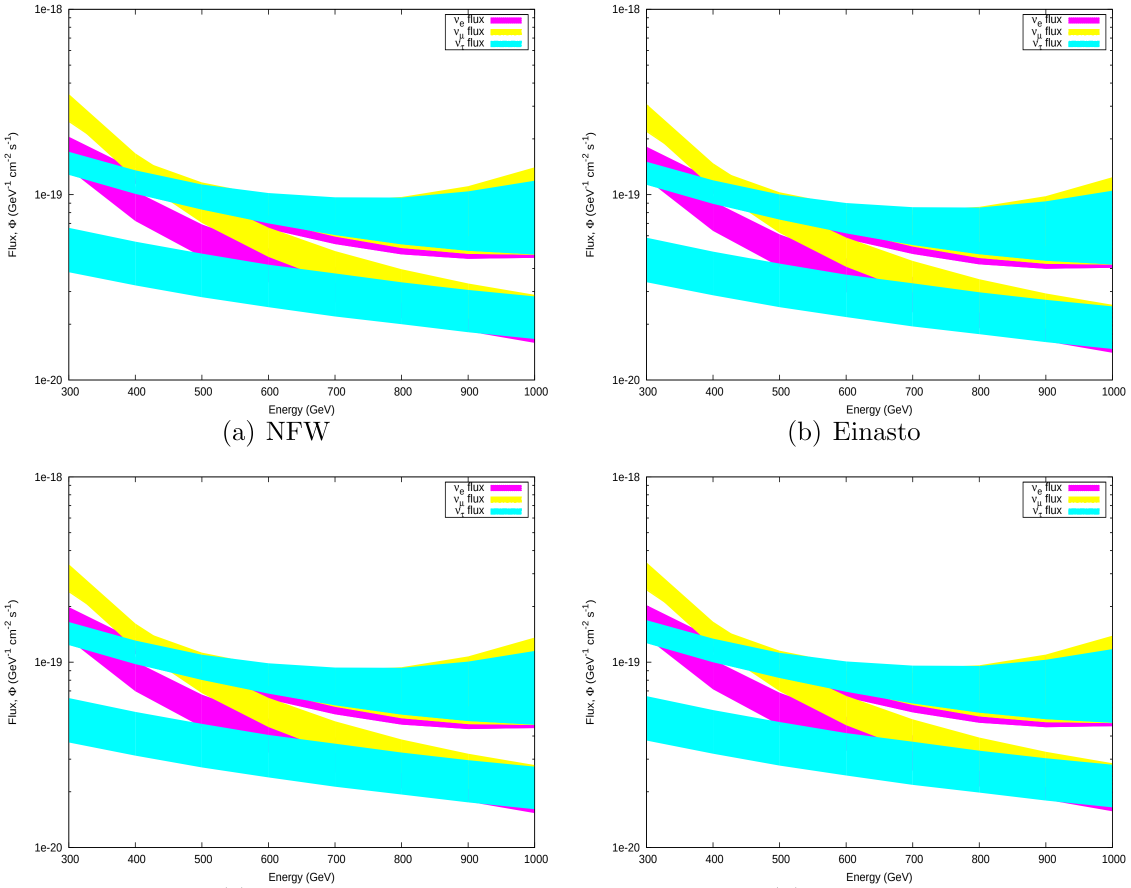

(a) NFW (b) Einasto

(c) Moore (d) Isothermal

Figure 4.15: *neutrino flux of three flavours (ν_e, ν_μ and ν_τ) for various energies for angle of sight, $\theta = 30^o$ from the galactic centre. The pink, yellow and cyan coloured zones describe the fluxes corresponding to ν_e, ν_μ and ν_τ respectively*

oscillations, whereby the flux of a particular flavour, say ν_μ, will be modified on reaching the earth from the galactic centre. Since the baseline length L is very large in this case in comparison to oscillation length, the osciillation part is averaged out. Thus in the limit $L \to \infty$, the probability that a neutrino with flavour α will oscillate to flavour β is given by

$$
\begin{aligned}
P(\nu_\alpha \to \nu_\beta; L = \infty) &= \delta_{\alpha\beta} - \sum_{i \neq j} U^*_{\alpha i} U_{\beta i} U_{\alpha j} U^*_{\beta j} \\
&= |U_{\alpha i}|^2 |U_{\beta i}|^2 \, , \qquad (4.25)
\end{aligned}
$$

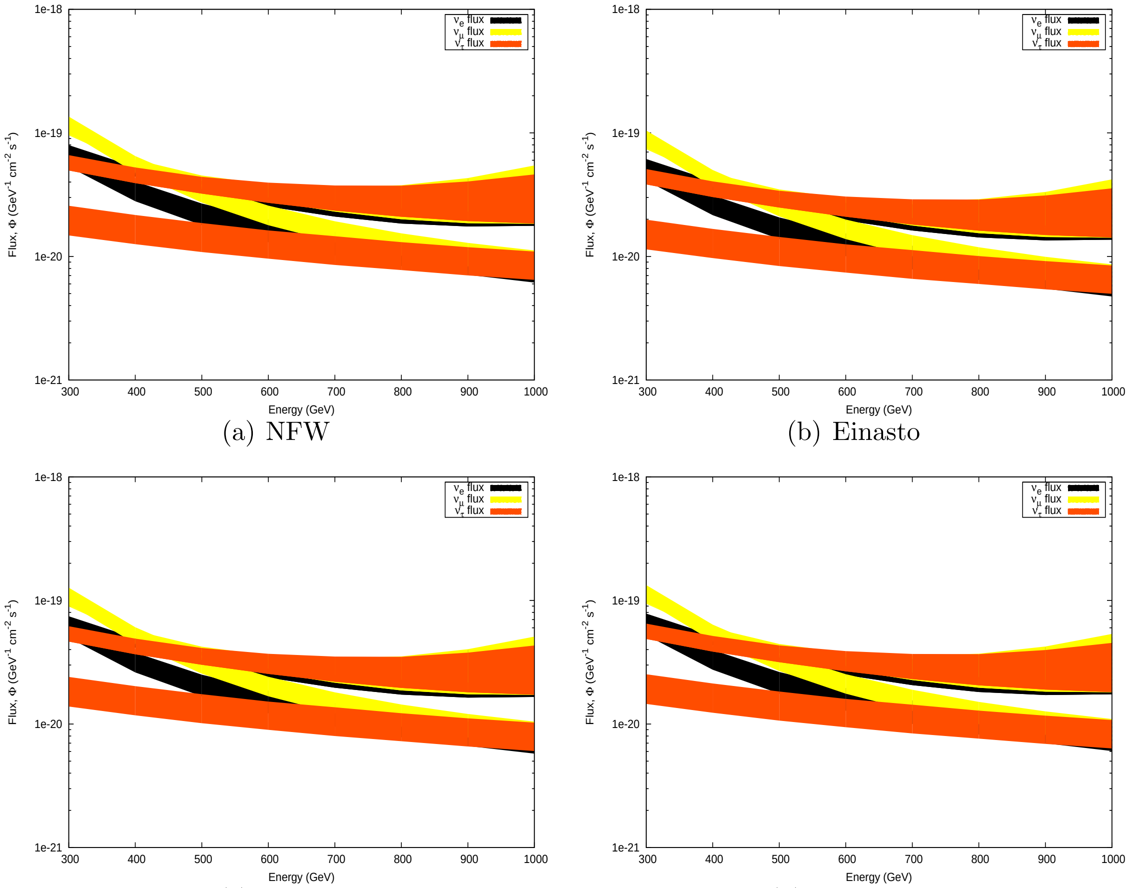

(a) NFW (b) Einasto

(c) Moore (d) Isothermal

Figure 4.16: *neutrino flux of three flavours (ν_e, ν_μ and ν_τ) for different energies for angle of sight, $\theta = 60^o$ from the galactic centre. The black, yellow and orange regions describe the fluxes corresponding to ν_e, ν_μ and ν_τ respectively*

where α, β denote different flavour indices, e, μ or τ and $i, j = 1, 2, 3$ denote the mass indices of three neutrinos. In the above, the oscillation part ($\sim \Delta m^2_{ij}(L/E)$) is averaged out due to large L/E ($\sim 10^{13}$ km/GeV). The mass-flavour mixing matrix U is denoted by

$$|\nu_\alpha\rangle \quad = \quad \sum_i U_{\alpha i}|\nu_i\rangle \tag{4.26}$$

and

$$U \equiv \begin{pmatrix} U_{e1} & U_{e2} & U_{e3} \\ U_{\mu 1} & U_{\mu 2} & U_{\mu 3} \\ U_{\tau 1} & U_{\tau 2} & U_{\tau 3} \end{pmatrix} \tag{4.27}$$

In fact U is the usual MNS mixing matrix given by

$$U = \begin{pmatrix} c_{12}c_{13} & s_{12}s_{13} & s_{13} \\ -s_{12}c_{23} - c_{12}s_{23}s_{13} & c_{12}c_{23} - s_{12}s_{23}s_{13} & s_{23}c_{13} \\ s_{12}s_{23} - c_{12}c_{23}s_{13} & -c_{12}s_{23} - s_{12}c_{23}s_{13} & c_{23}c_{13} \end{pmatrix} . \tag{4.28}$$

In the above, s, c denote $\sin\theta$, $\cos\theta$ respectively and θ_{12}, θ_{23} and θ_{13} are three mixing angles for three neutrino species. We consider here no CP violation in neutrino sector. From Eq. 4.25 probability P can be written as

$$P \equiv XX^T \tag{4.29}$$

where the matrix X is given by

$$X \equiv \begin{pmatrix} |U_{e1}|^2 & |U_{e2}|^2 & |U_{e3}|^2 \\ |U_{\mu 1}|^2 & |U_{\mu 2}|^2 & |U_{\mu 3}|^2 \\ |U_{\tau 1}|^2 & |U_{\tau 2}|^2 & |U_{\tau 3}|^2 \end{pmatrix} . \tag{4.30}$$

Hence, the oscillated flux of the neutrinos (of three flavours) at the detector is given by

$$\begin{pmatrix} \phi_{\nu_e} \\ \phi_{\nu_\mu} \\ \phi_{\nu_\tau} \end{pmatrix} = XX^T \begin{pmatrix} \phi^0_{\nu_e} \\ \phi^0_{\nu_\mu} \\ \phi^0_{\nu_\tau} \end{pmatrix} , \tag{4.31}$$

where the quantities in the RHS with superfix 0 denote the initial neutrino fluxes.

In the present work we estimate the muon yield for such a ν_μ flux from galactic centre at ANTARES neutrino detector. ANTARES is a deep sea neutrino telescope and is basically a water Cerenkov detector, which detect the neutrinos by detecting the Cerenkov light of a charged lepton that is produced by the charged current scattering of neutrino off the sea water. The telescope consists of several vertical strings of around 350 metres long, each of which is fixed with 75 optical modules containing photomultiplier tubes. The strings are installed at the Mediterranian sea bed at a depth of around 2.5 Km off the French coast of Toulon. Designed to detect neutrinos with high energy ($\sim$ 100 GeV to $\sim$ 100 TeV) of generally cosmic origin, this telescope looks in the direction of southern hemisphere. In fact due its position, ANTARES is very much suitable for observing the galactic plane and the galactic centre. In the present context, the dark matter mass from AMSB model that is allowed by WMAP, is in the region of $\sim$ 1 TeV - $\sim$ 2 TeV and since neutrinos from the annihilation of such dark matter at galactic centre is being studied, this telescope is best suited for the purpose.

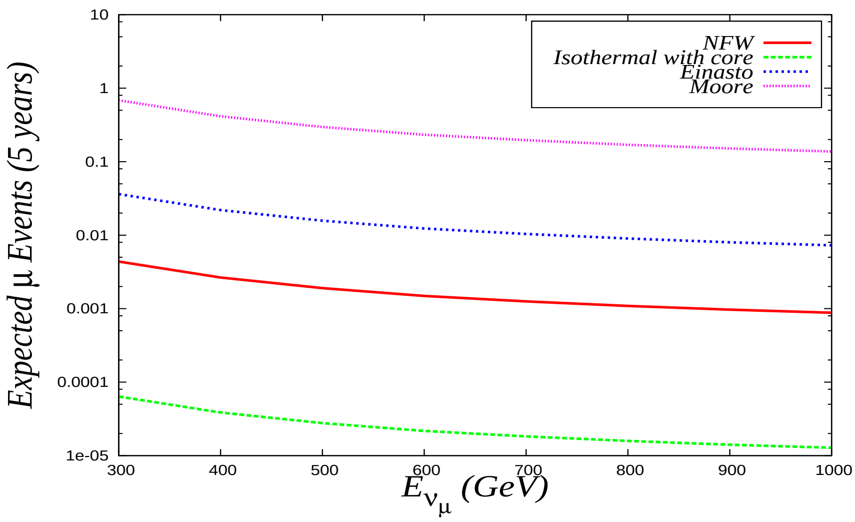

Figure 4.17: *Estimated μ events for five year run at ANTARES neutrino telescope for different ν_μ energies obtained from dark matter annihilations at the galactic centre in the framework of mAMSB model.*

The spectrum of muon yield, $\Phi_\mu(E_{\nu_\mu})$, for different enrgies E_{ν_μ} at ANTARES can be estimated using the relation

$$\Phi_\mu(E_{\nu_\mu}) \quad = \quad \phi_{\nu_\mu} A_{\mathrm{eff},\nu}(E_{\nu_\mu}) \ , \tag{4.32}$$

where, $A_{\mathrm{eff},\nu}$ is the neutrino effective area for ANTARES telescope and is obtained from Ref. [205].

The ν_μ flux, ϕ_{ν_μ}, at the earth from the galactic centre is calculated using Eqs. 4.25 - 4.31 with $\phi^0_{\nu_\mu}$, the flux at the source, given in Fig. 4.14 for different halo profiles. Note that, $\phi^0_{\nu_\mu}$ at galactic centre is considered only for the case $\theta = 0$ (see earlier in this section) in the present calculation. The values of three neutrino mixing angles in Eq. 4.28 are taken to be $\theta_{12} = 34.0^o$, $\theta_{23} = 46.1^o$ and $\theta_{13} = 9.2^o$ [238–241]. The results for estimated yield of muon spectrum $\Phi_\mu(E_{\nu_\mu})$ at ANTARES is shown in Fig. 4.17 for all the four halo profiles considered. The estimates are shown for 5 year run of the telescope. It is seen from Fig. 4.17, that while NFW profile predicts very large yield, the same using the isothermal profile is rather low. The NFW profile has a cuspy structure whereas the isothermal profile gives a flat halo.

If ANTARES detects ν_μ from galactic centre then the μ signal from such detection can be compared with the results given in Fig. 4.17 for different DM halo profiles. Such comparison could readily give an idea of the dark matter halo profile as also the viability of the present model for DM candidate. Thus these observations can be used to probe the nature of the halo profile and the particle physics model of the dark matter as well.

Chapter 5

A Possible Explanation of Low Energy γ-ray Excess from Galactic Centre and Fermi bubble by a Dark Matter Model with Two Real Scalars

In this chapter we consider the idea of multi-component Dark Matter (DM) to explain results from both direct and indirect detection experiments. In these models as contribution of each DM candidate to relic abundance is summed up to meet WMAP/Planck measurements of $\Omega_{\rm DM}$, these candidates have larger annihilation cross-sections compared to the single-component DM models. This results in larger γ-ray flux in indirect detection experiments of DM. We illustrate this fact by introducing an extra scalar to the popular single real scalar DM model. We also present detailed calculations for the vacuum stability bounds, perturbative unitarity and triviality constraints on this model. As direct detection experimental results still show some conflict, we kept our options open, discussing different scenarios with different DM mass zones. In the framework of our model we make an interesting observation: The existing direct detection experiments like CDMS II, CoGeNT, CRESST II, XENON 100 or LUX together with the observation of excess low energy γ-ray from Galactic Centre and Fermi Bubble by FGST already have the capability to distinguish between different DM halo profiles.

5.1 Introduction

The particle nature of DM candidate is still unknown. The relic density of dark matter deduced from cosmological observations mentioned above tends to suggest that most of the DM could be made of weakly interacting massive particles (WIMPs) [74, 180, 242, 243] and they are non-relativistic or cold in nature. This calls for an extension of the Standard Model (SM) of particle physics. Many such extensions have been suggested in the literature in the framework of supersymmetry, extra dimensions, axion *etc.* Models such as Kaluza Klein [182, 183], inert triplet [196] or supersymmetry breaking models like mAMSB [244] predict very massive DM whereas models like SMSSM [245], axion [187] predict DM of lower mass. Phenomenology of simpler extensions of SM like fermionic DM model [197] or inert doublet model [198] has been elaborately studied. Amongst all such options, extending the scalar sector is particularly interesting because of its simplicity.

The minimal extension with a single gauge singlet real scalar stabilised by a $\mathbb{Z}_2$ symmetry in the context of dark matter was proposed by Silveira and Zee in Ref. [191] and then it was extensively studied in the literature [192] - [246]. In Ref. [247] the singlet scalar DM model has been discussed with a global U(1) symmetry.

Amongst the non-minimal extensions, a DM model where SM is extended by a complex singlet scalar has been considered in Refs. [193–195]. A DM model with two real scalars has been discussed in Refs. [248, 249], where one scalar is protected by a $\mathbb{Z}_2$ symmetry, but the $\mathbb{Z}_2$ symmetry protecting the other one spontaneously breaks. In all these non-minimally extended models there is, however, only one DM candidate.

If our visible sector is enriched with so many particles, the DM sector should, in principle, be composed of more than one component. We therefore intend to discuss in this work a model with two DM candidates. In some earlier works [250–255] the idea of multicomponent dark matter has been discussed in details. The advantage of such a multi-component DM model is that the DM annihilation can be enhanced so that one can, in general, expect spectacular signals in the dark matter detection experiments. Hence the thermal averaged annihilation cross-sections in this model can enjoy enhancement upto a few orders of magnitude compared to that of the models with one real scalar. In this work, we consider a two-component dark matter model where the Standard Model sector is extended by adding two real gauge singlet scalars protected by a $\mathbb{Z}_2 \times \mathbb{Z}'_2$ symmetry. This ensures the two singlet scalars as two components of dark matter in this framework. In our present model with two real scalars our endeavour is to explain both direct and indirect detection DM experimental observations.

Direct detection DM experiments can detect DM by measuring the recoil energy of a target nucleon of detecting material in case a DM particle happens to scatter off such nucleons. Experiments like CDMS [112, 256, 257], DAMA [108, 258], CoGeNT [130] or CRESST [259] present their results indicating allowed zones in the scattering cross-section – DM mass plane. These experiments seem to prefer low dark matter masses ~ 10 GeV. Some earlier works on ~ 10 GeV DM mass have been done [260, 261]. XENON 100 [118, 262], however, did not observe any potential DM event contradicting claims of the earlier experiments and has presented an upper bound on DM-nucleon scattering cross-section for various DM masses. Recent findings by LUX [121] have fortified claims by XENON 100 collaboration.

The indirect detection of DM involves detecting the particles and their subsequent decay products, produced due to DM annihilations. Huge concentration of DM are expected at the centre of gravitating bodies such as the sun or the galactic centre (GC) as they can capture DM particles over time.

The regions in and around the GC are looked for detecting the dark matter annihilation products such as γ, ν *etc.* Fermi Gamma-ray Space Telescope (FGST), operated from mid of '08, has been looking for the gamma ray from the GC [263]. The low energy gamma ray from GC shows some bumpy structures around a few GeV which cannot be properly explained by known astrophysics. A plausible explanation of such a non-power law spectrum is provided by DM annihilations [168, 264].

The emission of gamma rays from Fermi bubble may also be partially caused by DM annihilations. The Fermi bubble is a lobular structure of gamma ray emission zone both upward and downward from the galactic plane and has been discovered recently by Fermi's Large Area Telescope [265]. The lobes spread up to a few kpc above and below the galactic plane and emit gamma ray with energy extending from a few GeV to about a hundred GeV. The gamma emission is supposed to be produced from the inverse Compton scattering (ICS) of cosmic ray electrons. But more involved study of this emission reveals that while the spectra from the high galactic latitude region can be explained by ICS taking into consideration cosmic electron distribution, it cannot satisfactorily explain the emission from the lower latitudes. The γ-ray flux from possible DM annihilation in the galactic halo may help explain this apparent anomaly [266–268].

As mentioned earlier, in this work, the proposed model of a two-component dark matter with two real gauge singlet scalars protected by a $\mathbb{Z}_2 \times \mathbb{Z}_2'$ symmetry is confronted with the experimental findings of both direct and indirect DM experiments. From the direct detection experimental results we first put constraints on the model parameter space. The model parameter space is further constrained by the relic density results given by WMAP/Planck experimental observations. We then choose benchmark points from this constrained parameter space to explain results from indirect detection experiments taking into consideration different DM halo profiles.

The present chapter is organised as follows. In Sec. 5.2 we discuss the theoretical framework of our proposed model. The theoretical constraints from vacuum stability, perturbative unitarity, triviality and experimental constraints from the invisible branching ratio of the Higgs boson have been discussed in Sec. 5.3. The following section contains the relevant relic density calculations. The model is confronted with direct detection experiments and Planck observations in Sec. 5.6. Explanation of the observed excess of γ-ray from GC and Fermi bubble by our model is studied in Sec. 5.8.

5.2 Theoretical Framework

We have already discussed in detail the model framework in Section 3.2 of Chapter 3. But for the sake of completeness of the following discussions, we shall briefly address the proposed model in this section.

We propose a model where two real scalar singlets (S and S') are added to the Standard Model. The general form of the renormalisable scalar potential is then given by (Eq. 3.7

in Chapter 3),

$$\begin{aligned} V(H,S,S') \;=\;& \frac{m^2}{2}H^\dagger H + \frac{\lambda}{4}(H^\dagger H)^2 \\ &+\frac{\delta_1}{2}H^\dagger HS + \frac{\delta_2}{2}H^\dagger HS^2 + \frac{\delta_1 m^2}{2\lambda}S + \frac{k_2}{2}S^2 + \frac{k_3}{3}S^3 + \frac{k_4}{4}S^4 \\ &+\frac{\delta_1'}{2}H^\dagger HS' + \frac{\delta_2'}{2}H^\dagger HS'^2 + \frac{\delta_1' m^2}{2\lambda}S' + \frac{k_2'}{2}S'^2 + \frac{k_3'}{3}S'^3 + \frac{k_4'}{4}S'^4 \\ &+\frac{\delta_2''}{2}H^\dagger HS'S + \frac{k_2''}{2}SS' + \frac{1}{3}(k_3^a SSS' + k_3^b SS'S') \\ &+\frac{1}{4}(k_4^a SSS'S' + k_4^b SSSS' + k_4^c SS'S'S') \ , \end{aligned} \tag{5.1}$$

where H is the ordinary (SM) Higgs doublet. In the above δ's denote the couplings between the singlets and the Higgs and k's are the couplings between these singlets themselves.

The stability of DM particles is achieved by imposing a discreet symmetry $\mathbb{Z}_2$ onto the Lagrangian. Depending on whether S and S' are odd under the same $\mathbb{Z}_2$ or not, we discuss two scenarios for completeness.

5.2.1 Lagrangian Invariant under $\mathbb{Z}_2 \times \mathbb{Z}_2$

If only S and S' are odd under the same $\mathbb{Z}_2$, and the rest of the particles are even,

$$\begin{pmatrix} S \\ S' \end{pmatrix} \xrightarrow{\mathbb{Z}_2\times\mathbb{Z}_2} \begin{pmatrix} -S \\ -S' \end{pmatrix} , \tag{5.2}$$

some parameters of the potential vanish:

$$\delta_1 = k_3 = \delta_1' = k_3' = k_3^a = k_3^b = 0 \ , \tag{5.3}$$

so that the scalar potential (5.1) reduces to the following (Eq. 3.10 in Chapter 3),

$$\begin{aligned} V(H,S,S') &= \frac{m^2}{2}H^\dagger H + \frac{\lambda}{4}(H^\dagger H)^2 \\ &+\frac{\delta_2}{2}H^\dagger H S^2 + \frac{k_2}{2}S^2 + \frac{k_4}{4}S^4 \\ &+\frac{\delta_2'}{2}H^\dagger H S'^2 + \frac{k_2'}{2}S'^2 + \frac{k_4'}{4}S'^4 \\ &+\frac{\delta_2''}{2}H^\dagger H S'S + \frac{k_2''}{2}SS' \\ &+\frac{1}{4}(k_4^a SSS'S' + k_4^b SSSS' + k_4^c SS'S'S') \ . \end{aligned} \tag{5.4}$$

After the spontaneous symmetry breaking the mass matrix for S and S' is given by

$$M_{SS'} = \begin{pmatrix} k_2 + \delta_2 v^2/2 & \delta_2'' v^2/4 + k_2''/2 \\ \delta_2'' v^2/4 + k_2''/2 & k_2' + \delta_2' v^2/2 \end{pmatrix} \equiv \begin{pmatrix} M_{11} & M_{12} \\ M_{12} & M_{22} \end{pmatrix} \ .$$

$\frac{v}{\sqrt{2}}$ denotes the vacuum expectation value of the Higgs. After diagonalisation the masses of the physical eigenstates S_1 and S_2 are given by

$$M_{S_1}^2 = \cos^2\theta M_{11} + \sin^2\theta M_{22} + 2\cos\theta\sin\theta M_{12} \ , \tag{5.5}$$

$$M_{S_2}^2 = \cos^2\theta M_{22} + \sin^2\theta M_{11} - 2\cos\theta\sin\theta M_{12} \ , \tag{5.6}$$

where

$$\tan 2\theta = \frac{2M_{12}}{M_{11} - M_{22}} \ . \tag{5.7}$$

5.2.2 Lagrangian Invariant under $\mathbb{Z}_2 \times \mathbb{Z}_2'$

If S and S' are stabilised by different discrete symmetries,

$$S \xrightarrow{\mathbb{Z}_2} -S \ \text{ and } \ S' \xrightarrow{\mathbb{Z}_2'} -S' \ , \tag{5.8}$$

$\delta_2'' = k_2'' = k_4^b = k_4^c = 0$, so that the scalar potential (5.4) further reduces to (Eq. 3.19 of Chapter 3)

$$\begin{aligned} V(H,S,S') &= \frac{m^2}{2}H^\dagger H + \frac{\lambda}{4}(H^\dagger H)^2 \\ &+\frac{\delta_2}{2}H^\dagger H S^2 + \frac{k_2}{2}S^2 + \frac{k_4}{4}S^4 \\ &+\frac{\delta_2'}{2}H^\dagger H S'^2 + \frac{k_2'}{2}S'^2 + \frac{k_4'}{4}S'^4 \\ &+\frac{1}{4}k_4^a SSS'S' \ . \end{aligned} \tag{5.9}$$

After spontaneous symmetry breaking the respective masses of S and S' are given by

$$M_S^2 = k_2 + \frac{\delta_2 v^2}{2} \ , \tag{5.10}$$

$$M_{S'}^2 = k_2' + \frac{\delta_2' v^2}{2} \ . \tag{5.11}$$

The four beyond SM parameters determining the masses of the scalars are k_2, k_2', δ_2 and δ_2'.

In both $\mathbb{Z}_2 \times \mathbb{Z}_2$ and $\mathbb{Z}_2 \times \mathbb{Z}_2'$ cases, if $SS \leftrightarrow S'S'$ scattering processes can be avoided, the model can give rise to a two-component DM scenario. However, as the later case has fewer number of beyond SM parameters, in the following we will restrict ourselves only to the $\mathbb{Z}_2 \times \mathbb{Z}_2'$ invariant Lagrangian.

5.3 Constraints on Model Parameters

The extra scalars present in the model modify the scalar potential. Hence it is prudent to revisit constraints emanating from vacuum stability conditions and triviality of the Higgs potential. Perturbative unitarity can also get affected by these scalars. Limit on the invisible decay width of Higgs from LHC severely restricts such models. In the following we elaborate on these constraints.

5.3.1 Vacuum Stability Conditions

Calculating the exact vacuum stability conditions for any model is generally difficult. However, for many dark matter models the quartic part of the scalar potential can be expressed as quadratic form ($\lambda_{ab} S_a^2 S_b^2$) with the squares of real fields as single entity. Lagrangian respecting $\mathbb{Z}_2$ symmetry which ensures the stability of scalar dark matter has the terms which can be expressed like that. The scalar potential of our proposed model can also be expressed in a similar form as above because of preservation of $\mathbb{Z}_2$ symmetry. The criteria for copositivity allow one to derive properly the analytic vacuum stability conditions for such matrix λ_{ab} from which sufficient conditions for vacuum stability can be obtained.[1]

The necessary conditions for a symmetric matrix A of order 3 to be copositive are given by [269, 270],

$$\begin{aligned} &a_{11} \geqslant 0, a_{22} \geqslant 0, a_{33} \geqslant 0, \\ &\bar{a}_{12} = a_{12} + \sqrt{a_{11}a_{22}} \geqslant 0, \\ &\bar{a}_{13} = a_{13} + \sqrt{a_{11}a_{33}} \geqslant 0, \\ &\bar{a}_{23} = a_{23} + \sqrt{a_{22}a_{33}} \geqslant 0, \end{aligned} \tag{5.12}$$

and

$$\sqrt{a_{11}a_{22}a_{33}} + a_{12}\sqrt{a_{33}} + a_{13}\sqrt{a_{22}} + a_{23}\sqrt{a_{11}} + \sqrt{2\bar{a}_{12}\bar{a}_{13}\bar{a}_{23}} \geqslant 0. \tag{5.13}$$

The last criterion given in Eq. (5.13) is a simplified form of the two conditions (Eqs. (5.14)

[1]Derivation of the necessary and sufficient conditions for the model is much simpler with copositivity than with the other used formalisms.

and (5.15)) below

$$\sqrt{a_{11}a_{22}a_{33}} + a_{12}\sqrt{a_{33}} + a_{13}\sqrt{a_{22}} + a_{23}\sqrt{a_{11}} \geqslant 0, \tag{5.14}$$

$$\det A = a_{11}a_{22}a_{33} - (a_{12}^2 a_{33} + a_{13}^2 a_{22} + a_{11}a_{23}^2) + 2a_{12}a_{13}a_{23} \geqslant 0, \tag{5.15}$$

where one *or* the other inequality has to be satisfied. [2]. The conditions Eq. (5.12) impose that the three 2×2 principal submatrices of A are copositive.

The matrix of quartic couplings Λ in the (h^2, S^2, S'^2) basis for the potential Eq. (5.9) is given by

$$4\,\Lambda = \begin{pmatrix} \lambda & \delta_2 & \delta_2' \\ \delta_2 & k_4 & \frac{k_4^a}{2} \\ \delta_2' & \frac{k_4^a}{2} & k_4' \end{pmatrix}. \tag{5.16}$$

Copositivity criteria of Eqs. (5.12) and (5.13) yield the necessary and sufficient vacuum stability conditions,

$$\begin{aligned} &\lambda \geqslant 0, k_4 \geqslant 0, k_4' \geqslant 0, \\ &\delta_2 + \sqrt{\lambda k_4} \geqslant 0, \\ &\delta_2' + \sqrt{\lambda k_4'} \geqslant 0, \\ &k_4^a + \sqrt{k_4 k_4'} \geqslant 0, \end{aligned} \tag{5.17}$$

and

$$\sqrt{\lambda k_4 k_4'} + \delta_2\sqrt{k_4'} + \delta_2'\sqrt{k_4} + 2k_4'\sqrt{\lambda} + \sqrt{(\delta_2 + \sqrt{\lambda k_4})(\delta_2' + \sqrt{\lambda k_4'})(k_4^a + \sqrt{k_4 k_4'})} \geqslant 0. \tag{5.18}$$

The conditions of Eqs. (5.17) and (5.18) simply determine the vacuum stability bounds

[2]The criterion, $\det A \geqslant 0$ is a part of well known Sylvester's criterion for positive semidefiniteness.

on our model. We restrict the parameter space by these conditions for later calculation.

5.3.2 Perturbative Unitarity Bounds

The potential of the $\mathbb{Z}_2 \times \mathbb{Z}_2'$ model is bounded from below if Eq. (5.17) and Eq. (5.18) are simultaneously satisfied. Then, $\lambda, k_4 > 0$ and $\delta_2 > 0$ or

$$\delta_2^2 < k_4\lambda \qquad \text{for } \delta_2 < 0. \tag{5.19}$$

The Higgs mechanism generates a mass of $M_H^2 = \frac{1}{2}\lambda v^2$ for the Higgs and also contributes to the masses of the S and S' particles

$$M_S^2 = k_2 + \frac{\delta_2 v^2}{2} \;, \tag{5.20}$$

$$M_{S'}^2 = k_2' + \frac{\delta_2' v^2}{2} \;. \tag{5.21}$$

For $\langle H\rangle = (0, v/\sqrt{2})$ and $\langle S\rangle = 0$, $\langle S'\rangle = 0$ to be a local minimum we should have $M_S^2 > 0$ and $M_{S'}^2 > 0$. This is also a global minimum as long as $k_2 > -\frac{1}{2}v^2\sqrt{k_4\lambda}$ and $k_2' > -\frac{1}{2}v^2\sqrt{k_4'\lambda}$ [271]. The potential of the scalar sector after electroweak symmetry breaking in the unitary gauge can be written as,

$$\begin{aligned} V_{SS'H} = {} & \frac{\lambda}{4}H^4 + \frac{m^2}{4}H^2 + \frac{m^2 v}{2}H + v\lambda H^3 + \frac{3v^2\lambda}{2}H^2 + v^3\lambda H \\ & + \frac{\delta_2}{2}H^2S^2 + v\delta_2 HS^2 + \frac{v^2\delta_2}{2}S^2 + \frac{k_2}{2}S^2 + \frac{k_4}{4}S^4 + \frac{\delta_2'}{2}H^2S'^2 \\ & + v\delta_2' HS'^2 + \frac{v^2\delta_2'}{2}S'^2 + \frac{k_2'}{2}S^2 + \frac{k_4'}{4}S'^4 + \frac{k_4^a}{4}S^2S'^2 \;. \end{aligned} \tag{5.22}$$

After that, tree-level perturbative unitarity [272] to scalar elastic scattering processes has been applied in this model (Eq. (5.22)). The zeroth partial wave amplitude,

$$a_0 = \frac{1}{32\pi}\sqrt{\frac{4p_f^{\rm CM}p_i^{\rm CM}}{s}}\int_{-1}^{+1} T_{2\to 2} d\cos\theta \tag{5.23}$$

must satisfy the condition $|{\rm Re}(a_0)| \leq \frac{1}{2}$ [273]. In the above, s is the centre of mass (CM) energy, $p_{i,f}^{\rm CM}$ are the initial and final momenta in CM system and $T_{2\to 2}$ denotes the matrix element for $2 \to 2$ processes with θ being the incident angle between two incoming particles.

The possible two particle states are $HH, HS, SS, S'S', S'S, HS'$ and the scattering processes include many possible diagrams such as $HH \to HH$, $SS \to SS$, $HS \to HS$, $HH \to SS$, $SS \to HH$, $S'S' \to HH$, $S'S' \to SS$, $HS' \to HS'$, $S'S \to S'S$, $HH \to S'S'$, $SS \to S'S'$, $S'S' \to S'S'$. The matrix elements ($T_{2\to 2}$) for the above $2 \to 2$ processes are calculated from the tree level Feynman diagrams for corresponding scattering and given by,

$$
\begin{aligned}
T_{HH\to HH} &= 3\frac{M_H^2}{v^2}\left(1+3M_H^2\left(\frac{1}{s-M_H^2}+\frac{1}{t-M_H^2}+\frac{1}{u-M_H^2}\right)\right) \quad , && (5.24)\\
T_{SS\to SS} &= 6k_4+\delta_2\left(\frac{\delta_2 v^2}{s-M_H^2}+\frac{\delta_2 v^2}{t-M_H^2}+\frac{\delta_2 v^2}{u-M_H^2}\right) \quad , && (5.25)\\
T_{SS\to HH} &= \delta_2\left(1+3M_H^2\frac{1}{s-M_H^2}+\delta_2 v^2\left(\frac{1}{t-M_S^2}+\frac{1}{u-M_S^2}\right)\right) \quad , && (5.26)\\
T_{HS\to HS} &= \delta_2\left(1+v^2\left(\frac{\delta_2}{s-M_S^2}+\frac{3\lambda}{t-M_H^2}+\frac{\delta_2}{u-M_S^2}\right)\right) \quad , && (5.27)\\
T_{S'S'\to HH} &= \delta_2'\left(1+3M_H^2\frac{1}{s-M_H^2}+\delta_2' v^2\left(\frac{1}{t-M_S^2}+\frac{1}{u-M_S^2}\right)\right) \quad , && (5.28)\\
T_{S'S'\to SS} &= k_4^a+\left(\frac{\delta_2\delta_2' v^2}{s-M_H^2}\right) \quad , && (5.29)\\
T_{HS'\to HS'} &= \delta_2'\left(1+v^2\left(\frac{\delta_2'}{s-M_{S'}^2}+\frac{3\lambda}{t-M_H^2}+\frac{\delta_2'}{u-M_{S'}^2}\right)\right) \quad , && (5.30)\\
T_{S'S\to S'S} &= k_4^a+\left(\frac{\delta_2\delta_2' v^2}{t-M_H^2}\right) \quad , && (5.31)\\
T_{S'S'\to S'S'} &= 6k_4'+\delta_2'\left(\frac{\delta_2' v^2}{s-M_H^2}+\frac{\delta_2' v^2}{t-M_H^2}+\frac{\delta_2 v^2}{u-M_H^2}\right) \quad . && (5.32)
\end{aligned}
$$

Now using Eq. (5.23), we have calculated the partial wave amplitude for each of the scattering processes and the coupled amplitude can be written as a matrix form,

$$\mathbb{M} = \begin{pmatrix} a_0^{HH\to HH} & a_0^{HH\to SS} & a_0^{HH\to SH} & a_0^{HH\to S'S'} & a_0^{HH\to S'S} & a_0^{HH\to S'H} \\ a_0^{SS\to HH} & a_0^{SS\to SS} & a_0^{SS\to SH} & a_0^{SS\to S'S'} & a_0^{SS\to S'S} & a_0^{SS\to S'H} \\ a_0^{SH\to HH} & a_0^{SH\to SS} & a_0^{SH\to SH} & a_0^{SH\to S'S'} & a_0^{SH\to S'S} & a_0^{SH\to S'H} \\ a_0^{S'S'\to HH} & a_0^{S'S'\to SS} & a_0^{S'S'\to SH} & a_0^{S'S'\to S'S'} & a_0^{S'S'\to S'S} & a_0^{S'S'\to S'H} \\ a_0^{S'S\to HH} & a_0^{S'S\to SS} & a_0^{S'S\to SH} & a_0^{S'S\to S'S'} & a_0^{S'S\to S'S} & a_0^{S'S\to S'H} \\ a_0^{S'H\to HH} & a_0^{S'H\to SS} & a_0^{S'H\to SH} & a_0^{S'H\to S'S'} & a_0^{S'H\to S'S} & a_0^{S'H\to S'H} \end{pmatrix}$$
$$\xrightarrow[s\gg M_H^2, M_S^2, M_{S'}^2]{} \frac{1}{16\pi} \begin{pmatrix} 3\lambda & \delta_2 & 0 & \delta_2' & 0 & 0 \\ \delta_2 & 6k_4 & 0 & k_4^a & 0 & 0 \\ 0 & 0 & 2\delta_2 & 0 & 0 & 0 \\ \delta_2' & k_4^a & 0 & 6k_4' & 0 & 0 \\ 0 & 0 & 0 & 0 & k_4^a & 0 \\ 0 & 0 & 0 & 0 & 0 & 2\delta_2' \end{pmatrix} . \tag{5.33}$$

Requiring $|\mathrm{Re}(a_0)| \leq \frac{1}{2}$ for each individual process above we obtain

$$\text{for } HH \to HH \qquad M_H \leq \sqrt{\frac{8\pi}{3}} v \ , \tag{5.34}$$

$$\text{for } HS \to HS \text{ and } HH \to SS \qquad |\delta_2| \leq 8\pi \ , \tag{5.35}$$

$$\text{for } SS \to SS \qquad |k_4| \leq \frac{8}{6}\pi \ , \tag{5.36}$$

$$\text{for } S'S' \to S'S' \qquad |k_4'| \leq \frac{8}{6}\pi \ , \tag{5.37}$$

$$\text{for } S'S' \to SS \text{ and } S'S \to S'S \qquad |k_4^a| \leq 8\pi \ , \tag{5.38}$$

$$\text{for } HS' \to HS' \text{ and } HH \to S'S' \qquad |\delta_2'| \leq 8\pi \ . \tag{5.39}$$

5.3.3 Triviality Bound

The requirement for 'triviality bound' on any model is guaranteed by one of the conditions that the renormalization group evolution should not push the quartic coupling constant of such models (say, λ) to infinite value up to the ultraviolet cut-off scale Λ of the model. This requires that Landau pole of the Higgs boson should be in higher scale than Λ.

Therefore to check the triviality in our model, namely the two scalar singlet model with $\mathbb{Z}_2 \times \mathbb{Z}_2'$ symmetry, we have to solve the renormalization group (RG) evolution equations for all the running parameters of this model. We have chosen only one-loop contribution in determining the beta functions for our model. The RG equations for the couplings in the model, namely, λ, k_2, k_2', k_4, k_4', k_4^a, δ_2, δ_2' are thus obtained at one-loop level as

$$16\pi^2 \frac{d\delta_2}{dt} = 4\delta_2^2 + \delta_2' k_4^a + \delta_2(2\gamma_h + 6k_4 + 3\lambda), \tag{5.40}$$

$$16\pi^2 \frac{d\delta_2'}{dt} = 4\delta_2'^2 + \delta_2 k_4^a + \delta_2'(2\gamma_h + 6k_4' + 3\lambda), \tag{5.41}$$

$$\begin{aligned} 16\pi^2 \frac{d\lambda}{dt} &= 6\lambda^2 + 4\lambda\gamma_h - 24y_t^4 \\ &\quad + \frac{3}{2}(g_1^4 + 2g_1^2 g_2^2 + 3g_2^4) + 2\delta_2^2 + 2\delta_2'^2, \end{aligned} \tag{5.42}$$

$$16\pi^2 \frac{dk_2}{dt} = 2m^2\delta_2 + 6k_2k_4 + k_4^a\delta_2', \tag{5.43}$$

$$16\pi^2 \frac{dk_2'}{dt} = 2m^2\delta_2' + 6k_2'k_4' + k_4^a\delta_2, \tag{5.44}$$

$$16\pi^2 \frac{dk_4}{dt} = 18k_4^2 + \frac{1}{2}k_4^{a2} + 2\delta_2^2, \tag{5.45}$$

$$16\pi^2 \frac{dk'_4}{dt} = 18k'^2_4 + \frac{1}{2}k^{a2}_4 + 2\delta'^2_2, \tag{5.46}$$

$$16\pi^2 \frac{dk^a_4}{dt} = 4k^{a2}_4 + 6k^a_4(k_4 + k'_4) + 4\delta_2\delta'_2, \tag{5.47}$$

where $t = \log(\mu/M)$. In Eq. (5.40) $-$ Eq. (5.47) μ denotes the renormalization scale and M is an arbitrary scale. Here $\gamma_h = -(9/4)g_2^2 - (3/4)g_1^2 + 3y_t^2$ and g_1, g_2, y_t are $\mathrm{U(1)_Y}$, $\mathrm{SU(2)_L}$ gauge couplings and top Yukawa coupling, respectively. In our calculation, the RG equations for gauge and top Yukawa couplings are also taken into account. We have taken the initial condition, $y_t(\mu = m_t) = \sqrt{2}m_t(1 + 4\alpha_s(m_t)/3\pi)^{-1}/v$ for running of top Yukawa coupling, where $m_t = 171$ GeV and $\alpha_s(m_t)$ is strong coupling at the scale of $\mu = m_t$ [274]

We have solved all the RG equations given above and checked the consistency of all the quartic couplings within the suitably chosen scale of the theory. For the initialisation, we have taken λ_{init} corresponding to the recent value of Higgs mass, 126 GeV. The other initial values of parameters in our model should have been chosen from the allowed region of parameter space. In Fig. 5.1 the variation of different parameters $(k_4, k'_4, k^a_4, k_2, k'_2, \delta_2, \delta'_2, \lambda)$ with scale used in this model is shown. The benchmark point 4A of Table 5.4 has been chosen for assigning initial values in the evaluation of the running of various couplings. The variation of mass of each scalar S (or S') with energy scale can be obtained from the plots as it is determined by couplings k_2 and δ_2 (or k_2 and δ'_2). Although we have solved the RG equation for δ_2 and δ'_2, the influence of δ_2 and δ'_2 on λ is very small as we can see from Eq. (5.42) that the RG equation of λ is deviated from the SM RG equation only by the almost smooth term $(2{\delta_2}^2 + 2{\delta'_2}^2)$. But the allowed region for 'triviality bound' for a given Higgs mass shrinks as the term, $(2{\delta_2}^2 + 2{\delta'_2}^2)$ starts growing.

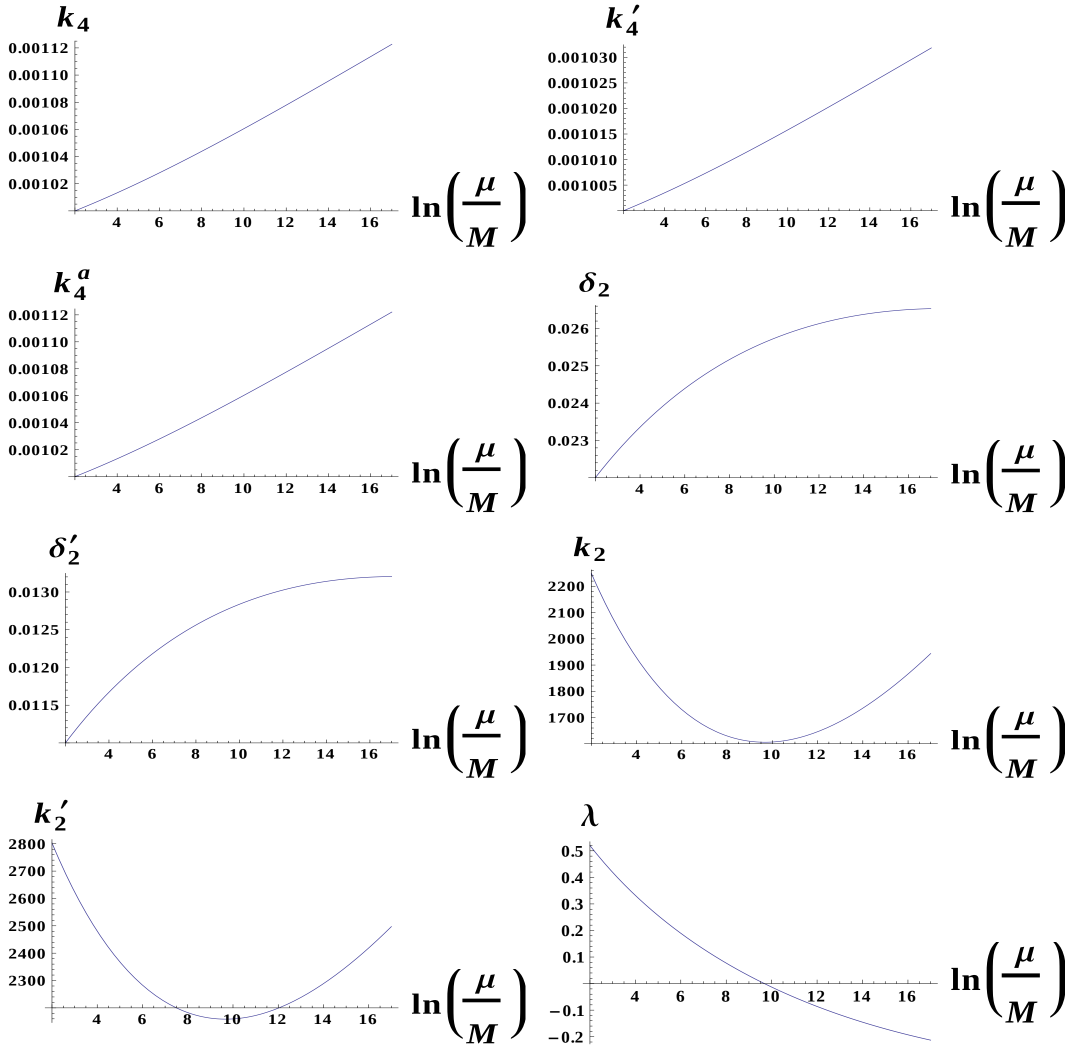

Figure 5.1: *Plot showing the variation of different couplings present in the framework of two scalar singlet model with $\mathbb{Z}_2 \times \mathbb{Z}_2'$ symmetry with different energy scales.*

5.3.4 Constraints from Invisible Higgs Decay Width

If kinematically allowed, Higgs boson can decay to SS or $S'S'$. Such invisible decay channels are severely restricted by the present data from Large Hadron Collider (LHC). The branching fraction

$$\mathcal{B}(H \to \text{inv}) = \frac{\Gamma_{\text{inv}}}{\Gamma_{\text{SM}} + \Gamma_{\text{inv}}} \ , \tag{5.48}$$

is bounded at 95% CL to be less than 19% by the global fits to the Higgs data keeping Higgs to fermion couplings fixed to their SM values. If such a restriction is lifted and additional particles are allowed in the loops the bound get relaxed to $\mathcal{B}(H \to \text{inv}) < 38\%$ [275]. Γ_{SM} denotes the SM Higgs decay width and Γ_{inv} is the invisible Higgs decay width, which in our model is given by [276],

$$\Gamma_{\text{inv}} = \frac{v^2}{32\pi M_H}\left(\delta_2^2\sqrt{1-\frac{4M_S^2}{M_H^2}} + \delta_2'^2\sqrt{1-\frac{4M_{S'}^2}{M_H^2}}\right) \quad . \tag{5.49}$$

The benchmark point 4A in Table 5.4, consistent with the XENON 100 direct detection results, gives $\mathcal{B}(H \to \text{inv}) \sim 0.26$ which at present is allowed at 95% CL [277–281]. However as we intend to interpret the low mass regions of dark matter claimed to be probed by several other dark matter direct search experiments (CDMS II, CRESST, CoGeNT *etc.*) along with indirect searches (low energy γ-ray from Fermi bubble and Galactic Centre), in some cases $M_S, M_{S'} \leq M_H/2$ and the Higgs boson decays invisibly to SS or $S'S'$, with a $\mathcal{B}(H \to \text{inv})$ disfavoured by the LHC observations. This is a well known problem with all such models, where DM annihilation is mediated by the SM Higgs. The present model consisting of two singlet scalars cannot perhaps evade the constraint from the Higgs invisible width data for explaining the low mass zones. For quantitative estimations we have chosen the Higgs to be the 126 GeV SM Higgs as a benchmark.

5.3.5 Constraints from LHC Mono-X searches

One of the techniques chosen by Large Handron Collider (LHC) to explore the signature of dark matter pair production by the 'mono-X' searches where the DM production at the collider is measured from the missing transverse energy ($\not{E}_T$) of the DM particles that escape the detector recoiling against some final state X (SM). The varieties of 'mono-X' studies which have been performed by the LHC include mono-hadronic jets (j), or monophotons (γ), or mono-$W^{\pm}/Z$, or mono-Higgs (h). The experimental technique used by the proton-proton ($p - p$) collider for studying the mono-X searches uses the quarks or gluons self-interactions leading to some final channels containing a pair of dark matters and a single SM (X) particle. The signature of the pair of dark matter has been assumed to be in the missing transverse energy and can be measured from the data. The emission channels of the single particles ($j/\gamma/W^{\pm}/Z$) in the $p-p$ collider (or LHC) follow from two processes, whereby the single particle emission can be due to initial state radiation from light quarks or alternatively this can be emitted along with $\chi\bar{\chi}$ (χ denoting a dark matter particle) as a consequence of effective couplings of DM to SM. In the present case of two singlet scalar dark matter model, the masses of the proposed dark matters constrained by different dark matter search experiments are low and hence the constraint from LHC mono-X searches are subleading. For the present model the signatures like mono-photon, mono-$W^{\pm}/Z$ are suppressed than the case with mono-Higgs since the former signatures (mono-γ, mono-$W^{\pm}/Z$ etc.) require loop-induced interactions. The study of mono-h search for singlet dark matter is given in Refs. [138, 139]. In the present scenario with two real scalar singlets added to SM, the qualitative discussion will be similar to that given in Refs. [138, 139] except now this is for two singlets. Since the DM masses are low, LHC is still insensitive to put strong constrains on the mono-X searches although the low mass dark matters are strongly constrained from the LHC data for the invisible decay width of Higgs. The future collider with much higher luminosity can probe the mono-X channels precisely and may put stronger limits on them. Other constraints from collider data such as effects on electroweak precision observables have been discussed for real singlet scalar model in Ref. [282] (Barger *et al.*) and the qualitative study is similar in our present two real singlet model.

5.4 Calculation of Relic Abundance in this Framework

The relic abundance for a dark matter species is calculated by solving the Boltzmann equation given as,

$$\frac{dn_S}{dt} + 3Hn_S = -\langle\sigma v\rangle(n_S^2 - n_{S_{\rm eq}}^2) \ , \tag{5.50}$$

where n_S and $n_{S_{\rm eq}}$ are the number density and equilibrium number density respectively of the dark matter candidate, S and $\langle\sigma v\rangle$ is the thermal averaged annihilation cross-section of the dark matter.

Defining dimensionless quantities $Y = \frac{n_S}{e}$ and $x = \frac{M_S}{T}$, where e is the total entropy density, Eq. (5.50) can be written in the form,

$$\frac{dY}{dx} = -\left(\frac{45}{\pi}G\right)^{-1/2} \frac{g_*^{1/2} M_S}{x^2} \langle\sigma v\rangle(Y^2 - Y_{eq}^2) \ , \tag{5.51}$$

where g_* is the degrees of freedom. The relic density Y_0 (value of Y at $T = T_0$) is obtained by integrating Eq. (5.51) from an initial value x_0 of x ($x_0 = M_S/T_0$) to x_f, the final value of x ($x_f = M_S/T_f$). Here T_0 and T_f are the present photon temperature (2.726^o K) and freeze-out temperature respectively.

The relic density of a dark matter candidate, S, in the units of critical energy density, $\rho_{cr} = 3H^2/8\pi G$, can be expressed as

$$\Omega_S = \frac{M_S\, n_S}{\rho_{cr}} = \frac{M_S\, e_0\, Y_0}{\rho_{cr}} \ , \tag{5.52}$$

where e_0 is the present entropy density evaluated at T_0. It follows that knowing Y_0, we can compute the relic density of the dark matter candidate from the relation [217],

$$\Omega_S h^2 \;=\; 2.755 \times 10^8 \, \frac{M_S}{\mathrm{GeV}} \, Y_0 \; . \tag{5.53}$$

In Eq. (5.53) h is the Hubble constant in the units of $100\,\mathrm{km\ sec^{-1} Mpc^{-1}}$. The Planck survey provides the constraints on the dark matter density $\Omega_{\rm DM}h^2$ from precision measurements of anisotropy of cosmic microwave background radiation as

$$0.1165 < \Omega_{\rm DM}h^2 < 0.1227 \;\; , \tag{5.54}$$

consistent with the previous WMAP measurement $0.1093 < \Omega_{\rm DM}h^2 < 0.1183$.

In the present work we consider a two component dark matter model with each component (S or S') is a singlet scalar. The total relic density is the sum of the relic densities of each component. Thus in our model with two real scalars, both S and S' contribute to the relic density. Their individual contributions can be obtained by solving the following coupled Boltzmann equations,

$$\frac{dn_S}{dt} + 3Hn_S \;=\; -\langle \sigma v \rangle_{SS\to XX}(n_S^2 - n_{S_{\rm eq}}^2) - \langle \sigma v \rangle_{SS\to S'S'} \left(n_S^2 - \frac{n_{S_{\rm eq}}^2}{n_{S'_{\rm eq}}^2} n_{S'}^2 \right) \; , \tag{5.55}$$

$$\frac{dn_{S'}}{dt} + 3Hn_{S'} \;=\; -\langle \sigma v \rangle_{S'S'\to XX}(n_{S'}^2 - n_{S'_{\rm eq}}^2) - \langle \sigma v \rangle_{S'S'\to SS} \left(n_{S'}^2 - \frac{n_{S'_{\rm eq}}^2}{n_{S_{\rm eq}}^2} n_S^2 \right) \tag{5.56}$$

where X stands for a Standard Model particle. In both the Eqs. (5.55) and (5.56) the first terms on the right hand side are for the contributions of annihilation to SM particles whereas the second terms of both the equations denote the contribution of the self-scattering of each of the two scalars in this two component dark matter scenario.

In the very early universe, both the scalars are in thermal and chemical equilibrium. But as the universe expands, the temperature falls resulting some species to be decoupled from the universe plasma and contribute to the relic density. The heavier scalar decouples earlier than the lighter one. But at the present epoch both components are frozen relics and give rise to a total contribution in relic abundance that is probed by WMAP/Planck or other cosmological observations. In the present two component model (with the components are singlet scalars S and S') therefore the total relic abundance ($\Omega_{\rm DM}$) is the sum of the individual contributions, Ω_S and $\Omega_{S'}$ of S and S' respectively. We therefore have,

$$\Omega_{\rm DM} = \Omega_S + \Omega_{S'} \,. \tag{5.57}$$

If the self-scattering cross-sections between the two scalars ($\langle\sigma v\rangle_{SS\leftrightarrow S'S'}$ or $\langle\sigma v\rangle_{S'S'\leftrightarrow SS}$) in the Eqs. (5.55) and (5.56) are small compared to the annihilation cross-section ($\langle\sigma v\rangle_{SS\leftrightarrow XX}$ or $\langle\sigma v\rangle_{SS\leftrightarrow XX}$) such that

$$\langle\sigma v\rangle_{SS\to XX}, \langle\sigma v\rangle_{S'S'\to XX} >> \langle\sigma v\rangle_{SS\leftrightarrow S'S'} \ , \tag{5.58}$$

then the coupled Boltzmann equations in the Eqs. (5.55) and (5.56) are reduced to two decoupled equations each one of which describes the evolution of each of the component scalars independently. In the present work we have ensured this condition by taking the masses of S and S' close enough[3] so that $\langle\sigma v\rangle_{SS\leftrightarrow S'S'}$ is negligible from phase space considerations. In such a scenario each of the Eqs. (5.55) and (5.56) is reduced to the Boltzmann equation given in Eq. (5.50). We have then used `micrOMEGAs` computer code [98, 218] to calculate Ω_S and $\Omega_{S'}$.

The thermally-averaged values of cross-section ($\langle\sigma v\rangle$) for the annihilation channels of dark matter to Standard Model particles ($DM + DM \to SM + SM$) can be expressed as

[3]A situation like this can be realised by assuming that M_S and $M_{S'}$ are degenerate at some high scale and then at low scale the degeneracy is slightly lifted due to some hidden sector physics.

([276], [217]),

$$\langle \sigma v \rangle = \frac{x}{16 M_S^5 K_2^2(x)} \int_{4M_S^2}^{\infty} ds\, K_1 \left(\frac{\sqrt{s}}{T} \right) \sqrt{s - 4M_S^2}\; \hat{\sigma}(s) \ , \tag{5.59}$$

with

$$\hat{\sigma}(s) = 2\sqrt{s(s-4M_S^2)}\, \sigma(s) \ ,$$

where $x = M_S/T$. $K_i(x)$ denote the ith order modified Bessel function of second kind. $\sigma(s)$ is the normalized annihilation cross-section of dark matter for $DM + DM \to SM + SM$ processes. For non-relativistic dark matter $\langle \sigma v \rangle$ can be approximated as $\langle \sigma v \rangle \sim \hat{\sigma}(4M_S^2)/4M_S^2$.

The Feynman diagrams for singlet scalar (S or S') pair annihilation into SM particles in the unitary gauge are shown in Fig. 5.2. The corresponding expressions for cross-sections can be found in Refs. [271, 276].

5.5 Calculation of Direct Detection Cross-section

The spin-independent singlet scalar – nucleus elastic scattering cross-section in the non-relativistic limit can be written as [271]

$$\sigma^{\rm SI}_{\rm nucleus} = \frac{\delta_2^2 v^2 |\mathcal{A}_N|^2}{4\pi} \left(\frac{\mu_r^2}{{M_S}^2 {M_H}^4} \right) \ , \tag{5.60}$$

where $\mu_r(N, S) = M_N M_S/(M_N + M_S)$ denotes the reduced mass for the system of singlet scalar and target nucleus with individual masses M_S and M_N respectively. $\mathcal{A}_N$ represents the relevant matrix element. The singlet scalar–nucleus and singlet scalar–nucleon elastic

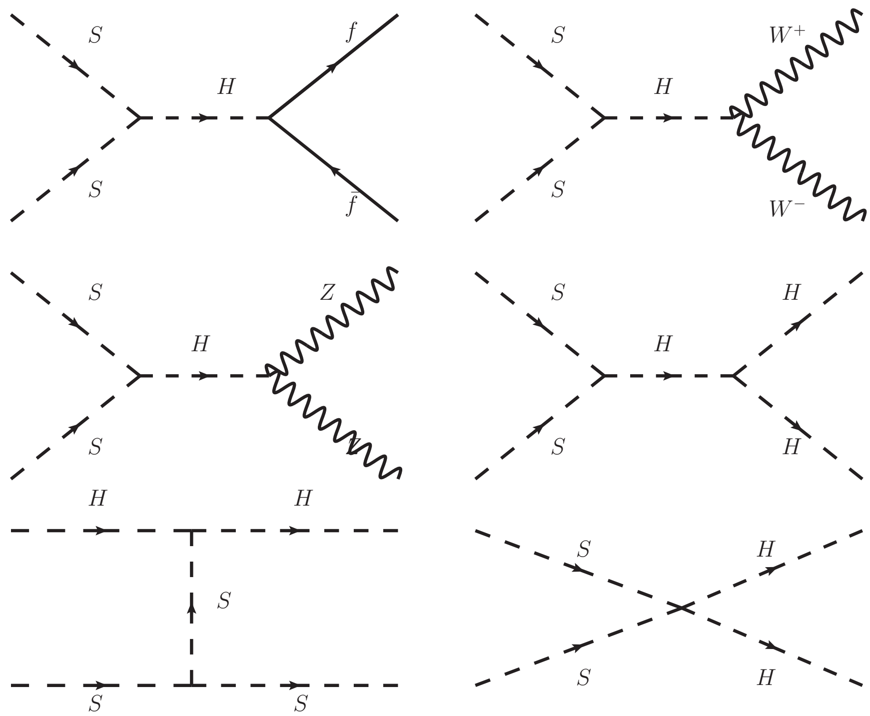

Figure 5.2: *Tree level Feynman diagrams of DM pair annihilation to a pair of fermion and anti-fermion, W^+W^-, ZZ and Higgs. Similar annihilation channels exist for both S and S'.*

scattering cross-sections for the non-relativistic limit are related as [271]

$$\sigma^{\rm SI}_{\rm nucleus} \quad = \quad \frac{A^2\mu_r^2({\rm nucleus}, S)}{\mu_r^2({\rm nucleon}, S)}\sigma^{\rm SI}_{\rm nucleon} \ , \tag{5.61}$$

where A is the atomic number of the nucleus. $\sigma^{\rm SI}_{\rm nucleon}$ can be expressed as,

$$\sigma^{\rm SI}_{p(n)} = \frac{4m^2_{p(n)}M_S^2}{\pi\left(M_S + m_{p(n)}\right)^2}\left[f^{p(n)}\right]^2 , \tag{5.62}$$

where the expression for hadronic matrix element, $f^{(p,n)}_{Tq}$, are proportional to the matrix element, $\langle\bar{q}q\rangle$, of quarks in a nucleon and are given by

$$f^{p(n)} = \sum_{q=u,d,s} f^{p(n)}_{T_q}\mathcal{G}_{Sq}\frac{m_{p(n)}}{m_q} + \frac{2}{27}f^{p(n)}_{T_g}\sum_{q=c,b,t}\mathcal{G}_{Sq}\frac{m_{p(n)}}{m_q}, \tag{5.63}$$

with suffix p and n denote proton and neutron respectively and $\mathcal{G}_{Sq}$ is the effective coupling between dark matter and nucleon [283],

$$\begin{aligned} f^p_{Tu} &= 0.020 \pm 0.004, \quad f^p_{Td} = 0.026 \pm 0.005, \quad f^p_{Ts} = 0.118 \pm 0.062, \\ f^n_{Tu} &= 0.014 \pm 0.003, \quad f^n_{Td} = 0.036 \pm 0.008, \quad f^n_{Ts} = 0.118 \pm 0.062\,. \end{aligned} \tag{5.64}$$

where we have used the relation between $f^{(p,n)}_{Tg}$ and $f^{(p,n)}_{Tq}$ stated as,

$$f^{(p,n)}_{Tg} = 1 - \sum_{q=u,d,s} f^{(p,n)}_{Tq}. \tag{5.65}$$

Thus $f^p_{TG} \approx 0.84$ and $f^n_{TG} \approx 0.83$ [284]. In fact, here $\sigma^{SI}_p \approx \sigma^{SI}_n$.

5.6 Constraining the Parameter Space with Dark Matter Direct Detection Experiments and Planck Survey

The dark matter particles S and S' can interact with the nuclei of the active material (see Fig. 5.3) in the direct detection experiments and leave their signature in form of a recoiled nucleus. These experiments have indicated some preferred or excluded zones in the mass of DM vs. DM-nucleon cross-section plane. If we can express these cross-sections in terms of the parameters of our model, we can translate the results obtained from direct detection experiments into some preferred or excluded region in the parameter space of our model comprising of δ_2, M_S, δ'_2 and $M_{S'}$. The requirement of producing the right relic abundance will further restrict the allowed parameter space.

As presented in Section 5.5, the expressions for singlet scalar-nucleon elastic scatter-

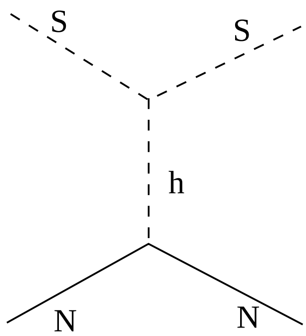

Figure 5.3: *Lowest order Feynman diagram for singlet scalar–nucleus elastic scattering via Higgs mediation. A similar diagram exists for S' as well.*

ing cross-section are rather involved. But for all practical purposes Eq. (5.62) can be approximated as [271]

$$\sigma^{\rm SI}_{\rm nucleon} = (\delta_2)^2 \left(\frac{100 \text{ GeV}}{M_H(\text{in GeV})}\right)^4 \left(\frac{50 \text{ GeV}}{M_S(\text{in GeV})}\right)^2 (5 \times 10^{-42} \text{cm}^2). \tag{5.66}$$

Similar expression works for S' as well.

In this model with two scalars, although the total event rate in a direct detection experiment, which is the sum total of individual event rates, carries no information about the types of dark matter particles, the nuclear recoil energy spectrum for the signal events depends on the mass of the dark matter particle. Hence the measured nuclear recoil energy can, in principle, be used to differentiate a multi-component dark matter from a single-component one [251, 285]. In our model, the masses of the two singlets S and S' are chosen to be nearly degenerate. Due to such mass degeneracy, it may not be possible to experimentally distinguish the components of dark matter in our model simply by measuring the recoil energies of the detector nuclei. Empowering ourselves with the expression of cross-section in terms of model parameters, we will now go ahead in constraining the model parameter space from direct detection experimental results and relic density requirements from Planck survey. We have broadly explored three DM mass ranges. CDMS II and CoGeNT vouch for low ($\sim$ 10 GeV) mass DM. CRESST II data prefer a relatively higher mass zone ($\sim$ 25 GeV), in addition to the low zone. XENON 100 and LUX provide exclusion regions from non-observation of any interesting event. Only high mass DM ($>$ 50 GeV) is consistent with these two experiments and Planck data. We will now elaborate more on them in the following.

5.6.1 Constraints from CDMS II and Planck data

The Cryogenic Dark Matter Search (CDMS) experiment was designed using germanium and silicon detectors cooled to very low temperatures (40 mK) in order to detect the electric charge and heat liberated by single dark-matter particle collisions with nuclei and distinguish them from the messier interactions created by normal matter. CDMS II (2003-08) located at Soudan Underground Laboratory, have used both Ge and Si detector array as Z-sensitive ionization and phonon (ZIP) detector that has total 19 Ge (4.6 kg) and 11 Si (1.2 kg) array. The background electronic recoils are thrown away from nuclear recoil from the ionization to phonon ratio of recoil energy. The analyses and results of the data taken from Ge detector has been done in Ref. [112]. The data from Si detector has been analyzed in Refs. [256, 257]. The atomic number (A) of Si is low, thus reducing its sensitivity on detection as the spin-independent scattering cross section is proportional to A^2. But to search for the WIMP-event at lower mass regime, Si is very suitable. The data taken by 8 Si detectors analyzed in Refs. [256, 257] represent a total 140.2 kg-days and 23.4 kg-days exposure before and after imposing the WIMP-selection criteria respectively. The cosmogenic and radioactive neutrons serve as background which can be subtracted from simulation. Finally the authors of Refs. [256, 257] have reported to have 3 events at recoil energies 8.2 keV, 9.5 KeV and 12.3 KeV with signal to noise ratio (SNR) measured to be 6.7σ, 4.9σ and 5.1σ respectively. Also they have shown 1σ and 90% CL contour on WIMP-nucleon spin independent (SI) cross section at low energies. Almost similar regions are probed by many other direct detection experiments like CoGeNT, CRESST, DAMA/LIBRA etc.

CDMS collaboration has recently reported observation of three WIMP events and provided a preferred contour in the mass of DM – SI scattering cross-section plane, with the maximum likelihood point at a mass of 8.6 GeV with cross-section 1.9×10^{-41} cm^2. This value of cross-section corresponds to $\delta_2 \simeq 0.45$ for $M_S = 8.6$ GeV. We first calculate the CDMS II region in $M_S - \delta_2$ plane which satisfies the CDMS direct detection experimental bounds and this is shown in Fig. 5.4(a) by the olive zone. It is straightforward to realise that the same contour also represents the allowed parametric space (CDMS II allowed region), $M_{S'} - \delta'_2$ for the other scalar S'. We now choose the benchmark point in the parameter space $M_S - \delta_2$ for the singlet S (say) to be $M_S = 8.6$ GeV, $\delta_2 = 0.45$ (as claimed by CDMS II). We could have chosen the point in the parameter space $M_{S'} - \delta'_2$ for the singlet S' to be $M_{S'} = 8.6$ GeV, $\delta'_2 = 0.45$. Needless to mention that this point is within the allowed parameter space of Fig. 5.4(a). With this choice of M_S and δ_2 for the singlet S (say), we now calculate the allowed region of parameter space $M_{S'} - \delta'_2$ for the other singlet S' which satisfies both CDMS II direct detection bound and Planck relic density constraints. This region is shown in Fig. 5.4(b) by the light purple zone. On the other hand, if the point ($M_{S'} = 8.6$ GeV, $\delta'_2 = 0.45$) is initially chosen in the $M_{S'} - \delta'_2$ parameter space shown by the olive colour in Fig. 5.4(a) for the other singlet S', this allowed region of parameter space in light purple colour would be in $M_S - \delta_2$ plane for singlet S. It is obvious that this allowed region in light purple is a part of the abovementioned total allowed parametric space (CDMS II allowed region) $M_S - \delta_2$ for the singlet S (or $M_{S'} - \delta'_2$ for the singlet S') as shown by olive zone in Fig. 5.4(a).

However in our model both S and S' contribute to the relic density and participate in direct detection experiments. So we fix Ω_S for singlet S (say) by choosing the point corresponding to the maximum likelihood point ($M_S = 8.6$ GeV, $\delta_2 \simeq 0.45$) in the $M_S - \delta_2$ plane. This restricts $\Omega_{S'}$ from Planck constraints on relic abundance of dark matter.

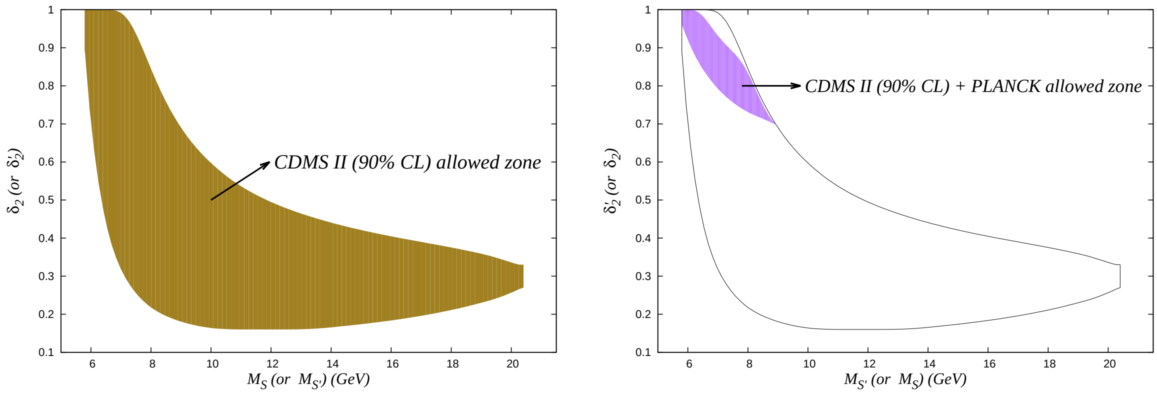

(a) (b)

Figure 5.4: *In panel (a) the olive region is the parameter space allowed in the* $M_{S'} - \delta_2'$ *plane by CDMS II 90%CL data. The same is true if drawn in* $M_S - \delta_2$ *plane. In panel (b) the light purple shaded region is the only parameter space allowed by Planck data in the* $M_{S'} - \delta_2'$ *plane choosing* $M_S = 8.6$ *GeV,* $\delta_2 = 0.45$ *in the* $M_S - \delta_2$ *plane. The same is true for the allowed parameter space in the* $M_S - \delta_2$ *plane when* $M_{S'} = 8.6$ *GeV,* $\delta_2' = 0.45$ *are chosen from* $M_{S'} - \delta_2'$ *plane.*

Table 5.1: Benchmark point consistent with CDMS II contour and Planck data

	M_S (or $M_{S'}$) (GeV)	δ_2 (or δ_2')	$\sigma^{\rm SI}$ ($\times 10^{-41}$ cm^2)	$\langle\sigma v\rangle$ ($\times 10^{-26}$ cm^3/s)	Annihilation Branching Fraction for S (or S')
Benchmark point 1	8.6	0.45	1.9	3.2 $\begin{cases} 2.6\ (b\bar{b}) \\ 0.4\ (c\bar{c}) \\ 0.2\ (l\bar{l}) \end{cases}$	81% 12% 7%
	6.7	0.82	9.9	8.3 $\begin{cases} 6.3\ (b\bar{b}) \\ 1.2\ (c\bar{c}) \\ 7.2\ (l\bar{l}) \end{cases}$	77% 15% 8%

Only a small part of the previously allowed region in the $M_{S'} - \delta_2'$ plane shown as the light purple shaded region in Fig. 5.4(b), can now account for such $\Omega_{S'}$. We then complete choosing our benchmark point (see Table 5.1) by taking $M_{S'} = 6.7$ GeV, $\delta_2' \simeq 0.82$ from this light purple region. This point in the parameter space is thus consistent with both CDMS II and Planck observations. The same prescription is valid if we first consider the other singlet S' and fix $\Omega_{S'}$ by choosing the point corresponding to the maximum likelihood point ($M_{S'} = 8.6$ GeV, $\delta_2' \simeq 0.45$) in the $M_{S'} - \delta_2'$ plane. Similarly the relic density of the singlet S, Ω_S is restricted from Planck data allowing only a small region (light purple shaded region in Fig. 5.4(b)) in $M_S - \delta_2$ plane. The point corresponding to $M_S = 6.7$ GeV, $\delta_2 \simeq 0.82$ in the light purple shaded region of $M_S - \delta_2$ plane is chosen to complete the benchmark point.

5.6.2 Constraints from CoGeNT and Planck data

The CoGeNT (Coherent Germanium Neutrino Technology) experiment [130] is a direct search for signals from interactions of dark matter particles in a low-background germanium detector located at Soudan Underground Laboratory in Soudan, USA. A very high-purity Ge ($A = 73$) crystal cooled at a temperature of liquid nitrogen is used to detect any dark matter event. The advantage of CoGeNT detector is that it has a very low energy threshold ($\sim$ 5 keV) which is helpful to measure the nuclear recoil events of comparatively low mass dark matter particles. Also, from the rise-time of its signal the detector can distinguish and reject background signals from the surface which is helpful to measure signals accurately. From the recent result of CoGeNT dark matter direct detection experiment, one can see that there is a clear zone near low mass which has been reported.

CoGeNT dark matter direct detection experiment predicts dark matter particle with a mass roughly $\sim$ 7-11 GeV and elastic scattering cross-section with nucleon which is $\sim 10^{-41}$–10^{-40} cm^2. The other direct detection experiments like DAMA/LIBRA or CRESST II have also reported signals nearly in that zone which is not consistent with the known background sources. Also the spectra of the events reported by experiments like CRESST II and CoGeNT are consistent with each other [286] and possibly attribute to dark matter of mass $\sim$ 10 GeV.

With CoGeNT preferred zone we can do similar analysis as we did with CDMS II and

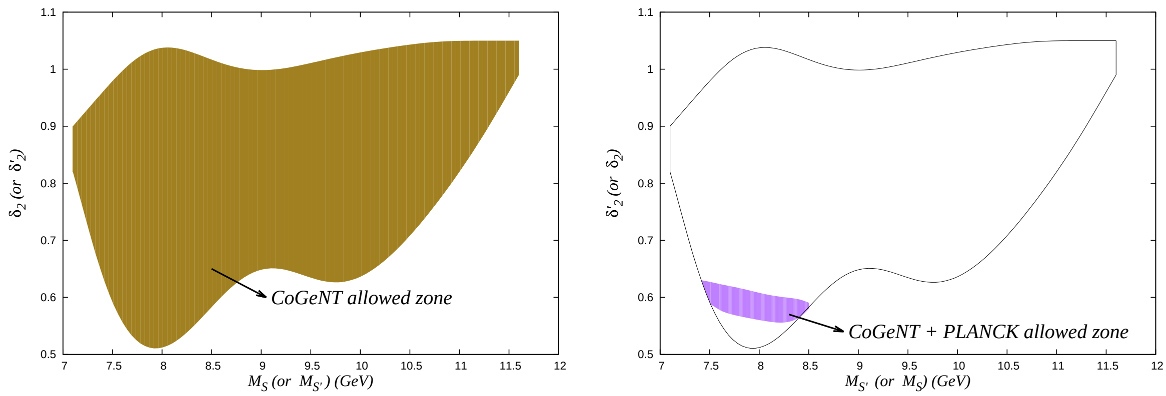

(a) (b)

Figure 5.5: *In panel (a) the olive region is the parameter space allowed in the $M_{S'} - \delta'_2$ plane by CoGeNT data. The same is true if drawn in $M_S - \delta_2$ plane. In panel (b) the light purple shaded region is the only parameter space allowed by Planck data in the $M_{S'} - \delta'_2$ plane choosing $M_S = 7.8$ GeV, $\delta_2 = 0.56$ in the $M_S - \delta_2$ plane. The same is true for the allowed parameter space in the $M_S - \delta_2$ plane when $M_{S'} = 7.8$ GeV, $\delta'_2 = 0.56$ are chosen from $M_{S'} - \delta'_2$ plane.*

Table 5.2: Benchmark point consistent with CoGeNT and Planck data

	M_S (or $M_{S'}$) (GeV)	δ_2 (or δ'_2)	$\sigma^{\rm SI}$ ($\times 10^{-41}$ cm^2)	$\langle \sigma v \rangle$ ($\times 10^{-26}$ cm^3/s)		Annihilation Branching Fraction for S (or S')
Benchmark point 2	7.8	0.56	9.0	4.6	3.7 ($b\bar{b}$)	80%
					0.6 ($c\bar{c}$)	12.5%
					0.4 ($l\bar{l}$)	7.5%
	8.2	0.61	9.8	5.7	4.6 ($b\bar{b}$)	81%
					0.7 ($c\bar{c}$)	12%
					0.4 ($l\bar{l}$)	7%

the allowed parameter zones for CoGeNT are shown in Fig. 5.5(a) and Fig. 5.5(b). If we are to explain CoGeNT findings with either S or S', we find the olive zone in the M_S – δ_2 or $M_{S'} - \delta'_2$ plane respectively (see Fig. 5.5(a)). We now choose a benchmark point ($M_S = 7.8$ GeV, $\delta_2 \simeq 0.56$) in the $M_S - \delta_2$ plane. This fixes Ω_S. Planck results then restrict $\Omega_{S'}$, which then can be reproduced by a tiny region in the $M_{S'} - \delta'_2$ plane (shown as light purple shaded region in Fig. 5.5(b)). We then take $M_{S'} = 8.2$ GeV, $\delta'_2 \simeq 0.61$ from this light purple region of Fig. 5.5(b) to complete the CoGeNT benchmark point presented in Table 5.2. The same is valid for the other case where we initially choose the point to be ($M_{S'} = 7.8$ GeV, $\delta_2' \simeq 0.56$) in the $M_{S'} - \delta_2'$ plane for the singlet S' and repeat the similar procedure mentioned above to obtain the CoGeNT benchmark point (Table 5.2).

5.6.3 Constraints from CRESST II and Planck data

The Cryogenic Rare Event Search with Superconducting Thermometers (CRESST) dark matter direct search experiment operating at the Gran Sasso laboratory looks for very small ($\sim$ few keV) WIMP-induced nuclear recoil energy with cryodetectors and scintillating crystal, $CaWO_4$ ($ZnWO_4$ for future project) as target element. The advantages of using cryogenic technique over the others are the lower threshold energy and high resolution which are much essential in detecting lower mass WIMPs. The recoil energy spectrum, dN/dE of the nucleon scattered by a WIMP falls rapidly with energy and is more sensitive for very low mass dark matter. The standard dark matter detector should have resolved these very small energies but in practice they fail as many detectors kept at very low temperature loose efficiency to resolve very small energies. This small energy resolving technique is well improvised in CRESST. The conventional detectors that use noble gases, liquids or some solid state materials with scintillation or ionisation technique are normally excited via electronic level with sensitivity $\sim$ eV but CRESST uses a superconducting film thermometer (usually tungsten) which have excitation level $\sim 10^{-1}$ meV generated from breaking of Cooper pairs. This enhances sensitivity in detection and thus smaller errors are eliminated. A pair of cryogenic channels are built for both heat (phonon) and scintillation light signal. The multi-target is another exciting feature in CRESST over the other experiments that use only one element as target. Comparison of events at different nuclei can be useful to verify positive signal whereas all the events at single nuclei cannot be fully relied without comparison due to some special features of that single element. So, the shape of the recoil spectrum on different target nuclei at the same event can be compared with each other for convincing WIMP signal detection. The strongly interacting neutron background are very hazardous. Due to the fact that the neutrons are multiple scattered as compared to the WIMP case, they are excluded via muon veto where veto is used to exclude events that are purely coincident with incoming muon particle. The nature of recoil (electronic or nuclear) is distinguished via scintillation light from $CaWO_4$ with a parametrization, namely quenching factor (QF) as ratio of output light to the event energy. QF is higher for light, faster particles and vice versa.

After subtracting the main four backgrounds, namely 'leakages' from $e - \gamma$ band and α band, ^{206}Pb and neutrons recoil, from the recent 730 kg days data (2011), results containing 67 events which can be thought to be possible WIMP-events [259]. The reported 1σ and 2σ regions of those events are around $\sim$ 25 GeV and $\sim$ 12 GeV respectively. The maximum likelihood points on those two regions have masses 25.3 GeV and 11.6 GeV with 4.7σ and 4.2σ statistical significance respectively. The corresponding best fit WIMP-nucleon scattering cross sections are given as 1.6×10^{-42} cm^2 (25.3 GeV) and 3.5×10^{-41} cm^2 (11.6 GeV).

We have analysed the 1σ contour of the CRESST II data. We could have chosen 2σ region of CRESST II data as well. But as the low mass part of the 2σ contour has crossover with CDMS II and CoGeNT low mass regions, the outcome is expected to be similar to these experiments. We rather prefer to work with DM of higher mass $\sim$ 25 GeV. CRESST II data of 1σ contour can similarly be translated to the hatched region in the M_S – δ_2 plane for the singlet S or in the $M_{S'} - \delta_2'$ plane for the singlet S' (see Fig. 5.6(a)). The best fit point for the CRESST II 1σ contour (mass of DM = 25.3 GeV, $\sigma^{\rm SI} = 1.6 \times 10^{-42}$ cm^2) corresponds to the point (M_S = 25.3 GeV, $\delta_2 \simeq 0.36$) in the $M_S - \delta_2$ plane for the singlet S. Choice of this point fixes Ω_S. The relic abundance constraint from Planck survey then restricts $\Omega_{S'}$, which in turn limits the allowed parameter space in the $M_{S'}$

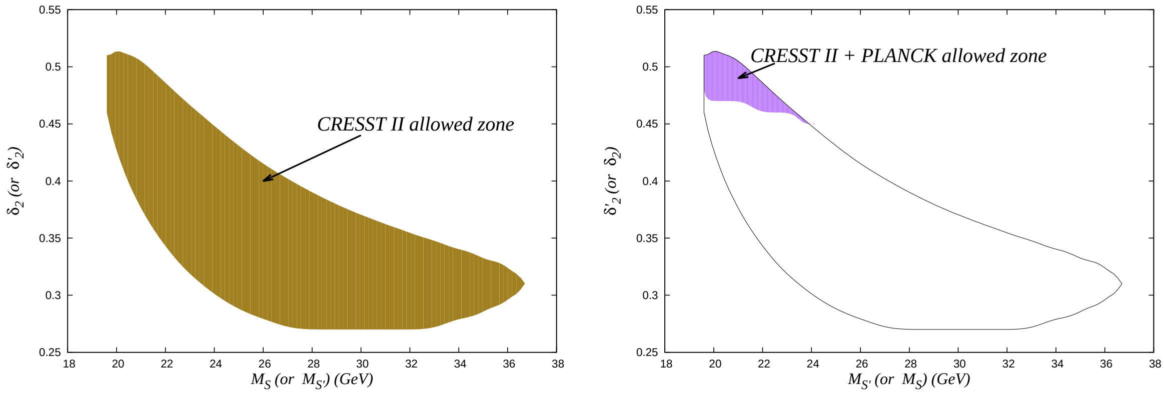

(a) (b)

Figure 5.6: *In panel (a) the olive region is the parameter space allowed in the* $M_{S'} - \delta'_2$ *plane by CRESST II data of* 1σ *contour. The same is true if drawn in* $M_S - \delta_2$ *plane. In panel (b) the light purple shaded region is the only parameter space allowed by Planck data in the* $M_{S'} - \delta'_2$ *plane choosing* $M_S = 25.3$ *GeV,* $\delta_2 = 0.36$ *in the* $M_S - \delta_2$ *plane. The same is true for the allowed parameter space in the* $M_S - \delta_2$ *plane when* $M_{S'} = 25.3$ *GeV,* $\delta'_2 = 0.36$ *are chosen from* $M_{S'} - \delta'_2$ *plane.*

– δ'_2 plane to the tip (shown as the light purple zone in Fig. 5.6(b)) of the CRESST II allowed zone. We then choose $M_{S'} = 23.3$ GeV, $\delta'_2 \simeq 0.47$ from this light purple region to complete the CoGeNT benchmark point presented in Table 5.3. We would have obtained the same benchmark point (Table 5.3) if our initial choice of the point which corresponds to the best fit point for the CRESST II 1σ contour is ($M_{S'} = 25.3$ GeV, $\delta'_2 \simeq 0.36$) in the $M_{S'} - \delta'_2$ plane for the other singlet S' and we repeat the similar procedure stated aboved.

Table 5.3: Benchmark Point consistent with CRESST II 1σ contour and Planck data

	M_S (or $M_{S'}$) (GeV)	δ_2 (or δ'_2)	$\sigma^{\rm SI}$ ($\times 10^{-41}$ cm^2)	$\langle\sigma v\rangle$ ($\times 10^{-26}$ cm^3/s)		Annihilation Branching Fraction for S (or S')
Benchmark point 3	25.3	0.36	1.6	3.0	2.4 ($b\bar{b}$)	81%
					0.4 ($c\bar{c}$)	12%
					0.2 ($l\bar{l}$)	7%
	23.3	0.47	3.2	4.8	3.9 ($b\bar{b}$)	81%
					0.6 ($c\bar{c}$)	12%
					0.3 ($l\bar{l}$)	7%

5.6.4 Constraints from XENON 100 and Planck data

The XENON 100 Dark Matter experiment which is installed underground at the Laboratory Nazionali del Gran Sasso of INFN, Italy uses a 62 kg liquid xenon target that is operated as a dual phase (liquid/gas) time projection chamber (TPC) to search for WIMP interactions. One of the advantages of XENON detector over other are that it uses Xe which has large mass number A ($\sim$ 131) that produce high rate for SI interactions ($\sigma \propto A^2$) if energy threshold for nuclear recoils is low. Also, Xe has high stopping power (Z=54 and ρ=3g/cm^3) and the active volume is thus self-shielding. Nuclear recoil discrimination with simultaneous measurement of scintillation and ionization is done to make the measurement more precise. An interaction in the target generates scintillation light that is recorded as S1 signal by two arrays of photomultiplier tubes at the top and bottom of the chamber. Again the electrons liberated from interaction are drifted by electric field in the liquid-gas phase and then a strong electric field extracts the electrons and produce proportional scintillation that is finally recorded as a S2 signal by the same photomultiplier. From the time delay between S1 and S2 signals, depth can be measured and from the hit-pattern of S2 signal, horizontal position can be reconstructed. Also from S1/S2 ratio, electronic signals are discriminated from nuclear events. Thus from all these techniques, the background events and all the other events which are not compatible for the expected dark matter events are rejected.

XENON 100 collaboration did not observe any prospective signal of DM. From this non-observation they have set an upper bound on spin independent scattering cross-section $\sigma^{\rm SI}$ for various dark matter masses [118, 262]. In the context of our model this translates into an allowed region in the $M_S - \delta_2$ (or $M_{S'} - \delta_2'$) plane, indicated as the olive region in Fig 5.7(a). Here we assume only S (or S') participates to have a conservative estimate. We need to find the parameter space suitable for producing DM relic abundance compatible with Planck observations. Our strategy here is somewhat different from the cases of other dark matter experimental results considered earlier in this work where the allowed zone in the plane of scattering cross-section and dark matter mass is given by closed contours.

Table 5.4: Benchmark Points consistent with XENON 100 and Planck data

	M_S (or $M_{S'}$) (GeV)	δ_2 (or δ'_2)	$\sigma^{\rm SI}$ ($\times 10^{-45}$ cm^2)	$\langle \sigma v \rangle$ ($\times 10^{-26}$ cm^3/s)		Annihilation Branching Fraction for S (or S')
Benchmark point 4A	54.0	0.022	1.4	9.94	7.83 ($b\bar{b}$)	78.8%
					1.29 ($c\bar{c}$)	13.2%
					0.82 ($l\bar{l}$)	8.2%
	56.0	0.011	0.8	3.95	3.11 ($b\bar{b}$)	78.7%
					0.52 ($c\bar{c}$)	13.2%
					0.32 ($l\bar{l}$)	8.1%
Benchmark point 4B	90.0	0.050	2.6	4.32	4.29 (W^+W^-)	99.3%
					0.024 ($b\bar{b}$)	0.55%
					0.004 ($c\bar{c}$)	0.10%
					0.002 ($l\bar{l}$)	0.05%
	92.0	0.045	2.0	3.78	3.28 (W^+W^-)	86.6%
					0.48 (ZZ)	12.8%
					0.016 ($b\bar{b}$)	0.43%
					0.003 ($c\bar{c}$)	0.08%
					0.002 ($l\bar{l}$)	0.05%

We first constrain the difference of masses $|M_S - M_{S'}|$ for the two components S and S' in our present two component dark matter model. The parameter space is thus reduced to M_S (or $M_{S'}$), δ_2 and δ'_2. We investigated this parameter space ($M_{S'}$, δ_2, δ'_2) keeping $|M_S - M_{S'}| = 2$ GeV and compute the allowed region in this parameter space which is consistent with XENON 100 bound for scattering cross-section and Planck results for relic density. The results are plotted in Fig 5.7(b). From Fig 5.7(b), it reveals that there are a small island of allowed parameter space at around $M_{S'} \sim 55$ GeV and a continuous region from ~ 85 GeV onwards. From each of these two regions we will now choose benchmark points.

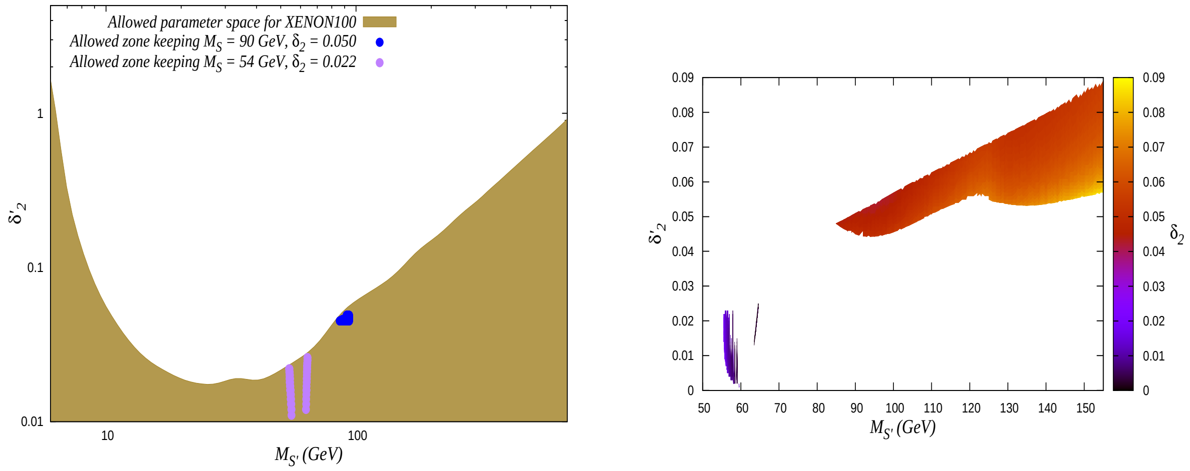

(a) (b)

Figure 5.7: *In panel (a) the solid olive region represents the parameter space allowed in the $M_S - \delta_2$ (or $M_{S'} - \delta'_2$) plane by XENON 100. Panel (b) shows the parameter space allowed by XENON 100 keeping $M_S - M_{S'} = 2$ GeV. Choosing $M_S = 54$ GeV, $\delta_2 \simeq 0.022$ ($M_S = 90$ GeV, $\delta_2 \simeq 0.05$) and keeping the DM mass difference less than 2 GeV, we now denote in panel (a) the parameter space consistent with both XENON 100 and Planck observations.*

First we choose ($M_S = 54$ GeV, $\delta_2 \simeq 0.022$). This fixes Ω_S. This in turn restricts $\Omega_{S'}$ from Planck data. In order to reproduce this $\Omega_{S'}$ window, we perform a parameter scan in the $M_{S'} - \delta'_2$ plane imposing the constrain $M_S - M_{S'} \leq 2$ GeV. We thus get the zone (shown as blue dots in Fig 5.7(a)) consistent with both XENON 100 and Planck observations. This is how the benchmark point 4A as given in Table 5.4, is obtained.

Again choosing ($M_S = 90$ GeV, $\delta_2 \simeq 0.05$) and proceeding similarly as above, leads to the benchmark point 4B shown in Table 5.4. Needless to mention that we could have as well chosen $M_{S'} = 54$ GeV, $\delta'_2 \simeq 0.022$ etc. which would have fixed $\Omega_{S'}$.

5.6.5 Constraints from LUX and Planck data

The Large Underground Xenon (LUX) experiment which is installed nearly 4850 ft. underground in the Black Hills of South Dakota, USA uses 370 kg liquid xenon as detector material in a time projection chamber (TPC) in order to search for the faint direct signal of dark matter. This is the lowest measured background detector in the world for the search of direct detection of dark matter with background at the level of $\sim 10^{-3}$ counts keV^{-1} kg^{-1} day^{-1}. The advantage of using Xe as the detector material over the other materials is similar to that for XENON experiment. The detector is isolated by the surrounding water tank and the earth shielding from above and thus the cosmic rays are shielded.

LUX collaboration has recently published their results which confirm to XENON 100 findings [121] As we have done for XENON 100, we show the allowed zones by LUX and Planck observations in Fig. 5.8. We see that similar to XENON 100, here also we get an island in the parameter space around $M_S \sim 57$ GeV. But the continuum starts around 135 GeV. For the $M_S \sim 57$ GeV point the phenomenology will be similar to XENON 100. However high DM masses ~ 135 GeV cannot reproduce the morphological features of indirect detection observations. So we will not discuss the LUX allowed parameter space any further in this work.

To compare with the literature which attempts explaining the experimental observations assuming certain branching fractions of Higgs to SM particles we have denoted in Tables 5.1—5.4 the relevant branching ratios for the chosen benchmark points. The main feature of our benchmark points is that in our case the braching ratios are determined from the model precisely whereas the previous analysis has been performed assuming certain branching fractions. Still the experimental data can be confronted remarkably well.

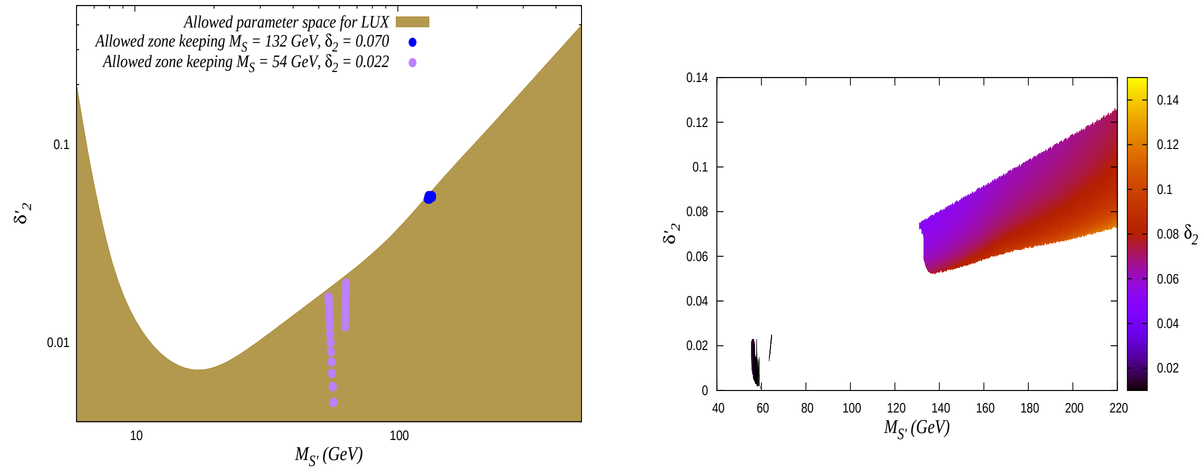

(a) (b)

Figure 5.8: *In panel (a) the solid olive region represents the parameter space allowed in the* $M_S - \delta_2$ *(or* $M_{S'} - \delta'_2$*) plane by LUX. Panel (b) shows the parameter space allowed by XENON 100 keeping* $M_S - M_{S'} = 2$ *GeV. Choosing* $M_S = 54$ *GeV,* $\delta_2 \simeq 0.022$ *(*$M_S = 132$ *GeV,* $\delta_2 \simeq 0.07$*) and keeping the DM mass difference less than 2 GeV, we now denote in panel (a) the parameter space consistent with both LUX and Planck observations.*

5.7 Calculation of Photon Flux Due to DM Annihilation in this Model

The differential flux of $\gamma-$ray due to dark matter annihilation in galactic halo in angular direction that produce a solid angle $d\Omega$ is given by [141]

$$\frac{d\Phi_\gamma}{d\Omega dE_\gamma} = \frac{1}{8\pi\alpha} \sum_f \frac{\langle\sigma v\rangle_f}{M^2_{S,S'}} \frac{dN^f_\gamma}{dE_\gamma} r_\odot \rho^2_\odot J \ , \tag{5.67}$$

$\alpha = 1$ for self-conjugated WIMP while $\alpha = 2$ when this is not the case. Here we consider α to be unity as the singlet scalars from the two scalar singlet model (the dark matter candidate chosen in the present work) are self-conjugated. In Eq. (6.14) $\frac{dN^f_\gamma}{dE_\gamma}$ is the energy spectrum of photons produced in a single annihilation channel of dark matter with some specific final state, $f\bar{f}$.

The integrated γ-flux over a solid angle $\Delta\Omega$ can be expressed in terms of averaged J factor, $\bar{J}$ as

$$\frac{d\Phi_\gamma}{dE_\gamma} = \frac{1}{8\pi\alpha}\sum_f \frac{\langle\sigma v\rangle_f}{M^2_{S,S'}}\frac{dN^f_\gamma}{dE_\gamma} r_\odot \rho^2_\odot \bar{J}\Delta\Omega \ , \tag{5.68}$$

with l and b denote galactic longitude and latitude respectively.

$$\bar{J} = \begin{cases} \frac{4}{\Delta\Omega}\int dl \int db \ \cos b \ J(l,b) & (l,b \ \text{ coordinate}) \\ \frac{2\pi}{\Delta\Omega}\int d\theta \sin\theta \ J(\theta) & (r,\theta \ \text{ coordinate}) \ , \end{cases} \tag{5.69}$$

where the factor, J can be written as,

$$J = \int_{l.o.s} \frac{ds}{r_\odot}\left(\frac{\rho(r)}{\rho_\odot}\right)^2 \tag{5.70}$$

and

$$\Delta\Omega = \begin{cases} 4\int dl \int db \ \cos b & (l,b \ \text{ coordinate}) \\ 2\pi \int d\theta \ \sin\theta & (r,\theta \ \text{ coordinate}) \ . \end{cases} \tag{5.71}$$

In the above $\rho(r)$ denote the DM halo profile.

The relation between radial distance r from GC and line of sight s, can be given by,

$$r = \begin{cases} \left(s^2 + r^2_\odot - 2sr_\odot \cos l \cos b\right)^{1/2} & (l,b \ \text{ coordinate}) \\ \left(s^2 + r^2_\odot - 2sr_\odot \cos\theta\right)^{1/2} & (r,\theta \ \text{ coordinate}) \ . \end{cases} \tag{5.72}$$

In Eqs. (5.69, 5.71, 6.16) θ represents the angle between the line of sight of an observer located at earth while looking at some point r from the galactic centre and the line connecting the observer at earth to the Galactic Centre.

One can make a rough estimate of the enhancement of flux for the case of two component dark matter as in the present framework. The relic abundance Ω_S (or $\Omega_{S'}$) of each singlet S (or S') in this model is generated by thermal freeze-out. Hence each of them is inversely proportional to the thermal averaged cross-section $\langle \sigma v \rangle_S$ (or $\langle \sigma v \rangle_{S'}$). Now from Eq. (6.14) one can find that the differential flux from the annihilation of each of the singlets S or S' is proportional to $\langle \sigma v \rangle_S$ or $\langle \sigma v \rangle_{S'}$ (for s-wave) respectively and hence inversely proportional to their corresponding abundance, Ω_S or $\Omega_{S'}$. Since in our case the masses of the singlets S and S' are nearly similar, we can take $M_S \approx M_{S'}$. Also the spectrum $\frac{dN_\gamma^f}{dE_\gamma}$, which is the photon spectrum produced in a single annihilation channel of singlet S or S' with particular final state $f\bar{f}$, would be similar in nature as both the singlet masses are chosen to be nearly equal and hence the branching fractions of the final states produced in the annihilation of one of the singlets are almost equal to that of the other. The J-factor of Eq. (6.15) contains the information of the density of each of the particular annihilating dark matter species. For the singlet S the density can be written as $\rho_{\rm DM}(\Omega_S/\Omega_{\rm DM})$, where $\rho_{\rm DM}$ is the total dark matter density (sum total densities of the singlets S and S') in this model. Likewise the density for the singlet S' is given by $\rho_{\rm DM}(\Omega_{S'}/\Omega_{\rm DM})$. Thus the total flux which is the sum total of the flux produced by each of the singlets can be approximately written with a constant factor C and $M_S \approx M_{S'} = M$ (say) as,

$$\begin{aligned}
\left(\frac{d\Phi_\gamma}{d\Omega dE_\gamma}\right)_{\rm tot} &= C\left(\frac{1}{M^2\Omega_S}\times(\Omega_S/\Omega_{\rm DM})^2 + \frac{1}{M^2\Omega_{S'}}\times(\Omega_{S'}/\Omega_{\rm DM})^2\right) \\
&= \frac{C}{M^2}\left(\frac{\Omega_S}{\Omega_{\rm DM}^2} + \frac{\Omega_{\rm DM}-\Omega_S}{\Omega_{\rm DM}^2}\right) \quad (\Omega_{\rm DM} = \Omega_S + \Omega_{S'}) \\
&= \left(\frac{C}{M^2}\right)\left(\frac{\Omega_S + \Omega_{\rm DM} - \Omega_S}{\Omega_{\rm DM}^2}\right) \\
&= \left(\frac{C}{M^2\Omega_{\rm DM}}\right) \quad ,
\end{aligned} \tag{5.73}$$

where $\Omega_{\rm DM}$ is the DM abundance as measured by Planck. In the above $\left(\frac{C}{M^2\Omega_{\rm DM}}\right)$ is the corresponding flux in the one scalar singlet model. Now in our case, the contributions to the abundances (Ω_S or $\Omega_{S'}$) for each singlet (S or S') are nearly equal. Hence from Eq. (5.73), the flux is found to be equal to the case when only one scalar singlet is considered. This is due to the choice of almost degenerate masses of the singlets S and S' (the mass difference lies within a few GeV in our case). If one chooses the masses of the singlets S and S' in this model to be effectively non-degenarate, then these different masses would serve as the weight-factors for the two contributing terms in the total flux. Hence the total flux for this multicomponet dark matter model would come out to be different than that would have been obtained from a single component dark matter case. The total photon flux is then expressed in general form as,

$$\left(\frac{d\Phi_\gamma}{d\Omega dE_\gamma}\right)_{\rm tot} = \left(\frac{C}{\Omega^2_{\rm DM}}\right)\left(\frac{\Omega_S}{M_S^2}+\frac{\Omega_{S'}}{M_{S'}^2}\right) \quad . \tag{5.74}$$

From Eq. (5.74), we can conclude that for the case of non-degenarate masses of two singlets, the total flux is then dependent on both the relic densities and masses of individual singlets. Even if one considers the relic densities of individual singlets to be nearly equal, the hierarchy of masses of the singlets can even yield considerable amount of total gamma ray flux. The observed photon flux produced in two scalar singlet model will in principle be nearly similar to that of one singlet scalar model for effectively degenerate masses of the dark matter components considered here.

5.7.1 Benchmark DM Halo Profiles

In this work we choose the dark matter halo distribution which is usually parametrised as a spherically symmetric profile,

$$\rho(r) = \rho_0 F_{\rm halo}(r) = \frac{\rho_0}{(r/r_c)^\gamma[1+(r/r_c)^\gamma]^{(\beta-\gamma)/\alpha}} \quad , \tag{5.75}$$

where α, β, γ and r_c are the parameters that represent some particular halo profile listed in Table 5.5. ρ_0 is the local dark matter halo density at solar location ($\rho(r_\odot)$) taken to be 0.4 GeV/cm^3 with $r_\odot$ is the distance between sun to the galactic centre ($\sim$ 8.5 kpc).

Table 5.5: Relevant parameters used for the benchmark dark matter halo models

Halo Model	α	β	γ	r_c (kpc)
Navarro, Frenk, White (NFW) [151]	1	3	1	20
Moore [153]	1.5	3	1.5	28
Isothermal [155]	2	2	0	3.5

Another halo profile, namely Einasto profile has also been involved for our study. A different kind of parametric form is adopted in this halo profile [158] which can be written as,

$$F_{\rm halo}^{Ein}(r) = exp\left[\frac{-2}{\tilde{\alpha}}\left(\left(\frac{r}{r_\odot}\right)^{\tilde{\alpha}} - 1\right)\right] \quad , \tag{5.76}$$

where $\tilde{\alpha}$ is a parameter of the halo profile. In our work value of $\tilde{\alpha}$ is chosen to be 0.17.

5.8 Confronting Indirect Dark Matter Detection Experiments

The region surrounding the Milky Way is rich in astrophysics and is assumed to have a high density of dark matter. This region is promising for better understanding of the properties of dark matter, as no other astrophysical source or region is as accessible as the galactic centre (GC). The Fermi Gamma Ray Space Telescope (FGST) has been employed to survey the high luminous gamma ray emission between $\sim$ 50 MeV to $\sim$ 100 GeV.

DM distribution follows a density function, $\rho(\vec{r})$, with $\vec{r}$ is the position vector from the centre of the galaxy. Several such DM halo profiles are available in the literature. We choose some representative cuspy to flat profiles for our numerical estimations presented in the Subsection 5.7.1. For a particular DM halo profile one can calculate the photon flux due to DM annihilation using Eq. (5.68) for the present model framework in Section 5.7.

We now discuss observations of excess γ-ray emission from GC and low latitude of Fermi bubble, which does not appear to have "standard" origins, but can be understood in the light of DM annihilation. In particular we show that the morphological features of these observations can be explained by our proposed model with parameter spaces consistent with DM direct detection experiments and DM relic abundance constraints from Planck survey. We will point out in subsequent discussions that the uncertainties involved in understanding the significance of such astrophysical observations are quite substantial. So at this point we do not intend to fit the data, but rather limit ourselves to reproduce the morphological features of the observations in terms of DM annihilation by our model.

5.8.1 Explanation of Excess Gamma Ray Emission from Galactic Centre

The low energy (few GeV) γ-ray data from galactic centre region observed by Fermi telescope give a hint of a low mass dark matter. In this section we have discussed the phenomenology of gamma ray from the annihilation of dark matter from galactic centre in this present formalism. We have computed γ-ray flux from the singlet scalars in this model constrained by CDMS II and CoGeNT experiments and finally comparison with the observed γ-ray flux has been done.

Detailed studies on spectral and morphological features of the gamma rays from the galactic centre region have been studied in Refs. [168, 286]. In Ref. [286], the spectrum of the gamma ray emission from the region that encompasses 5^o surrounding the galactic centre is studied after subtracting the known sources from the data of the Fermi Second Source Catalog (2FGL) [287] and disc emission template. [4] The main reason of the disc template emission is the gamma ray produced from the neutral pion decay which is outcome of cosmic ray interaction with gas. Though inverse Compton and Bremsstrahlung can also contribute. Assuming the gas distribution to be of the following form,

$$\begin{aligned} \rho_{\rm gas} &\propto e^{-|z|/z_{\rm sc}(R)}, &\text{for} \quad R < 7\,\text{kpc}, \\ \rho_{\rm gas} &\propto e^{-|z|/z_{\rm sc}(R)}\, e^{-R/R_{\rm sc}}, &\text{for} \quad R > 7\,\text{kpc}, \end{aligned} \tag{5.77}$$

where $(z,\ R)$ denotes the location relative to the GC in cylindrical coordinates. The chosen values of $R_{\rm sc} = 3.15$ kpc and $z_{\rm sc}(R) = 0.1 + 0.00208 \times (R/\text{kpc})^2$ [289] kpc as these values are best suitable to fit for the observational data of 21-cm H line surveys which is the conventional tool used to probe the density of neutral hydrogen. The flux of gamma rays from pion decay is estimated by integrating this distribution over the line-of-sight and it is found to be in good agreement with the observed morphology of the diffuse emission. The residual gamma ray spectrum is brighter for γ-energy range from 300 MeV to 10 GeV and drops by order of magnitude beyond 10 GeV. From the morphological characteristics of this residual gamma ray emission from the central region of our galaxy, it has been shown in [264, 286], that below 300 MeV the residual gamma ray could originate from a point-like source but at higher energies it could originate from spatially extended components or may be from annihilating dark matter. Also, if the very high energetic portion of the residual gamma ray emission from the galactic centre is analysed, the spectral shape is found to match fairly well with the gamma emission from galactic ridge. The galactic ridge is an inner region of galaxy extending up to a width of

[4] This is to mention that we had almost finished all the analyses for this thesis work, the Fermi Third Source Catalog (3FGL) [288] became publicly available, where the source catalog had been updated. We have used the analysed results from 2FGL data for Galactic Centre since no such analysed results for 3FGL data were available then. However, since the 'bumpy' feature of the Galactic Centre excess is still found to be present in the analysed results for 3FGL data but with slightly less distinct feature, the results of our analyses is therefore expected not to change substantially.

5^o galactic latitude and $\pm 40^o$ galactic longitude containing huge amount of white dwarfs. The standard convention is that the high energy cosmic nucleons interact with molecular cloud in the ridge and pions are produced in huge amount which subsequently decay to high energy gamma. Therefore, the residual emission from GC considered here can be assumed to contain low energy tail of ridge emission. Also very low energy part of the residual spectrum is supposed to be dominated by the point source [173, 264] which loses its dominance at above GeV scale.

However there are some astrophysical propositions that can morphologically explain the gamma-ray flux structure from the inner part of galactic centre. These include millisecond pulsar population [290], central supermassive black hole [168, 173] *etc.* which can explain this spatially extended gamma ray distribution feature from GC.

Super-massive black holes can also accelerate both electrons and cosmic ray protons. These accelerated electrons then produce gamma ray from inverse Compton scattering and can be accounted for any unresolved gamma ray emission from galactic centre region. But these electrons produce γ-ray in TeV-scale [291] which may in principle explain the high energy gamma ray from galactic centre observed by different experiments like HESS, HAWC. Hence this type of mechanism cannot fully account for the FGST data for low energy gamma rays. But the cosmic ray protons accelerated by the black hole can produce pions through the interaction with interstellar gas. Decay of these pions yield gamma rays of lower energy. This scenario may partially explain the FGST residual emission feature as there appear a lot of astrophysical parameters like ISM gas distribution or unknown diffusion coefficient for proton propagation through ISM gas *etc.* which are not fully understood.

The other astrophysical objects, the gamma rays from which may yield spectra similar to that observed by FGST data are *Millisecond pulsars*. The spectra from the millisecond

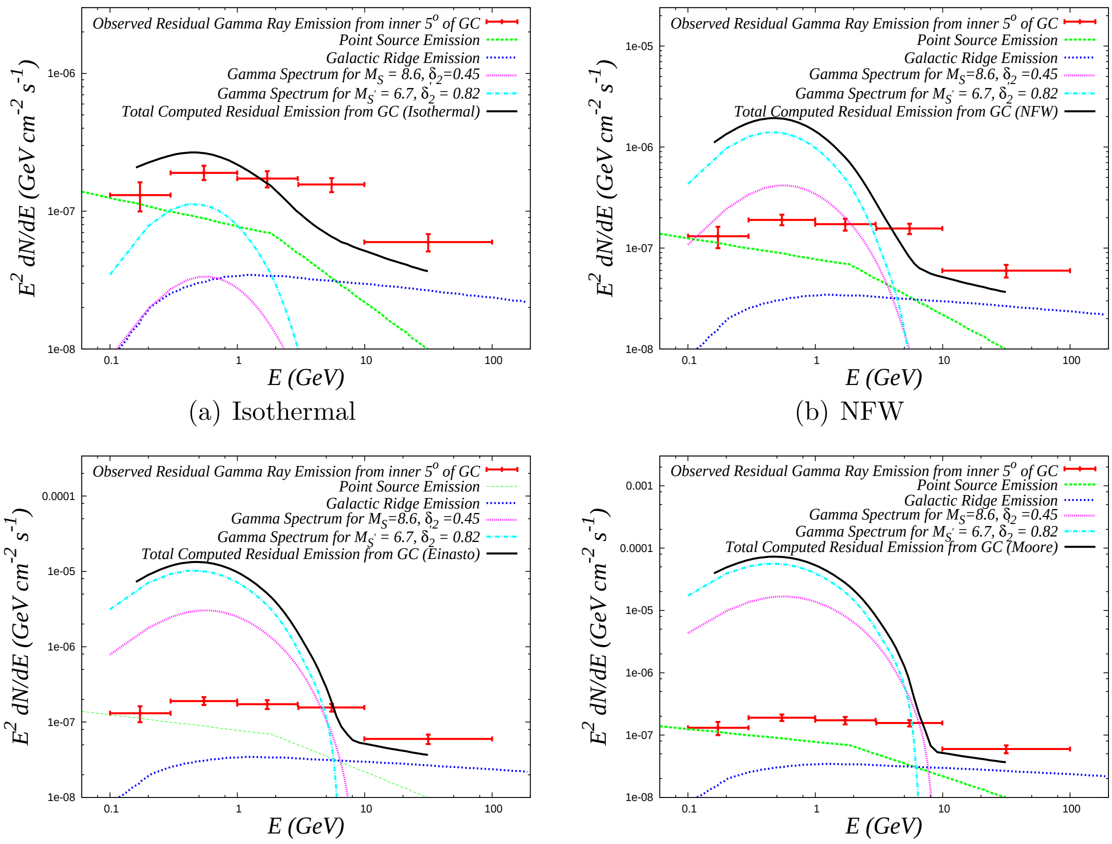

(a) Isothermal (b) NFW

(c) Einasto (d) Moore

Figure 5.9: *Residual γ-ray flux from the inner 5° of galactic centre. The red data points represent the observed flux. Point source and galactic ridge emissions are represented by the light green dashed and blue dotted lines respectively. DM annihilation in our model is calculated for benchmark point 1 consistent with CDMS II and Planck data (see Table 5.1). SS-annihilation is calculated for $M_S = 8.6$ GeV and $\delta_2 = 0.45$ and is denoted by the dotted violet line. For $S'S'$ annihilation we use $M_{S'} = 6.7$ GeV and $\delta_2' = 0.82$ and is represented by the dash-dotted cyan line. Total calculated residual γ-ray flux is denoted by the solid black curve. Each sub-figure is calculated for different DM halo profiles, as indicated in their respective captions.*

pulsars are hard in nature beyond a few GeV, *i.e.,* it falls off with much rapidity after a few GeV. This tends to indicate that surrounding the galactic centre, there may be other millisecond pulsars in considerable numbers which are still to be probed experimentally. But there are discrepancies which immediately contradict this scenario. From the FGST's first pulsar catalog, the spectral index of gamma from pulsars is centred at 1.38 but a much harder spectrum for the average pulsar is required to match the observed gamma spectrum. Although a very few pulsars have certainly a very hard spectral index that can be accounted for the residual emission [290] below 10 GeV but to fit the gamma flux of the bumpy spectral shape one needs to have larger number of these types of pulsars which are not present in Fermi pulsar catalog. The globular clusters, rich in gamma pulsars have also been studied to measure the spectral index but here too, the data do not favour very hard spectral nature. In order to comply the angular distribution pattern of the emission, the pulsar density should decrease very rapidly along the outward radial distance but the significance of such rapidity has not been found from astrophysical data. From all the above discussions, one may conclude the fact that some different mechanism is required to explain this bumpy spectral shape of the residual emission from galactic centre observed by FGST.

A potentially strong proposition about the nature of this bumpy feature of the residual gamma emission from GC is dark matter annihilation as indicated by Hooper *et al.* [174, 177,178]. As in dark matter scenario, the angular width of the spectra is narrow since the astrophysical factor for flux calculation contains $\rho^2(r)$ which falls off very rapidly with radial distance from GC explaining the "bump". It also resolves the problem posed from pulsar explanation.

In Ref. [174] it has been argued that by considering few annihilating dark matter scenarios with some standard dark matter halo profiles, low mass dark matter can fit the spectrum with good statistics. Few benchmark cases, such as 10 GeV dark matter annihilating to leptonic channels [292] or 30 GeV dark matter annihilating to $b\bar{b}$ channel with NFW halo profile have been shown to fit data [174]. In order to get an idea of where our specific model fits in such discussion of generic models, in Tables 5.1–5.4 we have quoted branching ratios for different DM annihilation channels for different benchmark points. We see that although for $10 - 55$ GeV DM the $b\bar{b}$ channel has a branching ratio $\sim 80\%$, but for higher masses, when the W^+W^- or ZZ channel opens up, it drastically

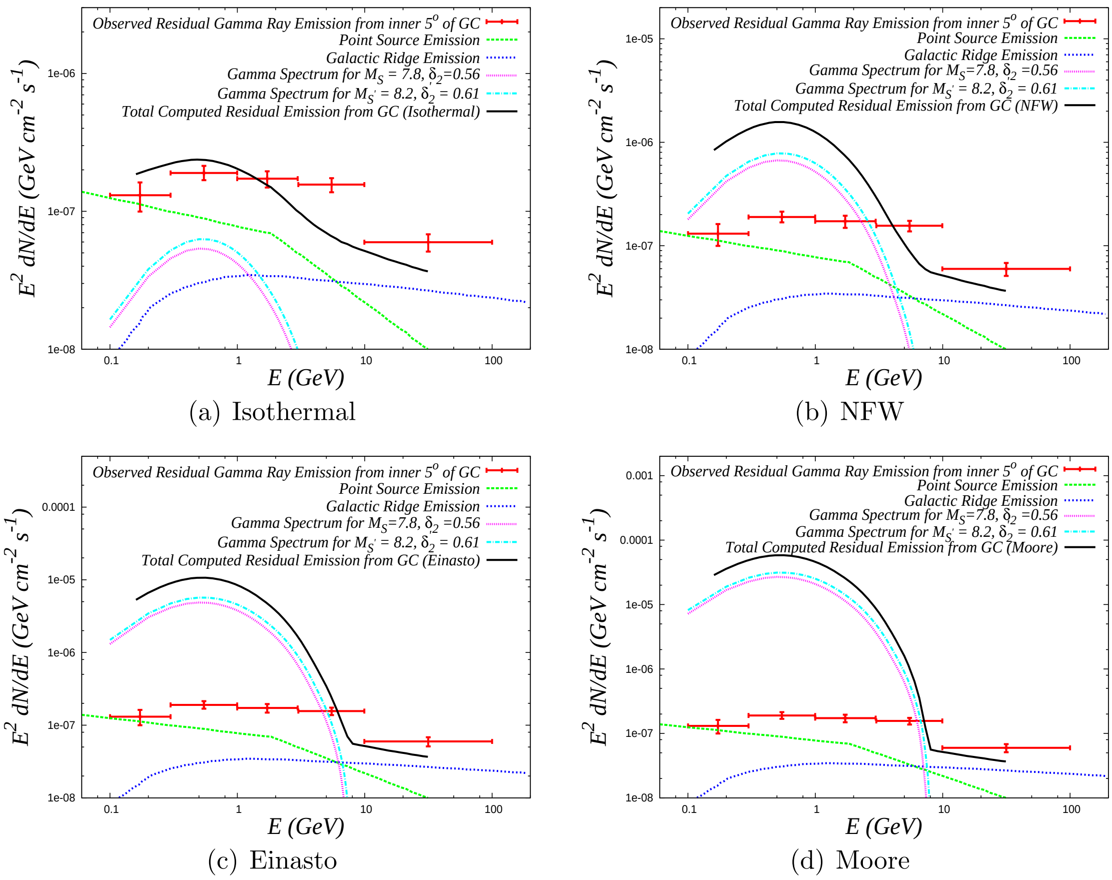

(a) Isothermal (b) NFW

(c) Einasto (d) Moore

Figure 5.10: *Residual γ-ray flux from the inner 5° of galactic centre. DM annihilation is calculated for benchmark point 2 consistent with CoGeNT and Planck data (see Table 5.2). SS-annihilation is calculated for $M_S = 7.8$ GeV and $\delta_2 = 0.56$. For $S'S'$ annihilation we use $M_{S'} = 8.2$ GeV and $\delta_2' = 0.61$. Notations are same as in Fig. 5.9.*

changes. However such a DM candidate is also compatible with data.

In this section we extend the above discussion for the multi-component DM scenario as discussed in our model. As mentioned in the abstract, presence of more than one DM candidate helps enhance the total γ-ray emission due to DM annihilation. We work with benchmark points chosen from the model parameter space already constrained by direct detection experiments and Planck survey. For each such benchmark points we try to match the observed spectra from the theoretically calculated ones. We plot the emission from point sources and galactic ridge from Ref. [174]. Then we add SS and

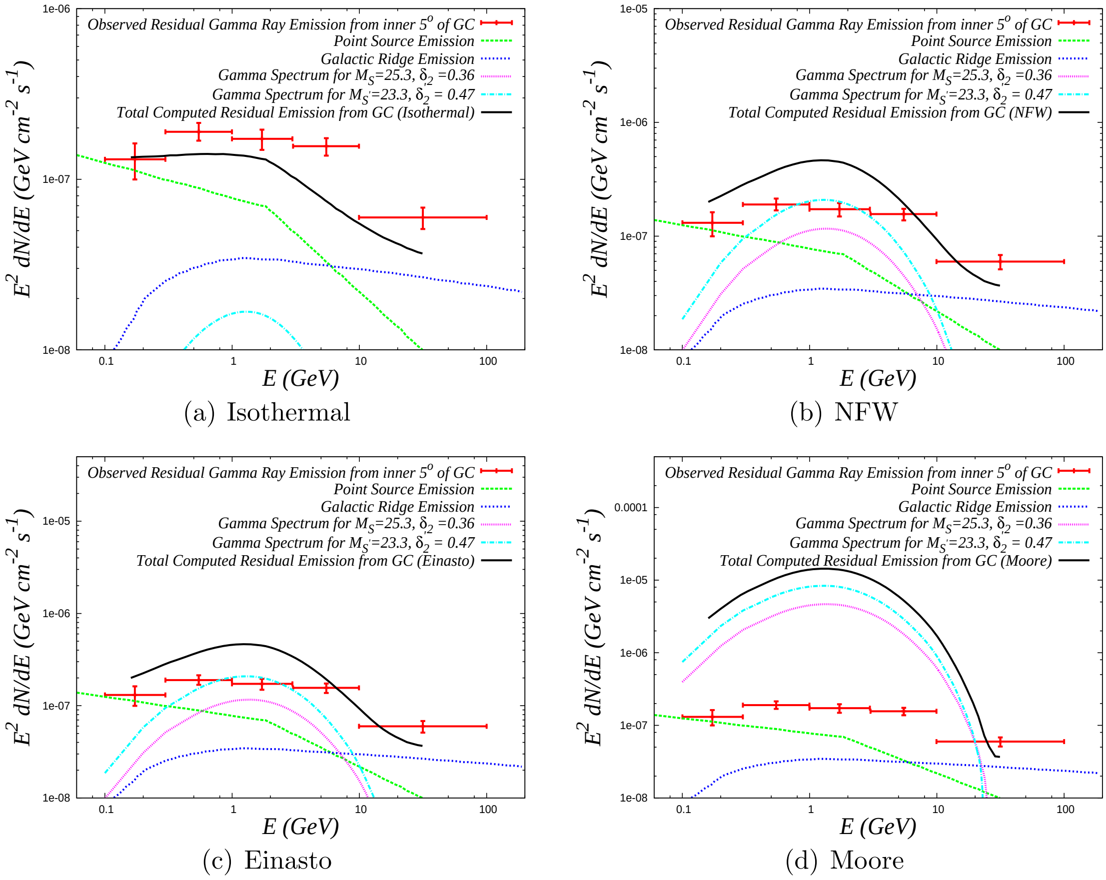

(a) Isothermal (b) NFW (c) Einasto (d) Moore

Figure 5.11: *Residual γ-ray flux from the inner 5º of galactic centre. DM annihilation is calculated for benchmark point 3 consistent with CRESST II and Planck data (see Table 5.3). SS-annihilation is calculated for $M_S = 25.3$ GeV and $\delta_2 = 0.36$. For $S'S'$ annihilation we use $M_{S'} = 23.3$ GeV and $\delta_2' = 0.47$. Notations are same as in Fig. 5.9.*

$S'S'$ annihilation spectra to get theoretically predicted residual flux for four DM halo profiles arranged in increasing order of “cuspiness”: (1) Isothermal [155], (2) NFW [150], (3) Einesto [158] and (4) Moore [293].

We see that for low mass DM, the plots in Fig. 5.9 and Fig. 5.10 corresponding to benchmark points 1 and 2 respectively, indicate that a flat DM halo profile like Isothermal profile offers a better agreement with the data. For benchmark point 3, Fig. 5.11 shows that Isothermal profile is still the promising one, whereas Moore profile overestimates the data. The XENON 100 benchmark point 4A is used for Fig. 5.12, where we see that

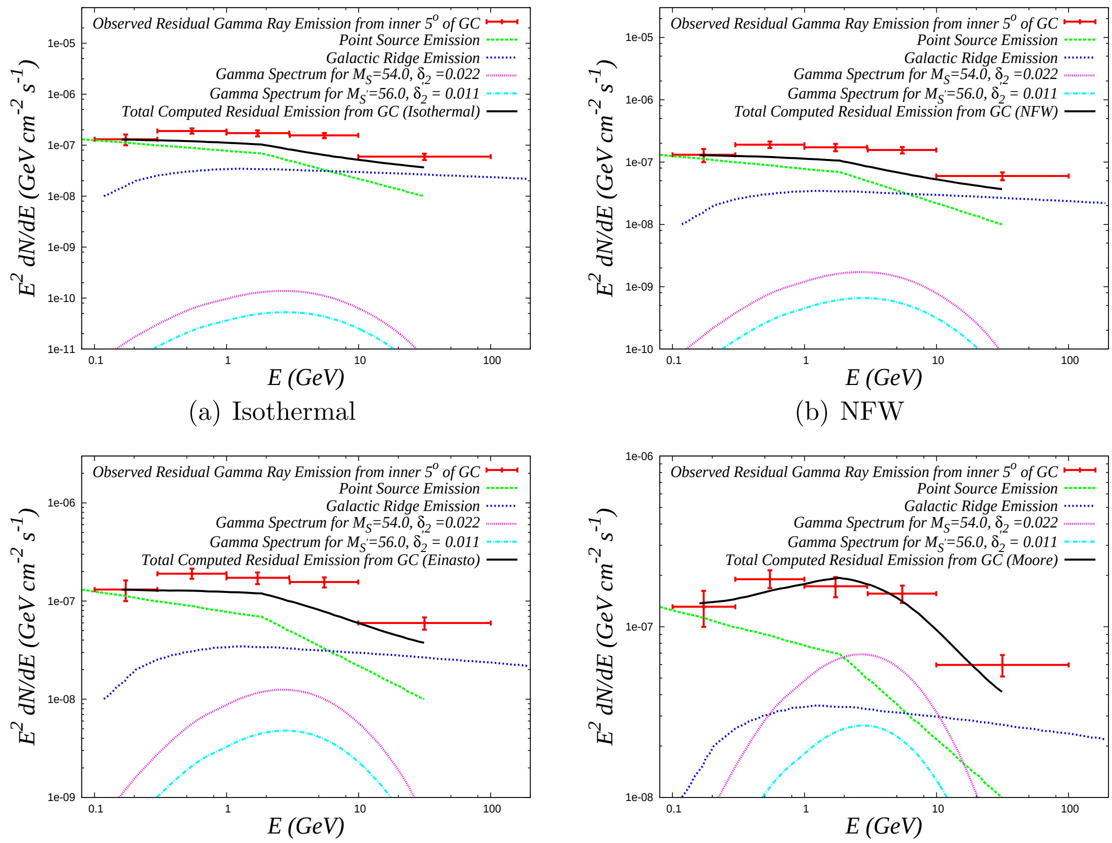

(a) Isothermal (b) NFW (c) Einasto (d) Moore

Figure 5.12: *Residual γ-ray flux from the inner 5º of galactic centre. DM annihilation is calculated for benchmark point 4A consistent with XENON 100 and Planck data (see Table 5.4). SS-annihilation is calculated for $M_S = 54$ GeV and $\delta_2 = 0.022$. For $S'S'$ annihilation we use $M_{S'} = 56$ GeV and $\delta_2' = 0.011$. Notations are same as in Fig. 5.9.*

for DM masses ~ 55 GeV and for all DM profiles other than the cuspy Moore profile, the DM annihilation contribution is rather small compared to contributions from point sources and galactic ridge. NFW profile works better for XENON 100 benchmark point 4B, used for Fig. 5.13.

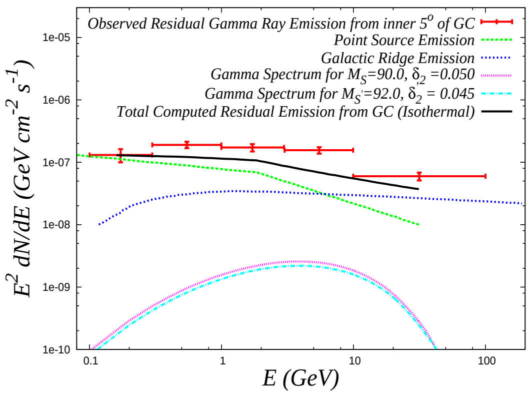

(a) Isothermal

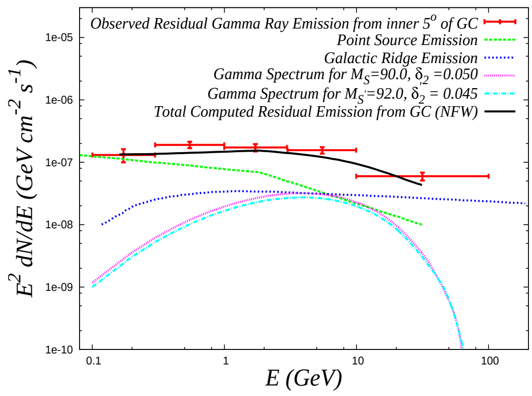

(b) NFW

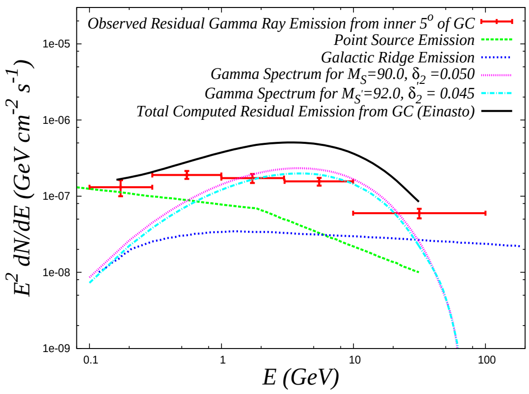

(c) Einasto

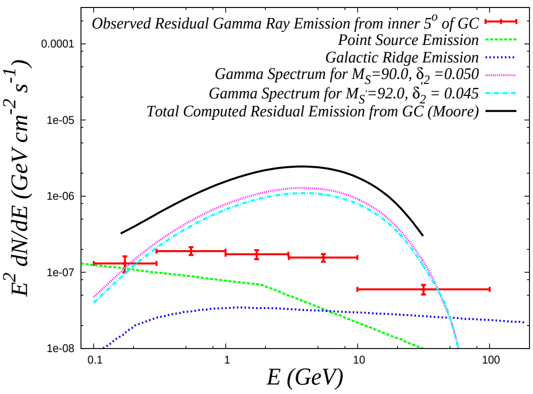

(d) Moore

Figure 5.13: *Residual γ-ray flux from the inner 5^o of galactic centre. DM annihilation is calculated for benchmark point 4B consistent with XENON 100 and Planck data (see Table 5.4). SS-annihilation is calculated for $M_S = 90$ GeV and $\delta_2 = 0.05$. For $S'S'$ annihilation we use $M_{S'} = 92$ GeV and $\delta_2' = 0.045$. Notations are same as in Fig. 5.9.*

5.8.2 Explanation of Gamma Ray Bump from Fermi bubble's Low Galactic Latitude

From the Fermi Gamma-Ray Space Telescope (FGST) data a pair of bilateral lobular structures that contain large amount of gamma-ray had been found in the upper and lower regions of galactic centre. These lobes, known as Fermi bubbles, emit γ rays between $\sim$ few GeV to $\sim$ 100 GeV range and they are extended almost $\sim 50^o$ ($r = \pm 10$ kpc) up and down from the galactic plane. In Ref. [294], the bubble emission has been studied as an extension of WMAP haze [295] which is the non-thermal, microwave emission from the inner part of the galaxy confirmed from data of different ongoing experiments worldwide such as Planck [296] and ROSAT [297] X-ray emission data. Evidences [296] show that near the galactic plane, the γ-ray bubbles and the haze can have a strong correlation that attribute to the fact that they might have been a common origin. When we move far from the galactic plane along the Fermi bubble the gamma ray spectrum follows a power law, $E^{-\alpha}$ with spectral index, $\alpha = 2$ over all the energy range observed by the FGST. This type of gamma ray spectrum can be well explained by approximate power law spectrum of electron distribution with spectral index, 3, i.e., E^{-3} where the inverse Compton scattering (ICS) is the mechanism of production of these types of gamma rays. Also, similar distribution can produce radio emission in the galaxy [294, 298] due to the synchrotron radiation effect with the interaction of microgauss galactic magnetic field.

The picture of the gamma ray emission from Fermi bubble from the low galactic latitude is somewhat different. In this case the γ-spectrum has a peak at a few GeV energy range. This cannot be explained by the known astrophysical processes like inverse Compton scattering of light source by cosmic electrons in steady-state. This non-ICS nature of the spectrum has generated some interest in astrophysics community and different origins for this bumpy nature of γ-ray spectrum from bubble very near the galactic plane have been proposed. Population of millisecond pulsars [171, 172], cosmic ray interaction with gas [207, 299] or an annihilating dark matter scenario [168, 174–176] have been studied in great details. A detailed study on the morphology and spectral signature of Fermi bubble is given in Hooper *et al.* [268].

The explanation of this low latitude excess γ-ray emission as given by the *diffuse emission mechanism* is due to the fact that the cosmic ray protons are scattered with the gas present in the Milky Way region. But the explanation cannot fully provide the observed phenomenology as the gas distribution is merely correlated with the morphological structure of the γ-emission and also the spectrum of the cosmic ray protons should follow a

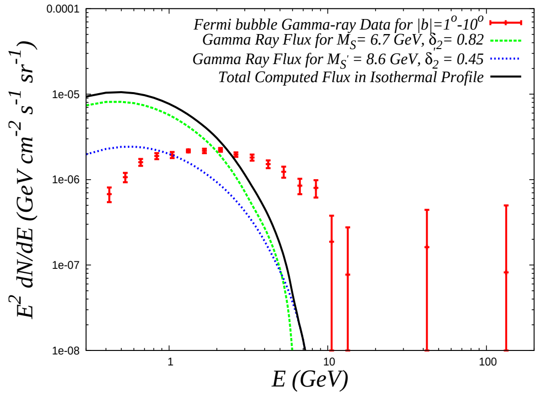

(a) Benchmark point 1

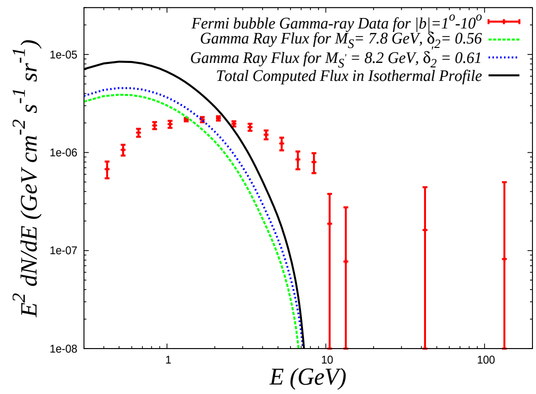

(b) Benchmark point 2

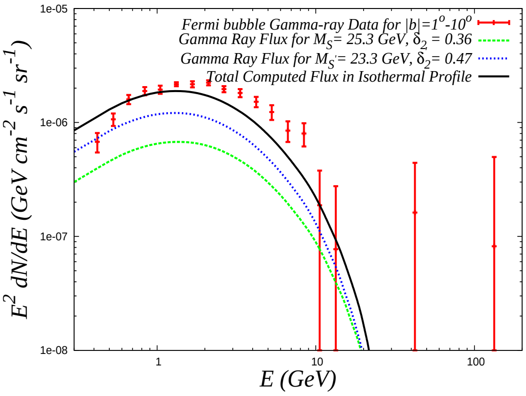

(c) Benchmark point 3

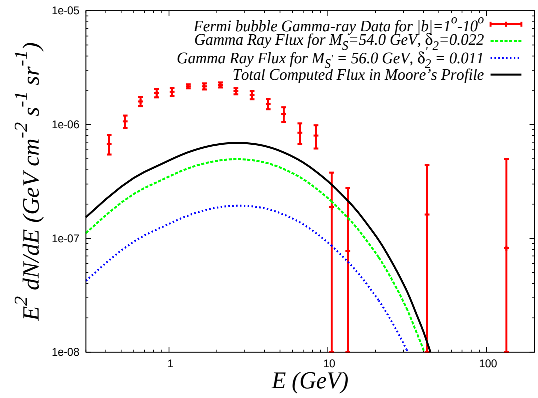

(d) Benchmark point 4A

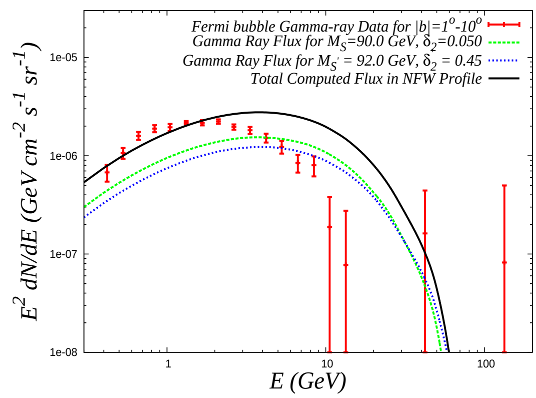

(e) Benchmark point 4B

Figure 5.14: *γ-ray emission spectrum from the Fermi bubble's low-latitude ($|b|$=1^o-10^o) region. The red points denote observed data after subtracting the ICS contribution. The green dashed line denote contribution from SS annihilation. $S'S'$ annihilation is represented by the blue dotted line. The total DM annihilation contribution is shown by the solid black line. Each sub-figure is plotted for a different benchmark point with a DM halo profile which explains GC low energy γ-ray bump the best.*

bumpy nature around ~ 25 GeV or so to provide a good description of the observed emission. But this type of peak in the cosmic proton spectral feature is not fully understood from the known astrophysical observation.

Another possibility of this γ-ray excess can be attributed to the excess population of *millisecond pulsars* which have the advantage of producing γ-ray emission with very high luminosity over another types of pulsars. But the nature of γ-ray spectrum generated by such objects is not very well understood as a very few pulsars of this type have been discovered. Also the distribution of such objects outside the galactic plane as proposed is much more constrained from various astrophysical observations.

On the other hand the spectral nature of excess gamma emission from the lower latitude of Fermi bubble may be consistent with the gamma spectrum calculated from the *annihilating dark matter* scenario at the galactic halo region.

As the DM density is expected to be high for regions close to the GC, we concentrate on DM annihilation from low latitude $|\,b\,| = 1^o - 10^o$ zone of Fermi bubble. Like we did for GC, we work with benchmark points consistent with direct detection experiments and Planck survey. However, rather than exploring for all DM halo profiles, we present the plot for that DM profile for which the GC data was better explained. These plots are presented in Fig. 5.14. Here the observed flux is shown after deducting inverse Compton scattering contribution of best-fit steady state electron spectrum of the bubble. We see that for very low DM mass $\sim 7 - 11$ GeV, as preferred by CDMS II or CoGeNT, the spectrum peaks at a lower energy than that obtained from the data. The higher mass zone ~ 25 GeV, as preferred by CRESST II or ~ 55 GeV, as allowed by XENON 100 works better. For very high DM masses ~ 90 GeV allowed by XENON 100, the calculated spectra tend to peak at a bit higher energy than the observed spectrum. But overall we can conclude that the model holds some promise to explain the morphological feature of the Fermi bubble low latitude γ-ray excess.

Chapter 6

Confronting Galactic and Extragalactic γ-ray observed by Fermi-LAT with Annihilating Dark Matter in Inert Higgs Doublet Model

In this chapter we focus, in a thorough study, on the indirect detection of Dark Matter (DM) through the confrontation of unexplained galactic and extragalactic γ-ray signatures for a low mass DM model. For this, we consider a simple Higgs-portal DM model, namely, the inert Higgs doublet model (IHDM) where the Standard Model is extended with an additional complex $\mathrm{SU}(2)_L$ doublet scalar. The stability of the DM candidate in this model, i.e., the lightest neutral scalar component of the extra doublet, is ensured by imposing discrete $\mathbb{Z}_2$ symmetry. The reduced-χ^2 analysis with the theoretical, experimental and observational constraints suggests the best-fit value of DM mass in this model to be $\sim$ 63.5 GeV. We analyse the anomalous GeV γ-ray excess from Galactic Centre in light of the best-fit IHDM parameters. We further check the consistency of the best-fit IHDM parameters with the Fermi-LAT obtained limits on photon flux for 18 Milky Way dwarf spheroidal satellite galaxies (dSphs) known to be mostly dominated by DM. Also since the γ-ray signal from DM annihilation is assumed to be embedded within the extragalactic γ-ray background (EGB), the theoretical calculations of photon flux for the best-fit parameter point in the IHDM framework are compared with the Fermi-LAT results for diffuse and isotropic EGB for different extragalactic and astrophysical background parametrisations. We show that the low mass DM in IHDM framework can satisfactorily confront all the observed continuum γ-ray fluxes originated from galactic as well as extragalactic sources. The extensive analysis performed in this chapter is valid for any Higgs-portal model with DM mass in the ballpark of that considered in this chapter.

6.1 Introduction

There are various ongoing experiments for the detection of dark matter both through direct and indirect mechanisms. In case of direct detection, the dark matter may scatter off a nucleus of a detecting nuclei and in such direct detection experiments attempts are made to measure this recoil energy of the nucleus as the signature of dark matter detection. There are various direct detection experiments around the world such as CDMS II [112, 256, 257], CRESST II [259], CoGeNT [130], XENON 100 [118, 262], LUX [121] etc. that use different detection material, e.g. Ge, Si, Xe etc.

On the other hand, for the indirect detection of dark matter, attempts are made to detect the products that a pair of dark matter particles can produce when they pair annihilate in dense heavenly bodies such as galactic centre, solar core etc. The dark matter in the universe, because of its all pervading nature, may be trapped by the enormous gravity at places like the ones mentioned above and may undergo multiple scattering with the dense matter present at those sites losing in the process their velocity of escape and eventually are trapped inside these bodies. When accumulated in large numbers, these trapped dark matter particles may undergo pair annihilation to produce the pairs of standard model particles such as $q\bar{q}$ or $\ell\bar{\ell}$ as primary or secondary products. Gammas can be obtained as secondary products from the pair annihilation of these primary pairs of SM fermions. The indirect dark matter search experiments look for these gamma rays or the other SM particles that the dark matter pair annihilation may produce at different sites of possible dark matter halo.

There are both earth-based detectors or detector arrays and satellite borne detectors for detecting signals of any anomalous gamma rays that can be attributed to have originated from dark matter annihilation. The satellite borne detectors also look for any anomalous antiparticle excesses. The terrestrial detectors like ICECUBE, Antares etc. may be able to detect the neutrinos that might have originated from dark matter annihilation. The signal of anomalous GeV gamma-ray excess from the Galactic Centre and inner galaxy region as *seen* by the satellite borne experiment Fermi-LAT or Fermi Large Area Telescope which detects the gamma rays from the cosmos. The observational results of Fermi-LAT have acquired considerable interests in the community. Very important observations of gamma rays by Fermi-LAT from the direction of galactic centre indicate the dark matter annihilation at the galactic centre and its neighbourhood. Fermi-LAT also discovered a bi-lobular structure of gamma-ray emission extending 25,000 light-years upward (north) and downward (south) from the galactic centre of the Milky Way galaxy and this came to be known as Fermi Bubble [265, 300]. While the inverse Compton Scattering (ICS) process of the cosmic ray electrons could well explain the observed gamma-ray emission (ranging from a few GeV to ~ 100 GeV) from the higher galactic latitude (b) of the lobe, the observed gamma ray spectrum by the Fermi-LAT from the lower latitudes of the Fermi Bubble indicates a bump-like feature in the energy regime, $E_\gamma \sim 1 - 3$ GeV which could not be explained solely by the ICS mechanism [268]. This excess gamma-ray signal at the lower galactic latitude can be explained with DM models where DM particle annihilates mainly into $q\bar{q}$ channels with the desired value of thermally averaged annihilation cross-section similar to the canonical cross-section of typical thermal production of DM. This bump-like features indicating gamma ray excess are also reported by Fermi-LAT collaboration for the gamma rays from the galactic centre region. An early analysis of Fermi-LAT data reveals that the gamma rays from the galactic centre region exhibit excesses (bump) in the energy range $\sim 0.3 - 10$ GeV. More involved and modified recent analysis [179] including more recent data restricts the range of excess gamma to be in the energy region of $\sim 1 - 4$ GeV. Another earlier analysis of Fermi-LAT data [301, 302] even reported such gamma ray excess at gamma energy of ~ 130 GeV.

Since any known astrophysical sources in the galactic centre region cannot satisfactorily explain these anomalous excesses in the photon spectrum, one invokes the possibility of annihilating dark matter to explain such excesses in which the dark matter primarily pair annihilates to fermionic states. The early analyses [174] by Dan Hooper *et al.* suggest that the gamma-ray excesses mentioned above and the morphological features of these excesses can be satisfactorily explained by considering DM particles in the mass range of $\sim 30 - 60$ GeV annihilating only through $b\bar{b}$ channel. From the latter analysis [266, 268], the authors also derived the best fit value of the dark matter mass to be $61.8^{+6.9}_{-4.9}$ GeV annihilating only into $b\bar{b}$ pair with thermally averaged annihilation cross-section $\langle\sigma v\rangle = 3.30^{+0.69}_{-0.49} \times 10^{-26}$ cm^{3}s^{-1} for explaining the above mentioned gamma ray excess. Another analysis [292] considering the dark matter to have primarily annihilated only to $\tau\bar{\tau}$, yields the dark matter mass in the range $\sim 7-10$ GeV with thermally averaged annihilation cross-section $\langle\sigma v\rangle = 5.6\times10^{-27}$ cm^{3}s^{-1}. A very recent analyses [179,303] however indicate that a DM particle with mass $\sim 31-40$ GeV and annihilating entirely into $b\bar{b}$ channel with thermally averaged annihilation cross-section $\langle\sigma v\rangle = (1.4-2.0)\times 10^{-26}$ cm^{3}s^{-1} (normalised to a local DM density of 0.3 GeV/cm^3) can provide much better agreement with the nature of the low energy gamma-ray spectrum (with an excess in the energy range $\sim 1-4$ GeV). This new analyses also disfavour the possibility of very previous proposition of $\sim$ 10 GeV DM annihilating solely into $\tau\bar{\tau}$ channels. [1] There are several attempts [175, 304–350] done for building DM models and studying various aspects. In very much recent analyses [13, 14, 336, 351] the galactic centre excess has been reanalysed considering several distinct galactic diffuse emission models and the allowed DM mass range for the generation of such galactic centre gamma ray excess is severely relaxed. The preferred mass range of DM annihilating solely to $b\bar{b}$ channel is derived to be $35-165$ GeV [336]. In Ref. [13] the Fermi-LAT galactic centre GeV excess is interpreted with DM mass allowed up to 74 GeV with $b\bar{b}$ annihilation channel. Alternative propositions other than annihilating DM explanations such as unresolved millisecond pulsars to be the main origin of this observed gamma-ray excess have been discarded since the observed anomalous gamma-ray emission extends much beyond the central stellar cluster.

Besides galactic centre, the dwarf spheroidal galaxies or dSphs also are supposed to be very rich in dark matter. These are faint companion galaxies of Milky Way. That these galaxies are dark matter rich can be conjectured from the measurement of mass to luminosity ($\frac{M}{L}$) ratios of such galaxies. These ratios are found to be much higher than $\left|\frac{M}{L}\right|_\odot$ where $\left|\frac{M}{L}\right|_\odot$ denotes the mass to luminosity ratio of the sun. Also estimation of dynamical mass from the stellar velocity measurements in these dSphs are found to outweigh the masses of the stars. Due to their enormous presence, the dark matter in dSphs can in principle undergo pair annihilation producing secondary photons. Such photons from the dwarf galaxies also could be strong indirect signature for dark matter.

[1] cosmic ray positron data also disfavour the possibility of DM annihilating into τ lepton pairs with the proposed mass of DM ($\sim$ 10 GeV) and annihilation cross-section to accommodate GeV gamma-ray excess.

With the wealth of Fermi-LAT γ-ray data, much detailed and thorough analyses [352–357] performed on several dSphs to constrain DM annihilation.

Apart from the galactic cases, the observed γ-ray signal by Fermi LAT from the extragalactic sources also may contain the signature of the dark matter annihilation at extragalactic sites [358–363]. The signal may also have embedded in it the γ-ray from other possible effects other than DM annihilation. To this end, there are attempts [15, 16, 364, 365] to extract DM signal from such extragalactic γ-ray background (EGB) and to provide limits on DM annihilation cross sections for different DM masses. This requires proper modelling of the extragalactic parameters as well as proper knowledge about the other astrophysical backgrounds that contribute dominantly to the EGB signal. With the analyses of new data collected by Fermi LAT mission, a much detailed and clear picture of EGB has been put forward. The information regarding the astrophysical sources such as BL Lacs, millisecond pulsars, star forming galaxies, radio galaxies etc. which possibly contribute to this EGB are unveiled from various observations in radio and gamma wavelengths. As Fermi LAT collects more data, one can precisely measure the EGB spectra and put stringent constraints on DM annihilation cross section. This constraints are contemporary to that obtained from dSphs and galactic centre regions and may, in principle, put limits on various DM models in future.

A number of particle physics models for the dark matter candidate has been proposed and studied in literature. They include various extensions of Standard Model [182–190, 199, 203] whose DM phenomenologies are explored at length. Amongst them, the Higgs portal models such as singlet scalar DM [191, 193–195, 271], inert Higgs doublet model (IHDM) [366, 367] and two Higgs doublet model (2HDM) [368], singlet vector DM [369–371], singlet fermionic DM [197] could be of particular interest for the present scenario in explaining the observed anomalous gamma emission by Fermi-LAT. The Higgs-portal models are interesting to study since the low mass DM candidates of these models annihilate into quark pairs with the cross-section in the right ball park of thermal production. A special feature of these types of models is that the DM candidates in these models exhibit resonance phenomena when their masses reach the value of $\sim$ half of the Higgs mass while satisfying bounds given by PLANCK experiment (relic density) and dark matter direct detection experiments.

In this work, we focus on the Inert Higgs Doublet model (IHDM), proposed by Deshpande and Ma [366] and confront the recently observed gamma-ray excesses from Galactic Centre and Fermi Bubble with the dark matter candidate in this model. We also explore the possibilities of the observation of gamma rays from 25 dwarf spheroidal galaxies by this IDM dark matter candidate. In addition, we study the extragalactic gamma ray signals obtained by Fermi-LAT with this inert Higgs doublet dark matter. In the inert Higgs doublet model or IHDM an extra scalar doublet is added to the Standard Model which is assumed to develope zero vacuum expectation value after spontaneous symmetry breaking. Imposition of a $\mathbb{Z}_2$ symmetry under which SM Lagrangian is even and the inert doublet is odd ensures the stability of dark matter particles in this IHDM scenario. The model has been extensively studied in the context of both collider and DM phenomenology [367, 372, 373, 373–390]. More recently an involved study of this model including the results of ATLAS and CMS have been performed [391]. In addition to the ATLAS and CMS results, other applicable constraints on dark matter obtained from DM direct detection experiment (LUX [219]), DM relic abundance (PLANCK data [42]), DM indirect search results (Fermi-LAT, AMS-02, PAMELA), collider data (monojet) etc. are imposed for the dark matter candidate in the framework of this model (IHDM). For the dark matter candidate in this IHDM framework (IHDM DM or lightest inert particle), reduced χ^2 analysis is performed considering all the above data and constraints and the best fit values for dark matter mass, annihilation cross-section and other parameters of the model (various coupling constants) are found out. In the present work we adopt those best fit values as the benchmark point and study the Fermi-LAT gamma-ray flux results from both galactic (galactic centre, Fermi Bubbles, dSphs) and extragalactic sources.

The present chapter is organised as follows. In Section 6.2 the theoretical framework of the IHDM is briefly described. Also the theoretical, observational and experimental constraints imposed on this model are discussed in this section. Confronting the observed gamma-ray excess from Galactic Centre in this model framework with a detailed study of the computed gamma-ray spectra is performed in Section 6.3. In Section 6.4 gamma ray flux from Fermi Bubble is discussed in the light of IHDM framework. We compare the calculated results with the bin-by-bin upper limits on photon energy spectra for various Milky Way dSphs in Section 6.5. The Section 6.6 contains the confrontation of the extragalactic γ-ray background with calculated photon spectra in IHDM considering different extragalactic parametrisations and astrophysical non-DM backgrounds.

6.2 Inert Higgs Doublet Model (IHDM) framework

Although we have previously discussed this model framewok in Section 3.3 of Chapter 3, we shall briefly furnish the model framework here for completeness.

The Inert Higgs Doublet Model is basically a very simple extension of Standard Model (SM) Higgs sector where an additional complex scalar doublet, Φ, odd under the discrete symmetry $\mathbb{Z}_2$, is considered alongwith the SM Higgs doublet, H_1. After spontaneous symmetry breaking, while the SM Higgs gets a vacuum expectation value (vev) v, the additional doublet does not acquire any vev. Thus under $\mathbb{Z}_2$ symmetry $\Phi \to -\Phi$ and $H \to H$ (even under $\mathbb{Z}_2$) and after symmetry breaking the two doublets H and Φ can be expanded as,

$$H = \begin{pmatrix} G^+ \\ \frac{1}{\sqrt{2}}\left(v + h^0 + \mathrm{i}G^0\right) \end{pmatrix}, \qquad \Phi = \begin{pmatrix} H^+ \\ \frac{1}{\sqrt{2}}\left(H^0 + \mathrm{i}A^0\right) \end{pmatrix}, \tag{6.1}$$

where $G^\pm$ and G^0 are charged and neutral Goldstone bosons respectively. Note that vev of these scalar doublet fields are $\langle H \rangle = v/\sqrt{2}$ ($v \simeq 246$ GeV) and $\langle \Phi \rangle = 0$.

With the unbroken $\mathbb{Z}_2$ symmetry the model consists of a CP-even neutral scalar H^0, a CP-odd neutral scalar A^0, and a pair of charged scalars $H^\pm$. Since the $\mathbb{Z}_2$ symmetry excludes the couplings of fermions with H^0, A^0, $H^\pm$, the decay of the latter particles to fermions are thus prevented. This ensures the stability of lightest neutral scalar (H^0 or A^0) and hence the lightest among these two can serve as a possible DM candidate. Either H^0 or A^0 is chosen as the lightest inert particle or LIP and is the candidate of dark matter in the present model.

The generalised tree-level scalar potential of IHDM consistent with imposed $\mathbb{Z}_2$ symmetry can be given as (Eq. 3.21 in Chapter 3),

$$V_0 = \mu_1^2|H|^2+\mu_2^2|\Phi|^2+\lambda_1|H|^4+\lambda_2|\Phi|^4+\lambda_3|H|^2|\Phi|^2+\lambda_4|H^\dagger\Phi|^2+\frac{\lambda_5}{2}\left[(H^\dagger\Phi)^2+\mathrm{h.c.}\right] , \tag{6.2}$$

where μ_is and λ_is denote various coupling parameters. The model has set of six parameters, namely

$$\{M_{h^0}, \;\; M_{H^0}, \;\; M_{A^0}, \;\; M_{H^\pm}, \;\; \lambda_L, \;\; \lambda_2\}\,, \tag{6.3}$$

where M_{h^0}, M_{H^0}, M_{A^0}, $M_{H^\pm}$ are the masses of Higgs h, CP-even scalar H^0, pseudoscalar A^0 and charged scalars $H^{\pm}$. λ_L and λ_S are in couplings given by,

$$\lambda_L = \frac{1}{2}(\lambda_3 + \lambda_4 + \lambda_5)\,, \tag{6.4}$$

$$\lambda_S = \frac{1}{2}(\lambda_3 + \lambda_4 - \lambda_5)\,. \tag{6.5}$$

The parameters λ_L denotes the coupling strength for $H^0 H^0 h^0$ (if H^0 is considered to be the lightest inert particle or LIP) while λ_S is for $A^0 A^0 h^0$ (if A^0 is the LIP) interaction. In the tree-level processes, the self-quartic coupling λ_2 does not contribute to the observables.

A detailed study of this model had been done in Ref. [391] where the authors made use of the various constraints available from DM experiments and other results and made a χ^2 analysis with the IHDM theory of the dark matter mentioned above. From these analyses they provide the best fit values of the quantities M_{h^0}, $M_{H^\pm}$, M_{H^0}, M_{A^0} and the parameters λ_L, λ_2. The experimental and theoretical constraints that they have used for the analysis are summarised below.

1. The perturbative calculations require all the quartic couplings of scalar potential, Eq. 6.2 to be $|\lambda_i| < 8\pi$

2. The potential in Eq. 6.2 should satisfy vacuum stability condition (potential should be bounded from below and should have a stable and global minimum) given by [368]

$$\lambda_{1,2} > 0 \quad \text{and} \quad \lambda_3 + \lambda_4 - |\lambda_5| + 2\sqrt{\lambda_1 \lambda_2} > 0 \quad \text{and} \quad \lambda_3 + 2\sqrt{\lambda_1 \lambda_2} > 0\,. \tag{6.6}$$

3. The coupling parameters of the scalar potential in Eq. 6.2 should satisfy the unitarity

conditions given by the constraints [385]

$$\lambda_3 \pm \lambda_4 < 8\pi \quad , \quad \lambda_3 \pm \lambda_5 < 8\pi \quad , \tag{6.7}$$

$$\lambda_3 + 2\lambda_4 \pm 3\lambda_5 < 8\pi \quad , \quad -\lambda_1 - \lambda_2 \pm \sqrt{(\lambda_1 - \lambda_2)^2 + \lambda_4^2} < 8\pi \quad , \tag{6.8}$$

$$-3\lambda_1 - 3\lambda_2 \pm \sqrt{9(\lambda_1 - \lambda_2)^2 + (2\lambda_3 + \lambda_4)^2} < 8\pi \quad , \tag{6.9}$$

$$-\lambda_1 - \lambda_2 \pm \sqrt{(\lambda_1 - \lambda_2)^2 + \lambda_5^2} < 8\pi \quad . \tag{6.10}$$

4. The theory for the IHDM model should respect the LEP I measurements of the decay width of Z boson giving rise to the constraints $M_{H^0} + M_{A^0} \geq M_Z$ and $2M_{H^\pm} \geq M_Z$ [392]. Also from LEP II data the constraint $\max(M_{H^0}, M_{A^0}) \geq 100$ GeV [388] is used in their analysis.

5. The new physics model IHDM can affect the electroweak precision test (EWPT) parameters or the oblique parameters S, T, U that constrain the physics beyond the Standard Model. After keeping the oblique parameter U fixed at zero, the central values of the other oblique parameters S and T, taking the SM Higgs boson mass $\sim$ 126 GeV, are given by [393]

$$S = 0.05 \pm 0.09 \ , \quad T = 0.08 \pm 0.07 \ . \tag{6.11}$$

6. The recent measurement of the mass of SM Higgs-like particle in ATLAS and CMS data is used as the constraint in the proposed IHDM theory and is included in their analysis. The experimentally measured value of the SM Higgs value [394, 395] is adopted to be

$$m_{h^0} = 125.8 \pm 0.6 \ \text{ GeV} \ . \tag{6.12}$$

7. Constraints [275, 279, 396–398] are also used from the LHC bound on the invisible

(non-standard) decay of SM Higgs. The bound on invisible branching ratio of Higgs boson is that it should not exceed 19% at 95% CL. The ratio can reach at most 29% (95% CL) if other possible deviations ($h^0\gamma\gamma$, h^0gg loop contributions) are taken into account. This is also taken as a constraint in the analysis of Ref. [275].

8. The signal strength of diphoton production from the decay of Higgs boson is measured at 95% CL to be $1.14^{+0.26}_{-0.23}$ [399] by CMS and 1.17 ± 0.27 [400] by ATLAS respectively. This signal strength for the IHDM theory can be represented as

$$R_{\gamma\gamma} \equiv \frac{\sigma(gg \to h^0) \times \mathrm{BR}(h^0 \to \gamma\gamma)}{\sigma(gg \to h^0)^{\mathrm{SM}} \times \mathrm{BR}(h^0 \to \gamma\gamma)^{\mathrm{SM}}} \ . \tag{6.13}$$

The measured value of $R_{\gamma\gamma}$ are also considered in the analysis.

9. In Ref. [391] the analysis also includes the LHC monojet searches where a DM production at the collider may be detected from the large missing transverse energy of the DM particles that escape the detector producing SM jet.

10. The relic abundance of Dark Matter as given by the PLANCK experiment [42] ($\Omega_{\mathrm{DM}} = 0.1199 \pm 0.0027$) is used as a constraint.

11. Various dark matter direct detection experiments put strong constraints on the scattering cross-sections for different values of Dark Matter mass. The latest stringent limit on the spin-independent (SI) scattering cross-sections for LUX direct detection experiment [121] is used as constraints in their analysis. In IHDM theory, the DM scattering cross-section depends on the coupling parameters λ_L (or λ_S).

12. In their analysis they also ensured that the limits on continuum galactic gamma rays from Fermi-LAT data are not exceeded.

13. The evidence of the excess of positrons at higher energetic portion of the cosmic ray has been confirmed by PAMELA satellite [221] and recently by AMS-02 [401]. Also

the excess in the flux of electron and positron has been probed by different satellite, namely ATIC [226], HESS [402], Fermi LAT [403], MAGIC [404] etc. confirming the fact that there is the existence of extra astrophysical sources such as pulsars, supernova remnants or DM. It has been shown that the existence of pulsars is more or less sufficient explaining the electron and positron excess fluxes. The electron and positron fluxes from annihilation of DM in this model work as extra components other than that from pulsars. The computed sum total electron and positron excess should not supersede the measured fluxes. Hence this model is constrained from cosmic ray e^+e^- excess.

14. The anti-proton flux or its excess as measured by PAMELA [405] plays an important role in severely constraining the DM in this framework since the model for cosmic ray background can explain the observed anti-proton excess. This is included in the analysis of Ref. [391].

Table 6.1: Benchmark Point : IHDM Parameters

Model	M_{h^0} (GeV)	$M_{H^\pm}$ (GeV)	M_{H^0} (GeV)	M_{A^0} (GeV)	λ_L	λ_2
Parameters	126.016	73.78	63.54	166.16	-3.29×10^{-3}	5.67×10^{-4}

In Ref. [391] the detailed χ^2 analysis of the IHDM parameters using only DM relic density and collider constraints results DM with mass of 70.37 GeV. When the DM direct detection bounds are taken into the calculation, the value of χ^2-minimised DM mass reduces to 69.04 GeV. The value of χ^2-minimised DM mass further reduces to 63.54 GeV when the limits of DM indirect detection are included into the study. Considering all the constraints (DM relic density, collider constraints, DM direct detection and DM indirect detection) discussed above, a best-fit parameter point in IHDM framework is obtained [391]. Using the values tabulated in Table 6.1, we first compute the relic density for the IHDM dark matter candidate of mass 63.54 GeV after calculating the annihilation cross-section $\langle \sigma v \rangle$. The calculated annihilation cross-section satisfies the observed results by PLANCK experiment. We also calculate the spin independent scattering cross-section to verify that it agrees with the limits given by the dark matter direct detection experiments. The results are tabulated in Table 6.2.

Table 6.2: Benchmark Point : Observables

DM Observables	Ωh^2		$\langle\sigma v\rangle$ (cm^{3}s^{-1})		$\sigma_{\rm SI}$ (pb)	
	0.1173		2.37×10^{-26}		8.89×10^{-11}	
Annihilation Cross-section	$H^0H^0 \to b\bar{b}$	$H^0H^0 \to W^+W^-$	$H^0H^0 \to gg$	$H^0H^0 \to l\bar{l}$	$H^0H^0 \to c\bar{c}$	$H^0H^0 \to ZZ$
	69.2%	9.61%	9.49%	7.37%	3.29%	0.48%

6.3 Confronting Gamma Ray flux from Galactic Centre in this framework

It has been discussed earlier [168, 286] that the observed low energy gamma ray excess (bump) from the region of the galactic centre by Fermi Gamma-ray Space Telescope could have been caused by the self annihilation of low mass ($\sim$ 10 GeV) dark matter at the galactic centre region. Other propositions [290] like unresolved excess from millisecond pulsars in the galactic region are discarded [174, 177, 178, 292] as an explanation to this observed bump of photon flux at the low energy domain. In our work, we address the gamma-ray flux from self-annihilation of DM where the particle candidate for dark matter is LIP in the IHDM framework.

The differential gamma-ray flux due to the annihilating DM coming from the galactic DM halo per unit solid angle can be written as [141],

$$\frac{d\Phi_\gamma}{d\Omega dE_\gamma} = \frac{1}{8\pi\alpha}\sum_f \frac{\langle\sigma v\rangle_f}{M^2_{H^0,A^0}}\frac{dN^f_\gamma}{dE_\gamma} r_\odot \rho^2_\odot J \ , \tag{6.14}$$

where m_{H^0} is the mass of DM candidate H^0, $\alpha = 1$ (or 2) is for self-conjugated (or non self-conjugated) DM case. Since the DM particle H^0 in IHDM is self-conjectured, the value of α is taken to be 1. In the above $\frac{dN_\gamma^f}{dE_\gamma}$ and $\langle \sigma v \rangle_f$ are the photon-energy spectrum produced in a single annihilation channel of DM with final pair $f\bar{f}$ and velocity-averaged annihilation cross-section of DM for this particular channel respectively. In Eq. 6.14, $r_\odot$ and $\rho_\odot$ are the distance of the solar system from the galactic centre and the local DM halo density respectively. The factor J in Eq. 6.14 can be expressed as,

$$J = \int_{l.o.s} \frac{ds}{r_\odot} \left(\frac{\rho(r)}{\rho_\odot} \right)^2 \tag{6.15}$$

with r being the radial distance of the site of DM annihilation at galactic centre neighbourhood from the galactic centre and can be expressed in terms of line of sight, s as,

$$r = \begin{cases} \left(s^2 + r_\odot^2 - 2sr_\odot \cos l \cos b\right)^{1/2} & \text{(galactic } l, b \text{ coordinate)} \\ \left(s^2 + r_\odot^2 - 2sr_\odot \cos\theta\right)^{1/2} & \text{(galactic } r, \theta \text{ coordinate)} \end{cases} \tag{6.16}$$

In the above $\rho(r)$ is the DM halo profile and for a generalised NFW DM halo the analytical expression can be given [150, 151] as,

$$\rho(r) = \frac{\rho_0}{(r/r_c)^\gamma [1 + (r/r_c)^\gamma]^{(3.0-\gamma)}} \ , \tag{6.17}$$

with ρ_0 being the local DM halo density at the solar location ($\rho(r_\odot)$, $r_\odot$ (~ 8 kpc) is the distance of sun from GC) chosen to be ~ 0.3 GeV/cm^3. In the above relation, the values of the parameters r_c and γ are taken to be 20 kpc and 1.26 respectively in the present calculation following Ref. [179]. We use `micrOMEGAs` [98, 218] code to compute various DM observables in this model.

The chosen dark matter candidate, LIP, of mass 63.54 GeV (Table 6.1) can primarily annihilate via Higgs to the pairs of $b\bar{b}$, W^+W^-, gg, $l\bar{l}$, $c\bar{c}$, ZZ, $s\bar{s}$, $\gamma\gamma$ etc. Out of these channels the secondary photons produced from primary $b\bar{b}$ is worth considered for

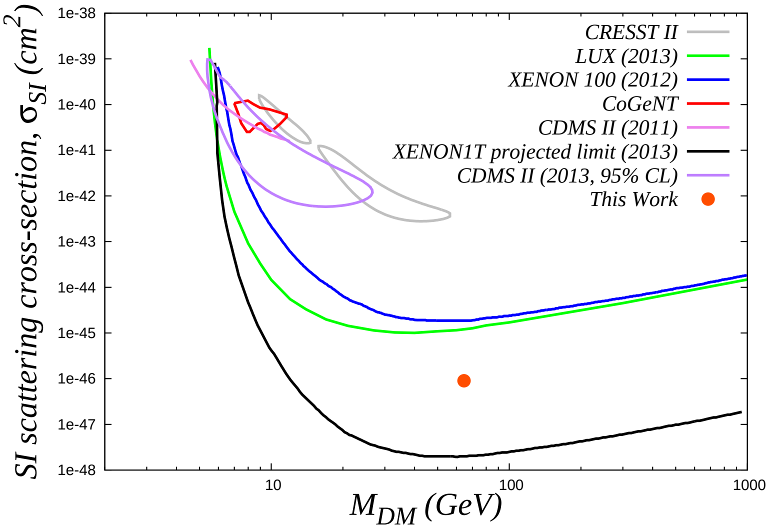

Figure 6.1: *Various DM direct detection experimental bounds on the benchmark point of Table 6.1. See text for details.*

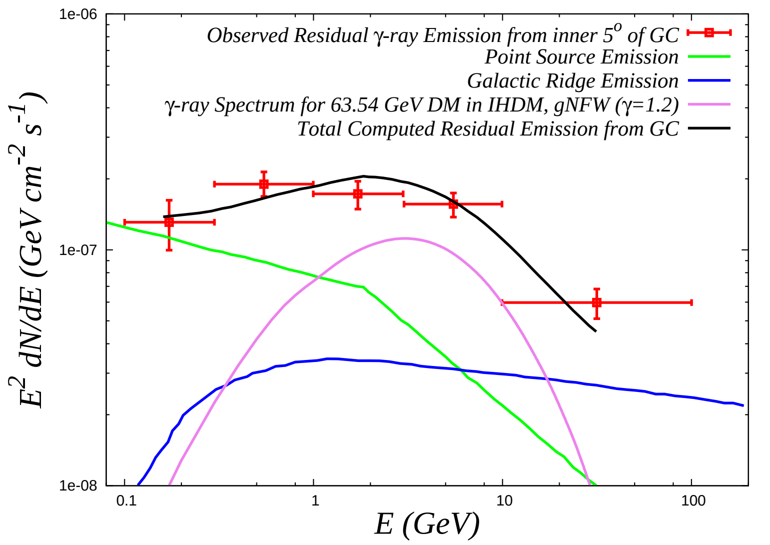

Figure 6.2: *Residual GeV gamma-ray flux from the inner 5^o surrounding the galactic centre. See text for details.*

explaining the continuum gamma ray spectrum [179]. The calculated branching ratio for the channel LIP LIP $\rightarrow b\bar{b}$ is found to be 69.2%. The branching ratios for other annihilation channels in case of LIP dark matter in the present IHDM are also computed and they are tabulated in Table 6.2. The DM candidate in this model obtained along with the particular set of parameters of the model (Table 6.1) are found to be compatible with the recently observed $\sim$ 125-126 GeV CP-even Higgs ($J^P = 0^+$). Since the DM mass is close to half of the SM Higgs ($\sim m_h/2$), we will have resonance effect in obtaining the required cross-section (2.37×10^{-26} cm^{3}s^{-1}) with $b\bar{b}$ as dominant channel for the typical thermal production of DM. Also DM-nucleon scattering cross-section for the chosen benchmark point in this model is about 8.89×10^{-11} pb (averaged value per nucleon for interaction with Xe nucleus) which is just under the the present bounds for XENON 100 and LUX experiments. This is shown in Fig. 6.1. The future DM direct searches like XENON1T [406] can easily probe this point as seen from Fig. 6.1.

The Fermi LAT data for gamma-ray flux from the inner 5^o surrounding the Galactic Centre has been studied in Ref. [292]. This region of GC is astrophysically very rich and contains various astrophysical components which may contribute to the observed γ-ray flux. The known sources in this region can be found in (extracted from) Fermi Second Source Catalog [287]. Although Fermi Third Source Catalog (3FGL) has recently been made available [288], but no analysis of the background or analysis for γ-ray from other known processes at the region of interest has been reported yet. Also cosmic ray interaction with gas distributed in this galactic region produces neutral pions that subsequently decay to produce enormous amount of γ-ray. This is a viable mechanism for known disc template emission. Now, the spectral and morphological feature of the photon flux from inner 5^o subtending the GC after subtracting the contribution from both the known sources of Fermi Second Source Catalog and disc template emission shows a 'bumpy' nature, i.e., the photon count is higher for γ-ray energy ranging from $\sim$ 300 MeV to $\sim$ 10 GeV. The count drops significantly after 10 GeV of γ-ray energy. Also the spectrum of this residual emission suggests that the lower energetic portion of this emission spectrum may be originated from some point-like sources whereas the high-energetic tail of the spectrum is well explained with the galactic ridge emission data. The interaction of energetic cosmic ray nuclei with molecular cloud present in the galactic ridge which

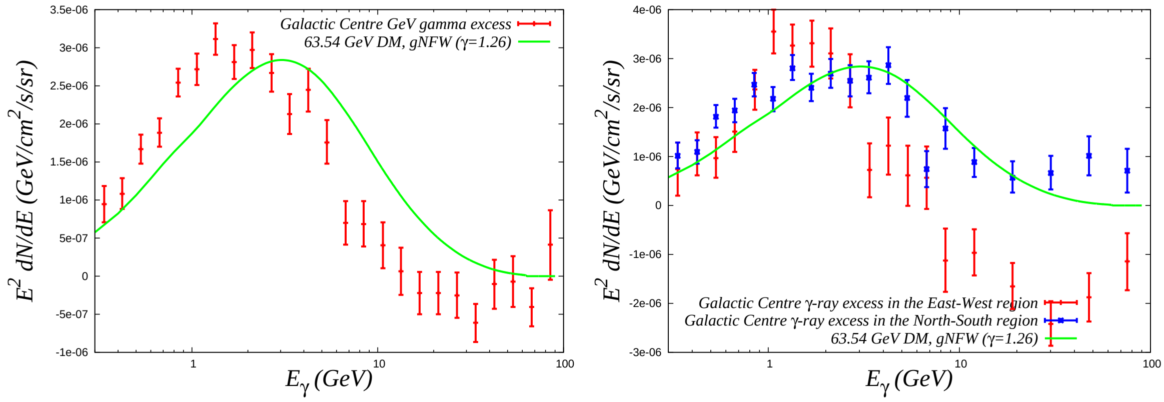

Figure 6.3: *Comparison of observed $\sim 1-3$ GeV gamma-ray excess at galactic centre with the calculated gamma ray flux for low mass DM in IHDM (adopted from Table 6.1) is shown in the left panel. The red points denote the analysed data points in the left panel. In the right panel the galactic centre gamma ray excess from galactic 'North-South' region ($|b| < |\ell|$, shown by red data points) and galactic 'East-West' region ($|b| > |\ell|$, shown by blue data points) around the galactic centre. The computed photon spectra in IHDM framework are shown by green lines in both plots. See text for detailed discussion.*

extends up to a width of 5^o galactic latitude and $\pm 40^o$ galactic longitude, yields neutral pions and then gamma ray. However, the middle portion of the spectrum cannot be well explained by point source or ridge emission and requires the presence of some spatially extended objects or DM halo.

We have computed the γ-ray spectrum from inner 5^o subtending the GC from DM annihilation within the present framework of inert Higgs doublet model for dark matter particle. The chosen benchmark points for the parameters of the model such as dark matter mass, coupling constants etc. are given in Table 6.1. The flux have been computed for the generalised NFW DM halo profile. Also included in the calculation are the contributions from both point source and galactic ridge emission. The total calculated flux is then compared with the observed residual photon flux and the results are shown in Fig. 6.2. In Fig. 6.2, the green-coloured and blue-coloured lines represent the fluxes for point source and galactic ridge emission respectively. The γ-ray spectrum for DM annihilation for the benchmark points mentioned above, are shown in purple line whereas the black line is for the total γ-ray flux obtained by summing over all the fluxes represented by green, blue and purple coloured lines in Fig. 6.2. For these calculations we have adopted the generalised NFW (gNFW) halo profile with $\gamma = 1.26$. The total flux (black line) is then compared with the observed residual emission data. These observed data are denoted by red-coloured points in this figure. It is clear from Fig. 6.2 that our computation of total residual gamma emission (black line) agrees satisfactorily with the observational results.

In a recent analysis of γ-ray flux from GC region where the analysis is only for the GC gamma ray (subtracting all possible contributions from other known astrophysical sources), [179] an excess of gamma ray in the gamma energy region of $\sim 1 - 3$ GeV has been reported. This excess is shown in the left panel of Fig. 6.3 with the red-coloured points. It is suggested in the same analysis that in order to explain this anomalous gamma ray excess from dark matter annihilation scenario, the DM mass should be in the range of 31-40 GeV which is to annihilate purely into $b\bar{b}$ pair. We calculated these gamma ray fluxes in our framework of inert Higgs doublet dark matter for the dark matter mass of 63.54 GeV (adopted from Table 6.1 (benchmark point)) and compared our results with the analysed data points mentioned above (red coloured points shown in the left panel of Fig 6.3). In the left window of Fig. 6.3, the green coloured line represents the present calculation. These calculations are performed considering gNFW halo profile with the halo parameter $\gamma = 1.26$. It is to be noted from the left panel of Fig. 6.3 that although the morphological feature of the spectrum from our calculation (green line) is similar in nature to that obtained from the analysis of Fermi-LAT observational data (red-coloured points) from GC, the position of the maxima of excess gamma ray in our calculation is shifted to somewhat higher energy at ~ 3.1 GeV instead of being within the expected energy range of $\sim 1 - 3$ GeV as obtained from the Fermi-LAT data.

We mention again at this point that the choice of our IHDM dark matter mass (63.54 GeV) has been made from the reduced χ^2 analysis with various theoretical and experimental constraints for IHDM dark matter particle candidate as given in Ref. [391]. In the left panel of Fig. 6.3, we demonstrate that the excess gamma ray spectrum due to annihilation of IHDM dark matter with mass 63.54 GeV suffers a shift from that obtained from the experimental observation. However the calculated position of the peak (green line) is at $\sim 2.84 \times 10^{-6}$ GeV/cm^2/s/sr which is in the same ballpark of the observed peak (red points).

It may be recalled that the analysis given in Ref. [179] suggested a dark matter mass in this range annihilating to $b\bar{b}$ for explaining the anomalous gamma excess shown in the left panel of Fig. 6.3. One may obtain in the present IHDM framework, a dark matter candidate with mass in the range of 30-40 GeV which satisfies the Planck bound on relic density and the bounds obtained from recent dark matter experiments. But the parameter space for such a choice does not agree with the constraints such as invisible Higgs decay as obtained from LHC experiment.

More detailed analysis of the observed γ-ray excess reveals [179] a further anomaly between the gamma ray spectra for the gamma rays from galactic East-West region and from galactic North-South region. The North-South region is designated as $|b| < |\ell|$, where b and ℓ are the galactic latitude and longitude respectively and for the East-West region, $|b| > |\ell|$. The two spectra are shown in the right panel of Fig. 6.3. The red coloured points are for gamma spectrum from galactic East-West region while the blue coloured points represent the spectrum from North-South region. As can be seen from the right panel of Fig. 6.3, the gamma flux from the present calculation (shown by green line in the right panel of Fig. 6.3) agrees more satisfactorily with the "North-South" gamma emission spectrum than the "East-West" spectrum.

Although the galactic centre γ-ray excess is statistically significant, it depends on the choice of diffuse background model that characterises the diffuse emission over the entire sky. But for the galactic centre, it is very hard to get best suited model. The systematic uncertainty on the background model provided by the Fermi-LAT is very large compared to the statistical uncertainty. Attempts [13, 14] are made to quantify such systematics for galactic central region. We confront the flux obtained for our IHDM benchmark scenario (Table 6.1) using these two complementary approaches. Since the dark matter distribution near the galactic centre is very uncertain, the proper estimation of the form of J-factor of Eq. 6.15 is also very tough to obtain. We adopt the proposed method of Ref. [336] for this uncertainty estimation. The uncertainty in the halo profile may arise from the two factors, namely from the factor of dark matter distribution profile γ and local dark matter density $\rho_\odot$ at a distance $r = r_\odot = 8.5$ kpc. Since $\gamma = 1.2 \pm 0.1$ for different galactic diffuse emission models and $\rho_\odot = 0.4 \pm 0.2$ GeV/cm^3 for different normalisation of halo, these can introduce uncertainty in the astrophysical J-factor. To parametrised the uncertainty in the J-factor the following quantity is used,

$$\bar{J} = \frac{1}{\Delta\Omega} \int_{\Delta\Omega} J(\psi) d\Omega \equiv \mathbb{J} \times \bar{J}_{\rm canonical} \,, \tag{6.18}$$

where $\bar{J}_{\rm canonical}$ is the central value of $\bar{J}$. In the above $\Delta\Omega$ is the region of interest (ROI) for a given analysis. The astrophysical factor $J(\psi)$ is same as that in Eq. 6.15. The factor $\mathbb{J}$ signifies the deviation from the canonical halo profile due to the uncertainties of the profile.

In Ref. [13] the authors thoroughly analyse Fermi-LAT data in the inner galaxy region over the photon energy ranging from 300 MeV – 500 GeV. The chosen ROI in Ref [13] is extended to a $20^\circ \times 20^\circ$ ($-20^\circ < \ell < 20^\circ$, $-20^\circ < b < 20^\circ$) square region surrounding the galactic centre with the inner galactic latitude of 2° ($|b| < 2^\circ$) being masked out. For the canonical halo profile $r_\odot = 8.5$ kpc, $\rho_\odot = 0.4$ GeV/cm^3, $r_c = 20$ kpc and $\gamma = 1.20$ which yield the value of $\bar{J}_{\rm canonical} = 2.0 \times 10^{23}$ GeV^2 cm^{-5}. By studying a large number (60) of background models for galactic diffuse emission and the correlations in the γ-ray

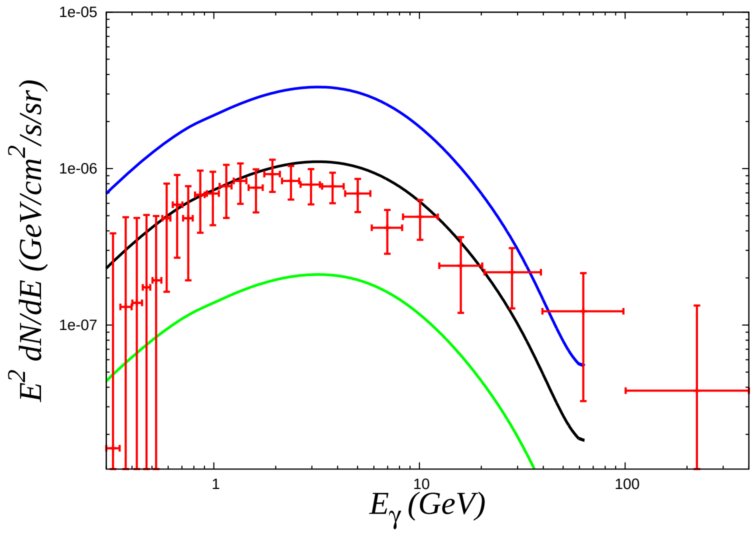

Figure 6.4: *The computed γ-ray spectrum in this work is compared with the observed residual γ-ray spectrum obtained for the best-fit galactic diffuse emission model of Ref. [13] by studying $|\ell| < 20°$, $2° < |b| < 20°$ subtending the galactic centre. The red points denote the analysed residual spectrum reported in Ref. [13]. The blue and green lines are the calculated spectra using maximum and minimum values of deviations from the canonical J-factor whereas the black line is for canonical J-factor. See text for details.*

spectrum along the galactic disk containing very faint signal, the residual emission signal and the systematics uncertainties are extracted. The uncertainty in the $\bar{J}$ factor produces $\mathbb{J} \in [0.19, 3]$ in their analysis.

To have an estimation of the galactic γ-ray excess from the annihilation of dark matter in such parametrisation, we consider the LIP dark matter in IHDM framework and study the photon spectrum produced from its annihilation. Plugging in all of the canonical parameters for the dark matter halo model, we compute the canonical γ-ray flux obtained from annihilation channels of 63.54 GeV LIP DM (adopted from Table 6.2 (benchmark point)). The resulting plot is shown in Fig. 6.4 by black coloured line. The red coloured points denote the residual spectrum of γ-ray excess in the galactic centre with highly correlated errors obtained from Ref. [13]. We also consider the cases taking the uncertainties $\mathbb{J} \in [0.19, 3]$ in the $\bar{J}$ factor. The blue and the green coloured lines in Fig. 6.4 denote the galactic γ-ray flux from 63.54 GeV DM annihilation for the maximum value of the uncer-

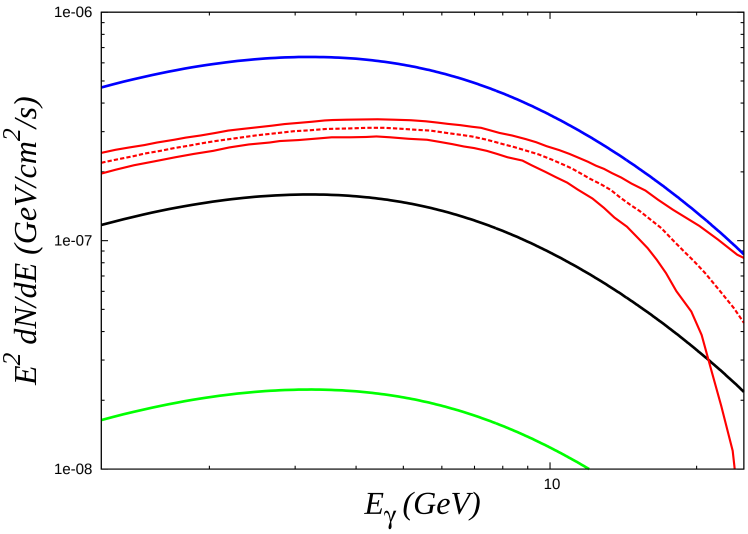

Figure 6.5: *The computed γ-ray spectrum in this work is compared with one of the four observed residual γ-ray spectra obtained using distinct galactic diffuse emission models of Ref. [14] by studying $15° \times 15°$ region surrounding the galactic centre. Notations used here are same as those in Fig. 6.4. See text for details.*

tainty $\mathbb{J}_{\rm max} \sim 3.0$ and the minimum value of the uncertainty $\mathbb{J}_{\rm min} \sim 0.19$ respectively. We can conclude from Fig. 6.4 that the uncertainty factor $\mathbb{J}$ needs to be smaller than unity to have a better fit to the data for 63.54 GeV LIP dark matter.

On the other hand, recently the Fermi collaboration [14] has also studied the region surrounding the galactic centre using different background models of galactic diffuse emission. The fit to the galactic centre γ-ray data is observed to improve very significantly when an additional contribution similar to that from dark matter annihilation is added. To perform the analysis the Fermi collaboration has chosen a different region $(15° \times 15°)$ surrounding the galactic centre smaller than that chosen by Ref. [13]. However the galactic centre is not masked out in the analysis of Fermi unlike that done Ref. [13]. Based on their preliminary analysis the Fermi collaboration has reported four best fit γ-ray spectra for the four distinct choices of background models for galactic diffuse emission. The nature of these four best fit γ-ray spectra differ notably after a few GeV photon energy. The obtained γ-ray spectra is found to yield much more conservative measurement of the systematic uncertainty. Although the Fermi has analysed the data using NFW halo profiles with slope values of 1.0 and 1.2, Ref. [336] has chosen a more conservative approach on γ factor and set it to 1.2 ± 0.1. Also the value of $\rho_\odot$ is chosen to be 0.4 ± 0.2 GeV/cm^3. Keeping the parameters of the J-factor fixed, one would obtain $\bar{J}_{\text{canonical}} = 1.58 \times 10^{24}$ GeV^2 cm^{-5}. The uncertainty in the $\bar{J}$ factor as obtained from such parametrisation is $\mathbb{J} \in [0.14, 4.0]$ for the Fermi analysis.

We also make an estimation of the galactic γ-ray excess from the annihilation of 63.54 GeV LIP dark matter (Table 6.1) in IHDM and confront the results with the γ-ray spectra obtained by Fermi collaboration. We make the comparison of the calculated spectrum with that reported by Fermi after preliminary analysis and show it in Fig. 6.5. The black line the photon flux obtained using the canonical parametrisation of the halo profile ($\mathbb{J} = 1$). The blue and the green coloured lines in Fig. 6.5 represent the calculated galactic γ-ray flux from the annihilation of 63.54 GeV DM for the maximum uncertainty $\mathbb{J}_{\text{max}} \sim 4.0$ and the minimum uncertainty $\mathbb{J}_{\text{min}} \sim 0.14$ respectively. The red coloured line denote the upper and the lower limits of the photon flux from the galactic centre as provided by Fermi in one of the four obtained spectra. [2] We can draw a conclusion from Fig. 6.5 that unlike the previous case the uncertainty factor $\mathbb{J}$ should be more than unity to provide a better fit to the data for the considered IHDM benchmark point.

[2]Out of the four spectra given by the preliminary analysis of Fermi, we choose only a particular spectrum which provides the best fittings for dark matters with low masses since our interest in this work is on the low mass region in IHDM.

6.4 Confronting Residual Gamma Ray from Fermi Bubbles in this framework

The Fermi Bubbles [265, 300] are two gamma-ray emitting bubbles that originate from the GC and extends up to $\sim 50^o$ ($\sim$ 10 kpc) in the form of two lobes on each side of the galactic plane in the direction perpendicular to the galactic plane. Fermi-LAT observations reveal that the Fermi bubbles also emit γ-ray with energy spanning from $\sim$ few GeV to $\sim$ few 100 GeV. The other satellite based experiments like ROSAT [297] and PLANCK [296] suggest that the emission is strongly correlated with the extension of non-thermal, microwave WMAP haze emission [294, 295]. The γ-ray flux from the higher galactic latitude of the bubble can be well explained by the ICS or inverse Compton scattering mechanism of the high-energetic electrons present in the bubble. But the photon emission spectra from the lower galactic latitude which is very close to galactic centre region show reasonable deviation from the projected flux from ICS of the distributed electrons. The observational results for such gamma ray emissions from different zones (galactic latitude) of Fermi bubble are shown as red points (with error bars) in Fig. 6.6.

The observational data are available [268] for each of the five different regions of the bubble designated by the galactic latitudes $|b| = 1^o - 10^o, 10^o - 20^o, 20^o - 30^o, 30^o - 40^o, 40^o - 50^o$. This excess in γ-ray (in the region upto $|b| \sim 30^{\rm o}$) spectra near the galactic plane does not exhibit any power law dependence which is one of the key features of the spectra produced in ICS mechanism. This is also observed from the data (Fig. 6.6) that the excess in gamma spectra from the lobes of the bubble gradually declines as one moves from the lower to higher latitude regions of the bubble. For latitudes $|b| > 30^{\rm o}$, the feature of the spectra show almost no anomalous excess. A possible explanation for such an emission from inner latitudes of Fermi bubble could well be due to the annihilation of DM. That no significant excess is observed from higher latitude region of the bubble may be attributed to the fact that as one moves away from the GC, the dark matter density falls off as a result of which the annihilation of dark matter cannot produce observable excess of gamma emission.

We compute the gamma ray spectra from such Fermi bubble due to the annihilation of inert doublet dark matter within the present framework. The calculation of gamma ray flux is performed for each of the five different regions of the bubble designated by five different ranges of galactic latitudes mentioned above for the observational data. The calculated gamma fluxes for all those five zones of the Fermi bubble are then compared with the observational results and are shown in Fig. 6.6. It can be seen from Fig. 6.6 that the calculated flux shows an excess in the similar region obtained from the observational results for the zones $|b| = 1^o - 10^o, 10^o - 20^o, 20^o - 30^o$. For the rest of two zones, the observational data do not exhibit any excess feature. However, the peak values of the calculated flux are in the same ball park of the peak values of the observational data. But certainly the shapes of the calculated spectra are not similar for those of observation in the high latitude regions.

6.5 Confronting Gamma-ray flux from Dwarf Spheroidal Galaxies in this framework

One of the most promising targets for the search of dark matter via indirect detection (γ-ray) is the dwarf spheroidal galaxies (dSphs) of the Milky Way. The dSphs are considered to be promising for the study of DM phenomenology because of their proximity, low astrophysical background and huge amount of DM content. In Section 2.5 of Chapter 2, we have already discussed in detail about the dsph as a potentially suitable target for the indirect search of dark matter.

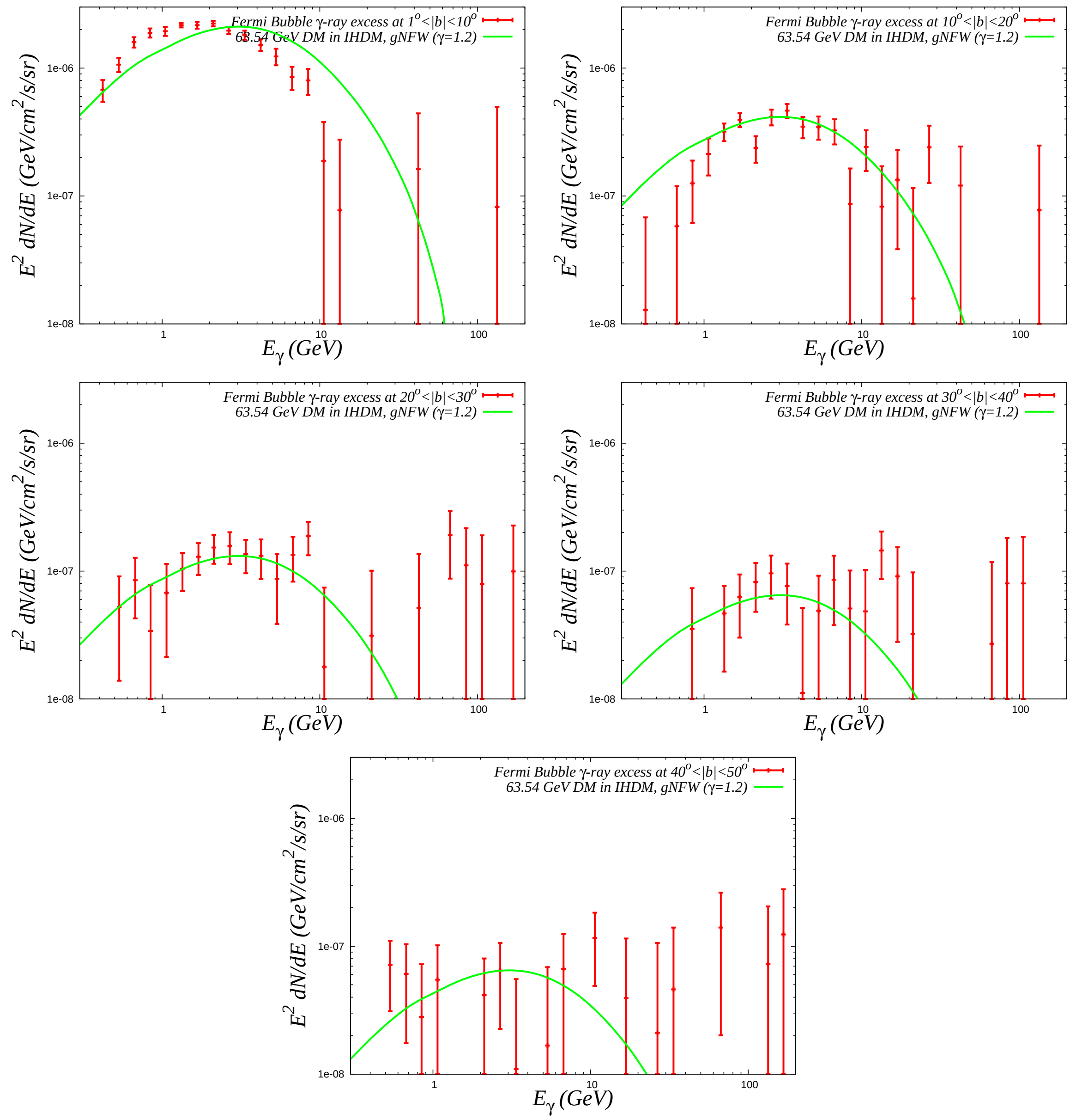

Figure 6.6: *Comparison of the computed photon flux for the low mass DM in IHDM (Table 6.1) with the residual gamma ray emission from five different zones of Fermi Bubble, namely regions with galactic latitudes $|b| = 1^o - 10^o, 10^o - 20^o, 20^o - 30^o, 30^o - 40^o, 40^o - 50^o$. The red points represent the observed spectra after subtracting the contribution from inverse Compton scattering of high energy electrons. The blue line is the contribution from DM annihilation in IHDM. See text for more details.*

The satellite-bourne gamma-ray experiment, Fermi-LAT, from the starting of its data collection have searched for the γ-ray sky in the energy range spanning from ~ 20 MeV to more than 300 GeV [263]. In an early analysis Abdo *et al.* [352] have considered 11-

Table 6.3: Limits on DM annihilation cross-section from γ-ray flux limits for various dwarf spheroidal galaxies for the benchmark DM mass of Table 6.1

dSphs name	longitude l (deg)	latitude b (deg)	distance (kpc)	$\overline{log_{10}(\mathrm{J}^{\mathrm{NFW}})}$ (log_{10}[GeV^{2}cm^{-5}sr])	$\overline{log_{10}(\alpha_s^{\mathrm{NFW}})}$ (log_{10}[deg])	upper limit on $\langle\sigma v\rangle$ (cm^{3}s^{-1})
Bootes I [407]	358.1	69.6	66	18.8 ± 0.22	-0.6 ± 0.3	2.33×10^{-24}
Bootes II	353.7	68.9	42	–	–	–
Bootes III	35.4	75.4	47	–	–	–
Canes Venatici I [408]	74.3	79.8	218	17.7 ± 0.26	-1.3 ± 0.2	9.65×10^{-25}
Canes Venatici II [408]	113.6	82.7	160	17.9 ± 0.25	-1.1 ± 0.4	8.14×10^{-25}
Canis Major [409]	240.0	-8.0	7	–	–	–
Carina [408]	260.1	-22.2	105	18.1 ± 0.23	-1.0 ± 0.3	2.28×10^{-25}
Coma Berenices [408]	241.9	83.6	44	19.0 ± 0.25	-0.6 ± 0.5	1.11×10^{-24}
Draco [410]	86.4	34.7	76	18.8 ± 0.16	-0.6 ± 0.2	3.87×10^{-25}
Fornax [409]	237.1	-65.7	147	18.2 ± 0.21	-0.8 ± 0.2	2.53×10^{-25}
Hercules [408]	28.7	36.9	132	18.1 ± 0.25	-1.1 ± 0.4	9.97×10^{-26}
Leo I [411]	226.0	49.1	254	17.7 ± 0.18	-1.1 ± 0.3	4.37×10^{-25}
Leo II [412]	220.2	67.2	233	17.6 ± 0.18	-1.1 ± 0.5	3.88×10^{-25}
Leo IV [408]	265.4	56.5	154	17.9 ± 0.28	-1.1 ± 0.4	3.72×10^{-24}
Leo V	261.9	58.5	178	–	–	–
Pisces II	79.2	-47.1	182	–	–	–
Sagittarius	5.6	-14.2	26	–	–	–
Sculptor [409]	287.5	-83.2	86	18.6 ± 0.18	-0.6 ± 0.3	3.41×10^{-24}
Segue 1 [413]	220.5	50.4	23	19.5 ± 0.29	-0.4 ± 0.5	1.16×10^{-24}
Segue 2	149.4	-38.1	35	–	–	–
Sextans [409]	243.5	42.3	86	18.4 ± 0.27	-0.9 ± 0.2	1.14×10^{-25}
Ursa Major I [408]	159.4	54.4	97	18.3 ± 0.24	-1.0 ± 0.3	1.64×10^{-25}
Ursa Major II [408]	152.5	37.4	32	19.3 ± 0.28	-0.5 ± 0.4	1.33×10^{-24}
Ursa Minor [410]	105.0	44.8	76	18.8 ± 0.19	-0.5 ± 0.2	6.54×10^{-24}
Willman 1 [414]	158.6	56.8	38	19.1 ± 0.31	-0.6 ± 0.5	4.03×10^{-24}

month Fermi-LAT observational data for eight individual dSphs and put a limit on the DM annihilation cross section considering that the only source of observed γ-ray comes from DM annihilation. Subsequently Ackermann *et al.* [353] have performed a more elaborate analysis by taking ten such dSphs using Fermi-LAT observational data on dSphs for 2 years with more improved sensitivity. The latter analysis conclude that in order to explain the observed γ-ray from dSphs galaxies, one needs to have DM particle annihilating to $b\bar{b}$ and $\tau\bar{\tau}$ pairs with mass $\leq$ 30 GeV with the canonical annihilation cross-section value needed for obtaining thermal DM relic abundance. Similar conclusions have been indicated by other studies [354–356]. In a more recent study by Ackermann *et al.* [357], 4-year gamma ray data of Fermi-LAT on dSphs (04-08-2008 to 04-08-2012) with energy ranging from 500 MeV to 500 GeV have been chosen for 25 independent Milky Way dSphs galaxies. The chosen dSphs galaxies are Bootes I, Bootes II, Bootes III, Canes Venatici I, Canes Venatici II, Canis Major, Carina, Coma Berenices, Draco, Fornax, Hercules, Leo I, Leo II, Leo IV, Leo V, Pisces II, Sagittarius, Sculptor, Segue 1, Segue 2, Sextans, Ursa Major I, Ursa Major II, Ursa Minor and Willman 1. The galactic coordinates as well as the radial distances from the galactic centre of these dwarf galaxies are tabulated in Table 6.3. From the analysis of their data, they set robust upper limits on DM annihilation cross-section for different DM masses.

It is possible to assess the total DM content of dSphs galaxies from the dynamical modeling of the stellar density of the dwarf galaxies and the velocity dispersion profiles [415–417]. The dynamical masses of these dwarf galaxies are measured only from stellar velocity dispersion and half-light radius. The calculated total mass within the half-light radius for a dSphs galaxy is used to obtain the integrated J-factor of that dSphs galaxy. Both the total mass within the half-light radius and the J-factor are found to be almost independent on the choice of DM halo profiles [418–420]. Out of the 25 independent dSphs mentioned earlier, J-factors of only 18 dSphs are determined using stellar kinematics data [420] while other seven lack proper statistical significances. Thus, from such independent determination of J-factors of these dwarf galaxies and incorporating uncertainties on these J-factors, the upper bounds on DM annihilation cross-section for various DM masses have been derived with 95% CL. Also a combined analysis of 15 such dwarf galaxies have been performed [357] to obtain combined limit on DM annihilation cross-section for different DM masses considering them in such a way that when the ROIs of some dSphs coincide, they only consider one with the largest J-factor. This ensures statistical independence.

In the present formalism the dark matter candidate is the inert doublet dark matter. For this dark matter candidate we compute the gamma ray spectra from the annihilation of DM for the dwarf galaxies. The mass of the DM is taken to be 63.54 GeV which is the best fit value of the inert doublet DM in the present formalism as discussed earlier. The RHS of Eq. 6.14 contains the J-factor, the spectrum $\frac{dN}{dE}$ and the annihilation cross-section with the dark matter mass dependence as $\sim \frac{1}{M^2}$. The J-factor is given by the astrophysical calculations and it is different for different dSphs. The γ-ray spectrum, $\frac{dN}{dE}$ can be obtained for a given DM mass. The different particle processes for the calculation of $\frac{dN}{dE}$ are tabulated in Table 6.2. We compute $\frac{dN}{dE}$ for the inert doublet dark matter mass of 63.54 GeV and using the integrated J-factor for a particular dSph, the maximum value of the velocity-averaged annihilation cross-section ($\langle\sigma v\rangle_{\rm max}$) is estimated from the upper bound of the flux (LHS of Eq. 6.14) of that dSph. In this way the upper bounds of annihilation cross-section in case of the present inert doublet DM candidate, LIP with mass 63.54 GeV are computed for all the 18 dSphs considered and they are tabulated in Table 6.3. The statistics for the rest of dwarf galaxies is very poor and their J-factors cannot be determined kinematically. Hence these 7 dSphs are not considered in this work.

In Figs. 6.7, 6.8 and 6.9, the bin-by-bin upper limits on the gamma ray energy flux at 95% CL from each dwarf galaxy are shown by downward red-coloured arrows. The

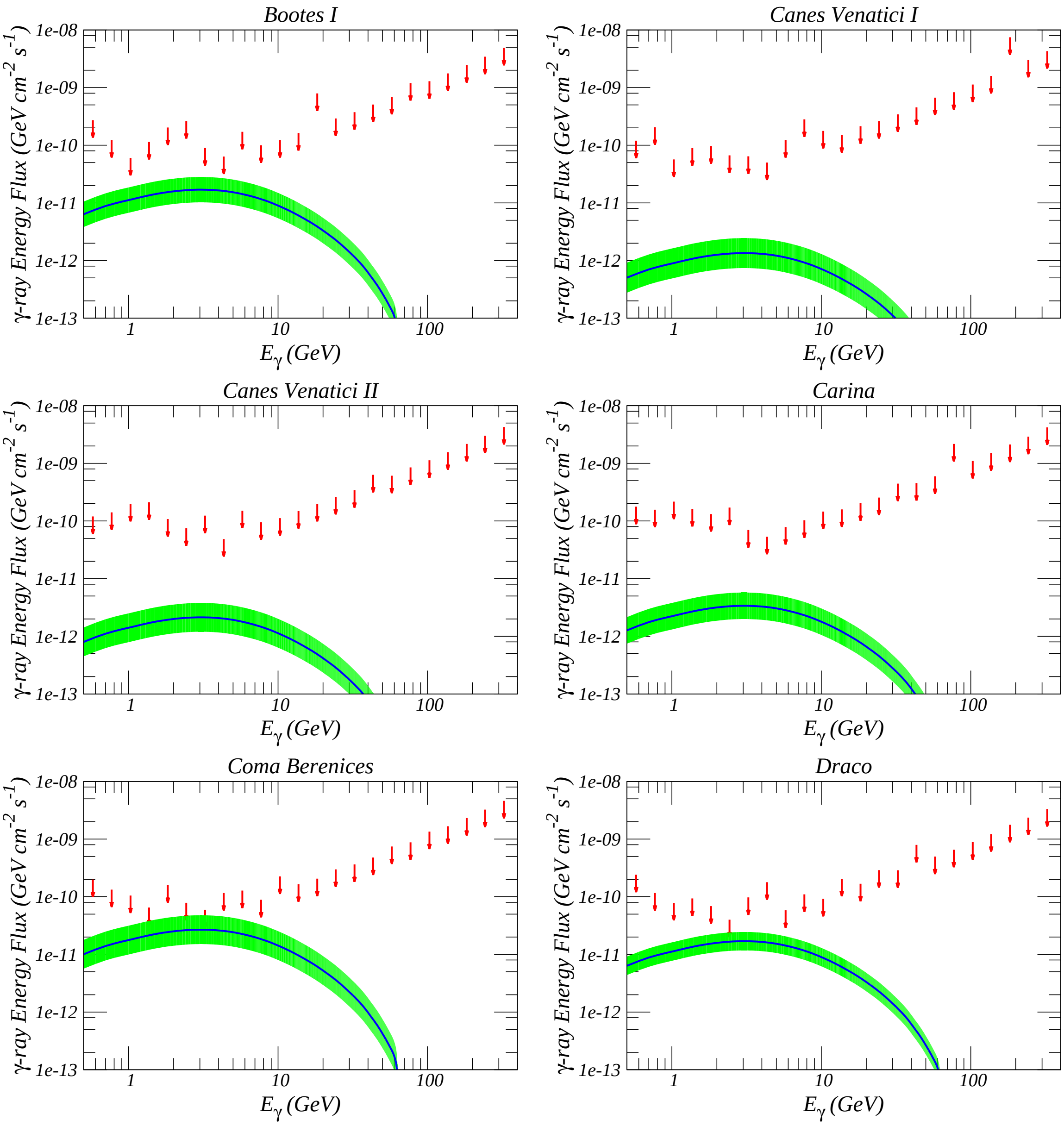

Figure 6.7: *Comparison of computed γ-ray flux from annihilation of 63.54 GeV DM in IHDM with the bin-by-bin integrated γ-ray energy-flux upper limits for each dSph. The downward red-coloured arrows represent bin-by-bin upper limits on the γ-ray energy-flux at 95% CL. The blue lines denote the γ-ray fluxes calculated using the central values of integrated J-factor whereas the green band is for the uncertainties in the measurement of integrated J-factors for Bootes I, Canes Venatici I, Canes Venatici II, Carina, Coma Berenices and Draco dSphs. See text for details.*

maximum, minimum and central values of integrated J-factor for each dwarf galaxy which are measured from stellar kinematics data are tabulated in Table 6.3 [357]. It is also

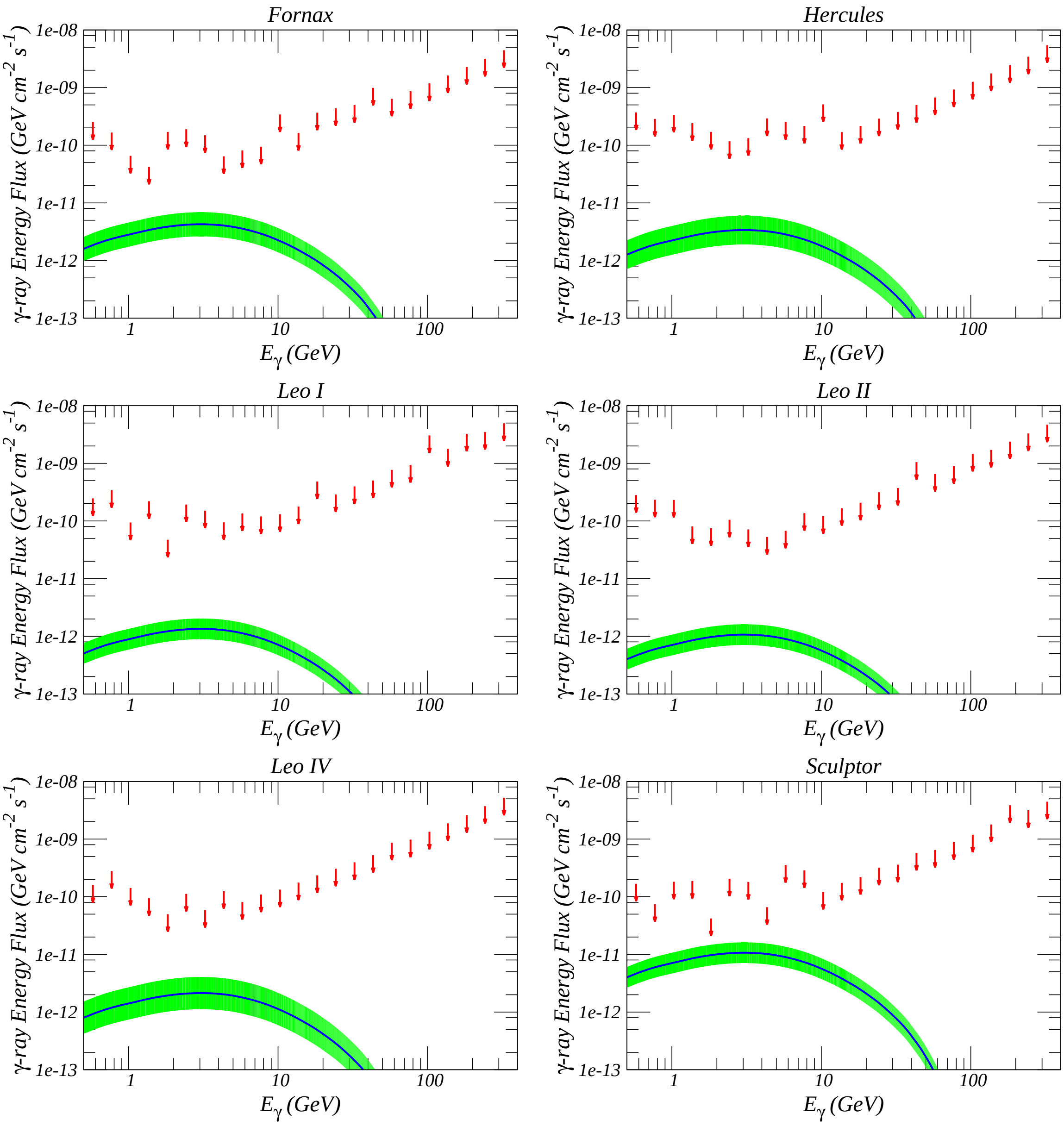

Figure 6.8: *Comparison of computed γ-ray flux from annihilation of 63.54 GeV DM in IHDM with the bin-by-bin integrated γ-ray energy-flux upper limits for each dSph. The notations used here are same as those in Fig. 6.7. But the plots in this figure are for Fornax, Hercules, Leo I, Leo II, Leo IV and Sculptor dSphs. See text for details.*

important to mention that the integrated J-factors (obtained by integrating Eq. 6.15 over the solid angle Ω) for each dSph galaxy of Table 6.3 are calculated by a line-of-sight integration of squared DM distribution. Then the integration over a solid angle $\Delta\Omega$ of $\sim 2.4 \times 10^{-4}$ sr is performed. Note that the field of view of Fermi-LAT is within the

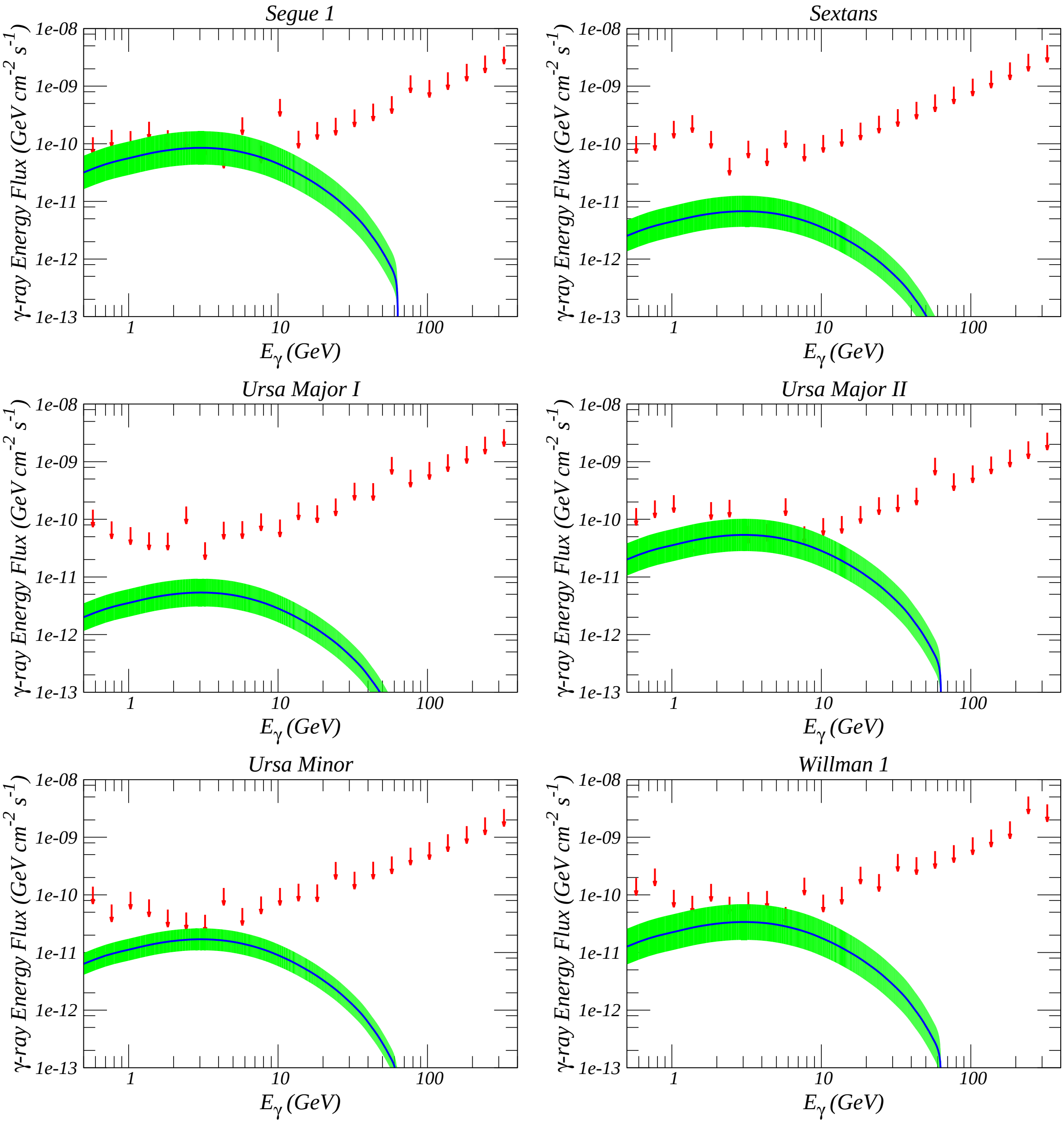

Figure 6.9: *Comparison of computed γ-ray flux from annihilation of 63.54 GeV DM in IHDM with the bin-by-bin integrated γ-ray energy-flux upper limits for each dSph. The notations used here are same as those in Fig. 6.7. But the plots in this figure are for Segue 1, Sextans, Ursa Major I, Ursa Major II, Ursa Minor and Willman 1 dSphs. See text for details.*

angular radius of 0.5^{o} which can be translated into a solid angle $\Delta\Omega \sim 2.4 \times 10^{-4}$ sr. We have calculated the gamma ray spectrum for the 63.54 GeV DM annihilation in this IHDM framework for various dSph galaxies under consideration considering NFW DM profile. Since the value of the integrated J-factor is almost insensitive to DM halo with factor $\gamma < 1.2$ [421], our consider NFW profile for theoretical calculation in this model does not affect integrated J-factor. The calculation for the gamma ray spectra in this framework for each dwarf galaxy differs from other one only by the measured values of integrated J-factors. In Figs. 6.7, 6.8 and 6.9, the flux of a dSph are compared with the upper bound of the flux in each energy bin. The spread (band) of this flux shown by green indicate the upper and lower limits of the flux when calculated with the upper and lower limits of integrated J-factors. The photon flux calculated using the central value of J-factors are shown by blue lines in these figures.

6.6 Confronting Extragalactic gamma ray background in this framework

Just the galactic component of gamma ray can have contribution from the γ-rays produced by dark matter annihilation, for the extragalactic γ-rays too their comes signatures of γ-rays from dark matter annihilation of extragalactic sources [358–363, 422–424]. The cosmic gamma rays can have their origins from both galactic and extragalactic sources in addition to other astrophysical origins. The cosmic γ-ray detected by the satellite borne experiments such as Fermi LAT should therefore have embedded in it, the γ signal from extragalactic sources too. Such gamma rays from extragalactic sources can remain hidden in the huge background of the observationally measured gamma flux by satellite-borne experiments such as SAS-2 satellite [425], EGRET [426], Fermi-LAT [12, 427]. In order to extract information regarding the extragalactic signature of gamma rays from the background one should be able to understand and subtract the galactic astrophysical components, other sources that may contribute to the background and the backgrounds that the detector may give rise to in the process of detection. After this process of subtraction the residual gamma-ray signal thus obtained is found to be diffuse and isotropic in nature and is known as diffuse isotropic gamma-ray background (DIGRB). Recently in the light of 50-month Fermi-LAT data an updated tight constraint on DM annihilation is given with the modelling of integrated emission of blazars with such diffuse background absorption [428]. This may also be noted that the DIGRB thus obtained embeds in it the irreducible contributions from galactic origin as well. In this section we estimate such diffuse isotropic gamma ray background or DIGRB for the case of dark matter annihilating into gamma rays in the framework of the chosen IHDM dark matter candidate. We then compare our theoretical calculations with EGRET and Fermi-LAT results for extragalactic DIGRB.

6.6.1 Formalism

The number of photons which are isotropically emitted from the volume element dV in time interval dt, in energy range dE and are collected by detector with effective area dA during time interval dt_0 with redshifted energy range dE_0 can be given by [358],

$$dN_\gamma = e^{-\tau(z,E_0)} \left[(1+z)^3 \int dM \, \frac{dn}{dM}(M,z) \, \frac{d\mathcal{N}_\gamma}{dE} \, (E,M,z)\right] \, \frac{dV \, dA}{4\pi[R_0 S_k(r)]^2} \, dE_0 \, dt_0 \ . \tag{6.19}$$

In the above, the volume element dV is expressed in terms of a particular redshift z and the angular acceptance of the detector $d\Omega_{\rm detector} = \sin\theta d\theta d\phi$ and is given as

$$dV = \frac{[R_0 S_k(r)]^2 \, R_0}{(1+z)^3} dr d\Omega_{\rm detector} \ . \tag{6.20}$$

In Eq. 6.19 and Eq. 6.20, $S_k(r)$ is given by the Robertson Walkter metric for homogeneous and isotropic universe

$$ds^2 = c^2 dt^2 - R^2(t)\left[dr^2 + S_k^2(r)(d\theta^2 + \sin^2\theta d\phi^2)\right] \ , \tag{6.21}$$

where k is the curvature parameter. The term $S_k(r)$ takes the forms

$$S_k(r) = \begin{cases} r, & k = 0; \\ \arcsin r, & k = +1; \\ \operatorname{arcsinh} r, & k = -1. \end{cases} \tag{6.22}$$

for different curvature of the universe's geometry (flat ($k = 0$), closed ($k = +1$) or open ($k = -1$)). In Eq. 6.19, $\frac{d\mathcal{N}_\gamma}{dE}(E, M, z)$ is the differential photon energy spectrum for a generic halo with mass M at some redshift z. The term $\frac{dn}{dM}(M, z)$ is called the halo mass function and is defined as number density of bound objects with mass M at redshift z. The term $e^{-\tau(z,E_0)}$ represents the attenuation of extragalactic γ-rays which may come from the absorption of these high energy γ-rays on the extragalactic background light (EBL). Detailed studies regarding this attenuation have been studied in Ref. [141]. The optical depth $\tau(z, E_0)$ represents the nature of absorption at redshift z. We have adopted the minimal model for ultraviolet background [429, 430] obtained after a recent study on blazars. The integral in Eq. 6.19 is over energy and time ($dtdE$). Note that $dtdE = \frac{dt_0}{(1+z)}.(1 + z)dE_0$, where t_0 and E_0 are the time and energy respectively corresponding to the redshift $z = 0$. Summing over all the above contributions, the diffuse extragalactic γ-ray flux due to DM annihilation, can be written as,

$$\begin{aligned}\frac{d\phi_\gamma}{dE_0} \equiv \frac{dN_\gamma}{dA\, d\Omega\, dt_0\, dE_0} &= \frac{1}{4\pi}\int dr\, R_0 e^{-\tau(z,E_0)} \int dM\, \frac{dn}{dM}(M, z)\, \frac{d\mathcal{N}_\gamma}{dE}\,(E_0\,(1+z), M, z) \\ &= \frac{c}{4\pi}\int dz \frac{e^{-\tau(z,E_0)}}{H_0\, h(z)} \int dM\, \frac{dn}{dM}(M, z)\, \frac{d\mathcal{N}_\gamma}{dE}\,(E_0\,(1+z), M, z)\end{aligned} \tag{6.23}$$

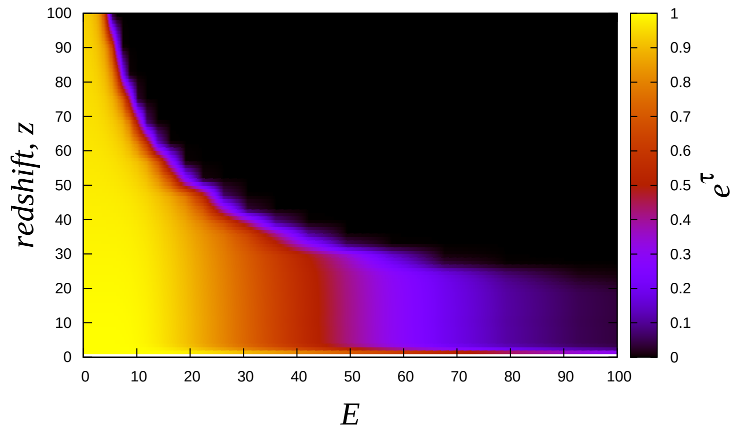

Figure 6.10: *The variation of optical depth (transparency coefficient) e^{τ} with the energy at detection (E) and the redshift (z) of photon emission for minimum UV background model. The black zone in this figure represents total opaque region while the yellow zone is for total transparent one. See text for details.*

where c is the speed of light in vacuum, H_0 is the Hubble constant at the present epoch and $h(z)$ is a redshift dependent function which depends on the choice of the cosmological models and can be written in the form,

$$h(z) = \sqrt{\Omega_M(1+z)^3 + \Omega_k(1+z)^2 + \Omega_\Lambda}. \tag{6.24}$$

where Ω_M, Ω_k and Ω_Λ are respectively the matter, curvature and dark energy densities normalised to the critical density of the universe. Since the observational results indicate the spatial flatness of the universe $\Omega_k = 0$. the γ-ray flux In Eq. 6.23, the line of sight integral (integral over dr) has been replaced by redshift integral (integral over dz). [3] Following Press-Schechter [431], the cosmological dark matter halo function $\frac{dn}{dM}(M,z)$

[3]The relation between the co-moving distance, χ and the redshift z can be written as, $\frac{d\chi}{dz} = \frac{c}{H(z)}$, where $H(z) = H_0 h(z)$ and $\chi = R_0 r$.

can be written in the form,

$$\frac{dn}{dM} = \frac{\rho_{0,m}}{M^2}\nu f(\nu)\frac{d\,\log\nu}{d\,\log M}\ , \tag{6.25}$$

where $\rho_{0,m}$ is the comoving background matter density. [4] In the above the parameter $\nu = \delta_{\rm sc}/\sigma(M)$, defined as the ratio between the critical overdensity for spherical collapse $\delta_{\rm sc}$ ($\simeq 1.686$) and $\sigma(M)$ denoting the variance or the root mean square density fluctuations of the linear density field in sphere that contains the mean mass M. The term $\sigma^2(M)$ can be written in terms of the linear power spectrum $P(k)$ of the fluctuations [432] as,

$$\sigma^2(M) \equiv \int d^3k\ \tilde{W}^2(kR)\,P(k) \tag{6.26}$$

where $\tilde{W}(kR)$ is the Fourier transform of the top hat window function and R is the comoving length scale. For collapsed halos, the mass is found to be $M \simeq (4/3)\pi R^3\rho_c(z_c)$ with z_c being the redshift where collapsing of halos occurs. In the above the power spectrum can be parametrised as $P(k) \propto k^n T^2(k)$ where n is the spectral index and T being the transfer function which incorporates the effect of scale dependency of the primordial power spectrum generated during inflation. This transfer function depends on the nature of DM and baryon density in the universe. Thus the transfer function can be calculated from the cosmic microwave background data. The variation of the power spectrum $P(k)$ with wavenumber k for different redshifts is shown in the left panel of Fig. 6.11. The right panel of Fig. 6.11 corresponds to the plot showing the variation of variance σ with halo mass M for different values of redshift. The function $f(\nu)$ in Eq. 6.25, known as the multiplicity function, can be modelled in the ellipsoidal collapse model [432] by,

$$\nu f(\nu) = 2A\left(1+\frac{1}{\nu'^{2p}}\right)\left(\frac{\nu'^2}{2\pi}\right)^{1/2}\exp\left(-\frac{\nu'^2}{2}\right)\ , \tag{6.27}$$

[4] $\rho_{0,m} \simeq \rho_c\Omega_M$ with ρ_c being the critical density at the present epoch ($z = 0$). More precisely $\bar{\rho}_{z,m} = \rho_c\Omega_{\rm M}(1+z)^3$.

where $\nu' = \sqrt{a}\nu, a = 0.707, p = 0.3$ are obtained by fitting Eq. 6.25 to N-body simulation of Virgo consortium [433]. The value of the parameter A can be fixed by using the relation $\int d\nu f(\nu) = 1$ which follows from the condition that the total mass should lie within a given halo, i.e, $\int dM\ M dn/dM = \rho_0$. For the choice of parameter values, $a = 1, p = 0$ and $A = 0.5$, Eq. 6.25 reduces to the original Press-Schechter theory [431]. It is found in N-body simulations that the estimations of higher and lower mass halos differ from that predicted by Press-Schechter model. This problem can be handled in Sheth-Torman model by considering ellipsoidal collapse model instead of spherical one.

In the left panel of Fig. 6.12 the variations of the fraction of mass collapsed or $f(\sigma)$ in the ellipsoidal collapse model with redshifts z and the halo mass M are shown. Note that $f(\sigma)$ as shown in the left panel of Fig. 6.12 can be obtained by simple transformation of $f(\nu)$ by plugging in $\nu = \delta_{\rm sc}/\sigma(M)$ and is given by $f(\sigma) = A\sqrt{\frac{2a}{\pi}}\left[1 + \left(\frac{\sigma^2}{a\delta_{\rm sc}^2}\right)^p\right]\frac{\delta_{\rm sc}}{\sigma}\exp\left[-\frac{a\delta_{\rm sc}^2}{2\sigma^2}\right]$. In the right panel of Fig. 6.12 we have shown the variations of the considered halo mass function dn/dM of Sheth-Torman model [432] with redshift z as well as with the halo mass M. All the numerical calculations related to Fig. 6.12 have been performed using `HMFcalc` [434] code.

The ΛCDM cosmological model suggests that the DM halos are formed hierarchically with bottom-up structure via gravitational amplification of the initial density functions. The small structure of the universe merge into larger ones and thus larger halos are formed. The N-body simulation indicate that the DM density profile in a DM halo can be written as,

$$\rho(r) = \rho_s\, g(r/r_s)\ , \tag{6.28}$$

where r_s is the scale radius and ρ_s is the scale density for a particular halo model. The nature of the function $g(r/r_s)$ depends on the choice of the DM halo profiles. For the halo

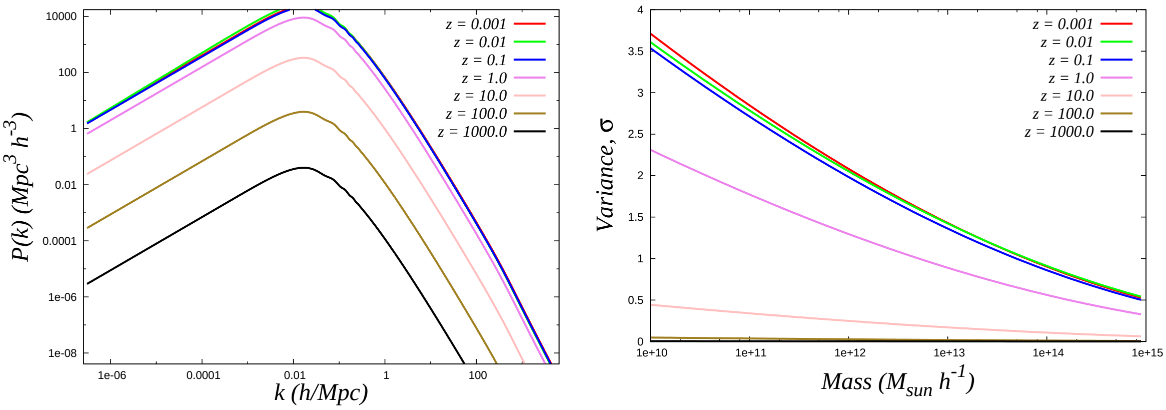

Figure 6.11: *The variation of the linear power spectrum $P(k)$ of matter density perturbations with the wavenumber k of the fluctuations for different redshifts is shown in the left panel. In the right panel the variance σ of the density perturbations is shown as a function of halo mass for different redshifts. In both plots the values of redshift* $z = 10^{-3}, 10^{-2}, 10^{-1}, 10^{0}, 10^{1}, 10^{2}$ and 10^{3}. *See text for details.*

profile we have chosen NFW halo profile [150, 151] given by,

$$\rho(r) = \rho_s\, g(r/r_s) = \rho_s \frac{1}{\frac{r}{r_s}\left(1 + \frac{r}{r_s}\right)^2}\ , \tag{6.29}$$

Needless to mention that for NFW profile the function $g(x)$ is given by,

$$g_{\rm NFW}\,(x) = \frac{1}{x\,(1+x)^2}. \tag{6.30}$$

Similarly for Moore profile [293], the function $g(x)$ takes the following form,

$$g_{\rm Moore}\,(x) = \frac{1}{x^{1.5}\,(1+x^{1.5})}. \tag{6.31}$$

Any DM halo of mass M_h enclosed at a radius r_h is,

$$M_h = 4\pi\rho_s r_h^3 f(r_s/r_h)\ \ , \tag{6.32}$$

where $f(x) = x^3[\ln(1 + x^{-1}) - (1 + x)^{-1}]$.

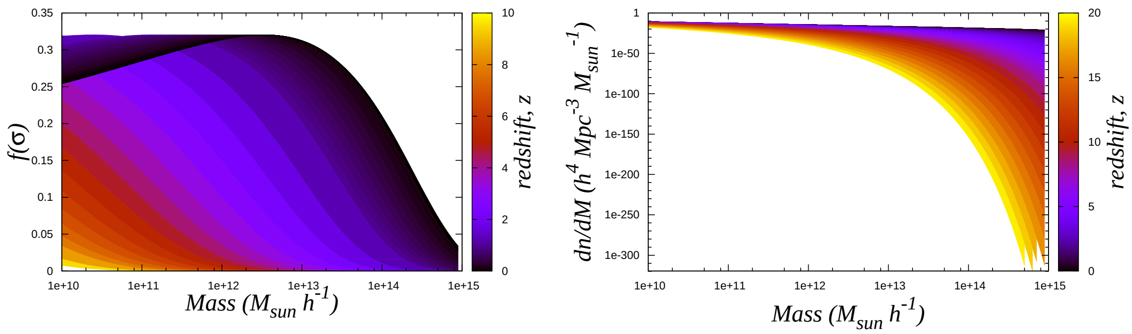

Figure 6.12: *The fraction of mass collapsed, $f(\sigma)$ in Sheth-Torman model for different redshifts z and the halo masses M is shown in left panel. The variation of Sheth-Torman halo mass function $\frac{dn}{dM}$ with the redshift z and the halo mass M is shown in right panel. See text for details.*

Also a halo of mass M at some redshift z can be written in terms of mean background $\bar{\rho}(z)$ as,

$$M \equiv \frac{4\pi}{3}\Delta_{vir}\bar{\rho}(z)\, R_{vir}^3 \quad , \tag{6.33}$$

where R_{vir} is the virial radius defined as the radius within which the total halo mass M is contained with mean halo density $\Delta_{vir}\bar{\rho}(z)$. Δ_{vir} is the virial overdensity with respect to the mean matter density which can density can depend on the cosmology but not on the halo mass M_h. For the flat cosmology $\Delta_{vir}(z)$ can be cast into the following [435],

$$\Delta_{vir} \simeq (18\pi^2 + 82d - 39d^2) \quad , \tag{6.34}$$

with $d(z) = \frac{\Omega_m(1+z)^3}{(\Omega_m(1+z)^3+\Omega_\Lambda)} - 1$. We choose the value of $\Delta_{vir}(z)$ to be 200.

The γ-ray energy spectrum $\frac{d\mathcal{N}_\gamma}{dE}\,(E_0\,(1+z), M, z)$ (Eq. 6.23) for the gamma-ray emitted inside a halo of mass M at redshift z is written to the form,

$$\frac{d\mathcal{N}_\gamma}{dE}(E, M, z) = \frac{\langle \sigma v\rangle}{2}\frac{dN_\gamma(E)}{dE}\int dc'_{vir}\;\mathcal{P}(c'_{vir})\left(\frac{\rho'}{M_\chi}\right)^2\int d^3r\; g^2(r/a)\;, \tag{6.35}$$

where $\langle \sigma v \rangle$ is the thermally averaged value of annihilation cross-section times the relative velocity, $\frac{dN_\gamma(E)}{dE}$ is the differential γ-ray energy spectrum produced per unit annihilation of dark matter and M_χ is the corresponding mass of dark matter. The log-normal distribution $\mathcal{P}(c_{vir})$ of the concentration parameter c_{vir} around the mean value chosen within 1σ deviation [436], for halos with mass M. Finally one can write,

$$\frac{d\mathcal{N}_\gamma}{dE}(E, M, z) = \frac{\sigma v}{2} \frac{dN_\gamma(E)}{dE} \frac{M}{M_\chi^2} \frac{\Delta_{vir}\bar{\rho}(z)}{3} \int dc'_{vir}\ \mathcal{P}(c'_{vir}) \frac{(c'_{vir}\, r_{-2})^3}{[I_1(c'_{vir}\, r_{-2})]^2}\, I_2(x_{min}, c'_{vir}\, r_{-2})\ . \tag{6.36}$$

In the above r_{-2} is the ratio between $r_s^{(-2)}$ and r_s where $r_s^{(-2)}$ is the radius at which the effective logarithmic slope -2 that follows from the relation, $d/dr\ (r^2 g(r))|_{r=r_s^{(-2)}} = 0$. For NFW profile, $r_s^{(-2)} = r_s$. Hence $c_{vir} r_{-2} = R_{vir}/r$ and the form of integration $I_n(x_{min}, x_{max})$ in Eq. 6.36 can be cast into the form,

$$I_n(x_{min}, x_{max}) = \int_{x_{min}}^{x_{max}} dx\, x^2 g^n(x)\ . \tag{6.37}$$

Plugging the above equation in Eq. 6.23, the analytic form of extragalactic gamma-ray flux from DM annihilation can be obtained as [358]

$$\frac{d\phi_\gamma}{dE_0} = \frac{\sigma v}{8\pi} \frac{c}{H_0} \frac{\rho_0^2}{M_\chi^2} \int dz\ (1+z)^3 \frac{\Delta^2(z)}{h(z)} \frac{dN_\gamma(E_0\,(1+z))}{dE} e^{-\tau(z,E_0)}\ , \tag{6.38}$$

where the expression for $\Delta^2(z)$ can be given by,

$$\Delta^2(z) \equiv \int dM \frac{\nu(z,M) f\,(\nu(z,M))}{\sigma(M)} \left|\frac{d\sigma}{dM}\right| \Delta_M^2(z, M) \tag{6.39}$$

with

$$\Delta_M^2(z, M) \equiv \frac{\Delta_{vir}(z)}{3} \int dc'_{vir}\ \mathcal{P}(c'_{vir}) \frac{I_2(x_{min}, c'_{vir}(z,M)\, r_{-2})}{[I_1(x_{min}, c'_{vir}(z,M)\, r_{-2})]^2} (c'_{vir}(z,M)\, r_{-2})^3\ . \tag{6.40}$$

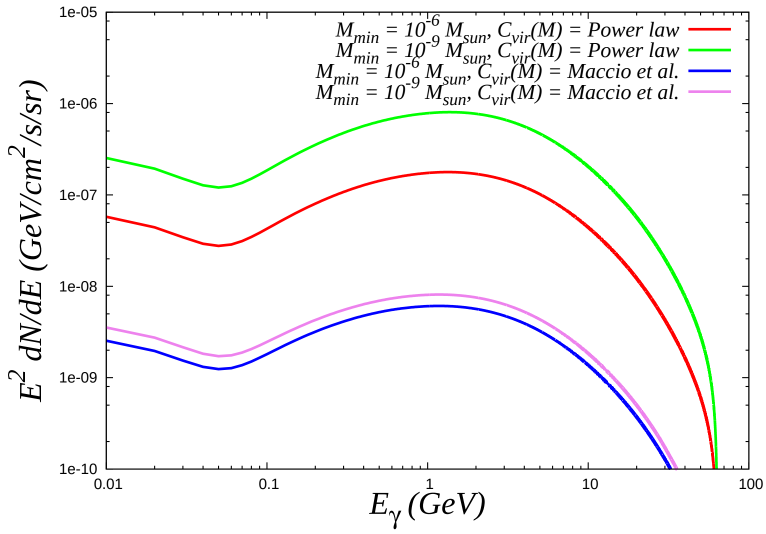

Figure 6.13: *Comparison of the computed extragalactic gamma-ray fluxes from the annihilation of 63.54 GeV dark matter (benchmark point) in IHDM framework for different extragalactic parametrisations. We consider two models of the concentration parameter* c_{vir}*, namely a)power law model and b)Macciò et al. model. Also the minimum extragalactic subhalo mass* $M_{\rm min}$ *are chosen to be* $10^{-6}M_\odot$ and $10^{-9}\,M_\odot$. *Calculation with power law model yields enhanced* γ*-ray flux compared to that with Macciò et al. model. For low* $M_{\rm min}$*,* γ*-ray flux increases and this enhancement is smaller for Macciò et al. model compared to that for power law model. See text for details.*

In all of the above the concentration parameter, c_{vir} is defined as

$$c_{vir} = \frac{R_{vir}}{r_s^{(-2)}} \quad , \tag{6.41}$$

We have chosen two forms of concentration parameter c_{vir} following Macciò *et al.* [437] and power law model [437, 438]. For the first choice (Macciò *et al.*), $c_{vir}(M,z) = k_{200}$ $(\mathcal{H}(z_f(M))/\mathcal{H}(z))^{2/3}$, where $k_{200} \simeq 3.9$, $\mathcal{H}(z) = H(z)/H_0$ and $z_c(M)$ is the effective redshift during the formation of a halo with mass M. In the power law model (second choice) however the expression of $c_{vir}(M,z)$ is adopted as $c_{vir}(M,z) = 6.5\,\mathcal{H}(z)^{-2/3}\ (M/M_*)^{-0.1}$, $M_* = 3.37\,10^{12} h^{-1} M_\odot$. This choice of $c_{vir}(M,z)$ provides a reasonable fit within the resolved mass range in the simulations.

The dark matter substructures are present within halo and form bound objects. The mass of the smallest possible such bound object (subhalo) is denoted as $M_{\rm min}$. The value of this minimum subhalo mass, $M_{\rm min}$ is determined from the temperature at which the DM particles just start decoupling kinematically from the cosmic background.

In this work we perform our analysis for two typical values of $M_{\rm min}$; $M_{\rm min} = 10^{-6} M_\odot$ and $10^{-9}\, M_\odot$ [418, 439]. The boost factor for γ-ray flux due to these subhalos depends inversely on $M_{\rm min}$.

6.6.2 Non-DM Contributions in DIGRB

The extragalactic gamma-ray spectrum in the energy range between $\sim$ few hundred MeV and $\sim$ few hundred GeV as observed by the Fermi-LAT telescope is found to follow almost a power law spectrum ($\frac{dN_\gamma}{dE} \propto E^{-2.41}$). There are contributions from astrophysical sources other than that from possible dark matter annihilation [16]. The possible sources that contribute to the diffuse γ-ray background other than the DM include BL Lacertea objects (BL Lacs), flat spectrum radio quasars (FSRQs), millisecond pulsars (MSPs), star forming galaxy (SFG), Fanarof-Riley (FR) radio galaxies of type I (FRI) and type II (FRII), ultra high energy cosmic rays (UHECRs), gamma ray bursts (GRBs), star burst galaxy (SBG), Ultra High Energy protons in the inter-cluster material (UHEp ICM) and gravitationally induced shock waves (IGS) etc. The physics of such possible sources that contribute to the diffuse γ-ray background other than the DM are briefly discussed below,

1. **BL Lac Objects**

   BL Lacertea objects better known as BL Lacs are one of the classes of blazars which are so far considered to yield a major portion of the extragalactic background since the unresolved ones among these objects are expected to contribute to the extragalactic background. The differential γ-ray spectrum for such unresolved BL

Lacs can be written [440] as,

$$\frac{dN_\gamma}{dE}_{\rm BLLac} = 3.9 \times 10^{-8} E_\gamma^{-2.23}\,{\rm GeV}^{-1}\,{\rm cm}^{-2}\,{\rm s}^{-1}\,{\rm sr}^{-1} \ . \quad (6.42)$$

An estimation of the contribution of BL Lacs to the extragalactic background using the above relation yields a photon flux of 5.4×10^{-7} photons cm^{-2}s^{-1}sr^{-1} in the range $0.01\,{\rm GeV} < E_\gamma < 10\,{\rm GeV}$.

2. **FSRQ**

Similar to BL Lacs, another class of blazars known as flat spectrum radio quasars (FSRQs) also contribute to the extragalactic background. The spectrum of these objects are relatively softer than BL Lacs [440] and is given by,

$$\frac{dN_\gamma}{dE}_{\rm FSRQ} = 3.1 \times 10^{-8} E_\gamma^{-2.45}\,{\rm GeV}^{-1}\,{\rm cm}^{-2}\,{\rm s}^{-1}\,{\rm sr}^{-1} \ . \quad (6.43)$$

The contribution to extragalactic background from these objects is nearly equivalent to that from other kind of blazars, namely BL Lacs.

3. **MSP**

The millisecond pulsars (MSPs) also contribute significantly to this extragalactic gamma-ray background at high galactic latitude regions. MSPs are rapidly rotating neutron stars with period of rotation being millisecond scale, which convert the kinetic energy to radiation at gamma-ray as well as radio zones. The long lifetime and the expected spatial distribution of these objects make them potentially good candidate for the source of the high latitude diffuse gamma-ray background radiation. The Fermi collaboration has so far identified many MSPs whose spatial distribution can be calculated from data. By using the spatial features of MSPs [441], the differential spectrum of gamma-ray can be modeled at high galactic latitude as,

$$\frac{dN_\gamma}{dE}_{\rm MSP} = 1.8 \times 10^{-7} E_\gamma^{-1.5} \exp\left(-\frac{E_\gamma}{1.9}\right) \,{\rm GeV^{-1}\,cm^{-2}\,s^{-1}\,sr^{-1}} \quad . \tag{6.44}$$

Using the above relation, the minimal contribution of total gamma-ray flux $|b| > 40^{\rm o}$ can be estimated [442] to be 8.0×10^{-7} photons $\rm cm^{-2}s^{-1}sr^{-1}$ in the range $0.01\,{\rm GeV} < E_\gamma < 10\,{\rm GeV}$.

4. **SFG**

   The star forming galaxy (SFG) is a major candidate thats contribute significantly to the total extragalactic background γ-ray radiation [443]. The fractional contribution of these galaxies to the extragalactic background may be significant. The gamma from these galaxies are obtained from various processes such as decay of cosmic ray pions, inverse Compton scattering and Bremsstrahlung. By studying the infrared and radio emission from the galaxies, the luminosity functions for gamma rays are determined. For the gamma-rays produced from hadronic origin in SFGs, the differential gamma-ray spectrum for such SFGs can be modeled as,

$$\frac{dN_\gamma}{dE}_{\rm SFG} = 1.3 \times 10^{-7} E_\gamma^{-2.75} \,{\rm GeV^{-1}\,cm^{-2}\,s^{-1}\,sr^{-1}} \;\; {\rm for}\;\; E_\gamma > 1\,{\rm GeV} \quad . \tag{6.45}$$

   Below 1 GeV the gamma-ray spectrum shows peak near 0.5 GeV.

5. **FR**

   In general, the radio galaxies are active galactic nuclei (AGN) with the direction of the emitted relativistic jets being misaligned to the line of sight. Fanarof-Riley (FR) radio galaxies of type I (FRI) and type II (FRII) are the AGN populations of the misaligned BL Lacs and FSRQs respectively. These faint objects yield comparable fraction of gamma-ray flux of the total extragalactic background radiation. The observed correlation between the radio emission and the gamma-ray emission is used to compute the differential spectrum of the emitted gamma-rays. The modeling of such gamma-ray spectrum [444] with attenuation being considered can be cast into the following form,

$$\frac{dN_\gamma}{dE}_{\rm FR} = 5.7 \times 10^{-8} E_\gamma^{-2.39} \exp\left(-\frac{E_\gamma}{50.0}\right) \, {\rm GeV^{-1}\, cm^{-2}\, s^{-1}\, sr^{-1}} \quad , \tag{6.46}$$

where the above relation is used to find the total extragalactic photon flux as 1.0×10^{-6} photons $\rm cm^{-2}s^{-1}sr^{-1}$ in the range $0.01\,{\rm GeV} < E_\gamma < 10\,{\rm GeV}$.

6. **UHECR**

There is another type of hard spectrum of high energy gamma-ray produced by the interaction of CMB with protons and nuclei of ultra high energy cosmic rays (UHECRs) via the electromagnetic cascading. With the assumption that the UHECRs are dominated with protons up to very high energy scale, one can estimate the minimal differential gamma-ray spectrum [445] as,

$$\frac{dN_\gamma}{dE}_{\rm UHECR} = 4.8{\times}10^{-9} E_\gamma^{-1.8} \exp\left[-\left(\frac{E_\gamma}{100.0}\right)^{0.35}\right] \, {\rm GeV^{-1}\, cm^{-2}\, s^{-1}\, sr^{-1}} \;\; {\rm for} \;\; E_\gamma > 1\,{\rm GeV} \quad , \tag{6.47}$$

where the total extragalactic photon flux is computed to be 3.3×10^{-8} photons $\rm cm^{-2}s^{-1}sr^{-1}$ in the range $0.01\,{\rm GeV} < E_\gamma < 10\,{\rm GeV}$.

7. **GRB**

The gamma ray bursts (GRBs) contribute a small amount ($\sim 1\%$) of gamma-ray flux in extragalactic background radiation. The GRB differential gamma-ray spectrum without any attenuation at higher energies (~ 50 GeV) can be written [446] as,

$$\frac{dN_\gamma}{dE}_{\rm GRB} = 8.9 \times 10^{-9} E_\gamma^{-2.1} \, {\rm GeV^{-1}\, cm^{-2}\, s^{-1}\, sr^{-1}} \quad . \tag{6.48}$$

The spectrum generates $1.0{\times}10^{-7}$ photons $\rm cm^{-2}s^{-1}sr^{-1}$ in the range $0.01\,{\rm GeV} < E_\gamma$.

8. **SBG**

The star burst galaxy (SBG) that possesses denser interstellar medium than Milky Way and higher star formation rate produces significant amount of extragalactic background radiation dominantly via inverse Compton scattering process of high energetic electrons and protons. Following Ref. [447] the differential photon spectrum in this case is expressed as,

$$\frac{dN_\gamma}{dE}_{\rm SBG} = 0.3 \times 10^{-7} E_\gamma^{-2.4}\,{\rm GeV}^{-1}\,{\rm cm}^{-2}\,{\rm s}^{-1}\,{\rm sr}^{-1} \ . \tag{6.49}$$

Since the above-mentioned inverse Compton process produce high energetic photons, the SBG γ-ray spectrum plays important role at high energy regions. The above spectrum gives 5.4×10^{-7} photons ${\rm cm}^{-2}{\rm s}^{-1}{\rm sr}^{-1}$ in the range $0.01\,{\rm GeV} < E_\gamma$.

9. **UHEp ICM**

Gamma radiation can also be generated in clusters which is motivated by the fact that cosmic ray is confined in the inter-cluster material (ICM). Inverse Compton scattering (ICS) of high energy electrons, accelerated at cosmological shocks up to energies of tens of TeV, off the universal photon background can result ICS emission up to multi-TeV energies. Other possible mechanisms of production of gamma rays in the ICM include ICS from secondary electrons, non-thermal Bremsstrahlung and ICS from pairs generated in Bethe-Heitler processes between Ultra High Energy protons (UHEp) ($E > 10^{21}$ eV) and photons of the cosmic microwave background. The latter case is worth studying for diffuse extragalactic background. The conservative contribution of gamma-ray spectrum produced via UHEp interacting with ICM can be approximated as [448, 449],

$$\frac{dN_\gamma}{dE}_{\rm UHEp\ ICM} = 3.1 \times 10^{-9} E_\gamma^{-2.75}\,{\rm GeV}^{-1}\,{\rm cm}^{-2}\,{\rm s}^{-1}\,{\rm sr}^{-1} \ , \tag{6.50}$$

which results 1.0×10^{-7} photons $\mathrm{cm}^{-2}\mathrm{s}^{-1}\mathrm{sr}^{-1}$ in the range $0.01\,\mathrm{GeV} < E_\gamma$ similar to that from GRBs.

10. **IGS**

The electrons and the protons present in the intergalactic medium are accelerated by gravitationally induced shock waves (IGS) and they subsequently transfer their high energies to the low energetic photons via ICS. Such photons are also considered as non-DM contribution to extragalactic γ-ray background since they contribute to the higher galactic latitude. The differential gamma-ray spectrum for such a process [450, 451] is as follows,

$$\frac{dN_\gamma}{dE}_{\,\mathrm{IGS}} = 0.87 \times 10^{-10} \times \left\{ \begin{array}{ll} \left(\frac{E_\gamma}{10}\right)^{-2.04} & \text{for } E_\gamma < 10 \text{ GeV} \\ \left(\frac{E_\gamma}{10}\right)^{-2.13} & \text{for } E_\gamma > 10 \text{ GeV} \end{array} \right\} \mathrm{GeV}^{-1}\mathrm{cm}^{-2}\mathrm{s}^{-1}\mathrm{sr}^{-1}. \tag{6.51}$$

The spectral features of photon spectra originated from the non-DM objects [16] considered in this work are concisely summarised in Table 6.4. All of these minimal non-DM contributions discussed above, in principle, be summed up and it is found that they make up for $\sim 40\%$ of the extragalactic gamma-ray observed by the Fermi-LAT telescope [427].

We add up the contributions to EGB both from the annihilating DM in IHDM framework (63.54 GeV DM considered in this work) and the other possible non-DM astrophysical sources. The comparison of the sum total value of the γ-ray flux with the observed EGB by EGRET and Fermi LAT is shown in Fig. 6.14. Needless to mention here that the four plots in Fig. 6.14 are for different parametrisations of concentration parameter c_{vir} and subhalo mass M_{min}. As mentioned earlier we have considered BL Lacs, FSRQs, MSPs, SFGs, FR (type I and II), UHECR, GRBs, SBGs, UHEp interacting with ICM and IGS as contributors to EGB other than DM and their contributions to EGB are shown with different lines in Fig. 6.14. The computed total photon spectra in the plots of

Table 6.4: Overview of the minimal non-DM contributions to the total extragalactic γ-ray background [16]

Non-DM objects	Photon Energy Spectra ($\frac{dN}{dE}$ in GeV^{-1}cm^{-2}s^{-1}sr^{-1})
BL Lacs	$3.9 \times 10^{-8} E_\gamma^{-2.23}$
FSRQ	$3.1 \times 10^{-8} E_\gamma^{-2.45}$
MSP	$1.8 \times 10^{-7} E_\gamma^{-1.5} \exp\left(-\frac{E_\gamma}{1.9}\right)$
SFG	$1.3 \times 10^{-7} E_\gamma^{-2.75}$
FR I & FR II	$5.7 \times 10^{-8} E_\gamma^{-2.39} \exp\left(-\frac{E_\gamma}{50.0}\right)$
UHECR	$4.8 \times 10^{-9} E_\gamma^{-1.8} \exp\left[-\left(\frac{E_\gamma}{100.0}\right)^{0.35}\right]$
GRB	$8.9 \times 10^{-9} E_\gamma^{-2.1}$
SBG	$0.3 \times 10^{-7} E_\gamma^{-2.4}$
UHEp ICM	$3.1 \times 10^{-9} E_\gamma^{-2.75}$
IGS	$0.87 \times 10^{-10} \times \left\{ \begin{array}{ll} \left(\frac{E_\gamma}{10}\right)^{-2.04} & \text{for } E_\gamma < 10 \text{ GeV} \\ \left(\frac{E_\gamma}{10}\right)^{-2.13} & \text{for } E_\gamma > 10 \text{ GeV} \end{array} \right\}$

Fig. 6.14 are shown by black solid lines while the red solid line is for the minimal non-DM contribution to EGB. The black lines are found to be on top of the red lines for Macciò *et al.* models.

We also mention that the extragalactic γ-ray signal is analysed within the dark matter annihilation scenario in Ref. [15]. In their analysis they have constructed a model for the non-DM astrophysical contributions to the extragalactic γ-ray background and they have also adopted a substructure model based on numerical simulations. The authors in Ref. [15] have considered subhalo boost factor b_{sh} in their analyses to be the following form [452]

$$b_{sh}(M) \approx 110 \times (M_{200}/10^{12} M_{sun})^{0.39} \tag{6.52}$$

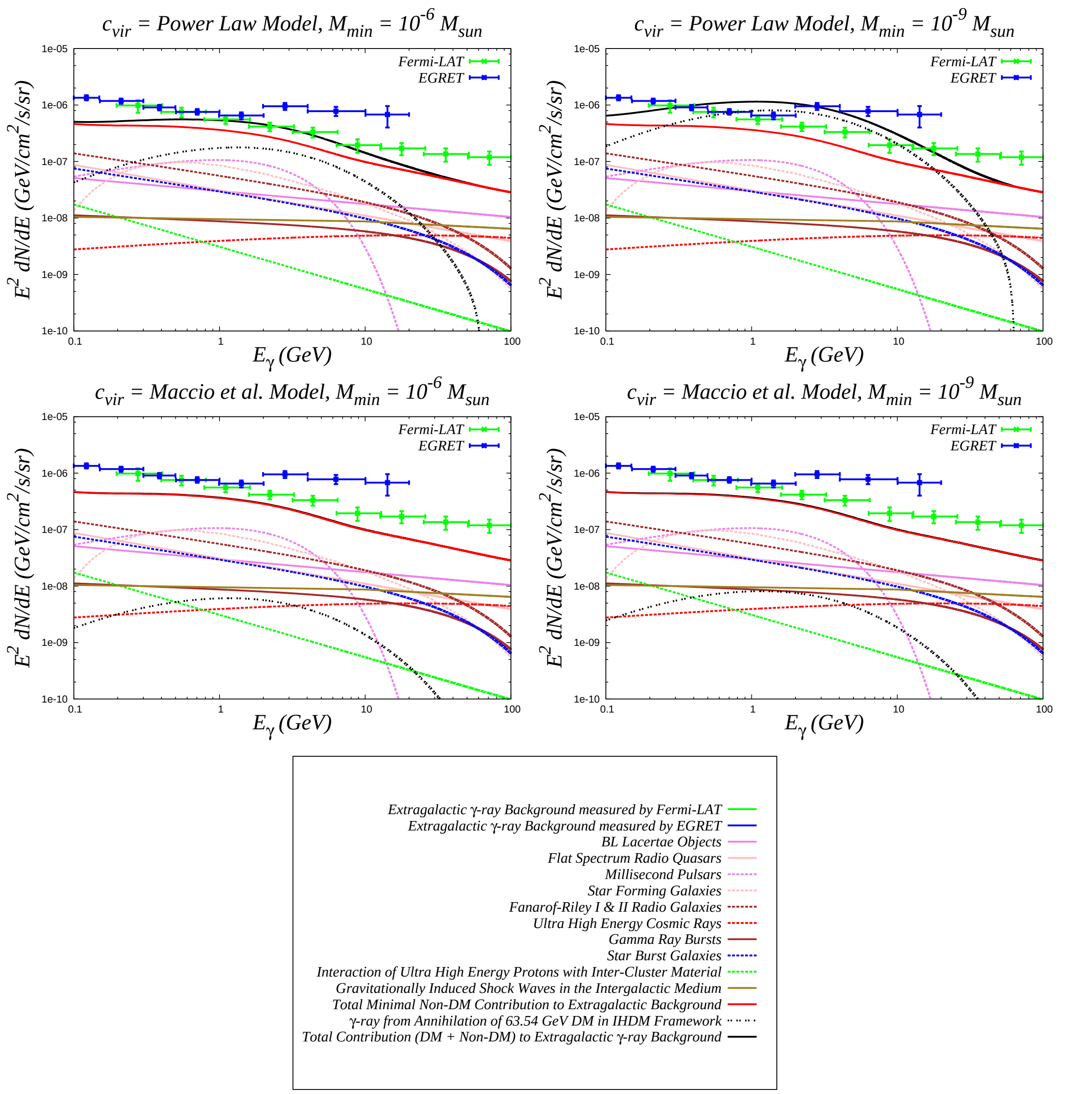

Figure 6.14: *The observed extragalactic γ-ray fluxes by EGRET and Fermi LAT are compared with the sum total value of the γ-ray fluxes obtained from the present calculation. The calculated value of extragalactic γ-ray flux is obtained by summing over the γ-ray flux calculated from DM annihilation for IHDM LIP DM (considered in this work) and other possible γ-rays (extragalactic γ-ray sources of non-DM origin) from extragalactic sources. See text for details.*

where M_{200} denotes the mass enclosed within a radial region where the avaraged density is 200 times more than the critical density of the universe. We have performed the calculation of extragalactic photon flux for DM for the best-fit model parameter in IHDM

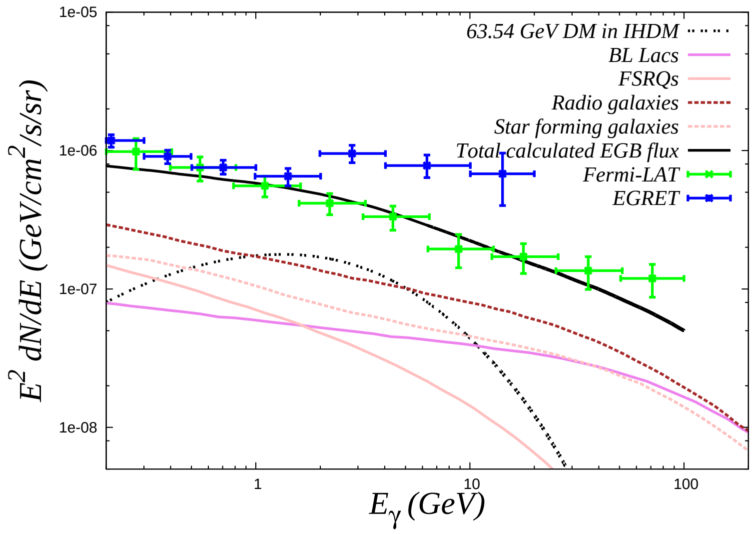

Figure 6.15: *Comparison of the observed γ-ray fluxes by EGRET and Fermi LAT theoretical results for γ-ray spectra for 63.54 GeV DM in IHDM considering the modelling of extragalactic and astrophysical parameters as done in Ref. [15]. See text for details*

based on their extragalactic modelling. The result is shown in Fig. 6.15. In Fig. 6.15 we have only considered the contributions to EGB only from radio galaxies, BL lacs, FSRQs and SFGs other than that from DM annihilation. The sum total contributions to EGB is found to fit reasonably well with Fermi LAT data.

6.6.3 Galactic (sub)halo contribution to DIGRB

There could be a significant contribution to DIGRB which is of galactic origin along the line of sight due to the passing of the signal from extragalactic sources through the Milky Way galactic halos and subhalos. Different N-body simulations predict highly galactocentric smooth DM density profiles far beyond our visible galaxy. Also the main DM halo is found to host a large amount of substructures in form of subhalos in these simulations [453, 454].

The DM density profile of galactic main halo, in principle, yields an anisotropic γ-ray signal from DM annihilation. But the signal from the DM annihilation at the galactic substructures could potentially give rise to an almost isotropic signal since this generated γ-ray flux is proportional to the less centrally concentrated number density distribution of subhalos which is not the case of the smooth DM annihilation signal in the main halo DM distribution [59].

The smooth galactic halo assumes only the host halo density without any effect of substructures embedded in it. The averaged photon intensity from DM annihilation in such smooth halo of the Milky Way can be written as,

$$\frac{dI_{\rm sm}(E_\gamma)}{dE_\gamma} = \frac{\langle\sigma v\rangle}{2m_{\rm DM}^2}\frac{dN_\gamma}{dE_\gamma}\frac{1}{\Omega_e}\int_{V_*} dV\ \frac{\rho_{\rm MW}^2(s,b,\ell)}{4\pi s^2}, \tag{6.53}$$

where s and Ω_e are the distance from the galactic centre and the observed solid angle. In the above b and ℓ are galactic coordinates (latitude and longitude respectively) chosen to be $30° \le |b| \le 90°$, $0 \le \ell < 2\pi$ [15]. $r_{s,\rm MW} = 21.5$ kpc, $r_{\rm vir,MW} = 258$ kpc, $\rho_{s,\rm MW} = 4.9\times10^6\,M_\odot$ kpc^{-3}, $M_{\rm vir,MW} = 1.0\times10^{12}\,M_\odot$ [3] are chosen for our calculation. [5]

The photon flux produced in the smooth halo component are much subdominant than that yielded in the subhalos and hence they contribute negligibly to extragalactic γ-ray background. In ΛCDM cosmology, the formation of the structures is assumed to be hierarchical. The smaller DM halos are formed first and the larger ones later. In the period of structure formation the smaller halos are tidally disrupted after being captured by the larger host halos of galaxies and clusters and hence the outer low density layers are stripped in this process. Thus the central dense cores only survive and behave as subhalos of the host halos. These substructures of DM halo enrich DM phenomenology by giving rise to substantially enhancement of the DM annihilation rates within a halo.

[5]The NFW halo profile of Milky Way is chosen as $\rho_{\rm MW}(r) = \frac{\rho_{s,\rm MW}}{(r/r_{s,\rm MW})(1+r/r_{s,\rm MW})}$ where r and $r_{s,\rm MW}$ are the galactocentric and scale radii respectively and $\rho_{s,\rm MW}$ is the scale density. The above-mentioned halo profile is assumed to extend up to the virial radius $r_{\rm vir,MW}$ with the virial mass $M_{\rm vir,MW}$.

The contribution to differential gamma-ray flux from subhalo can be obtained from the differential luminosity profile of each subhalo which can be given by,

$$\frac{dL_\gamma}{dE_\gamma} = \frac{\langle\sigma v\rangle}{2m_{\rm DM}^2}\frac{dN_\gamma}{dE_\gamma}\int dV_{\rm sh}\,\rho_{\rm sh}^2. \tag{6.54}$$

For an individual subhalo with mass M, the photon intensity can be written as,

$$\frac{d\mathcal{I}(E_\gamma,s,M)}{dE_\gamma} = \frac{1}{4\pi s^2}\frac{dL(E_\gamma,M)}{dE_\gamma} = \frac{1}{4\pi s^2}\frac{b_{\rm gs}\langle\sigma v\rangle}{2m_{\rm DM}^2}\frac{dN_\gamma}{dE_\gamma}\frac{M^2}{r_{s,{\rm sh}}(M)^3}\mathcal{G}[c_{\rm cut}(M)]. \tag{6.55}$$

where $r_{s,{\rm sh}}$ denotes the scale radius of the subhalo. In the above the factor $b_{\rm gs}$ determines the contribution from substructure within each subhalo ('subsubhalo') and is chosen to be 2 [455]. The function $\mathcal{G}[c_{\rm cut}(M)]$ which can be obtained using integral over the volume of each satellite and the form of subhalo concentration $c_{\rm cut}$ [6] following Ref. [456], can be given as,

$$\mathcal{G}[c_{\rm cut}(M)] = \frac{1}{12\pi}\left[1-\frac{1}{(1+c_{\rm cut})^3}\right]\left[\ln(1+c_{\rm cut})-\frac{c_{\rm cut}}{1+c_{\rm cut}}\right]^{-2}, \tag{6.57}$$

The total γ-ray intensity at Earth from the annihilation of dark matter particles in galactic subhalos can be written after integrating Eq. 6.55 over the distribution of Milky Way subhalos as,

$$\frac{d\mathcal{I}_{\rm sh}(E_\gamma)}{dE_\gamma} = \int dV dM \frac{dn_{\rm sh}(M,s,\ell,b)}{dM}\frac{d\mathcal{I}(E_\gamma,s,M)}{dE_\gamma}, \tag{6.58}$$

where $\int dMdV(dn_{\rm sh}/dM)$ is the total number of subhalos in the Milky Way. The form

[6] We choose the DM density within each subhalo of mass M to be truncated NFW halo profile,

$$\rho_{\rm sh}(r_{\rm sh}|M) = \begin{cases} \rho_{\rm NFW}(r_{\rm sh}|M) & \text{for} \quad r_{\rm sh} \leq r_{\rm cut}, \\ 0 & \text{for} \quad r_{\rm sh} > r_{\rm cut}, \end{cases} \tag{6.56}$$

where $c_{\rm cut}$ is the cutoff radius for this profile.

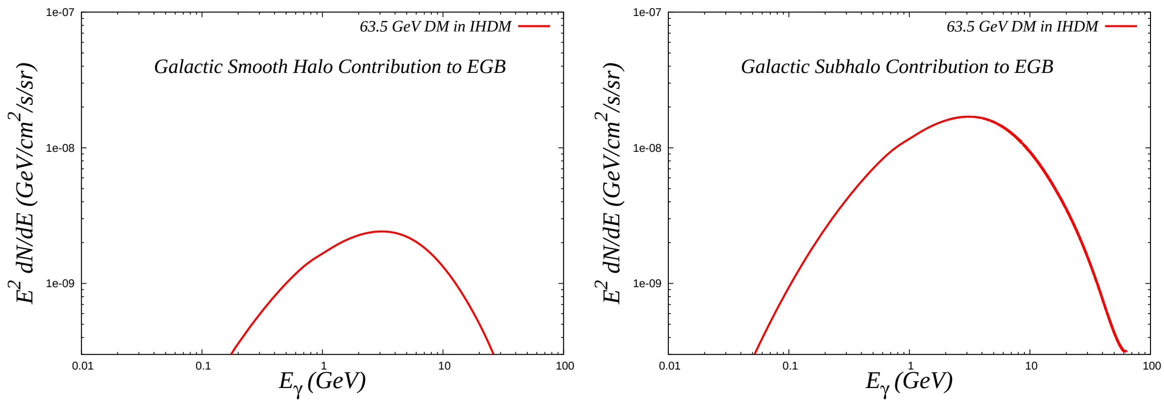

Figure 6.16: *Galactic smooth halo and subhalo contributions to the extragalactic gamma-ray flux for LIP 63.54 GeV dark matter in IHDM. See text for details.*

of subhalo mass function, $dn_{\rm sh}/dM$ is chosen to be the anti-biased model [7] following Ref. [456] for our calculation.

In order to confront observations, we are interested in the averaged intensity of γ-rays per unit energy emitted due to DM annihilation over the whole galaxy,

$$\begin{aligned}\frac{dI_{\rm sh}(E_\gamma)}{dE_\gamma} &= \frac{1}{\Omega_e}\frac{d\mathcal{I}_{\rm sh}(E_\gamma)}{dE_\gamma} = \frac{1}{\Omega_e}\int_{M_*}\int_{V_*(M)} dV\,dM \frac{dn_{\rm sh}(M,s,\ell,b)}{dM}\frac{d\mathcal{I}(E_\gamma,s,M)}{dE_\gamma} \\ &= \int_{M_*} dM \int_{V_*(M)} dV \frac{dn_{\rm sh}(M,s,\ell,b)}{dM}\frac{1}{4\pi s^2}\frac{\langle\sigma v\rangle}{m_{\rm DM}^2}\frac{dN_\gamma}{dE_\gamma}\frac{M^2}{r_{s,\rm sh}(M)^3}\mathcal{G}[c_{\rm cut}(M)] \quad (6.59)\end{aligned}$$

where V_* is the volume beyond which satellites remain unresolved. The considered mass range of the subhalos is $10^{-6}M_\odot \leq M_* \leq 10^{10}M_\odot$. Since from the luminosity L one gets the knowledge of the subhalo mass M we consider the subhalo mass range in such a way that bright as well as faint subhalos are included in the calculation. Also since luminosity is directly related to the flux sensitivity of Fermi ($F_{\rm sens}$) by the relation, $L(M) = 4\pi s_*^2(M)F_{\rm sens}$, they remain unresolvable beyond the distance $s_*(M) = \sqrt{L(M)/4\pi F_{\rm sens}}$, where the flux sensitivity of Fermi-LAT, $F_{\rm sens} = 2\times10^{-10}{\rm cm}^{-2}{\rm s}^{-1}$ [456] and $L(M)$ is the

[7] In another model ('unbiased') for $n_{\rm sh}(r)$, the subhalo distribution is assumed to follow its parent NFW halo distribution whereas in the anti-biased model the subhalo distribution is flatter than NFW halo [456].

luminosity obtained by integrating Eq. 6.54 over energy.

In Fig. 6.16, we show the contributions to the EGB from both galactic smooth halos and subhalos. From the left panel of Fig. 6.16 we see that the contribution to the EGB is much subdominant for the annihilation of DM within galactic smooth halo. For our chosen galactic substructure model, this contribution is comparable to that from extragalactic dark matter annihilations calculated using c_{vir} of Macciò *et al.* model. For the other case where the gamma ray flux from extragalactic dark matter annihilations have been calculated using c_{vir} of power law model, the contributions from the galactic subhalos are much negligible.

Chapter 7

3.5 keV X-ray Line Signal from Decay of Right-Handed Neutrino due to Transition Magnetic Moment

In this chapter we consider the dark matter model with radiative neutrino mass generation where the Standard Model is extended with three right-handed singlet neutrinos (N_1, N_2 and N_3) and one additional $\mathrm{SU}(2)_L$ doublet scalar η. One of the right-handed neutrinos (N_1), being lightest among them, is a leptophilic fermionic dark matter candidate whose stability is ensured by the imposed $\mathbb{Z}_2$ symmetry on this model. The second lightest right-handed neutrino (N_2) is assumed to be nearly degenerated with the lightest one enhancing the co-annihilation between them. The effective interaction term among the lightest, second lightest right-handed neutrinos and photon containing transition magnetic moment is responsible for the decay of heavier right-handed neutrino to the lightest one and a photon ($N_2 \to N_1 + \gamma$). This radiative decay of heavier right-handed neutrino with charged scalar and leptons in internal lines could explain the X-ray line signal ~ 3.5 keV recently claimed by XMM-Newton X-ray observatory from different galaxy clusters and

Andromeda galaxy (M31). The value of the transition magnetic moment is computed and found to be several orders of magnitude below the current reach of various direct dark matter searches. The other parameter space in this framework in the light of the observed signal is further investigated.

7.1 Introduction

Recently an evidence of X-ray line of energy 3.55 keV with more than 3σ CL has been reported from the analysis of X-ray data of 73 galaxy clusters from XMM-Newton observatory [457]. Another group has also claimed a similar line (3.52 keV X-ray line at 4.4σ CL) from the data of X-ray spectra of Andromeda galaxy (M31) and Perseus cluster [458]. The galaxy clusters are assumed to contain huge amount of DM. Thus the signal may have a possible origin related to DM. The observed line has been explained as decay of sterile neutrino DM ($\nu_s \to \nu + \gamma$) with mass of the sterile neutrino 7.06 ± 0.05 keV and mixing angle $\sin^2(2\theta) = (2.2 - 20) \times 10^{-11}$ [458]. Recently many other interesting ideas have been proposed to explain this line signal to come from DM [459–481].

The neutrino oscillation data [482–485] provide strong evidences for neutrino mass. The non-zero neutrino masses and evidences of DM give hints to the physics beyond the Standard Model (SM). The two beyond SM phenomenon, namely the origin of neutrino masses and the existence of cold DM may have a connection. In this work we focus on the simplest framework which invokes this idea of connecting both sectors has been proposed by Ma [203]. In this model the neutrino masses are generated via radiative processes with only the DM particles in the loop. The right-handed neutrino which can be a possible DM candidate interacts with lepton doublets and hence DM in this scenario is leptophilic in nature. The imposed discreet $\mathbb{Z}_2$ symmetry on this model not only forbids the tree-level Dirac mass terms but also assure a stable cold DM candidate. Phenomenological prospects for collider and DM in this model have been done in Refs. [486–495]. In this work we consider the case where the lightest right-handed neutrino (N_1) is the cold DM candidate and the second lightest right-handed neutrino (N_2) is nearly degenerated with the cold DM candidate. This situation provides rich phenomenology in direct detection of such DM candidate [496]. Elastic scattering cross section for DM-nucleon interaction is suppressed in this case and inelastic scattering that occurs radiatively dominates. The transition from N_2 to N_1 gives rise to monochromatic photon with energy equal to the mass difference between the lightest and second lightest right-handed neutrinos. If the mass difference between N_2 and $N1$ is of $\sim$ keV, then the recent observation of X-ray line can be accommodated in this beyond SM scenario.

The present chapter is organised as follows. In Sec. 7.2 the theoretical framework of the model is briefly discussed. Explanation of the observed X-ray line in this model framework and a study of the constrained parameter space are done in the next section (Sec. 7.4).

7.2 Radiative Neutrino Mass Model

We have already furnished about this model framewok in Section 3.4 of Chapter 3. But for the sake of completeness of the following discussions, we shall briefly discuss the model here.

We have considered the model which is nothing but an extension of the Standard Model with three gauge singlet right-handed neutrinos N_1, N_2, N_3 and extra $\mathrm{SU}(2)_L$ doublet scalar η as the extra fields in this framework. The model framework was first proposed by Ernest Ma [203] in 2006. The fields in this model can be written as,

$$N_1, \quad N_2, \quad N_3, \quad \eta \ = \begin{pmatrix} \eta^+ \\ \eta^0 \end{pmatrix}. \tag{7.1}$$

The doublet scalar η is considered to be inert in the sense that it does not obtain any vacuum expectation value via any process. We impose an additional discreet $\mathbb{Z}_2$ symmetry on the model. in order to stabilise some field in this model. The cold DM candidate in this model is thus guaranteed by this symmetry. In addition, this additional $\mathbb{Z}_2$ symmetry prevents any tree-level Dirac mass term of the neutrinos in this model. The Standard Model gauge charges and the $\mathbb{Z}_2$ charges of the additional particles are given in Tab. 3.1 in Chapter 3.

For the case of right-handed neutrinos, N_k $(k = 1, 2, 3)$ that are invariant under both SM gauge symmetry and $\mathbb{Z}_2$ symmetry, the Lagrangian can be given as (Eq. 3.32 in Chapter 3),

$$\mathcal{L}_N = \overline{N_i} i \partial\!\!\!/ P_R N_i + \left(D_\mu \eta\right)^\dagger \left(D^\mu \eta\right) - \frac{M_i}{2} \overline{N_i{}^c} P_R N_i + h_{\alpha i} \overline{\ell_\alpha} \eta^\dagger P_R N_i + \text{h.c.}. \tag{7.2}$$

In the above $h_{\alpha k}$, ℓ_α and M_k denote Yukawa couplings, lepton doublet and the mass of the right-handed neutrino of type k (N_k) respectively. We choose the values of the parameter M_k to be real since this does not pose any loss of generality.

For the case of the Higgs doublet Φ and the additional $\mathrm{SU}(2)_L$ doublet η the invariant scalar potential is written as (Eq. 3.33 in Chapter 3),

$$\begin{aligned}\mathcal{V}(\phi, \eta) = \ & m_\phi^2 \phi^\dagger \phi + m_\eta^2 \eta^\dagger \eta + \frac{\lambda_1}{2} \left(\phi^\dagger \phi\right)^2 + \frac{\lambda_2}{2} \left(\eta^\dagger \eta\right)^2 \\ & + \lambda_3 \left(\phi^\dagger \phi\right) \left(\eta^\dagger \eta\right) + \lambda_4 \left(\phi^\dagger \eta\right) \left(\eta^\dagger \phi\right) + \frac{\lambda_5}{2} \left(\phi^\dagger \eta\right)^2 + \text{h.c.}.\end{aligned} \tag{7.3}$$

As mentioned earlier, the tree-level Dirac mass terms for neutrinos can not be generated as seen from Eq. 7.3. This is because of the fact that the vacuum expectation value of the doublet η ($\langle\eta\rangle$) is zero. On the other hand, the SM Higgs doublet gets vacuum expectation value $v = 246$ GeV after electroweak symmetry breaking and as a result, the Majorana masses of neutrinos can be generated radiatively via one-loop diagrams with η^0 and N_k in internal lines. The model could also explain both the possibilities of scalar (η^0) DM as well as fermionic (N_k) DM. Here we consider the mass of one of the three right-handed neutrinos (N_1) to be lightest among all the additional fields added to the SM. As a result, the lightest right-handed neutrino becomes a stable candidate for DM. Needless to mention in this context that the right-handed neutrino is leptophilic in nature since it only interacts with the SM lepton doublet as seen in Eq. 7.2 (the forth term of the Lagrangian in Eq. 7.2).

The radiatively generated effective Majorana neutrino masses can be expressed as [203],

$$(m_\nu)_{\alpha\beta} \simeq \sum_{i=1}^{3} \frac{2\lambda_5 h_{\alpha i} h_{\beta i} v^2}{(4\pi)^2 M_i} I\left(\frac{M_i^2}{M_\eta^2}\right), \tag{7.4}$$

where $M_\eta^2 \simeq m_\eta^2 + (\lambda_3 + \lambda_4)\, v^2/2$, M_i are the masses of η and N_i respectively [1]. The smallness of the mass term is guaranteed by the coupling λ_5. The factor $I\,(x)$ can be written as,

$$I\,(x) = \frac{x}{1-x}\left(1 + \frac{x \log x}{1-x}\right). \tag{7.5}$$

Assuming the mass matrix of Eq. 7.4 to be diagonalised using the PMNS matrix which provides very well explanation for the neutrino oscillation data, one can find some

[1]Masses of the real and imaginary parts of η^0 and $\eta^\pm$ are taken to be degenerated for simplicity

conditions imposed on $h_{\alpha i}$ as [488],

$$\sum_{k=1}^{3}\Big(2h_{ek}^2\sin 2\theta+2\sqrt{2}h_{ek}(h_{\mu k}-h_{\tau k})\cos 2\theta-(h_{\tau k}-h_{\mu k})^2\sin 2\theta\Big)=0,$$
$$\sum_{k=1}^{3}h_{ek}\,(h_{\mu k}+h_{\tau k})=0,\qquad \sum_{k=1}^{3}(h_{\mu k}-h_{\tau k})\,(h_{\mu k}+h_{\tau k})=0. \tag{7.6}$$

One of the simple solutions for these conditions on $h_{\alpha i}$ (Eq. 7.6) is achieved by choosing the flavour structure of $h_{\alpha i}$ as,

$$h_{ei}=0,\quad h_{\mu i}=h_{\tau i};\quad h_{ej}\neq 0,\quad h_{\mu j}=-h_{\tau j},\quad (i\neq j) \tag{7.7}$$

Thus either i or j takes any two values of k (1,2,3). In matrix notation the structure of the chosen Yukawa couplings of Eq. 7.7 can be written as,

$$h_{\alpha i}=\begin{pmatrix}0 & 0 & h'_3\\ h_1 & h_2 & h_3\\ h_1 & h_2 & -h_3\end{pmatrix}. \tag{7.8}$$

The Yukawa couplings of Eq. 7.8 imply the values of θ_{12}, θ_{23} and θ_{13} to be $\tan^{-1}(\frac{h'_3}{\sqrt{2}h_3})$, $\pi/4$ and 0 respectively. But recent observations suggest different values of these mixing angles. Then the structure of the matrix will be slightly modified [493–495]. The result of this work will not be vastly modified due to such changes.

7.3 Estimation of DM Relic Abundance in this Model Framework

A rough estimate for the thermal production of the DM relic abundance can be made in the present framework. The right-handed neutrinos in this model can, in principle, be produced in the early universe via few processes such as active-sterile neutrino transition, resonant active-sterile neutrino oscillations when lepton asymmetries are present or during the period of inflation. The production of both N_1 and N_2 in the early universe are assumed to be similar. Since the mass of N_2 is slightly higher than that of N_1 in this model, there will be the decay channels from $N_2 \to N_1$. The decay mode such as $N_2 \to N_1+\nu+\bar{\nu}$ is more suppressed than the $N_2 \to N_1 + \gamma$ because the former is a 3-body decay mode of N_2 being phase space suppressed and also it requires an additional suppression from Z-mass squared term other than the similar loop contributions of $N_2 \to N_1 + \gamma$ channel. The Yukawa coupling is also needed to be small to suppress the transition. Thus the production of DM relic abundance which is dependent on the Yukawa coupling should have been affected. But the co-annihilation effect between the two lightest fermions N_1 and N_2 which are very degenerate in mass leads to an effective enhanced annihilation cross-section [497] written as $\langle\sigma v\rangle_{\rm eff} = a_{\rm eff} + b_{\rm eff} v^2 + \mathcal{O}(v^4)$ with

$$a_{\rm eff} = \frac{\xi^2}{2\pi}\frac{M_1^2}{\left(M_\eta^2+M_1^2\right)^2}, \tag{7.9}$$

$$b_{\rm eff} = \frac{|h_1^2+h_2^2|^2}{24\pi}\frac{M_1^2\left(M_\eta^4+M_1^4\right)}{\left(M_\eta^2+M_1^2\right)^4} + \frac{\xi^2}{2\pi}\frac{M_1^2\left(M_\eta^4-3M_\eta^2M_1^2-M_1^4\right)}{\left(M_\eta^2+M_1^2\right)^4}, \tag{7.10}$$

where ξ is the phase difference between the Yukawa couplings h_1 and h_2. In the above, the terms proportional to ξ^2 come from $N_1 - N_2$ co-annihilation effect. In Eq. 7.10 the terms proportional to the square of the Yukawa couplings, h_1^2 and h_2^2 are due to $N_1 - N_1$ and $N_2 - N_2$ annihilations respectively. Thus $a_{\rm eff}$-term in Eq. 7.9 which is responsible for

s-wave is solely dependent on the co-annihilation effect. Hence it is possible to produce correct DM relic density by thermal production although the Yukawa coupling is very small. In addition to $N_1 - N_2$ co-annihilation, the co-annihilation of N_1 with inert doublet η also plays an important role in obtaining correct DM relic abundance. Hence for very small or negligible ξ, the contribution from $N_1 - \eta$ co-annihilation also helps to produce proper DM relic density. Thus suitable DM relic density set by the thermal production can always be obtained in this framework by the collective contributions from both the co-annihilations, $N_1 - N_2$ and $N_1 - \eta$ [496].

7.4 X-ray line in this framework

One of the terms in the Lagrangian of this framework that represents the interaction among the lightest right-handed neutrino (N_1), second lightest right-handed neutrino (N_2) and photon is given by [496],

$$\mathcal{L} = i\left(\frac{\mu_{12}}{2}\right)\overline{N_2}\sigma^{\mu\nu}N_1F_{\mu\nu} \ , \tag{7.11}$$

where μ_{12} is the coefficient of this interaction and called *transition magnetic moment* between the right-handed neutrinos, N_1 and N_2. In the above $F_{\mu\nu}$ is the so-called electromagnetic field tensor. The three-point vertex interaction term of this type is also responsible in contributing to the inelastic scattering of the right-handed neutrinos with nucleons via 1-loop processes.

The X-ray line appears when there is a transition from the state, N_2 to N_1. The presence of transition magnetic moment solely triggers such a decay process to occur.

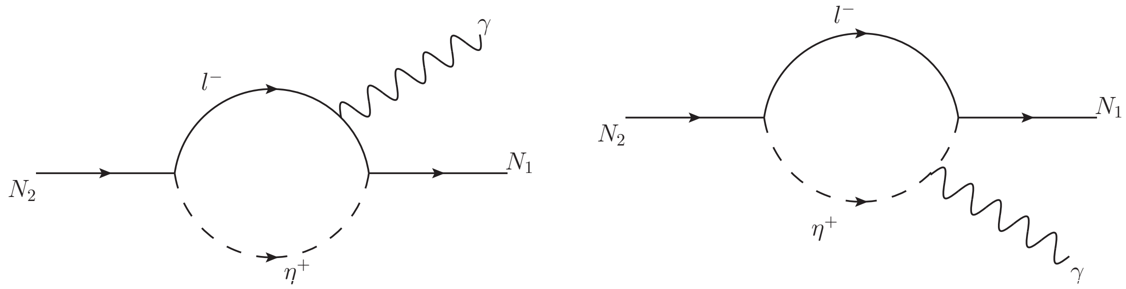

Figure 7.1: *Feynman diagrams showing the decay of second lightest right-handed neutrino, N_2 to lightest right-handed neutrino, N_1 and photon (γ) via radiative processes.*

The expression of decay width for this process can be written as,

$$\Gamma(N_2 \to N_1\gamma) = \frac{\mu_{12}^2}{\pi}\delta^3 \quad , \tag{7.12}$$

where $\delta = E_\gamma$ is the energy of the emitted photon which is nothing but the mass difference between the lightest and the second lightest right handed neutrinos present in this framework. The Feynman diagrams responsible for such process are shown in Fig. 7.1.

The calculated value of the decay width for the decay process of N_2 to N_1 and a photon from the observed X-ray line data is $\sim 1.15 \times 10^{-52}$ GeV [478]. Thus one can find from Eq. 7.12 that to comply the observed data for X-ray line with the framework of this model, the absolute value of μ_{12} should be $\sim 2.9 \times 10^{-18}$ GeV^{-1}.

The order of the value of $|\mu_{12}|$ is particularly important for studying the prospects of the direct detection of DM. The predicted value of $|\mu_{12}|$ from the recently reported X-ray line data is several orders of magnitude below from the current reach of various DM direct detection experiments [496]. As the mass of the DM in this model is the lightest right-handed neutrino with heavy mass possibly in the range from few hundreds of GeV to few thousands of GeV, the direct DM searches should probe these massive right-handed neutrinos in this mass range.

The expression for μ_{12} in the present scenario can be written in terms of model parameters [496] as,

$$\mu_{12} = -\sum_{\alpha} \frac{\mathrm{Im}\,(h^*_{\alpha 2} h_{\alpha 1})\, e}{2(4\pi)^2 M_\eta^2} 2 M_1 I_{\mathrm{m}} \left(\frac{M_1^2}{M_\eta^2}, \frac{m_\alpha^2}{M_\eta^2} \right), \tag{7.13}$$

m_α is the mass eigenvalue of ordinary neutrino of flavour α, e is the electric charge of proton. The term $\mathrm{Im}\,(h^*_{\alpha 2} h_{\alpha 1})$ in Eqn. 7.13 is related to the phase difference, ξ between the Yukawa couplings $h_{\alpha 2}$ and $h_{\alpha 1}$ for flavour α. For the matrix of Yukawa couplings of Eq. 7.8 the value of the factor, $\mathrm{Im}\,(h^*_{\alpha 2} h_{\alpha 1})$ is zero for one flavour and contributes equally for the remaining flavours. In the above the function I_{m} comes from loop integral and can be expressed as,

$$I_{\mathrm{m}}(x, y) = -\int_0^1 \frac{z(1-z)}{xz^2 - (1 + x - y)z + 1} dz. \tag{7.14}$$

Considering masses of ordinary charged leptons are negligible with respect to that of η, i.e., $m_\alpha \ll M_\eta$, the allowed parameter space for the model parameters, M_1, M_η and ξ is obtained from the computed value of $|\mu_{12}|$ from 3.5 keV X-ray line data. [2] The plot showing the variation of the parameters constrained from observed X-ray line data is shown in Fig. 7.2. In this plot the ratio (r) of M_η to M_1 is taken to be between 1.0 to 10.0, i.e., $1.0 < M_\eta/M_1 \leq 10.0$. The range of the constrained values of the phase factor, ξ for those mass ratios ($1.0 < r \leq 10.0$) spanning from $\sim 10^{-14}$ to $\sim 10^{-8}$. The situation would have been slightly modified if one incorporate the precise values of mixing angles (for example, non-zero θ_{13}). The Yukawa matrix structure is then modified and the phase factor for each flavour α will be different in general. But it can be shown that for such cases the order of the sum of the phase factors will be almost of similar order that has been obtained in this case. The phase factor determines the co-annihilation

[2] The mass of ordinary neutrino is several orders of magnitude smaller than the mass of doublet scalar η which is few hundreds of GeV or more in this framework and hence the ratio, $\frac{m_\alpha}{M_\eta}$ is $\ll 1$

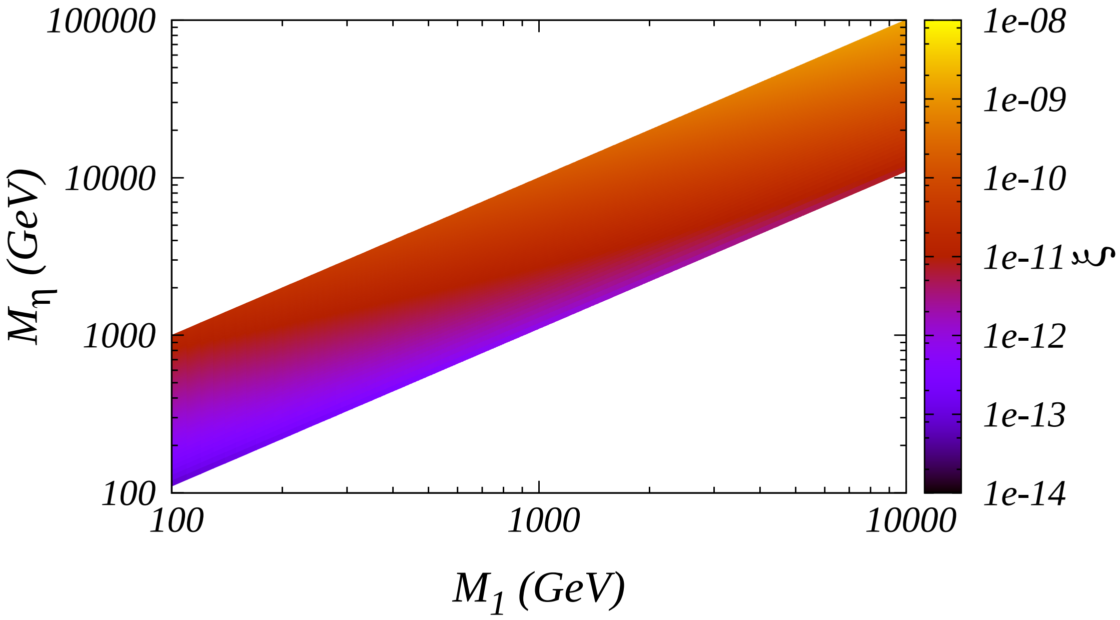

Figure 7.2: *The allowed parameter space consisting of M_1, M_η and ξ consistent with the recently reported 3.5 keV X-ray line data. The value of ratio of the mass of N_1 to that of η is chosen to be within 10.0, i.e.,* $1.0 < M_\eta/M_1 \leq 10.0$ *in this plot. The considered range of M_1 is from* 10^2 *GeV to* 10^4 *GeV. The phase factor ξ are shown by the colour index where ξ varies from blue coloured region to yellow region as its value increases. See text for more details.*

of $N_1 - N_2$ and the effective interaction of right-handed neutrino DM with nuclei. The result shows the values of phase factor ξ with much smaller orders for the considered mass range than expected to be give signatures of direct detection. Hence the co-annihilation channels and the DM-nuclei interaction is much lowered from the computed value of ξ constrained by the 3.5 keV X-ray line data. Thus the possibility of direct detection of DM in this framework is suppressed by few orders from the reach of ongoing direct DM search experiments.

Chapter 8

Summary, Conclusion & Future Outlook

In this thesis some particle physics models for dark matter are proposed and some other known models are explored in detail in order to study the phenomenology of indirect detection of dark matter through gamma rays. The theoretical frameworks for the unresolved emission of excess gamma rays from Galactic Centre, Fermi bubble, galactic dark matter halo region, dwarf galaxies as well as from extragalactic sources are explored in the light of various well-motivated particle physics models for dark matter. Moreover, the anomalous X-ray lines from the observation of Andromeda galaxy and 73 other galaxy clusters are confronted with a simple leptophilic model for dark matter in this thesis. In the first three chapters the physics of dark matter, its indirect detection as well as the particle physics models for dark matter that are addressed in this thesis are discussed at length. In the following four chapters thorough analyses of the considered particle physics models are furnished. These include the detailed theoretical aspects of such models are explored and the interpretation of indirect detection signatures of dark matter. Finally the important conclusions obtained in this whole thesis work and future outlook on dark matter physics will be addressed in this chapter.

In Chapter 1, we motivate our work starting with the elaborate discussion on the very basic physics of dark matter such as the evidences of dark matter, the nature and types of dark matter etc. The detailed discussions about the indirect detection of dark matter are made in the following chapter (Chapter 2). Chapter 2 starts with a discussion on the possible dark matter annihilation products that can be detected in ongoing and future experiments. This is followed by a discussion about the formalism of dark matter indirect detection via neutral particles such as gamma rays and neutrinos. Moreover, different dark matter halo profiles and their nature are also mentioned. Finally at the end of this chapter (Chapter 2) we briefly furnish the potentially suitable astrophysical targets that have been considered in this thesis for studying dark matter indirect detections. Chapter 3 is devoted to the particle physics models (beyond the Standard Model) for dark matter that we have been studied throughout this thesis.

In Chapter 4, we have investigated the phenomenological implications of dark matter coming from a very well known SUSY breaking model, namely minimal anomaly mediated supersymmetry breaking (mAMSB) model. The suitable candidate in this model is the neutralino stabilised by the conservation of R-parity in SUSY theory. We have randomly scanned the parameter space of this model within the theoretical bounds of the parameter space of this model and for each point in paremeter space, we obtain a neutral stable candidate (neutralino) of dark matter. In doing so, latest bound on the chargino mass as given by the ATLAS collaboration is adopted.

The mass of the LSP neutralino in the present scenario is obtained in two regions of which one is around 1 TeV and the other is at a somewhat higher range of $\sim$ 2 TeV. We have checked that these neutralinos are predominantly of wino type. The measure of the naturalness which is expressed in terms of the commonly used fine tuning parameters are obtained for the constrained neuralino masses (vide earlier) in the present scenario,

$$\frac{\delta {M_Z}^2}{{M_Z}^2}(\mu^2) \sim 10^4, \quad \frac{\delta {M_Z}^2}{{M_Z}^2}(B_\mu) \sim 10^3$$

$$\frac{\delta M_t}{M_t}(\mu^2) \sim 10^4, \quad \frac{\delta M_t}{M_t}(\mu^2) \sim 10^3 \ ,$$

where the symbols have their usual significance.

We calculate the relic densities of such neutralinos and compare them with WMAP bounds to obtain the mass zones of these mAMSB neutralinos that satisfy WMAP limits. The allowed parameters determined from such constraints are then used to study the direct and indirect detections of the proposed dark matter candidate which in this case is neutralino, in the present mAMSB model.

The scattering cross sections for the dark matter particles scattered off the nucleus of the detecting material are determined by the nuclear form factors and the dark matter-nucleon coupling. The two types of cross sections, namely spin independent (zero nuclear spin at the ground state) and spin dependent, are determined by the different form factors and dark matter-nucleon couplings. We calculate both the spin dependent and spin independent scattering cross sections with the constrained zone(s) of the present neutralino dark matter parameter space and hence compared our results with several recent ongoing direct detection experimental results. The calculated cross sections for different dark matter masses are thus calculated and are found to be below the upper limits of many well known experiments. From experimental point of view, the future advanced direct detection techniques may probe those regions in mass-cross section plane given from the model.

We have computed the gamma ray flux from the galactic centre and its neighbourhood, considering that they are produced from the annihilation of dark matter in mAMSB model. For this reason, we have taken several well known theoretically motivated dark matter halo profiles such as NFW profile, Moore profile, isothermal profiles with core and Einasto profiles and compute the flux from different positions of the halo plane. As the allowed mass of the neutralino (dark matter) is high ($\sim$ few GeV to $\sim 10^3$ GeV), the energies of the gamma rays from dark matter annihilations are also of that order. Therefore high energy gamma ray search experiments may verify the present model. For this purpose, we have chosen the HESS experiment and compared our results for different halo profiles considered, with the observed γ-flux of this experiment. In the passing we also mention that another water $\hat{C}$erenkov detector namely HAWC (High-Altitude Water Cherenkov Gamma-Ray Observatory) near Puebla, Mexico can also detect gamma ray annihilation signal in the energy domain of $1 \sim 2$ TeV. But as mentioned, in this work we consider only HESS experiment. We find that the γ-fluxes for non-cuspy profiles like isothermal profile (flat) and Einasto profile, are orders below the HESS results whereas the cuspy profiles like Moore profile overestimate the HESS result. Calculations using the other cuspy profile, namely the NFW profile requires a boost of $\sim 10^3$ for comparison with HESS results. The Moore profile has an asymptotic slope, $\alpha = 1.5$, while the same for the NFW profile is $\alpha = 1.0$. Thus the former is steeper than the latter. Cuspy nature appears to influence the result. It is still a matter of investigation to understand whether halo profile at the galactic centre has a flat profile or a steep profile. The present analysis, within the framework of mAMSB model for dark matter candidate, seems to suggest that the cuspy nature of the profile appears to explain the HESS data better than the flat ones. We also like to add that we performed similar calculations with another flat halo profile namely Burkert profile [156], but the calulated γ flux is found to be even below than what is obtained for isothermal profile.

Different flavours of neutrinos from the dark matter annihilation at galactic centre are also addressed in the present work. The flux and detection of muon species of such neutrinos are calculated for the neutralino dark matter in mAMSB model. Given the masses of such dark matter candidates the energies of such neutrinos will also be in the range GeV to TeV. The location of the galactic centre with respect to earth is such that it can be best observed from southern hemisphere. The high energetic muon neutrinos may produce muons by the charged current scattering off ice or water and may be detected by their Cerenkov lights. We calculate the fluxes of neutrinos of different flavours due to annihilations of dark matter when viewed in the direction of the galactic centre as also at the other two chosen positions in its neighbourhood. The results are shown for the four halo profiles considered. In order to estimate the detection yield of such neutrinos in a terrestrial neutrino observatory, we have chosen the ANTARES under sea detector and calculated the muon yield for muon neutrinos from galactic centre for all the four halo profiles considered. The calculations of neutrinos in case of different halo profiles also exhibit similar trend as those for the calculation of γ flux. The value of thermal average of the squared halo density, $\langle\rho^2(r)\rangle$ is generally greater than $(\langle\rho(r)\rangle)^2$ due to the influence of a probable clumpy structure of dark matter halo profile, F_c(r), which is related to dark matter halo profile by,

$$\langle\rho^2(\tilde{r})\rangle = \rho_0^2 F_{halo}^2(r) F_c(r) \tag{8.1}$$

The clump structure of dark matter halo gives rise to enhancement factor. In the present study of different models of galactic halo structures, we did not consider any clumpy halo of dark matter. This study is for posterity. The WMAP allowed zone(s) for the mAMSB model for dark matter, are around (~ 1 TeV and ~ 2 TeV) which are high in mass regime. They may be addressed by, say, Kaluza-Klein dark matter. The future collider experiment may verify their existence.

In Chapter 5, we have addressed the apparently anomalous nature of gamma-spectrum from galactic centre and Fermi Bubbles. To this end, we promote the idea of multi-component Dark Matter (DM) to explain results from both direct and indirect detection experiments. In these models, since contribution of each DM candidate to relic abundance is summed up to meet WMAP/Planck measurements of $\Omega_{\rm DM}$, these candidates have larger annihilation cross-sections compared to the single-component DM models. We illustrate this fact by introducing an extra scalar to the popular single real scalar DM model. Thus a viable annihilating multicomponent dark matter model consists of two real gauge singlet scalars that are stabilized by $Z_2 \times Z_2'$ symmetry. Theoretical aspects of the model such as the vacuum stability bounds, perturbative unitarity and triviality constraints are checked for this model. As direct detection experimental results still show some conflict, we kept our options open, discussing different scenarios with different DM mass zones.

Guided by results of the direct detection experiments we considered three DM mass zones. The "low" zone of $7-11$ GeV is indicated by CDMS II, CoGeNT and CRESST II experiments. CRESST II also favours a "mid" zone ~ 25 GeV. As XENON 100 and LUX seem to rule out these zones, the only DM masses consistent with both XENON 100 or LUX and Planck observations belong to a "high" mass zone > 50 GeV. The advantage of dealing with this zone is that they do not give rise to unacceptable invisible branching ratio for Higgs. But a too high DM mass > 100 GeV predicts a photon flux from DM annihilations peaked at higher energies than what has been observed in the indirect detection experiments. This high DM mass zone will be probed by future XENON 1T [406] and LUX measurements.

We have chosen some representative benchmark points from the parameter space allowed by the direct detection experiments and Planck data. Now the obvious question comes regarding the robustness of the chosen benchmark points. In order to address the issue, DM annihilation cross-sections which do depend on M_S (or $M_{S'}$) and δ_2 (or δ_2') can be taken. Since DM annihilation cross-section is proportional to δ_2^2 (or ${\delta'}_2^2$), it is quite sensitive to the choice of δ_2 (or δ_2'). The allowed zones in the plots are shown so that the changes in the DM annihilation cross-section can be estimated. In addition, the individual photon flux for each of the singlet scalars, S and S' are given when we choose different benchmark points within the allowed parameter space.

There is some advantage of addressing both direct and indirect detection experiments. The allowed model parameter space is rather restricted by the direct DM detection experiments and relic density constraints as imposed by Planck. This makes indirect DM detection predictions quite sensitive to the assumed DM halo profiles. It may be noted that once some agreement in the direct DM sector is established and the background effects in the indirect detection experiments are better understood to delineate DM annihilation effects, in the framework of a given model, the experiments with the existing precision show some promise to identify the right DM halo profile. We have illustrated this with our proposed DM model.

In the framework of our proposed model, we wanted to exploit the advantage of having a multi-component DM model satisfying both direct and indirect DM experiments and in this process comment on the viability to choose the right DM halo profile. For completeness we also presented detailed calculations for theoretical constraints on this model as mentioned earlier.

In another detailed study in Chapter 6, we focus on the indirect detection of Dark Matter through the confrontation of unexplained galactic and extragalactic γ-ray signatures for a low mass DM model. For this, we have chosen a simple dark matter (DM) model, namely inert Higgs doublet model (IHDM) where scalar sector of Standard Model is extended by adding another SU$(2)_L$ doublet. The newly added doublet does not generate any VEV after spontaneous symmetry breaking. The 'inert' doublet is considered to be the DM candidate. The stability of DM is ensured by imposing discrete $\mathbb{Z}_2$ symmetry. The model, in general, provides a broad range of DM mass from GeV to TeV range. In this study we only consider the lower mass range of DM in this model. The analysis of experimental data for DM relic density from PLANCK experiment and the other direct detection experimental results for the case of this IHDM gives a set of best fit values for DM mass, annihilation cross section and other model parameters. The reduced-χ^2 analyses with the theoretical, experimental and observational constraints suggest the best-fit value of DM mass in this model to be $\sim$ 63.54 GeV. We adopt this best fit point (obtained using χ^2 minimisation) for IHDM mass from such analyses. Thus the DM mass of 63.54 GeV is our chosen benchmark point in the present work. We study the γ-ray spectrum obtained from the annihilation of this chosen DM particle in IHDM framework and interpret various types of continuum γ-ray fluxes with astrophysical origins measured by Fermi-LAT satellite.

In this chapter (Chapter 6) we compare our calculated γ-ray flux with the galactic centre γ-ray excess in the light of this model. For this we have employed different analysed Fermi-LAT residual γ-ray flux data for different angular regions around the galactic centre. The calculated low energetic photon spectra from the annihilation of the DM particle with benchmark value of mass (63.54 GeV) in IHDM for various chosen regions surrounding the galactic centre are found to be in the same ballpark as reported by these studies. Although in some previous analyses it was argued that the photon spectra originated from different annihilation channels of dark matter particles with low masses can possibly fit the obtained data, very recent analyses have obtained the resulting best fit masses of dark matter to be much more conservative (and also somewhat higher as well). We have computed the photon spectra for our benchmark scenario in IHDM framework and have confronted with the residual photon spectra obtained for all of the above-mentioned studies. Our theoretical calculations for photon spectra in this model have been performed after suitable parametrisation of the dark matter halo parameters, region of interest surrounding the galactic centre etc.

We then consider the γ-rays from Fermi Bubble region and compare the low energy residual γ-ray excess from the lower galactic latitudes in the light of the IHDM framework. Theoretical calculations are performed for photon flux from annihilating IHDM dark matter of chosen mass for five zones covering the total extent of the Fermi Bubble. These zones are divided in terms of the galactic latitudes $|b| = 1^o - 10^o, 10^o - 20^o, 20^o - 30^o, 30^o - 40^o, 40^o - 50^o$. The calculated results are then compared with the Fermi-LAT observation. However the observation hints much prominent signature of bumpy features in the residual photon flux only in the regions with $|b| = 1^o - 10^o, 10^o - 20^o, 20^o - 30^o$. The annihilating low mass DM in IHDM is also found to yield similar nature of photon spectra from Fermi Bubble.

We also address the prospects of the continuum γ-ray signal which may come from DM-dominated dwarf spheroidal galaxies (dSphs) in case they originate from dark matter annihilation. We then compare the γ-ray flux that can be obtained from the IHDM dark matter with mass 63.54 GeV. For this we choose 18 Milky Way dSphs whose J-factor can be estimated from measurements. The uncertainties in the measurement of J-factor for different dSphs are also incorporated in our calculations. The calculated photon spectra for IHDM benchmark point are seen to obey the allowed limits for observed spectra of continuum γ-ray.

After addressing the issues regarding indirect DM searches with γ-ray signals from various galactic cases, we finally confront the extragalactic γ-ray signal with that from the annihilation of low mass DM (considered in this work) in IHDM scenario. We calculate the extragalactic γ-ray flux for different extragalactic parametrisations and compare with the observed extragalactic gamma ray background by EGRET and Fermi LAT. For this we consider several possible classes of non-DM astrophysical sources which may yield γ-ray signal embedded in the extragalactic background. Although there are too many uncertainties involved in modelling of such astrophysical sources and other parameters for extragalactic flux calculation, we have shown that the considered low mass DM in

IHDM can generate photon flux within the observed flux limit.

From the detailed study of various galactic and extragalactic γ-ray searches for probing the indirect signatures of DM in light of IHDM, we can conclude that the low mass DM in this model framework is still a viable candidate to be probed in future γ-ray searches. Although we have performed a thorough analysis considering only a single Higgs portal model, the analysis is valid for any simple Higgs-portal DM model such as singlet scalar DM model, singlet fermion DM, inert Higgs triplet model etc. with DM mass in the same ballpark as in our study.

In Chapter 7, we have shown that the radiative neutrino mass model can explain the observed 3.5 keV X-ray line signal from the data of various galaxy clusters and Andromeda galaxy (M31). Since the galaxy clusters are supposed to contain huge amount of dark matter and there is no suitable astrophysical explanation so far for this 3.55 keV X-ray line, this line is thought to be originated from DM present in the galaxy clusters. In order to explain such X-ray line in DM framework, we consider the DM model with radiative neutrino mass generation mechanism where the Standard Model (SM) sector is extended with three singlet right-handed neutrinos and an extra $\mathrm{SU}(2)_L$ doublet scalar. The imposition of discrete $\mathbb{Z}_2$ symmetry on this model ensures the stability of the DM candidate in this model, namely, the lightest right-handed neutrino among those. Therefore the DM candidate in this model is essentially fermionic and leptophilic in nature. This model can therefore accommodate naturally both neutrino mass and stable cold DM candidate. We also assume that the next-to-lightest right-handed neutrino is almost degenerate in mass with the lightest one (DM candidate) in this framework and this leads to open the co-annihilation channels between them. The decay of such next-to-lightest right-handed neutrino to the lightest right-handed neutrino DM and a photon due to the transition magnetic moment appearing in the effective interaction term among them. The small mass difference between the lightest and the second lightest right-handed neutrino have been considered to produce the energy of the X-ray signal. Thus the transition from $N_2 \to N_1 + \gamma$ due to transition magnetic moment via radiative processes involving leptons and charged scalar in internal lines can naturally accommodate all the requirements for the X-ray line signal. Therefore the 3.55 keV X-ray line signal from the galaxy clusters can suitably be explained by the emitted photon from the radiative decay of next-lo-lightest neutrino via charged scalar and leptons in the internal lines in this framework. The value of the transition magnetic moment (μ_{12}) for such an observed signal is estimated to be few orders of magnitude smaller than the reach of recent DM direct detection experimental limits sustaining the possibility of the cold DM candidate in this model to be detected directly. The other parameters of this model, namely masses of lightest right-handed neutrino (N_1), doublet scalar (η) and phase factor (ξ) between Yukawa couplings, h_1 and h_2 are further constrained from the observed X-ray line data. A very small but non-zero value of the phase difference between Yukawa couplings, h_1 and h_2 have been predicted. Also the co-annihilation between N_1 and N_2 becomes smaller and the s-wave contribution of dark matter annihilation cross section is calculated to be reduced. Finally the analysis performed here for this model framework would be viable for any DM signal in this energy regime. In addition the DM candidate (lightest right-handed neutrino), being leptophilic and massive, can potentially explain AMS-02 positron excess.

Future Outlook

In this thesis we have extensively studied some particle physics models for cold dark matter and primarily confronted the flux of neutral particles (gamma rays etc.) produced in the considered model frameworks with the observational findings at different energy regimes ($\sim$ 10 GeV, 3.5 keV etc.). The topics on which I would like to pursue my research further are briefly summarised below.

- The simplest framework for obtaining a viable DM beyond the Standard Model is the Higgs-portal DM model. To this end, we study the scalar singlet DM model (a singlet scalar is added to the SM), an inert Higgs doublet DM model (SM is extended with an additional Higgs-like doublet), a two-component scalar DM model (two singlet scalars are added to the SM). On the basis of these models, the thorough investigation of the experimental and observational data has been carried out. One more particle physics model has been proposed in my work to explain the observed keV X-ray line. Other such simple particle physics models beyond the Standard Model of particle physics can be extensively explored.

- The sources of DM in the astrophysical objects can be galactic as well as extra-galactic. Recent analyses of the data from the satellite-borne gamma ray experiment Fermi Large Area Telescope (Fermi-LAT) reveal an excess of gamma ray flux from the direction of the Galactic Centre. This excess is found to be in the gamma energy region of around 1-3 GeV and no known astrophysical phenomenon could explain this excess. Also Fermi Bubbles, a bi-lobular structure of gamma-ray emission perpendicular to the galactic plane, exhibit an anomaly in its gamma-ray emission spectrum. (a bump-like feature in the energy regime, $E_\gamma \sim 1-3$ GeV similar to that from the Galactic Centre). Therefore from such observations of excess γ-ray flux, one can put constrains on the mass of the DM and the interaction cross-section between DM and the SM. Also such data can be used to estimate the nature of dark matter density profile at the galactic region.

- Within our galactic halo, there are, in fact, subhalos (localised concentration of DM). The satellite galaxies (also known as dwarf galaxies) of Milky Way galaxy are rich in DM. There are several satellite galaxies or dwarf galaxies which are gravitationally bound to the Milky Way (and may rotate around the Milky Way). The measurement of mass-to-luminosity ratio of such galaxies strongly indicates the presence of DM in large amount in these dwarf galaxies. Therefore any unexplained gamma-ray flux from the dwarfs may possibly be attributed to the annihilation of DM in those sites. Recently evidence of such excess photon flux has been found from the observational data of Reticulum-2 dwarf galaxy which, in turn, can be used to constrain parameter space of DM models.

- Apart from the Milky Way galaxy, other galaxies or galaxy clusters in the universe also contain such DM halos. Any signature of gamma rays from extragalactic sources in excess of that from known astrophysical sources may hint to indirect detection of DM from extragalactic sources. The gamma ray spectrum that one may obtain by subtracting the known sources form the diffuse extragalactic gamma-ray background. The gamma rays from the other extragalactic objects like active galactic nuclei (AGN), BL Lac objects, millisecond pulsars (MSP), radio quasars, radio galaxies, star forming and star burst galaxies, ultra high energy cosmic rays, gamma ray bursts, ultra high energy protons in the inter-cluster material, gravitationally induced shock waves etc. will also contribute to the diffuse gamma-ray background for extragalactic sources. There are observational results of gamma rays (by EGRET, Fermi-LAT) from extragalactic sources which also hint to the DM annihilation in those sites. This may restrict DM mass and annihilation channels for different models of DM. This will be my endeavour to pursue a thorough analysis to this effect.

- Recently there is another interesting evidence of a weak unidentified line with energy 3.55 keV (more than 3σ CL) in the X-ray spectrum from the analysis of X-ray data of XMM-Newton observatory for observed 73 galaxy clusters. Another group has also claimed a similar line (3.52 keV X-ray line at 4.4σ CL) from the data of X-ray spectra of Andromeda galaxy (M31) and Perseus cluster. Since the galaxy clusters are supposed to contain huge amount of DM, this 3.55 keV X-ray line is thought to be originated from DM. Since there is no other substantial astrophysical explanation regarding the origin of the line, it is claimed that this may happen because of some decaying DM. It may be interesting to pursue to explore the limit of the mass and the decaying lifetime of such decaying DM particles.

- From another very interesting observations (such as Bullet Cluster, Abell 3827 observations), it is now claimed that there exists very strong self-interaction in the DM sector. The concept of self interacting DM was originally addressed to alleviate a variety of long-established discrepancies (*core-vs-cusp* problem, *missing satellite* problem, *too-big-to-fail* problem etc.) between the predictions by collision-less cold DM simulations and the astrophysical observations on galactic as well as subgalactic scales. Evidences for self interaction would have striking implications for particle nature of DM. From the observed self-interaction strength of DM, one can put bound on the known particle physics models for DM.

- Axion are considered to be one of the suitable candidates for DM. Interestingly, it has been claimed that Geomagnetic Conversion of Solar Axions to X-rays (GECOSAX) can yield a photon flux which is measurable by a satellite based X-ray observatory on the dark side of the Earth (in respect of artificial satellite). Therefore ASTROSAT, India's first dedicated multi-wavelength space observatory, will be potentially suitable in detecting such X-rays when it will face on the dark side of the Earth where the Earth acts as a barrier for direct X-rays coming from the Sun and other X-ray sources in the sky. Since the Earth works as a "shield" towards the Sun, the solar X-ray background is effectively removed. Therefore, from the study of the measured X-ray data of ASTROSAT, one can, in principle, put severe constraints on the models for axion or axion-like particle (ALP) or more specifically on the mass of the axion and the axion-photon coupling strength.

Bibliography

[1] K. G. Begeman, A. H. Broeils, and R. H. Sanders, "Extended rotation curves of spiral galaxies: Dark haloes and modified dynamics," *Mon. Not. Roy. Astron. Soc.*, vol. 249, p. 523, 1991. xxx, 7, 74

[2] M. Kamionkowski, "Possible relics from new physics in the early universe: Inflation, the cosmic microwave background, and particle dark matter," in *Workshop on The Early and Future Universe Beijing, China, June 22-27, 1998*, 1998. xxx, xxxiii, 7, 49

[3] A. Klypin, H. Zhao, and R. S. Somerville, "Lambda CDM-based models for the Milky Way and M31 I: Dynamical models," *Astrophys.J.*, vol. 573, pp. 597–613, 2002. xxx, 7, 243

[4] L. Bergström, "Nonbaryonic dark matter: Observational evidence and detection methods," *Rept. Prog. Phys.*, vol. 63, p. 793, 2000. xxx, 7

[5] D. Clowe, M. Bradac, A. H. Gonzalez, M. Markevitch, S. W. Randall, C. Jones, and D. Zaritsky, "A direct empirical proof of the existence of dark matter," *Astrophys. J.*, vol. 648, pp. L109–L113, 2006. xxxi, 13, 14

[6] M. Markevitch, "Chandra observation of the most interesting cluster in the universe," 2005. [ESA Spec. Publ.604,723(2006)]. xxxi, 14

[7] M. J. Jee *et al.*, “Discovery of a Ringlike Dark Matter Structure in the Core of the Galaxy Cluster Cl 0024+17,” *Astrophys. J.*, vol. 661, pp. 728–749, 2007. xxxii, 16

[8] R. Massey, T. Kitching, and J. Richard, “The dark matter of gravitational lensing,” *Rept. Prog. Phys.*, vol. 73, p. 086901, 2010. xxxii, 18

[9] K. A. Olive *et al.*, “Review of Particle Physics,” *Chin. Phys.*, vol. C38, p. 090001, 2014. xxxiii, 22

[10] J. Conrad, “Indirect Detection of WIMP Dark Matter: a compact review,” in *Interplay between Particle and Astroparticle physics London, United Kingdom, August 18-22, 2014*, 2014. xxxiv, 78

[11] K. Bechtol *et al.*, “Eight New Milky Way Companions Discovered in First-Year Dark Energy Survey Data,” *Astrophys. J.*, vol. 807, no. 1, p. 50, 2015. xxxiv, 82

[12] M. Ackermann *et al.*, “The spectrum of isotropic diffuse gamma-ray emission between 100 MeV and 820 GeV,” *Astrophys.J.*, vol. 799, no. 1, p. 86, 2015. xxxiv, 84, 224

[13] F. Calore, I. Cholis, and C. Weniger, “Background model systematics for the Fermi GeV excess,” 2014. xlii, 195, 211, 212, 213

[14] M. Ajello *et al.*, “Fermi-LAT Observations of High-Energy γ-Ray Emission Toward the Galactic Center,” *Astrophys. J.*, vol. 819, no. 1, p. 44, 2016. xlii, 195, 211, 213

[15] I. Cholis, D. Hooper, and S. D. McDermott, “Dissecting the Gamma-Ray Background in Search of Dark Matter,” *JCAP*, vol. 1402, p. 014, 2014. xlv, 196, 240, 242, 243

[16] M. Tavakoli, I. Cholis, C. Evoli, and P. Ullio, “Constraints on dark matter annihilations from diffuse gamma-ray emission in the Galaxy,” *JCAP*, vol. 1401, p. 017, 2014. xlvi, 196, 234, 239, 240

[17] J. H. Oort, "The force exerted by the stellar system in the direction perpendicular to the galactic plane and some related problems," *Bulletin of the Astronomical Institutes of the Netherlands*, vol. 6, p. 249, 1932. 1

[18] H. W. Babcock, "The rotation of the andromeda nebula," *Lick Observatory Bulletin*, vol. 19, pp. 41–51, 1939. 1

[19] F. Zwicky, "Die Rotverschiebung von extragalaktischen Nebeln," *Helv. Phys. Acta*, vol. 6, pp. 110–127, 1933. 1, 2, 5

[20] S. Smith, "The mass of the virgo cluster," *The Astrophysical Journal*, vol. 83, p. 23, 1936. 1, 5

[21] F. Zwicky, "On the Masses of Nebulae and of Clusters of Nebulae," *Astrophys. J.*, vol. 86, pp. 217–246, 1937. 2, 5

[22] A. Vikhlinin, A. Kravtsov, W. Forman, C. Jones, M. Markevitch, S. S. Murray, and L. Van Speybroeck, "Chandra sample of nearby relaxed galaxy clusters: Mass, gas fraction, and mass-temperature relation," *Astrophys. J.*, vol. 640, pp. 691–709, 2006. 5

[23] F. Pacaud *et al.*, "The XMM-LSS survey: The Class 1 cluster sample over the initial 5 square degrees and its cosmological modelling," *Mon. Not. Roy. Astron. Soc.*, vol. 382, pp. 1289–1308, 2007. 5

[24] S. D. M. White, J. F. Navarro, A. E. Evrard, and C. S. Frenk, "The Baryon content of galaxy clusters: A Challenge to cosmological orthodoxy," *Nature*, vol. 366, pp. 429–433, 1993. 5, 37

[25] M. Aaronson, J. Huchra, and J. Mould, "The infrared luminosity/hi velocity-width relation and its application to the distance scale," *The Astrophysical Journal*, vol. 229, pp. 1–13, 1979. 5

[26] R. B. Tully and J. R. Fisher, "A New method of determining distances to galaxies," *Astron. Astrophys.*, vol. 54, pp. 661–673, 1977. 5

[27] S. M. Faber and R. E. Jackson, "Velocity dispersions and mass to light ratios for elliptical galaxies," *Astrophys. J.*, vol. 204, p. 668, 1976. 5

[28] K. Freeman, "On the disks of spiral and so galaxies," *The Astrophysical Journal*, vol. 160, p. 811, 1970. 8

[29] V. C. Rubin and W. K. Ford, Jr., "Rotation of the Andromeda Nebula from a Spectroscopic Survey of Emission Regions," *Astrophys. J.*, vol. 159, pp. 379–403, 1970. 8

[30] V. C. Rubin, N. Thonnard, and W. Ford Jr, "Extended rotation curves of high-luminosity spiral galaxies. iv-systematic dynamical properties, sa through sc," *The Astrophysical Journal*, vol. 225, pp. L107–L111, 1978. 8

[31] V. C. Rubin, D. Burstein, W. K. Ford, Jr., and N. Thonnard, "Rotation velocities of 16 SA galaxies and a comparison of Sa, Sb, and SC rotation properties," *Astrophys. J.*, vol. 289, p. 81, 1985. 8

[32] A. Bosma, "The distribution and kinematics of neutral hydrogen in spiral galaxies of various morphological types," 1978. 8

[33] A. Bosma, "21-cm line studies of spiral galaxies. i-observations of the galaxies ngc 5033, 3198, 5055, 2841, and 7331. ii-the distribution and kinematics of neutral hydrogen in spiral galaxies of various morphological types," *The Astronomical Journal*, vol. 86, pp. 1791–1846, 1981. 8

[34] T. S. van Albada, J. N. Bahcall, K. Begeman, and R. Sancisi, "The Distribution of Dark Matter in the Spiral Galaxy NGC-3198," *Astrophys. J.*, vol. 295, pp. 305–313, 1985. 8

[35] G. Gamow, "The origin of elements and the separation of galaxies," *Physical Review*, vol. 74, no. 4, p. 505, 1948. 9

[36] G. Gamow *et al.*, "The evolution of the universe," *Nature*, vol. 162, no. 4122, pp. 680–682, 1948. 9

[37] A. A. Penzias and R. W. Wilson, "A Measurement of excess antenna temperature at 4080-Mc/s," *Astrophys. J.*, vol. 142, pp. 419–421, 1965. 9

[38] A. Penzias and R. Wilson, "Measurement of the flux density of cas a at 4080 mc/s.," *The Astrophysical Journal*, vol. 142, p. 1149, 1965. 9

[39] W. Hu and S. Dodelson, "Cosmic microwave background anisotropies," *Ann. Rev. Astron. Astrophys.*, vol. 40, pp. 171–216, 2002. 9

[40] D. Samtleben, S. Staggs, and B. Winstein, "The Cosmic microwave background for pedestrians: A Review for particle and nuclear physicists," *Ann. Rev. Nucl. Part. Sci.*, vol. 57, pp. 245–283, 2007. 9

[41] G. Hinshaw *et al.*, "Nine-Year Wilkinson Microwave Anisotropy Probe (WMAP) Observations: Cosmological Parameter Results," *Astrophys. J. Suppl.*, vol. 208, p. 19, 2013. 11

[42] P. A. R. Ade *et al.*, "Planck 2013 results. XVI. Cosmological parameters," *Astron. Astrophys.*, vol. 571, p. A16, 2014. 11, 38, 197, 202

[43] D. Clowe, A. Gonzalez, and M. Markevitch, "Weak lensing mass reconstruction of the interacting cluster 1E0657-558: Direct evidence for the existence of dark matter," *Astrophys. J.*, vol. 604, pp. 596–603, 2004. 13

[44] M. Markevitch, A. H. Gonzalez, D. Clowe, A. Vikhlinin, L. David, W. Forman, C. Jones, S. Murray, and W. Tucker, "Direct constraints on the dark matter self-

interaction cross-section from the merging galaxy cluster 1E0657-56," *Astrophys. J.*, vol. 606, pp. 819–824, 2004. 13

[45] M. Milgrom, "A Modification of the Newtonian dynamics as a possible alternative to the hidden mass hypothesis," *Astrophys. J.*, vol. 270, pp. 365–370, 1983. 13

[46] B. Famaey and S. McGaugh, "Modified Newtonian Dynamics (MOND): Observational Phenomenology and Relativistic Extensions," *Living Rev. Rel.*, vol. 15, p. 10, 2012. 13

[47] A. Einstein, "Lens-Like Action of a Star by the Deviation of Light in the Gravitational Field," *Science*, vol. 84, pp. 506–507, 1936. 15

[48] D. Walsh, R. F. Carswell, and R. J. Weymann, "0957 + 561 A, B - Twin quasistellar objects or gravitational lens," *Nature*, vol. 279, pp. 381–384, 1979. 15

[49] J. A. Tyson, G. P. Kochanski, and I. P. Dell'Antonio, "Detailed mass map of CL0024+1654 from strong lensing," *Astrophys. J.*, vol. 498, p. L107, 1998. 16

[50] R. Massey *et al.*, "Dark matter maps reveal cosmic scaffolding," *Nature*, vol. 445, p. 286, 2007. 16

[51] C. Alcock *et al.*, "Possible Gravitational Microlensing of a Star in the Large Magellanic Cloud," 1993. 18, 36

[52] E. Aubourg *et al.*, "Evidence for gravitational microlensing by dark objects in the galactic halo," *Nature*, vol. 365, pp. 623–625, 1993. 18, 36

[53] C. Alcock *et al.*, "The MACHO project: Microlensing results from 5.7 years of LMC observations," *Astrophys. J.*, vol. 542, pp. 281–307, 2000. 18, 36

[54] M. Colless *et al.*, "The 2dF Galaxy Redshift Survey: Spectra and redshifts," *Mon. Not. Roy. Astron. Soc.*, vol. 328, p. 1039, 2001. 19

[55] S. Cole *et al.*, "The 2dF Galaxy Redshift Survey: Power-spectrum analysis of the final dataset and cosmological implications," *Mon. Not. Roy. Astron. Soc.*, vol. 362, pp. 505–534, 2005. 19, 20

[56] M. Tegmark *et al.*, "The 3-D power spectrum of galaxies from the SDSS," *Astrophys. J.*, vol. 606, pp. 702–740, 2004. 19, 20

[57] V. Springel *et al.*, "Simulating the joint evolution of quasars, galaxies and their large-scale distribution," *Nature*, vol. 435, pp. 629–636, 2005. 19

[58] J. Diemand, M. Kuhlen, and P. Madau, "Dark matter substructure and gamma-ray annihilation in the Milky Way halo," *Astrophys. J.*, vol. 657, pp. 262–270, 2007. 19

[59] V. Springel, J. Wang, M. Vogelsberger, A. Ludlow, A. Jenkins, *et al.*, "The Aquarius Project: the subhalos of galactic halos," *Mon.Not.Roy.Astron.Soc.*, vol. 391, pp. 1685–1711, 2008. 19, 74, 243

[60] J. Diemand, M. Kuhlen, P. Madau, M. Zemp, B. Moore, D. Potter, and J. Stadel, "Clumps and streams in the local dark matter distribution," *Nature*, vol. 454, pp. 735–738, 2008. 19

[61] W. J. Percival *et al.*, "Baryon Acoustic Oscillations in the Sloan Digital Sky Survey Data Release 7 Galaxy Sample," *Mon. Not. Roy. Astron. Soc.*, vol. 401, pp. 2148–2168, 2010. 20, 21

[62] J. Silk, "Cosmic black body radiation and galaxy formation," *Astrophys. J.*, vol. 151, pp. 459–471, 1968. 20

[63] D. N. Schramm and M. S. Turner, "Big bang nucleosynthesis enters the precision era," *Rev. Mod. Phys.*, vol. 70, pp. 303–318, 1998. 21

[64] C. Angulo, M. Arnould, M. Rayet, P. Descouvemont, D. Baye, C. Leclercq-Willain, A. Coc, S. Barhoumi, P. Aguer, C. Rolfs, *et al.*, "A compilation of charged-particle

induced thermonuclear reaction rates," *Nuclear Physics A*, vol. 656, no. 1, pp. 3–183, 1999. 21

[65] A. Coc, E. Vangioni-Flam, P. Descouvemont, A. Adahchour, and C. Angulo, "Updated Big Bang nucleosynthesis confronted to WMAP observations and to the abundance of light elements," *Astrophys. J.*, vol. 600, pp. 544–552, 2004. 22

[66] G. Steigman, "Primordial Nucleosynthesis in the Precision Cosmology Era," *Ann. Rev. Nucl. Part. Sci.*, vol. 57, pp. 463–491, 2007. 22

[67] F. Iocco, G. Mangano, G. Miele, O. Pisanti, and P. D. Serpico, "Primordial Nucleosynthesis: from precision cosmology to fundamental physics," *Phys. Rept.*, vol. 472, pp. 1–76, 2009. 22

[68] W. L. Freedman *et al.*, "Final results from the Hubble Space Telescope key project to measure the Hubble constant," *Astrophys. J.*, vol. 553, pp. 47–72, 2001. 22

[69] K. A. Olive, G. Steigman, and T. P. Walker, "Primordial nucleosynthesis: Theory and observations," *Phys. Rept.*, vol. 333, pp. 389–407, 2000. 23

[70] F. Spite and M. Spite, "Abundance of lithium in unevolved halo stars and old disk stars-interpretation and consequences," *Astronomy and astrophysics*, vol. 115, pp. 357–366, 1982. 24

[71] M. Asplund, D. L. Lambert, P. E. Nissen, F. Primas, and V. V. Smith, "Lithium isotopic abundances in metal-poor halo stars," *Astrophys. J.*, vol. 644, pp. 229–259, 2006. 24

[72] J. Dunkley *et al.*, "Five-Year Wilkinson Microwave Anisotropy Probe (WMAP) Observations: Likelihoods and Parameters from the WMAP data," *Astrophys. J. Suppl.*, vol. 180, pp. 306–329, 2009. 25

[73] K. Jedamzik and M. Pospelov, "Big Bang Nucleosynthesis and Particle Dark Matter," *New J. Phys.*, vol. 11, p. 105028, 2009. 25

[74] G. Bertone, D. Hooper, and J. Silk, "Particle dark matter: Evidence, candidates and constraints," *Phys. Rept.*, vol. 405, pp. 279–390, 2005. 26, 136

[75] D. Fabricant, M. Lecar, and P. Gorenstein, "X-ray measurements of the mass of m87," *The Astrophysical Journal*, vol. 241, pp. 552–560, 1980. 29

[76] D. Fabricant and P. Gorenstein, "Further evidence for m87's massive, dark halo," *The Astrophysical Journal*, vol. 267, pp. 535–546, 1983. 29

[77] J. P. Hughes, "The mass of the coma cluster-combined x-ray and optical results," *The Astrophysical Journal*, vol. 337, pp. 21–33, 1989. 29

[78] R. Lynds, "The absorption-line spectrum of 4c 05.34," *The Astrophysical Journal*, vol. 164, p. L73, 1971. 30

[79] M. Taoso, G. Bertone, and A. Masiero, "Dark Matter Candidates: A Ten-Point Test," *JCAP*, vol. 0803, p. 022, 2008. 33

[80] E. W. Kolb and M. S. Turner, "The Early Universe," *Front. Phys.*, vol. 69, pp. 1–547, 1990. 33, 34, 35, 41

[81] C. Tao, "Astrophysical Constraints on Dark Matter," *EAS Publ. Ser.*, vol. 53, pp. 97–104, 2012. 35

[82] J. S. Bullock, "Notes on the Missing Satellites Problem," 2010. 35

[83] W. J. G. de Blok, "The Core-Cusp Problem," *Adv. Astron.*, vol. 2010, p. 789293, 2010. 35

[84] M. Boylan-Kolchin, J. S. Bullock, and M. Kaplinghat, "Too big to fail? The puzzling darkness of massive Milky Way subhaloes," *Mon. Not. Roy. Astron. Soc.*, vol. 415, p. L40, 2011. 35

[85] P. McDonald *et al.*, "The Lyman-alpha forest power spectrum from the Sloan Digital Sky Survey," *Astrophys. J. Suppl.*, vol. 163, pp. 80–109, 2006. 35

[86] M. Viel, J. Lesgourgues, M. G. Haehnelt, S. Matarrese, and A. Riotto, "Constraining warm dark matter candidates including sterile neutrinos and light gravitinos with WMAP and the Lyman-alpha forest," *Phys. Rev.*, vol. D71, p. 063534, 2005. 35

[87] M. Persic and P. Salucci, "The Baryon content of the Universe," *Submitted to: Mon. Not. Roy. Astron.*, 2005. 36

[88] E. Masso, "Baryonic dark matter: Theory and experiment. Overview," *Nucl. Phys. Proc. Suppl.*, vol. 48, pp. 13–21, 1996. 37

[89] M. S. Turner, "Cosmological parameters," pp. 113–128, 1998. [AIP Conf. Proc.478,113(1999)]. 37

[90] P. Gondolo, "Non-baryonic dark matter," *NATO Sci. Ser. II*, vol. 187, pp. 279–333, 2005. [,279(2003)]. 38

[91] P. Gondolo and G. Gelmini, "Cosmic abundances of stable particles: Improved analysis," *Nucl. Phys.*, vol. B360, pp. 145–179, 1991. 47, 51

[92] G. Belanger, F. Boudjema, A. Pukhov, and A. Semenov, "MicrOMEGAs: A Program for calculating the relic density in the MSSM," *Comput. Phys. Commun.*, vol. 149, pp. 103–120, 2002. 47

[93] G. Belanger, F. Boudjema, A. Pukhov, and A. Semenov, "micrOMEGAs: Version 1.3," *Comput. Phys. Commun.*, vol. 174, pp. 577–604, 2006. 47

[94] G. Belanger, F. Boudjema, A. Pukhov, and A. Semenov, "MicrOMEGAs 2.0: A Program to calculate the relic density of dark matter in a generic model," *Comput. Phys. Commun.*, vol. 176, pp. 367–382, 2007. 47

[95] G. Belanger, F. Boudjema, A. Pukhov, and A. Semenov, "micrOMEGAs 2.0.7: A program to calculate the relic density of dark matter in a generic model," *Comput. Phys. Commun.*, vol. 177, pp. 894–895, 2007. 47

[96] G. Belanger, F. Boudjema, A. Pukhov, and A. Semenov, "Dark matter direct detection rate in a generic model with micrOMEGAs 2.2," *Comput. Phys. Commun.*, vol. 180, pp. 747–767, 2009. 47

[97] G. Belanger, F. Boudjema, A. Pukhov, and A. Semenov, "micrOMEGAs: A Tool for dark matter studies," *Nuovo Cim.*, vol. C033N2, pp. 111–116, 2010. 47

[98] G. Belanger, F. Boudjema, A. Pukhov, and A. Semenov, "micrOMEGAs 3: A program for calculating dark matter observables," *Comput. Phys. Commun.*, vol. 185, pp. 960–985, 2014. 47, 156, 205

[99] G. Belanger, F. Boudjema, and A. Pukhov, "micrOMEGAs : a code for the calculation of Dark Matter properties in generic models of particle interaction," in *The Dark Secrets of the Terascale*, pp. 739–790, 2013. 47

[100] G. Bélanger, F. Boudjema, A. Pukhov, and A. Semenov, "micrOMEGAs4.1: two dark matter candidates," *Comput. Phys. Commun.*, vol. 192, pp. 322–329, 2015. 47

[101] P. Gondolo, J. Edsjo, L. Bergstrom, P. Ullio, and E. A. Baltz, "DarkSUSY: A Numerical package for dark matter calculations in the MSSM," in *Proceedings, 3rd International Workshop on The identification of dark matter (IDM 2000)*, pp. 318–323, 2000. 47

[102] P. Gondolo, J. Edsjo, P. Ullio, L. Bergstrom, M. Schelke, and E. A. Baltz, "Darksusy - a numerical package for supersymmetric dark matter calculations," in *Proceedings, 4th International Workshop on The identification of dark matter (IDM 2002)*, pp. 256–261, 2002. 47

[103] P. Gondolo, J. Edsjo, P. Ullio, L. Bergstrom, M. Schelke, and E. A. Baltz, "DarkSUSY: Computing supersymmetric dark matter properties numerically," *JCAP*, vol. 0407, p. 008, 2004. 47

[104] P. Gondolo, J. Edsjo, P. Ullio, L. Bergstrom, M. Schelke, and E. A. Baltz, "DarkSUSY 4.00 neutralino dark matter made easy," *New Astron. Rev.*, vol. 49, pp. 149–151, 2005. 47

[105] M. Hindmarsh and O. Philipsen, "WIMP dark matter and the QCD equation of state," *Phys. Rev.*, vol. D71, p. 087302, 2005. 50

[106] H. Baer, K.-Y. Choi, J. E. Kim, and L. Roszkowski, "Dark matter production in the early Universe: beyond the thermal WIMP paradigm," *Phys. Rept.*, vol. 555, pp. 1–60, 2014. 53, 56

[107] A. Drukier and L. Stodolsky, "Principles and Applications of a Neutral Current Detector for Neutrino Physics and Astronomy," *Phys. Rev.*, vol. D30, p. 2295, 1984. [,395(1984)]. 58

[108] R. Bernabei *et al.*, "First results from DAMA/LIBRA and the combined results with DAMA/NaI," *Eur. Phys. J.*, vol. C56, pp. 333–355, 2008. 59, 114, 137

[109] R. Bernabei *et al.*, "Results from DAMA," *AIP Conf. Proc.*, vol. 698, pp. 328–331, 2004. [,328(2003)]. 59, 114

[110] R. Bernabei *et al.*, "Dark matter particles in the Galactic halo: Results and implications from DAMA/NaI," *Int. J. Mod. Phys.*, vol. D13, pp. 2127–2160, 2004. 59, 114

[111] Z. Ahmed *et al.*, "Search for Axions with the CDMS Experiment," *Phys. Rev. Lett.*, vol. 103, p. 141802, 2009. 59, 114

[112] Z. Ahmed *et al.*, "Dark Matter Search Results from the CDMS II Experiment," *Science*, vol. 327, pp. 1619–1621, 2010. 59, 114, 137, 161, 192

[113] B. Beltran, "Dark matter searches with the PICASSO experiment at SNOLAB," *J. Phys. Conf. Ser.*, vol. 136, p. 042080, 2008. 59, 114

[114] S. Archambault *et al.*, "Searching for Dark Matter with PICASSO," *Phys. Procedia*, vol. 61, pp. 107–111, 2015. 59, 114

[115] J. Angle *et al.*, "First Results from the XENON10 Dark Matter Experiment at the Gran Sasso National Laboratory," *Phys. Rev. Lett.*, vol. 100, p. 021303, 2008. 59, 114

[116] E. Aprile and T. Doke, "Liquid Xenon Detectors for Particle Physics and Astrophysics," *Rev. Mod. Phys.*, vol. 82, pp. 2053–2097, 2010. 59, 114

[117] E. Aprile *et al.*, "First Dark Matter Results from the XENON100 Experiment," *Phys. Rev. Lett.*, vol. 105, p. 131302, 2010. 59, 114

[118] E. Aprile *et al.*, "Dark Matter Results from 100 Live Days of XENON100 Data," *Phys. Rev. Lett.*, vol. 107, p. 131302, 2011. 59, 114, 137, 169, 192

[119] E. Aprile *et al.*, "The XENON100 Dark Matter Experiment," *Astropart. Phys.*, vol. 35, pp. 573–590, 2012. 59, 114

[120] E. Behnke *et al.*, "Improved Spin-Dependent WIMP Limits from a Bubble Chamber," *Science*, vol. 319, pp. 933–936, 2008. 59, 114

[121] D. S. Akerib *et al.*, "First results from the LUX dark matter experiment at the Sanford Underground Research Facility," *Phys. Rev. Lett.*, vol. 112, p. 091303, 2014. 59, 137, 172, 192, 202

[122] M. Boulay and B. Cai, "Dark matter search at SNOLAB with DEAP-1 and DEAP/CLEAN-3600," *J. Phys. Conf. Ser.*, vol. 136, p. 042081, 2008. 59, 114

[123] R. Lemrani, "Search for dark matter with EDELWEISS: Status and future," *Phys. Atom. Nucl.*, vol. 69, pp. 1967–1969, 2006. 59, 114

[124] D. S. Akerib *et al.*, "The SuperCDMS proposal for dark matter detection," *Nucl. Instrum. Meth.*, vol. A559, pp. 411–413, 2006. 59, 114

[125] T. Sumner, "Direct dark matter searches: DRIFT and ZEPLIN," *PoS*, vol. HEP2005, p. 003, 2006. 59, 114

[126] V. N. Lebedenko *et al.*, "Result from the First Science Run of the ZEPLIN-III Dark Matter Search Experiment," *Phys. Rev.*, vol. D80, p. 052010, 2009. 59, 114

[127] H. S. Lee *et al.*, "Limits on WIMP-nucleon cross section with CsI(Tl) crystal detectors," *Phys. Rev. Lett.*, vol. 99, p. 091301, 2007. 59, 114

[128] S. C. Kim *et al.*, "New Limits on Interactions between Weakly Interacting Massive Particles and Nucleons Obtained with CsI(Tl) Crystal Detectors," *Phys. Rev. Lett.*, vol. 108, p. 181301, 2012. 59, 114

[129] H. S. Lee *et al.*, "First limit on wimp cross section with low background csi(tl) crystal detector," *Phys. Lett.*, vol. B633, pp. 201–208, 2006. 59, 114

[130] C. E. Aalseth *et al.*, "Results from a Search for Light-Mass Dark Matter with a P-type Point Contact Germanium Detector," *Phys. Rev. Lett.*, vol. 106, p. 131301, 2011. 59, 114, 137, 164, 192

[131] G. J. Alner *et al.*, "Limits on WIMP cross-sections from the NAIAD experiment at the Boulby Underground Laboratory," *Phys. Lett.*, vol. B616, pp. 17–24, 2005. 59, 114

[132] T. Morlat, F. Giuliani, M. F. da Costa, T. Girard, A. R. Ramos, R. F. Payne, H. S. Miley, D. Limagne, G. Waysand, and J. G. Marques, "First Results from a Prototype CF-3-I SIMPLE Dark Matter Search Detector," 2007. 59, 114

[133] A. Takeda, M. Minowa, K. Miuchi, H. Sekiya, Y. Shimizu, Y. Inoue, W. Ootani, and Y. Ootuka, "Limits on the WIMP - nucleon coupling coefficients from dark matter search experiment with NaF bolometer," *Phys. Lett.*, vol. B572, pp. 145–151, 2003. 59, 114

[134] S. Profumo and P. Ullio, "Multi-Wavelength Searches for Particle Dark Matter," 2010. 60, 62

[135] J. Lavalle and P. Salati, "Dark Matter Indirect Signatures," *Comptes Rendus Physique*, vol. 13, pp. 740–782, 2012. 60, 62

[136] T. Bringmann and C. Weniger, "Gamma Ray Signals from Dark Matter: Concepts, Status and Prospects," *Phys. Dark Univ.*, vol. 1, pp. 194–217, 2012. 60, 62

[137] A. Askew, S. Chauhan, B. Penning, W. Shepherd, and M. Tripathi, "Searching for Dark Matter at Hadron Colliders," *Int. J. Mod. Phys.*, vol. A29, p. 1430041, 2014. 60

[138] L. Carpenter, A. DiFranzo, M. Mulhearn, C. Shimmin, S. Tulin, and D. Whiteson, "Mono-Higgs-boson: A new collider probe of dark matter," *Phys. Rev.*, vol. D89, no. 7, p. 075017, 2014. 60, 153

[139] A. A. Petrov and W. Shepherd, "Searching for dark matter at LHC with Mono-Higgs production," *Phys. Lett.*, vol. B730, pp. 178–183, 2014. 60, 153

[140] S. Funk, "Indirect Detection of Dark Matter with gamma rays," in *Sackler Colloquium: Dark Matter Universe: On the Threshhold of Discovery Irvine, USA, October 18-20, 2012*, 2013. 62

[141] M. Cirelli, G. Corcella, A. Hektor, G. Hutsi, M. Kadastik, P. Panci, M. Raidal, F. Sala, and A. Strumia, "PPPC 4 DM ID: A Poor Particle Physicist Cookbook for Dark Matter Indirect Detection," *JCAP*, vol. 1103, p. 051, 2011. [Erratum: JCAP1210,E01(2012)]. 62, 173, 204, 226

[142] L. Bergstrom, P. Ullio, and J. H. Buckley, "Observability of gamma-rays from dark matter neutralino annihilations in the Milky Way halo," *Astropart. Phys.*, vol. 9, pp. 137–162, 1998. 68

[143] Y. P. Jing and Y. Suto, "Triaxial modeling of halo density profiles with high-resolution N-body simulations," *Astrophys. J.*, vol. 574, p. 538, 2002. 70

[144] D. R. Law, S. R. Majewski, and K. V. Johnston, "Evidence for a Triaxial Milky Way Dark Matter Halo from the Sagittarius Stellar Tidal Stream," *Astrophys. J.*, vol. 703, pp. L67–L71, 2009. 70

[145] O. Y. Gnedin, A. Gould, J. Miralda-Escude, and A. R. Zentner, "Probing the shape of the Galactic halo with hyper-velocity stars," *Astrophys. J.*, vol. 634, pp. 344–350, 2005. 70

[146] L. Hernquist, "An Analytical Model for Spherical Galaxies and Bulges," *Astrophys. J.*, vol. 356, p. 359, 1990. 71

[147] W. Dehnen, "A Family of Potential-Density Pairs for Spherical Galaxies and Bulges," *Mon. Not. Roy. Astron. Soc.*, vol. 265, p. 250, 1993. 71

[148] H. Zhao, "Analytical models for galactic nuclei," *Mon. Not. Roy. Astron. Soc.*, vol. 278, pp. 488–496, 1996. 71

[149] X. X. Xue *et al.*, "The Milky Way's Circular Velocity Curve to 60 kpc and an Estimate of the Dark Matter Halo Mass from Kinematics of 2400 SDSS Blue Horizontal Branch Stars," *Astrophys. J.*, vol. 684, pp. 1143–1158, 2008. 71

[150] J. F. Navarro, C. S. Frenk, and S. D. M. White, "The Structure of cold dark matter halos," *Astrophys. J.*, vol. 462, pp. 563–575, 1996. 72, 73, 184, 205, 230

[151] J. F. Navarro, C. S. Frenk, and S. D. M. White, "A Universal density profile from hierarchical clustering," *Astrophys. J.*, vol. 490, pp. 493–508, 1997. 72, 121, 177, 205, 230

[152] F. Prada, A. Klypin, J. Flix Molina, M. Martinez, and E. Simonneau, "Dark Matter Annihilation in the Milky Way Galaxy: Effects of Baryonic Compression," *Phys. Rev. Lett.*, vol. 93, p. 241301, 2004. 72, 74, 125

[153] B. Moore, F. Governato, T. R. Quinn, J. Stadel, and G. Lake, "Resolving the structure of cold dark matter halos," *Astrophys. J.*, vol. 499, p. L5, 1998. 72, 74, 121, 177

[154] J. Diemand, B. Moore, and J. Stadel, "Convergence and scatter of cluster density profiles," *Mon. Not. Roy. Astron. Soc.*, vol. 353, p. 624, 2004. 72, 74, 121

[155] J. N. Bahcall and R. M. Soneira, "The Universe at faint magnetidues. 2. Models for the predicted star counts," *Astrophys. J. Suppl.*, vol. 44, pp. 73–110, 1980. 72, 74, 121, 177, 184

[156] A. Burkert, "The Structure of dark matter halos in dwarf galaxies," *IAU Symp.*, vol. 171, p. 175, 1996. [Astrophys. J.447,L25(1995)]. 72, 74, 261

[157] A. V. Kravtsov, A. A. Klypin, J. S. Bullock, and J. R. Primack, "The Cores of dark matter dominated galaxies: Theory versus observations," *Astrophys. J.*, vol. 502, p. 48, 1998. 72, 74

[158] J. Einasto, "Influence of the atmospheric and instrumental dispersion on the brightness distribution in a galaxy," *Trudy Inst. Astrofiz. Alma-Ata*, vol. 51, no. 87, p. 8, 1965. 73, 121, 177, 184

[159] A. W. Graham, D. Merritt, B. Moore, J. Diemand, and B. Terzic, "Empirical models for Dark Matter Halos. I. Nonparametric Construction of Density Profiles and Comparison with Parametric Models," *Astron. J.*, vol. 132, pp. 2685–2700, 2006. 73, 74

[160] J. F. Navarro, A. Ludlow, V. Springel, J. Wang, M. Vogelsberger, S. D. M. White, A. Jenkins, C. S. Frenk, and A. Helmi, "The Diversity and Similarity of Cold Dark Matter Halos," *Mon. Not. Roy. Astron. Soc.*, vol. 402, p. 21, 2010. 73, 74

[161] O. Y. Gnedin, A. V. Kravtsov, A. A. Klypin, and D. Nagai, "Response of dark matter halos to condensation of baryons: Cosmological simulations and improved adiabatic contraction model," *Astrophys. J.*, vol. 616, pp. 16–26, 2004. 74

[162] P. B. Tissera, S. D. M. White, S. Pedrosa, and C. Scannapieco, "Dark matter response to galaxy formation," *Mon. Not. Roy. Astron. Soc.*, vol. 406, p. 922, 2010. 74

[163] A. Charbonnier, C. Combet, and D. Maurin, "CLUMPY: a code for gamma-ray signals from dark matter structures," *Comput. Phys. Commun.*, vol. 183, pp. 656–668, 2012. 75

[164] F. Aharonian *et al.*, "Discovery of very-high-energy gamma-rays from the galactic centre ridge," *Nature*, vol. 439, pp. 695–698, 2006. 80, 104, 119

[165] F. Aharonian *et al.*, "Spectrum and variability of the Galactic Center VHE gamma-ray source HESS J1745-290," *Astron. Astrophys.*, vol. 503, p. 817, 2009. 80, 104, 119

[166] F. Aharonian *et al.*, "Very high-energy gamma rays from the direction of Sagittarius A*," *Astron. Astrophys.*, vol. 425, pp. L13–L17, 2004. 80, 104, 119

[167] V. Vitale and A. Morselli, "Indirect Search for Dark Matter from the center of the Milky Way with the Fermi-Large Area Telescope," in *Fermi gamma-ray space telescope. Proceedings, 2nd Fermi Symposium, Washington, USA, November 2-5, 2009*, 2009. 80, 119

[168] D. Hooper and L. Goodenough, "Dark Matter Annihilation in The Galactic Center As Seen by the Fermi Gamma Ray Space Telescope," *Phys. Lett.*, vol. B697, pp. 412–428, 2011. 80, 138, 178, 180, 187, 204

[169] H. A. Mayer-Hasselwander *et al.*, "High-energy gamma-ray emission from the galactic center," *Astron. Astrophys.*, vol. 335, pp. 161–172, 1998. 80

[170] A. Cesarini, F. Fucito, A. Lionetto, A. Morselli, and P. Ullio, "The Galactic center as a dark matter gamma-ray source," *Astropart. Phys.*, vol. 21, pp. 267–285, 2004. 80

[171] K. N. Abazajian and M. Kaplinghat, "Detection of a Gamma-Ray Source in the Galactic Center Consistent with Extended Emission from Dark Matter Annihilation

and Concentrated Astrophysical Emission," *Phys. Rev.*, vol. D86, p. 083511, 2012. [Erratum: Phys. Rev.D87,129902(2013)]. 80, 187

[172] R. S. Wharton, S. Chatterjee, J. M. Cordes, J. S. Deneva, and T. J. W. Lazio, "Multiwavelength Constraints on Pulsar Populations in the Galactic Center," *Astrophys. J.*, vol. 753, p. 108, 2012. 80, 187

[173] M. Chernyakova, D. Malyshev, F. A. Aharonian, R. M. Crocker, and D. I. Jones, "The high-energy, Arcminute-scale galactic center gamma-ray source," *Astrophys. J.*, vol. 726, p. 60, 2011. 80, 105, 180

[174] D. Hooper and T. Linden, "On The Origin Of The Gamma Rays From The Galactic Center," *Phys. Rev.*, vol. D84, p. 123005, 2011. 80, 182, 183, 187, 194, 204

[175] L. A. Anchordoqui and B. J. Vlcek, "W-WIMP Annihilation as a Source of the Fermi Bubbles," *Phys. Rev.*, vol. D88, p. 043513, 2013. 80, 187, 195

[176] K. Hagiwara, S. Mukhopadhyay, and J. Nakamura, "10 GeV neutralino dark matter and light stau in the MSSM," *Phys. Rev.*, vol. D89, no. 1, p. 015023, 2014. 80, 187

[177] D. Hooper and T. Linden, "Gamma Rays From The Galactic Center and the WMAP Haze," *Phys. Rev.*, vol. D83, p. 083517, 2011. 80, 182, 204

[178] D. Hooper, C. Kelso, and F. S. Queiroz, "Stringent and Robust Constraints on the Dark Matter Annihilation Cross Section From the Region of the Galactic Center," *Astropart. Phys.*, vol. 46, pp. 55–70, 2013. 80, 182, 204

[179] T. Daylan, D. P. Finkbeiner, D. Hooper, T. Linden, S. K. N. Portillo, *et al.*, "The Characterization of the Gamma-Ray Signal from the Central Milky Way: A Compelling Case for Annihilating Dark Matter," 2014. 80, 194, 205, 206, 209, 210

[180] G. Jungman, M. Kamionkowski, and K. Griest, "Supersymmetric dark matter," *Phys. Rept.*, vol. 267, pp. 195–373, 1996. 86, 136

[181] S. P. Martin, "A Supersymmetry primer," 1997. [Adv. Ser. Direct. High Energy Phys.18,1(1998)]. 86

[182] H.-C. Cheng, J. L. Feng, and K. T. Matchev, "Kaluza-Klein dark matter," *Phys. Rev. Lett.*, vol. 89, p. 211301, 2002. 86, 136, 196

[183] G. Servant and T. M. P. Tait, "Is the lightest Kaluza-Klein particle a viable dark matter candidate?," *Nucl. Phys.*, vol. B650, pp. 391–419, 2003. 86, 136, 196

[184] D. Hooper and S. Profumo, "Dark matter and collider phenomenology of universal extra dimensions," *Phys. Rept.*, vol. 453, pp. 29–115, 2007. 86, 196

[185] G. Belanger, M. Kakizaki, and A. Pukhov, "Dark matter in UED: The Role of the second KK level," *JCAP*, vol. 1102, p. 009, 2011. 86, 196

[186] R. D. Peccei and H. R. Quinn, "Cp conservation in the presence of pseudoparticles," *Physical Review Letters*, vol. 38, no. 25, p. 1440, 1977. 87, 196

[187] L. D. Duffy and K. van Bibber, "Axions as Dark Matter Particles," *New J. Phys.*, vol. 11, p. 105008, 2009. 87, 136, 196

[188] S. Weinberg, "A New Light Boson?," *Phys. Rev. Lett.*, vol. 40, pp. 223–226, 1978. 87, 196

[189] P. Sikivie, "Axion Cosmology," *Lect. Notes Phys.*, vol. 741, pp. 19–50, 2008. [,19(2006)]. 87, 196

[190] F. Wilczek, "Problem of Strong p and t Invariance in the Presence of Instantons," *Phys. Rev. Lett.*, vol. 40, pp. 279–282, 1978. 87, 196

[191] V. Silveira and A. Zee, "SCALAR PHANTOMS," *Phys. Lett.*, vol. B161, p. 136, 1985. 87, 136, 196

[192] M. J. G. Veltman and F. J. Yndurain, "RADIATIVE CORRECTIONS TO W W SCATTERING," *Nucl. Phys.*, vol. B325, p. 1, 1989. 87, 136

[193] V. Barger, P. Langacker, M. McCaskey, M. Ramsey-Musolf, and G. Shaughnessy, "Complex Singlet Extension of the Standard Model," *Phys. Rev.*, vol. D79, p. 015018, 2009. 87, 136, 196

[194] V. Barger, M. McCaskey, and G. Shaughnessy, "Complex Scalar Dark Matter vis-à-vis CoGeNT, DAMA/LIBRA and XENON100," *Phys. Rev.*, vol. D82, p. 035019, 2010. 87, 136, 196

[195] M. Gonderinger, H. Lim, and M. J. Ramsey-Musolf, "Complex Scalar Singlet Dark Matter: Vacuum Stability and Phenomenology," *Phys. Rev.*, vol. D86, p. 043511, 2012. 87, 136, 196

[196] T. Araki, C. Q. Geng, and K. I. Nagao, "Dark Matter in Inert Triplet Models," *Phys. Rev.*, vol. D83, p. 075014, 2011. 87, 136

[197] Y. G. Kim, K. Y. Lee, and S. Shin, "Singlet fermionic dark matter," *JHEP*, vol. 05, p. 100, 2008. 87, 136, 196

[198] L. Lopez Honorez, E. Nezri, J. F. Oliver, and M. H. G. Tytgat, "The Inert Doublet Model: An Archetype for Dark Matter," *JCAP*, vol. 0702, p. 028, 2007. 87, 136

[199] L. Randall and R. Sundrum, "Out of this world supersymmetry breaking," *Nucl. Phys.*, vol. B557, pp. 79–118, 1999. 89, 102, 103, 104, 196

[200] G. F. Giudice, M. A. Luty, H. Murayama, and R. Rattazzi, "Gaugino mass without singlets," *JHEP*, vol. 12, p. 027, 1998. 89, 102, 103, 104

[201] H. E. Haber and G. L. Kane, "The Search for Supersymmetry: Probing Physics Beyond the Standard Model," *Phys. Rept.*, vol. 117, pp. 75–263, 1985. 90, 103

[202] G. Aad *et al.*, “Search for anomaly-mediated supersymmetry breaking with the ATLAS detector based on a disappearing-track signature in pp collisions at $\sqrt{s} = 7$ TeV,” *Eur. Phys. J.*, vol. C72, p. 1993, 2012. 91, 103

[203] E. Ma, “Verifiable radiative seesaw mechanism of neutrino mass and dark matter,” *Phys. Rev.*, vol. D73, p. 077301, 2006. 98, 196, 248, 250, 251

[204] A. Datta, A. Kundu, and A. Samanta, “New bounds on slepton and Wino masses in anomaly mediated supersymmetry breaking models,” *Phys. Rev.*, vol. D64, p. 095016, 2001. 103

[205] M. Ageron *et al.*, “ANTARES: the first undersea neutrino telescope,” *Nucl. Instrum. Meth.*, vol. A656, pp. 11–38, 2011. 104, 126, 127, 134

[206] D. Albornoz Vasquez, G. Belanger, and C. Boehm, “Astrophysical limits on light NMSSM neutralinos,” *Phys. Rev.*, vol. D84, p. 095008, 2011. 104

[207] T. Linden, E. Lovegrove, and S. Profumo, “The Morphology of Hadronic Emission Models for the Gamma-Ray Source at the Galactic Center,” *Astrophys. J.*, vol. 753, p. 41, 2012. 105, 187

[208] H. Baer, R. Dermisek, S. Rajagopalan, and H. Summy, “Neutralino, axion and axino cold dark matter in minimal, hypercharged and gaugino AMSB,” *JCAP*, vol. 1007, p. 014, 2010. 105

[209] T. Moroi and L. Randall, “Wino cold dark matter from anomaly mediated SUSY breaking,” *Nucl. Phys.*, vol. B570, pp. 455–472, 2000. 105

[210] P. Ullio, “Indirect detection of neutralino dark matter candidates in anomaly mediated supersymmetry breaking scenarios,” *JHEP*, vol. 06, p. 053, 2001. 105

[211] D. Majumdar, “Mass and scalar cross-sections for neutralino dark matter in anomaly mediated supersymmetry breaking model,” *J. Phys.*, vol. G28, pp. 2747–2754, 2002. 105

[212] S. Dodelson, D. Hooper, and P. D. Serpico, “Extracting the Gamma Ray Signal from Dark Matter Annihilation in the Galactic Center Region,” *Phys. Rev.*, vol. D77, p. 063512, 2008. 105

[213] P. D. Serpico and D. Hooper, “Gamma-rays from Dark Matter Annihilation in the Central Region of the Galaxy,” *New J. Phys.*, vol. 11, p. 105010, 2009. 105

[214] R. Allahverdi, S. Campbell, and B. Dutta, “Extragalactic and galactic gamma-rays and neutrinos from annihilating dark matter,” *Phys. Rev.*, vol. D85, p. 035004, 2012. 105

[215] Ya. B. Zeldovich, A. A. Klypin, M. Yu. Khlopov, and V. M. Chechetkin, “Astrophysical constraints on the mass of heavy stable neutral leptons,” *Sov. J. Nucl. Phys.*, vol. 31, pp. 664–669, 1980. [Yad. Fiz.31,1286(1980)]. 105

[216] D. Fargion, M. Yu. Khlopov, R. V. Konoplich, and R. Mignani, “Bounds on very heavy relic neutrinos by their annihilation in galactic halo,” *Phys. Rev.*, vol. D52, pp. 1828–1836, 1995. 105

[217] J. Edsjo and P. Gondolo, “Neutralino relic density including coannihilations,” *Phys. Rev.*, vol. D56, pp. 1879–1894, 1997. 107, 108, 109, 155, 157

[218] G. Belanger, F. Boudjema, P. Brun, A. Pukhov, S. Rosier-Lees, P. Salati, and A. Semenov, “Indirect search for dark matter with micrOMEGAs2.4,” *Comput. Phys. Commun.*, vol. 182, pp. 842–856, 2011. 110, 116, 156, 205

[219] D. S. Akerib *et al.*, “The Large Underground Xenon (LUX) Experiment,” *Nucl. Instrum. Meth.*, vol. A704, pp. 111–126, 2013. 114, 197

[220] T. Falk, A. Ferstl, and K. A. Olive, "Variations of the neutralino elastic cross-section with CP violating phases," *Astropart. Phys.*, vol. 13, pp. 301–316, 2000. 114

[221] O. Adriani *et al.*, "An anomalous positron abundance in cosmic rays with energies 1.5-100 GeV," *Nature*, vol. 458, pp. 607–609, 2009. 119, 202

[222] O. Adriani *et al.*, "A new measurement of the antiproton-to-proton flux ratio up to 100 GeV in the cosmic radiation," *Phys. Rev. Lett.*, vol. 102, p. 051101, 2009. 119

[223] J. J. Beatty *et al.*, "New measurement of the cosmic-ray positron fraction from 5 to 15-GeV," *Phys. Rev. Lett.*, vol. 93, p. 241102, 2004. 119

[224] M. Aguilar *et al.*, "Cosmic-ray positron fraction measurement from 1 to 30-GeV with AMS-01," *Phys. Lett.*, vol. B646, pp. 145–154, 2007. 119

[225] A. A. Abdo *et al.*, "Measurement of the Cosmic Ray e+ plus e- spectrum from 20 GeV to 1 TeV with the Fermi Large Area Telescope," *Phys. Rev. Lett.*, vol. 102, p. 181101, 2009. 119

[226] J. Chang *et al.*, "An excess of cosmic ray electrons at energies of 300-800 GeV," *Nature*, vol. 456, pp. 362–365, 2008. 119, 203

[227] A. W. Strong, R. Diehl, H. Halloin, V. Schoenfelder, L. Bouchet, P. Mandrou, F. Lebrun, and R. Terrier, "Gamma-ray continuum emission from the inner galactic region as observed with integral/spi," *Astron. Astrophys.*, vol. 444, p. 495, 2005. 119

[228] D. J. Thompson, "Gamma ray astrophysics: the EGRET results," *Rept. Prog. Phys.*, vol. 71, p. 116901, 2008. 119

[229] C. Meurer, "Dark Matter Searches with the Fermi Large Area Telescope," *AIP Conf. Proc.*, vol. 719, p. 1085, 2009. 119

[230] J. Albert *et al.*, "Observation of gamma-rays from the galactic center with the magic telescope," *Astrophys. J.*, vol. 638, pp. L101–L104, 2006. 119

[231] G. Maier, "Observation of Galactic Gamma-ray Sources with VERITAS," *AIP Conf. Proc.*, vol. 1085, pp. 187–190, 2009. 119

[232] K. Tsuchiya *et al.*, "Detection of sub-TeV gamma-rays from the Galactic Center direction by CANGAROO-II," *Astrophys. J.*, vol. 606, pp. L115–L118, 2004. 119

[233] F. Acero, "Localising the VHE gamma-ray source at the Galactic Centre," *Mon. Not. Roy. Astron. Soc.*, vol. 402, pp. 1877–1882, 2010. 119

[234] F. Stoehr, S. D. M. White, V. Springel, G. Tormen, and N. Yoshida, "Dark matter annihilation in the halo of the Milky Way," *Mon. Not. Roy. Astron. Soc.*, vol. 345, p. 1313, 2003. 119

[235] D. Merritt, "Dark matter at the centres of galaxies," in *Particle dark matter: Observations, Models and Searches* (G. Bertone, ed.), ch. 5, pp. 83–98, Cambridge University Press, 2010. 119

[236] K. Kosack *et al.*, "TeV gamma-ray observations of the galactic center," *Astrophys. J.*, vol. 608, pp. L97–L100, 2004. 119

[237] Y. Mambrini, C. Munoz, E. Nezri, and F. Prada, "Adiabatic compression and indirect detection of supersymmetric dark matter," *JCAP*, vol. 0601, p. 010, 2006. 125

[238] M. C. Gonzalez-Garcia, M. Maltoni, and J. Salvado, "Updated global fit to three neutrino mixing: status of the hints of theta13 > 0," *JHEP*, vol. 04, p. 056, 2010. 134

[239] G. L. Fogli, E. Lisi, A. Marrone, A. Palazzo, and A. M. Rotunno, "Evidence of $\theta_{13} > 0$ from global neutrino data analysis," *Phys. Rev.*, vol. D84, p. 053007, 2011. 134

[240] T. Schwetz, M. Tortola, and J. W. F. Valle, "Where we are on θ_{13}: addendum to 'Global neutrino data and recent reactor fluxes: status of three-flavour oscillation parameters'," *New J. Phys.*, vol. 13, p. 109401, 2011. 134

[241] J. K. Ahn *et al.*, "Observation of Reactor Electron Antineutrino Disappearance in the RENO Experiment," *Phys. Rev. Lett.*, vol. 108, p. 191802, 2012. 134

[242] K. Griest and M. Kamionkowski, "Supersymmetric dark matter," *Phys. Rept.*, vol. 333, pp. 167–182, 2000. 136

[243] H. Murayama, "Physics Beyond the Standard Model and Dark Matter," in *Les Houches Summer School - Session 86: Particle Physics and Cosmology: The Fabric of Spacetime Les Houches, France, July 31-August 25, 2006*, 2007. 136

[244] K. P. Modak and D. Majumdar, "Gamma Ray and Neutrino Flux from Annihilation of Neutralino Dark Matter at Galactic Halo Region in mAMSB Model," *J. Phys.*, vol. G40, p. 075201, 2013. 136

[245] R. Kappl, M. Ratz, and M. W. Winkler, "Light dark matter in the singlet-extended MSSM," *Phys. Lett.*, vol. B695, pp. 169–173, 2011. 136

[246] D. E. Holz and A. Zee, "Collisional dark matter and scalar phantoms," *Phys. Lett.*, vol. B517, pp. 239–242, 2001. 136

[247] J. McDonald, "Gauge singlet scalars as cold dark matter," *Phys. Rev.*, vol. D50, pp. 3637–3649, 1994. 136

[248] A. Abada and S. Nasri, "Phenomenology of a Light Cold Dark Matter Two-Singlet Model," *Phys. Rev.*, vol. D85, p. 075009, 2012. 136

[249] A. Abada and S. Nasri, "Renormalization group equations of a cold dark matter two-singlet model," *Phys. Rev.*, vol. D88, no. 1, p. 016006, 2013. 136

[250] K. R. Dienes, J. Kumar, and B. Thomas, "Dynamical Dark Matter and the positron excess in light of AMS results," *Phys. Rev.*, vol. D88, no. 10, p. 103509, 2013. 137

[251] K. R. Dienes, J. Kumar, and B. Thomas, "Direct Detection of Dynamical Dark Matter," *Phys. Rev.*, vol. D86, p. 055016, 2012. 137, 160

[252] K. R. Dienes, S. Su, and B. Thomas, "Distinguishing Dynamical Dark Matter at the LHC," *Phys. Rev.*, vol. D86, p. 054008, 2012. 137

[253] K. R. Dienes and B. Thomas, "Phenomenological Constraints on Axion Models of Dynamical Dark Matter," *Phys. Rev.*, vol. D86, p. 055013, 2012. 137

[254] K. R. Dienes and B. Thomas, "Dynamical Dark Matter: II. An Explicit Model," *Phys. Rev.*, vol. D85, p. 083524, 2012. 137

[255] K. R. Dienes and B. Thomas, "Dynamical Dark Matter: I. Theoretical Overview," *Phys. Rev.*, vol. D85, p. 083523, 2012. 137

[256] R. Agnese *et al.*, "Silicon detector results from the first five-tower run of CDMS II," *Phys. Rev.*, vol. D88, p. 031104, 2013. [Erratum: Phys. Rev.D88,no.5,059901(2013)]. 137, 161, 192

[257] R. Agnese *et al.*, "Silicon Detector Dark Matter Results from the Final Exposure of CDMS II," *Phys. Rev. Lett.*, vol. 111, no. 25, p. 251301, 2013. 137, 161, 192

[258] R. Bernabei *et al.*, "New results from DAMA/LIBRA," *Eur. Phys. J.*, vol. C67, pp. 39–49, 2010. 137

[259] G. Angloher *et al.*, "Results from 730 kg days of the CRESST-II Dark Matter Search," *Eur. Phys. J.*, vol. C72, p. 1971, 2012. 137, 167, 192

[260] B. Kyae and J.-C. Park, “Light dark matter for Fermi-LAT and CDMS observations,” *Phys. Lett.*, vol. B732, pp. 373–379, 2014. 137

[261] G. Bélanger, A. Goudelis, J.-C. Park, and A. Pukhov, “Isospin-violating dark matter from a double portal,” *JCAP*, vol. 1402, p. 020, 2014. 137

[262] E. Aprile *et al.*, “Dark Matter Results from 225 Live Days of XENON100 Data,” *Phys. Rev. Lett.*, vol. 109, p. 181301, 2012. 137, 169, 192

[263] W. B. Atwood *et al.*, “The Large Area Telescope on the Fermi Gamma-ray Space Telescope Mission,” *Astrophys. J.*, vol. 697, pp. 1071–1102, 2009. 138, 217

[264] A. Boyarsky, D. Malyshev, and O. Ruchayskiy, “A comment on the emission from the Galactic Center as seen by the Fermi telescope,” *Phys. Lett.*, vol. B705, pp. 165–169, 2011. 138, 179, 180

[265] M. Su, T. R. Slatyer, and D. P. Finkbeiner, “Giant Gamma-ray Bubbles from Fermi-LAT: AGN Activity or Bipolar Galactic Wind?,” *Astrophys. J.*, vol. 724, pp. 1044–1082, 2010. 138, 193, 215

[266] W.-C. Huang, A. Urbano, and W. Xue, “Fermi Bubbles under Dark Matter Scrutiny. Part I: Astrophysical Analysis,” 2013. 138, 194

[267] W.-C. Huang, A. Urbano, and W. Xue, “Fermi Bubbles under Dark Matter Scrutiny Part II: Particle Physics Analysis,” *JCAP*, vol. 1404, p. 020, 2014. 138

[268] D. Hooper and T. R. Slatyer, “Two Emission Mechanisms in the Fermi Bubbles: A Possible Signal of Annihilating Dark Matter,” *Phys. Dark Univ.*, vol. 2, pp. 118–138, 2013. 138, 187, 194, 215

[269] K. Kannike, “Vacuum Stability Conditions From Copositivity Criteria,” *Eur. Phys. J.*, vol. C72, p. 2093, 2012. 143

[270] J. Chakrabortty, P. Konar, and T. Mondal, "Copositive Criteria and Boundedness of the Scalar Potential," *Phys. Rev.*, vol. D89, no. 9, p. 095008, 2014. 143

[271] C. P. Burgess, M. Pospelov, and T. ter Veldhuis, "The Minimal model of nonbaryonic dark matter: A Singlet scalar," *Nucl. Phys.*, vol. B619, pp. 709–728, 2001. 145, 157, 158, 160, 196

[272] B. W. Lee, C. Quigg, and H. B. Thacker, "Weak Interactions at Very High-Energies: The Role of the Higgs Boson Mass," *Phys. Rev.*, vol. D16, p. 1519, 1977. 146

[273] G. Cynolter, E. Lendvai, and G. Pocsik, "Note on unitarity constraints in a model for a singlet scalar dark matter candidate," *Acta Phys. Polon.*, vol. B36, pp. 827–832, 2005. 146

[274] J. A. Casas, J. R. Espinosa, and M. Quiros, "Improved Higgs mass stability bound in the standard model and implications for supersymmetry," *Phys. Lett.*, vol. B342, pp. 171–179, 1995. 150

[275] G. Belanger, B. Dumont, U. Ellwanger, J. F. Gunion, and S. Kraml, "Global fit to Higgs signal strengths and couplings and implications for extended Higgs sectors," *Phys. Rev.*, vol. D88, p. 075008, 2013. 152, 201, 202

[276] W.-L. Guo and Y.-L. Wu, "The Real singlet scalar dark matter model," *JHEP*, vol. 10, p. 083, 2010. 152, 157

[277] S. Choi, S. Jung, and P. Ko, "Implications of LHC data on 125 GeV Higgs-like boson for the Standard Model and its various extensions," *JHEP*, vol. 10, p. 225, 2013. 152

[278] S. K. Kang and J. Park, "Unitarity Constraints in the standard model with a singlet scalar field," *JHEP*, vol. 04, p. 009, 2015. 152

[279] G. Belanger, B. Dumont, U. Ellwanger, J. F. Gunion, and S. Kraml, "Status of invisible Higgs decays," *Phys. Lett.*, vol. B723, pp. 340–347, 2013. 152, 201

[280] A. Djouadi and G. Moreau, "The couplings of the Higgs boson and its CP properties from fits of the signal strengths and their ratios at the 7+8 TeV LHC," *Eur. Phys. J.*, vol. C73, no. 9, p. 2512, 2013. 152

[281] S. Banerjee, S. Mukhopadhyay, and B. Mukhopadhyaya, "New Higgs interactions and recent data from the LHC and the Tevatron," *JHEP*, vol. 10, p. 062, 2012. 152

[282] V. Barger, P. Langacker, M. McCaskey, M. J. Ramsey-Musolf, and G. Shaughnessy, "LHC Phenomenology of an Extended Standard Model with a Real Scalar Singlet," *Phys. Rev.*, vol. D77, p. 035005, 2008. 153

[283] J. R. Ellis, K. A. Olive, Y. Santoso, and V. C. Spanos, "Update on the direct detection of supersymmetric dark matter," *Phys. Rev.*, vol. D71, p. 095007, 2005. 159

[284] J. R. Ellis, A. Ferstl, and K. A. Olive, "Reevaluation of the elastic scattering of supersymmetric dark matter," *Phys. Lett.*, vol. B481, pp. 304–314, 2000. 159

[285] S. Profumo, K. Sigurdson, and L. Ubaldi, "Can we discover multi-component WIMP dark matter?," *JCAP*, vol. 0912, p. 016, 2009. 160

[286] C. Kelso, D. Hooper, and M. R. Buckley, "Toward A Consistent Picture For CRESST, CoGeNT and DAMA," *Phys. Rev.*, vol. D85, p. 043515, 2012. 164, 178, 179, 204

[287] P. L. Nolan *et al.*, "Fermi Large Area Telescope Second Source Catalog," *Astrophys. J. Suppl.*, vol. 199, p. 31, 2012. 179, 207

[288] F. Acero *et al.*, "Fermi Large Area Telescope Third Source Catalog," *Astrophys.J.Suppl.*, vol. 218, p. 23, 2015. 179, 207

[289] H. Nakanishi and Y. Sofue, "Three-dimensional distribution of the ISM in the Milky Way Galaxy: 1. The HI disk," *Publ. Astron. Soc. Jap.*, vol. 55, p. 191, 2003. 179

[290] K. N. Abazajian, "The Consistency of Fermi-LAT Observations of the Galactic Center with a Millisecond Pulsar Population in the Central Stellar Cluster," *JCAP*, vol. 1103, p. 010, 2011. 180, 182, 204

[291] A. Atoyan and C. D. Dermer, "TeV emission from the Galactic Center black-hole plerion," *Astrophys. J.*, vol. 617, pp. L123–L126, 2004. 180

[292] D. Hooper, "The Empirical Case For 10 GeV Dark Matter," *Phys. Dark Univ.*, vol. 1, pp. 1–23, 2012. 182, 194, 204, 207

[293] B. Moore, T. R. Quinn, F. Governato, J. Stadel, and G. Lake, "Cold collapse and the core catastrophe," *Mon. Not. Roy. Astron. Soc.*, vol. 310, pp. 1147–1152, 1999. 184, 230

[294] G. Dobler, D. P. Finkbeiner, I. Cholis, T. R. Slatyer, and N. Weiner, "The Fermi Haze: A Gamma-Ray Counterpart to the Microwave Haze," *Astrophys. J.*, vol. 717, pp. 825–842, 2010. 186, 187, 215

[295] D. P. Finkbeiner, "Microwave ism emission observed by wmap," *Astrophys. J.*, vol. 614, pp. 186–193, 2004. 186, 215

[296] P. A. R. Ade *et al.*, "Planck Intermediate Results. IX. Detection of the Galactic haze with Planck," *Astron. Astrophys.*, vol. 554, p. A139, 2013. 187, 215

[297] S. L. Snowden, R. Egger, M. J. Freyberg, D. McCammon, P. P. Plucinsky, W. T. Sanders, J. H. M. Schmitt, J. Truemper, and W. Voges, "ROSAT Survey Diffuse X-Ray Background Maps. II.," *Astrophys. J.*, vol. 485, p. 125, 1997. 187, 215

[298] P. Mertsch and S. Sarkar, "Fermi gamma-ray 'bubbles' from stochastic acceleration of electrons," *Phys. Rev. Lett.*, vol. 107, p. 091101, 2011. 187

[299] T. Linden and S. Profumo, "Exploring the Nature of the Galactic Center Gamma-Ray Source with the Cherenkov Telescope Array," *Astrophys. J.*, vol. 760, p. 23, 2012. 187

[300] S. Profumo and T. Linden, "Gamma-ray Lines in the Fermi Data: is it a Bubble?," *JCAP*, vol. 1207, p. 011, 2012. 193, 215

[301] T. Bringmann, X. Huang, A. Ibarra, S. Vogl, and C. Weniger, "Fermi LAT Search for Internal Bremsstrahlung Signatures from Dark Matter Annihilation," *JCAP*, vol. 1207, p. 054, 2012. 194

[302] C. Weniger, "A Tentative Gamma-Ray Line from Dark Matter Annihilation at the Fermi Large Area Telescope," *JCAP*, vol. 1208, p. 007, 2012. 194

[303] T. Lacroix, C. Boehm, and J. Silk, "Fitting the Fermi-LAT GeV excess: On the importance of including the propagation of electrons from dark matter," *Phys.Rev.*, vol. D90, no. 4, p. 043508, 2014. 194

[304] H. E. Logan, "Dark matter annihilation through a lepton-specific Higgs boson," *Phys.Rev.*, vol. D83, p. 035022, 2011. 195

[305] M. R. Buckley, D. Hooper, and T. M. Tait, "Particle Physics Implications for CoGeNT, DAMA, and Fermi," *Phys.Lett.*, vol. B702, pp. 216–219, 2011. 195

[306] G. Zhu, "WIMPless dark matter and the excess gamma rays from the Galactic center," *Phys.Rev.*, vol. D83, p. 076011, 2011. 195

[307] G. Marshall and R. Primulando, "The Galactic Center Region Gamma Ray Excess from A Supersymmetric Leptophilic Higgs Model," *JHEP*, vol. 1105, p. 026, 2011. 195

[308] M. Boucenna and S. Profumo, "Direct and Indirect Singlet Scalar Dark Matter Detection in the Lepton-Specific two-Higgs-doublet Model," *Phys.Rev.*, vol. D84, p. 055011, 2011. 195

[309] M. R. Buckley, D. Hooper, and J. L. Rosner, "A Leptophobic Z' And Dark Matter From Grand Unification," *Phys.Lett.*, vol. B703, pp. 343–347, 2011. 195

[310] D. Hooper, N. Weiner, and W. Xue, "Dark Forces and Light Dark Matter," *Phys.Rev.*, vol. D86, p. 056009, 2012. 195

[311] M. R. Buckley, D. Hooper, and J. Kumar, "Phenomenology of Dirac Neutralino Dark Matter," *Phys.Rev.*, vol. D88, p. 063532, 2013. 195

[312] K. P. Modak, D. Majumdar, and S. Rakshit, "A Possible Explanation of Low Energy γ-ray Excess from Galactic Centre and Fermi Bubble by a Dark Matter Model with Two Real Scalars," *JCAP*, vol. 1503, p. 011, 2015. 195

[313] J. Guo, J. Li, T. Li, and A. G. Williams, "NMSSM Explanations of the Galactic Gamma Ray Excess and Promising LHC Searches," 2014. 195

[314] J.-H. Yu, "Vector Fermion-Portal Dark Matter: Direct Detection and Galactic Center Gamma-Ray Excess," *Phys.Rev.*, vol. D90, no. 9, p. 095010, 2014. 195

[315] M. Cahill-Rowley, J. Gainer, J. Hewett, and T. Rizzo, "Towards a Supersymmetric Description of the Fermi Galactic Center Excess," *JHEP*, vol. 1502, p. 057, 2015. 195

[316] D. Borah and A. Dasgupta, "Galactic Center Gamma Ray Excess in a Radiative Neutrino Mass Model," *Phys.Lett.*, vol. B741, pp. 103–110, 2015. 195

[317] A. D. Banik and D. Majumdar, "Low Energy Gamma Ray Excess Confronting a Singlet Scalar Extended Inert Doublet Dark Matter Model," 2014. 195

[318] N. Okada and O. Seto, "Galactic Center gamma-ray excess from two-Higgs-doublet-portal dark matter," *Phys.Rev.*, vol. D90, no. 8, p. 083523, 2014. 195

[319] C. Cheung, M. Papucci, D. Sanford, N. R. Shah, and K. M. Zurek, "NMSSM Interpretation of the Galactic Center Excess," *Phys.Rev.*, vol. D90, no. 7, p. 075011, 2014. 195

[320] T. Basak and T. Mondal, "Class of Higgs-portal Dark Matter models in the light of gamma-ray excess from Galactic center," 2014. 195

[321] A. Berlin, P. Gratia, D. Hooper, and S. D. McDermott, "Hidden Sector Dark Matter Models for the Galactic Center Gamma-Ray Excess," *Phys.Rev.*, vol. D90, no. 1, p. 015032, 2014. 195

[322] D. K. Ghosh, S. Mondal, and I. Saha, "Confronting the Galactic Center Gamma Ray Excess With a Light Scalar Dark Matter," *JCAP*, vol. 1502, no. 02, p. 035, 2015. 195

[323] P. Ko, W.-I. Park, and Y. Tang, "Higgs portal vector dark matter for GeV scale γ-ray excess from galactic center," *JCAP*, vol. 1409, p. 013, 2014. 195

[324] C. Balázs and T. Li, "Simplified Dark Matter Models Confront the Gamma Ray Excess," *Phys.Rev.*, vol. D90, no. 5, p. 055026, 2014. 195

[325] P. Agrawal, B. Batell, D. Hooper, and T. Lin, "Flavored Dark Matter and the Galactic Center Gamma-Ray Excess," *Phys.Rev.*, vol. D90, no. 6, p. 063512, 2014. 195

[326] P. Agrawal, M. Blanke, and K. Gemmler, "Flavored dark matter beyond Minimal Flavor Violation," *JHEP*, vol. 1410, p. 72, 2014. 195

[327] E. Izaguirre, G. Krnjaic, and B. Shuve, "The Galactic Center Excess from the Bottom Up," *Phys.Rev.*, vol. D90, no. 5, p. 055002, 2014. 195

[328] D. Cerdeño, M. Peiró, and S. Robles, "Low-mass right-handed sneutrino dark matter: SuperCDMS and LUX constraints and the Galactic Centre gamma-ray excess," *JCAP*, vol. 1408, p. 005, 2014. 195

[329] S. Ipek, D. McKeen, and A. E. Nelson, "A Renormalizable Model for the Galactic Center Gamma Ray Excess from Dark Matter Annihilation," *Phys.Rev.*, vol. D90, no. 5, p. 055021, 2014. 195

[330] C. Boehm, M. J. Dolan, and C. McCabe, "A weighty interpretation of the Galactic Centre excess," *Phys.Rev.*, vol. D90, no. 2, p. 023531, 2014. 195

[331] L. Wang and X.-F. Han, "A simplified 2HDM with a scalar dark matter and the galactic center gamma-ray excess," *Phys.Lett.*, vol. B739, p. 416, 2014. 195

[332] B. D. Fields, S. L. Shapiro, and J. Shelton, "Galactic Center Gamma-Ray Excess from Dark Matter Annihilation: Is There A Black Hole Spike?," *Phys.Rev.Lett.*, vol. 113, p. 151302, 2014. 195

[333] C. Arina, E. Del Nobile, and P. Panci, "Dark Matter with Pseudoscalar-Mediated Interactions Explains the DAMA Signal and the Galactic Center Excess," *Phys.Rev.Lett.*, vol. 114, p. 011301, 2015. 195

[334] J. Huang, T. Liu, L.-T. Wang, and F. Yu, "Supersymmetric subelectroweak scale dark matter, the Galactic Center gamma-ray excess, and exotic decays of the 125 GeV Higgs boson," *Phys.Rev.*, vol. D90, no. 11, p. 115006, 2014. 195

[335] P. Ko and Y. Tang, "Galactic center γ-ray excess in hidden sector DM models with dark gauge symmetries: local Z_3 symmetry as an example," *JCAP*, vol. 1501, p. 023, 2015. 195

[336] P. Agrawal, B. Batell, P. J. Fox, and R. Harnik, "WIMPs at the Galactic Center," 2014. 195, 211, 214

[337] N. Okada and O. Seto, "Gamma ray emission in Fermi bubbles and Higgs portal dark matter," *Phys.Rev.*, vol. D89, no. 4, p. 043525, 2014. 195

[338] C. Boehm, M. J. Dolan, C. McCabe, M. Spannowsky, and C. J. Wallace, "Extended gamma-ray emission from Coy Dark Matter," *JCAP*, vol. 1405, p. 009, 2014. 195

[339] A. Alves, S. Profumo, F. S. Queiroz, and W. Shepherd, "Effective field theory approach to the Galactic Center gamma-ray excess," *Phys.Rev.*, vol. D90, no. 11, p. 115003, 2014. 195

[340] A. Berlin, D. Hooper, and S. D. McDermott, "Simplified Dark Matter Models for the Galactic Center Gamma-Ray Excess," *Phys.Rev.*, vol. D89, no. 11, p. 115022, 2014. 195

[341] M. Abdullah, A. DiFranzo, A. Rajaraman, T. M. Tait, P. Tanedo, *et al.*, "Hidden on-shell mediators for the Galactic Center γ-ray excess," *Phys.Rev.*, vol. D90, no. 3, p. 035004, 2014. 195

[342] A. Martin, J. Shelton, and J. Unwin, "Fitting the Galactic Center Gamma-Ray Excess with Cascade Annihilations," *Phys.Rev.*, vol. D90, no. 10, p. 103513, 2014. 195

[343] J. M. Cline, G. Dupuis, Z. Liu, and W. Xue, "The windows for kinetically mixed Z'-mediated dark matter and the galactic center gamma ray excess," *JHEP*, vol. 1408, p. 131, 2014. 195

[344] W. Detmold, M. McCullough, and A. Pochinsky, "Dark Nuclei I: Cosmology and Indirect Detection," *Phys.Rev.*, vol. D90, no. 11, p. 115013, 2014. 195

[345] W.-F. Chang and J. N. Ng, "Minimal model of Majoronic dark radiation and dark matter," *Phys.Rev.*, vol. D90, no. 6, p. 065034, 2014. 195

[346] N. F. Bell, S. Horiuchi, and I. M. Shoemaker, "Annihilating Asymmetric Dark Matter," *Phys.Rev.*, vol. D91, no. 2, p. 023505, 2015. 195

[347] J. Cao, L. Shang, P. Wu, J. M. Yang, and Y. Zhang, "SUSY explanation of the Fermi Galactic Center Excess and its test at LHC Run-II," 2014. 195

[348] M. Freytsis, D. J. Robinson, and Y. Tsai, "Galactic Center Gamma-Ray Excess through a Dark Shower," *Phys.Rev.*, vol. D91, no. 3, p. 035028, 2015. 195

[349] M. Heikinheimo and C. Spethmann, "Galactic Centre GeV Photons from Dark Technicolor," *JHEP*, vol. 1412, p. 084, 2014. 195

[350] K. Agashe, Y. Cui, L. Necib, and J. Thaler, "(In)direct Detection of Boosted Dark Matter," *JCAP*, vol. 1410, no. 10, p. 062, 2014. 195

[351] F. Calore, I. Cholis, C. McCabe, and C. Weniger, "A Tale of Tails: Dark Matter Interpretations of the Fermi GeV Excess in Light of Background Model Systematics," 2014. 195

[352] A. Abdo *et al.*, "Observations of Milky Way Dwarf Spheroidal galaxies with the Fermi-LAT detector and constraints on Dark Matter models," *Astrophys.J.*, vol. 712, pp. 147–158, 2010. 196, 217

[353] M. Ackermann *et al.*, "Constraining Dark Matter Models from a Combined Analysis of Milky Way Satellites with the Fermi Large Area Telescope," *Phys.Rev.Lett.*, vol. 107, p. 241302, 2011. 196, 219

[354] A. Geringer-Sameth and S. M. Koushiappas, "Exclusion of canonical WIMPs by the joint analysis of Milky Way dwarfs with Fermi," *Phys.Rev.Lett.*, vol. 107, p. 241303, 2011. 196, 219

[355] M. Mazziotta, F. Loparco, F. de Palma, and N. Giglietto, "A model-independent analysis of the Fermi Large Area Telescope gamma-ray data from the Milky Way

dwarf galaxies and halo to constrain dark matter scenarios," *Astropart.Phys.*, vol. 37, pp. 26–39, 2012. 196, 219

[356] A. Geringer-Sameth and S. M. Koushiappas, "Dark matter line search using a joint analysis of dwarf galaxies with the Fermi Gamma-ray Space Telescope," *Phys.Rev.*, vol. D86, p. 021302, 2012. 196, 219

[357] M. Ackermann *et al.*, "Dark matter constraints from observations of 25 Milky Way satellite galaxies with the Fermi Large Area Telescope," *Phys.Rev.*, vol. D89, p. 042001, 2014. 196, 219, 220, 221

[358] P. Ullio, L. Bergstrom, J. Edsjo, and C. G. Lacey, "Cosmological dark matter annihilations into gamma-rays - a closer look," *Phys.Rev.*, vol. D66, p. 123502, 2002. 196, 224, 225, 232

[359] L. Bergstrom, J. Edsjo, and P. Ullio, "Spectral gamma-ray signatures of cosmological dark matter annihilation," *Phys.Rev.Lett.*, vol. 87, p. 251301, 2001. 196, 224

[360] Y.-T. Gao, F. W. Stecker, and D. B. Cline, "The Lightest supersymmetric particle and the extragalactic gamma-ray background," *Astron.Astrophys.*, vol. 249, pp. 1–4, 1991. 196, 224

[361] F. Stecker, "The Cosmic Gamma-Ray Background from the Annihilation of Primordial Stable Neutral Heavy Leptons," *Astrophys.J.*, vol. 223, pp. 1032–1036, 1978. 196, 224

[362] J. E. Taylor and J. Silk, "The Clumpiness of cold dark matter: Implications for the annihilation signal," *Mon.Not.Roy.Astron.Soc.*, vol. 339, p. 505, 2003. 196, 224

[363] K. C. Y. Ng, R. Laha, S. Campbell, S. Horiuchi, B. Dasgupta, *et al.*, "Resolving small-scale dark matter structures using multisource indirect detection," *Phys.Rev.*, vol. D89, no. 8, p. 083001, 2014. 196, 224

[364] T. Bringmann, F. Calore, M. Di Mauro, and F. Donato, "Constraining dark matter annihilation with the isotropic γ-ray background: updated limits and future potential," *Phys.Rev.*, vol. D89, no. 2, p. 023012, 2014. 196

[365] E. Sefusatti, G. Zaharijas, P. D. Serpico, D. Theurel, and M. Gustafsson, "Extragalactic gamma-ray signal from dark matter annihilation: an appraisal," *Mon.Not.Roy.Astron.Soc.*, vol. 441, pp. 1861–1878, 2014. 196

[366] N. G. Deshpande and E. Ma, "Pattern of Symmetry Breaking with Two Higgs Doublets," *Phys.Rev.*, vol. D18, p. 2574, 1978. 196, 197

[367] L. Lopez Honorez and C. E. Yaguna, "A new viable region of the inert doublet model," *JCAP*, vol. 1101, p. 002, 2011. 196, 197

[368] G. Branco, P. Ferreira, L. Lavoura, M. Rebelo, M. Sher, *et al.*, "Theory and phenomenology of two-Higgs-doublet models," *Phys.Rept.*, vol. 516, pp. 1–102, 2012. 196, 200

[369] S. Kanemura, S. Matsumoto, T. Nabeshima, and N. Okada, "Can WIMP Dark Matter overcome the Nightmare Scenario?," *Phys.Rev.*, vol. D82, p. 055026, 2010. 196

[370] O. Lebedev, H. M. Lee, and Y. Mambrini, "Vector Higgs-portal dark matter and the invisible Higgs," *Phys.Lett.*, vol. B707, pp. 570–576, 2012. 196

[371] A. Djouadi, O. Lebedev, Y. Mambrini, and J. Quevillon, "Implications of LHC searches for Higgs–portal dark matter," *Phys.Lett.*, vol. B709, pp. 65–69, 2012. 196

[372] A. Goudelis, B. Herrmann, and St 197

[373] M. Gustafsson, S. Rydbeck, L. Lopez-Honorez, and E. Lundstrom, "Status of the Inert Doublet Model and the Role of multileptons at the LHC," *Phys.Rev.*, vol. D86, p. 075019, 2012. 197

[374] T. Hambye and M. H. Tytgat, "Electroweak symmetry breaking induced by dark matter," *Phys.Lett.*, vol. B659, pp. 651–655, 2008. 197

[375] P. Agrawal, E. M. Dolle, and C. A. Krenke, "Signals of Inert Doublet Dark Matter in Neutrino Telescopes," *Phys.Rev.*, vol. D79, p. 015015, 2009. 197

[376] T. Hambye, F.-S. Ling, L. Lopez Honorez, and J. Rocher, "Scalar Multiplet Dark Matter," *JHEP*, vol. 0907, p. 090, 2009. 197

[377] E. Nezri, M. H. Tytgat, and G. Vertongen, "e+ and anti-p from inert doublet model dark matter," *JCAP*, vol. 0904, p. 014, 2009. 197

[378] S. Andreas, M. H. Tytgat, and Q. Swillens, "Neutrinos from Inert Doublet Dark Matter," *JCAP*, vol. 0904, p. 004, 2009. 197

[379] C. Arina, F.-S. Ling, and M. H. Tytgat, "IDM and iDM or The Inert Doublet Model and Inelastic Dark Matter," *JCAP*, vol. 0910, p. 018, 2009. 197

[380] L. Lopez Honorez and C. E. Yaguna, "The inert doublet model of dark matter revisited," *JHEP*, vol. 1009, p. 046, 2010. 197

[381] A. Melfo, M. Nemevsek, F. Nesti, G. Senjanovic, and Y. Zhang, "Inert Doublet Dark Matter and Mirror/Extra Families after Xenon100," *Phys.Rev.*, vol. D84, p. 034009, 2011. 197

[382] M. Krawczyk, D. Sokolowska, P. Swaczyna, and B. Swiezewska, "Constraining Inert Dark Matter by $R_{\gamma\gamma}$ and WMAP data," *JHEP*, vol. 1309, p. 055, 2013. 197

[383] E. M. Dolle and S. Su, “The Inert Dark Matter,” *Phys.Rev.*, vol. D80, p. 055012, 2009. 197

[384] S. Kanemura, Y. Okada, H. Taniguchi, and K. Tsumura, “Indirect bounds on heavy scalar masses of the two-Higgs-doublet model in light of recent Higgs boson searches,” *Phys.Lett.*, vol. B704, pp. 303–307, 2011. 197

[385] A. Arhrib, R. Benbrik, and N. Gaur, “$H \to \gamma\gamma$ in Inert Higgs Doublet Model,” *Phys.Rev.*, vol. D85, p. 095021, 2012. 197, 201

[386] B. Swiezewska and M. Krawczyk, “Diphoton rate in the inert doublet model with a 125 GeV Higgs boson,” *Phys.Rev.*, vol. D88, no. 3, p. 035019, 2013. 197

[387] B. Swiezewska and M. Krawczyk, “2-photon decay rate of the scalar boson in the Inert Doublet Model,” pp. 563–566, 2013. 197

[388] E. Lundstrom, M. Gustafsson, and J. Edsjo, “The Inert Doublet Model and LEP II Limits,” *Phys.Rev.*, vol. D79, p. 035013, 2009. 197, 201

[389] Q.-H. Cao, E. Ma, and G. Rajasekaran, “Observing the Dark Scalar Doublet and its Impact on the Standard-Model Higgs Boson at Colliders,” *Phys.Rev.*, vol. D76, p. 095011, 2007. 197

[390] E. Dolle, X. Miao, S. Su, and B. Thomas, “Dilepton Signals in the Inert Doublet Model,” *Phys.Rev.*, vol. D81, p. 035003, 2010. 197

[391] A. Arhrib, Y.-L. S. Tsai, Q. Yuan, and T.-C. Yuan, “An Updated Analysis of Inert Higgs Doublet Model in light of the Recent Results from LUX, PLANCK, AMS-02 and LHC,” *JCAP*, vol. 1406, p. 030, 2014. 197, 200, 202, 203, 210

[392] K. Nakamura *et al.*, “Review of particle physics,” *J.Phys.*, vol. G37, p. 075021, 2010. 201

[393] M. Baak, M. Goebel, J. Haller, A. Hoecker, D. Kennedy, *et al.*, "The Electroweak Fit of the Standard Model after the Discovery of a New Boson at the LHC," *Eur.Phys.J.*, vol. C72, p. 2205, 2012. 201

[394] G. Aad *et al.*, "Observation of a new particle in the search for the Standard Model Higgs boson with the ATLAS detector at the LHC," *Phys.Lett.*, vol. B716, pp. 1–29, 2012. 201

[395] S. Chatrchyan *et al.*, "Search for the standard model Higgs boson decaying into two photons in pp collisions at $\sqrt{s} = 7$ TeV," *Phys.Lett.*, vol. B710, pp. 403–425, 2012. 201

[396] K. Cheung, J. S. Lee, and P.-Y. Tseng, "Higgs Precision (Higgcision) Era begins," *JHEP*, vol. 1305, p. 134, 2013. 201

[397] J. R. Espinosa, M. Muhlleitner, C. Grojean, and M. Trott, "Probing for Invisible Higgs Decays with Global Fits," *JHEP*, vol. 1209, p. 126, 2012. 201

[398] C. Englert, M. Spannowsky, and C. Wymant, "Partially (in)visible Higgs decays at the LHC," *Phys.Lett.*, vol. B718, pp. 538–544, 2012. 201

[399] V. Khachatryan *et al.*, "Observation of the diphoton decay of the Higgs boson and measurement of its properties," *Eur.Phys.J.*, vol. C74, no. 10, p. 3076, 2014. 202

[400] G. Aad *et al.*, "Measurement of Higgs boson production in the diphoton decay channel in pp collisions at center-of-mass energies of 7 and 8 TeV with the ATLAS detector," *Phys.Rev.*, vol. D90, no. 11, p. 112015, 2014. 202

[401] M. Aguilar *et al.*, "First Result from the Alpha Magnetic Spectrometer on the International Space Station: Precision Measurement of the Positron Fraction in Primary Cosmic Rays of 0.5–350 GeV," *Phys.Rev.Lett.*, vol. 110, p. 141102, 2013. 202

[402] F. Aharonian *et al.*, "The energy spectrum of cosmic-ray electrons at TeV energies," *Phys.Rev.Lett.*, vol. 101, p. 261104, 2008. 203

[403] M. Ackermann *et al.*, "Fermi LAT observations of cosmic-ray electrons from 7 GeV to 1 TeV," *Phys.Rev.*, vol. D82, p. 092004, 2010. 203

[404] D. Borla Tridon, P. Colin, L. Cossio, M. Doro, and V. Scalzotto, "Measurement of the cosmic electron plus positron spectrum with the MAGIC telescopes," vol. 6, p. 47, 2011. 203

[405] F. Donato, D. Maurin, P. Brun, T. Delahaye, and P. Salati, "Constraints on WIMP Dark Matter from the High Energy PAMELA $\bar{p}/p$ data," *Phys.Rev.Lett.*, vol. 102, p. 071301, 2009. 203

[406] E. Aprile, "The XENON1T Dark Matter Search Experiment," *Springer Proc. Phys.*, vol. 148, pp. 93–96, 2013. 207, 263

[407] M. Dall'Ora, G. Clementini, K. Kinemuchi, V. Ripepi, M. Marconi, *et al.*, "Variable stars in the newly discovered Milky Way satellite in Bootes," *Astrophys.J.*, vol. 653, pp. L109–L112, 2006. 218

[408] J. D. Simon and M. Geha, "The Kinematics of the Ultra-Faint Milky Way Satellites: Solving the Missing Satellite Problem," *Astrophys.J.*, vol. 670, pp. 313–331, 2007. 218

[409] M. G. Walker, M. Mateo, and E. Olszewski, "Stellar Velocities in the Carina, Fornax, Sculptor and Sextans dSph Galaxies: Data from the Magellan/MMFS Survey," *Astron.J.*, vol. 137, p. 3100, 2009. 218

[410] R. R. Munoz, P. M. Frinchaboy, S. R. Majewski, J. R. Kuhn, M.-Y. Chou, *et al.*, "Exploring halo substructure with giant stars. 8. The Velocity dispersion profiles of

the Ursa Minor and Draco dwarf spheroidals at large angular separations," *Astrophys.J.*, vol. 631, pp. L137–L142, 2005. 218

[411] M. Mateo, E. W. Olszewski, and M. G. Walker, "The Velocity Dispersion Profile of the Remote Dwarf Spheroidal Galaxy Leo. 1. A Tidal Hit and Run?," *Astrophys.J.*, vol. 675, p. 201, 2008. 218

[412] A. Koch, J. Kleyna, M. Wilkinson, E. Grebel, G. Gilmore, *et al.*, "Stellar kinematics in the remote Leo II dwarf spheroidal galaxy – Another brick in the wall," *Astron.J.*, vol. 134, pp. 566–578, 2007. 218

[413] J. D. Simon, M. Geha, Q. E. Minor, G. D. Martinez, E. N. Kirby, *et al.*, "A Complete Spectroscopic Survey of the Milky Way Satellite Segue 1: The Darkest Galaxy," *Astrophys.J.*, vol. 733, p. 46, 2011. 218

[414] B. Willman, M. Geha, J. Strader, L. E. Strigari, J. D. Simon, *et al.*, "Willman 1 - a probable dwarf galaxy with an irregular kinematic distribution," *Astron.J.*, vol. 142, p. 128, 2011. 218

[415] G. Battaglia, A. Helmi, and M. Breddels, "Internal kinematics and dynamical models of dwarf spheroidal galaxies around the Milky Way," *New Astron.Rev.*, vol. 57, pp. 52–79, 2013. 219

[416] M. G. Walker, M. Mateo, E. W. Olszewski, J. Penarrubia, N. W. Evans, *et al.*, "A Universal Mass Profile for Dwarf Spheroidal Galaxies," *Astrophys.J.*, vol. 704, pp. 1274–1287, 2009. 219

[417] J. Wolf, G. D. Martinez, J. S. Bullock, M. Kaplinghat, M. Geha, *et al.*, "Accurate Masses for Dispersion-supported Galaxies," *Mon.Not.Roy.Astron.Soc.*, vol. 406, p. 1220, 2010. 219

[418] G. D. Martinez, J. S. Bullock, M. Kaplinghat, L. E. Strigari, and R. Trotta, "Indirect Dark Matter Detection from Dwarf Satellites: Joint Expectations from Astrophysics and Supersymmetry," *JCAP*, vol. 0906, p. 014, 2009. 219, 234

[419] L. E. Strigari, "Galactic Searches for Dark Matter," *Phys.Rept.*, vol. 531, pp. 1–88, 2013. 219

[420] G. D. Martinez, "A Robust Determination of Milky Way Satellite Properties using Hierarchical Mass Modeling," 2013. 219, 220

[421] L. E. Strigari, S. M. Koushiappas, J. S. Bullock, M. Kaplinghat, J. D. Simon, *et al.*, "The Most Dark Matter Dominated Galaxies: Predicted Gamma-ray Signals from the Faintest Milky Way Dwarfs," *Astrophys.J.*, vol. 678, p. 614, 2008. 224

[422] S. Ando, "Can dark matter annihilation dominate the extragalactic gamma-ray background?," *Phys.Rev.Lett.*, vol. 94, p. 171303, 2005. 224

[423] T. Oda, T. Totani, and M. Nagashima, "Gamma-ray background from neutralino annihilation in the first cosmological objects," *Astrophys.J.*, vol. 633, pp. L65–L68, 2005. 224

[424] L. Pieri, G. Bertone, and E. Branchini, "Dark Matter Annihilation in Substructures Revised," *Mon.Not.Roy.Astron.Soc.*, vol. 384, p. 1627, 2008. 224

[425] C. E. Fichtel, G. A. Simpson, and D. J. Thompson, "Diffuse gamma radiation," *Astrophys.J.*, vol. 222, pp. 833–849, June 1978. 224

[426] P. Sreekumar *et al.*, "EGRET observations of the extragalactic gamma-ray emission," *Astrophys.J.*, vol. 494, pp. 523–534, 1998. 224

[427] A. Abdo *et al.*, "The Spectrum of the Isotropic Diffuse Gamma-Ray Emission Derived From First-Year Fermi Large Area Telescope Data," *Phys.Rev.Lett.*, vol. 104, p. 101101, 2010. 224, 239

[428] M. Ajello, D. Gasparrini, M. Sánchez-Conde, G. Zaharijas, M. Gustafsson, *et al.*, "The Origin of the Extragalactic Gamma-Ray Background and Implications for Dark-Matter Annihilation," *Astrophys.J.*, vol. 800, no. 2, p. L27, 2015. 225

[429] A. Dominguez, J. Primack, D. Rosario, F. Prada, R. Gilmore, *et al.*, "Extragalactic Background Light Inferred from AEGIS Galaxy SED-type Fractions," *Mon.Not.Roy.Astron.Soc.*, vol. 410, p. 2556, 2011. 226

[430] A. Franceschini, G. Rodighiero, and M. Vaccari, "The extragalactic optical-infrared background radiations, their time evolution and the cosmic photon-photon opacity," *Astron.Astrophys.*, vol. 487, p. 837, 2008. 226

[431] W. H. Press and P. Schechter, "Formation of galaxies and clusters of galaxies by selfsimilar gravitational condensation," *Astrophys.J.*, vol. 187, pp. 425–438, 1974. 227, 229

[432] R. K. Sheth and G. Tormen, "Large scale bias and the peak background split," *Mon.Not.Roy.Astron.Soc.*, vol. 308, p. 119, 1999. 228, 229

[433] A. Jenkins *et al.*, "Evolution of structure in cold dark matter universes," *Astrophys.J.*, vol. 499, p. 20, 1998. 229

[434] S. Murray, C. Power, and A. Robotham, "HMFcalc: An Online Tool for Calculating Dark Matter Halo Mass Functions," 2013. 229

[435] G. Bryan and M. Norman, "Statistical properties of x-ray clusters: Analytic and numerical comparisons," *Astrophys.J.*, vol. 495, p. 80, 1998. 231

[436] R. K. Sheth and G. Tormen, "On the environmental dependence of halo formation," *Mon.Not.Roy.Astron.Soc.*, vol. 350, p. 1385, 2004. 232

[437] A. V. Maccio', A. A. Dutton, and F. C. d. Bosch, "Concentration, Spin and Shape of Dark Matter Haloes as a Function of the Cosmological Model: WMAP1, WMAP3 and WMAP5 results," *Mon.Not.Roy.Astron.Soc.*, vol. 391, pp. 1940–1954, 2008. 233

[438] A. F. Neto, L. Gao, P. Bett, S. Cole, J. F. Navarro, *et al.*, "The statistics of lambda CDM Halo Concentrations," *Mon.Not.Roy.Astron.Soc.*, vol. 381, pp. 1450–1462, 2007. 233

[439] T. Bringmann, "Particle Models and the Small-Scale Structure of Dark Matter," *New J.Phys.*, vol. 11, p. 105027, 2009. 234

[440] "The Fermi-LAT high-latitude Survey: Source Count Distributions and the Origin of the Extragalactic Diffuse Background," *Astrophys.J.*, vol. 720, pp. 435–453, 2010. 235

[441] A. Abdo *et al.*, "The First Fermi Large Area Telescope Catalog of Gamma-ray Pulsars," *Astrophys.J.Suppl.*, vol. 187, pp. 460–494, 2010. 235

[442] C.-A. Faucher-Giguere and A. Loeb, "The Pulsar Contribution to the Gamma-Ray Background," *JCAP*, vol. 1001, p. 005, 2010. 236

[443] R. Makiya, T. Totani, and M. Kobayashi, "Contribution from Star-Forming Galaxies to the Cosmic Gamma-Ray Background Radiation," *Astrophys.J.*, vol. 728, p. 158, 2011. 236

[444] Y. Inoue, "Contribution of the Gamma-ray Loud Radio Galaxies Core Emissions to the Cosmic MeV and GeV Gamma-Ray Background Radiation," *Astrophys.J.*, vol. 733, p. 66, 2011. 237

[445] V. Berezinsky, A. Gazizov, M. Kachelriess, and S. Ostapchenko, "Restricting UHECRs and cosmogenic neutrinos with Fermi-LAT," *Phys.Lett.*, vol. B695, pp. 13–18, 2011. 237

[446] T. Le and C. D. Dermer, "Gamma Ray Burst Predictions for GLAST," *Astrophys.J.*, vol. 700, p. 1026, 2009. 237

[447] T. A. Thompson, E. Quataert, and E. Waxman, "The Starburst Contribution to the Extra-Galactic Gamma-Ray Background," *Astrophys.J.*, vol. 654, pp. 219–225, 2006. 238

[448] P. Blasi, S. Gabici, and G. Brunetti, "Gamma rays from clusters of galaxies," *Int.J.Mod.Phys.*, vol. A22, pp. 681–706, 2007. 238

[449] C. Pfrommer, T. A. Ensslin, and V. Springel, "Simulating cosmic rays in clusters of galaxies - II. A unified model for radio halos and relics with predictions of the gamma-ray emission," *Mon.Not.Roy.Astron.Soc.*, vol. 385, p. 1211, 2008. 238

[450] U. Keshet, E. Waxman, A. Loeb, V. Springel, and L. Hernquist, "Gamma-rays from intergalactic shocks," *Astrophys.J.*, vol. 585, pp. 128–150, 2003. 239

[451] S. Gabici and P. Blasi, "The Gamma-ray background from large scale structure formation," *Astropart.Phys.*, vol. 19, pp. 679–689, 2003. 239

[452] S. Ando and E. Komatsu, "Constraints on the annihilation cross section of dark matter particles from anisotropies in the diffuse gamma-ray background measured with Fermi-LAT," *Phys.Rev.*, vol. D87, no. 12, p. 123539, 2013. 240

[453] V. Springel, S. White, C. Frenk, J. Navarro, A. Jenkins, *et al.*, "Prospects for detecting supersymmetric dark matter in the Galactic halo," *Nature*, vol. 456N7218, pp. 73–80, 2008. 242

[454] J. Diemand, M. Kuhlen, and P. Madau, "Formation and evolution of galaxy dark matter halos and their substructure," *Astrophys.J.*, vol. 667, pp. 859–877, 2007. 242

[455] M. Kuhlen, J. Diemand, and P. Madau, "The Dark Matter Annihilation Signal from Galactic Substructure: Predictions for GLAST," *Astrophys.J.*, vol. 686, p. 262, 2008. 244

[456] S. Ando, "Gamma-ray background anisotropy from galactic dark matter substructure," *Phys.Rev.*, vol. D80, p. 023520, 2009. 244, 245

[457] E. Bulbul, M. Markevitch, A. Foster, R. K. Smith, M. Loewenstein, and S. W. Randall, "Detection of An Unidentified Emission Line in the Stacked X-ray spectrum of Galaxy Clusters," *Astrophys. J.*, vol. 789, p. 13, 2014. 248

[458] A. Boyarsky, O. Ruchayskiy, D. Iakubovskyi, and J. Franse, "Unidentified Line in X-Ray Spectra of the Andromeda Galaxy and Perseus Galaxy Cluster," *Phys. Rev. Lett.*, vol. 113, p. 251301, 2014. 248

[459] H. Ishida, K. S. Jeong, and F. Takahashi, "7 keV sterile neutrino dark matter from split flavor mechanism," *Phys. Lett.*, vol. B732, pp. 196–200, 2014. 248

[460] D. P. Finkbeiner and N. Weiner, "An X-Ray Line from eXciting Dark Matter," 2014. 248

[461] T. Higaki, K. S. Jeong, and F. Takahashi, "The 7 keV axion dark matter and the X-ray line signal," *Phys. Lett.*, vol. B733, pp. 25–31, 2014. 248

[462] J. Jaeckel, J. Redondo, and A. Ringwald, "3.55 keV hint for decaying axionlike particle dark matter," *Phys. Rev.*, vol. D89, p. 103511, 2014. 248

[463] H. M. Lee, S. C. Park, and W.-I. Park, "Cluster X-ray line at 3.5 keV from axion-like dark matter," *Eur. Phys. J.*, vol. C74, p. 3062, 2014. 248

[464] J.-C. Park, S. C. Park, and K. Kong, "X-ray line signal from 7 keV axino dark matter decay," *Phys. Lett.*, vol. B733, pp. 217–220, 2014. 248

[465] K.-Y. Choi and O. Seto, "X-ray line signal from decaying axino warm dark matter," *Phys. Lett.*, vol. B735, pp. 92–94, 2014. 248

[466] S. Baek and H. Okada, "7 keV Dark Matter as X-ray Line Signal in Radiative Neutrino Model," 2014. 248

[467] T. Tsuyuki, "Neutrino masses, leptogenesis, and sterile neutrino dark matter," *Phys. Rev.*, vol. D90, p. 013007, 2014. 248

[468] F. Bezrukov and D. Gorbunov, "Relic Gravity Waves and 7 keV Dark Matter from a GeV scale inflaton," *Phys. Lett.*, vol. B736, pp. 494–498, 2014. 248

[469] C. Kolda and J. Unwin, "X-ray lines from R-parity violating decays of keV sparticles," *Phys. Rev.*, vol. D90, p. 023535, 2014. 248

[470] R. Allahverdi, B. Dutta, and Y. Gao, "keV Photon Emission from Light Nonthermal Dark Matter," *Phys. Rev.*, vol. D89, p. 127305, 2014. 248

[471] F. S. Queiroz and K. Sinha, "The Poker Face of the Majoron Dark Matter Model: LUX to keV Line," *Phys. Lett.*, vol. B735, pp. 69–74, 2014. 248

[472] K. S. Babu and R. N. Mohapatra, "7 keV Scalar Dark Matter and the Anomalous Galactic X-ray Spectrum," *Phys. Rev.*, vol. D89, p. 115011, 2014. 248

[473] E. Dudas, L. Heurtier, and Y. Mambrini, "Generating X-ray lines from annihilating dark matter," *Phys. Rev.*, vol. D90, p. 035002, 2014. 248

[474] S. V. Demidov and D. S. Gorbunov, "SUSY in the sky or a keV signature of sub-GeV gravitino dark matter," *Phys. Rev.*, vol. D90, p. 035014, 2014. 248

[475] Z. Kang, P. Ko, T. Li, and Y. Liu, "Natural X-ray Lines from the Low Scale Supersymmetry Breaking," *Phys. Lett.*, vol. B742, pp. 249–255, 2015. 248

[476] N. E. Bomark and L. Roszkowski, "3.5 keV x-ray line from decaying gravitino dark matter," *Phys. Rev.*, vol. D90, p. 011701, 2014. 248

[477] S. P. Liew, "Axino dark matter in light of an anomalous X-ray line," *JCAP*, vol. 1405, p. 044, 2014. 248

[478] R. Krall, M. Reece, and T. Roxlo, "Effective field theory and keV lines from dark matter," *JCAP*, vol. 1409, p. 007, 2014. 248, 255

[479] C. El Aisati, T. Hambye, and T. Scarnà, "Can a millicharged dark matter particle emit an observable gamma-ray line?," *JHEP*, vol. 08, p. 133, 2014. 248

[480] M. T. Frandsen, F. Sannino, I. M. Shoemaker, and O. Svendsen, "X-ray Lines from Dark Matter: The Good, The Bad, and The Unlikely," *JCAP*, vol. 1405, p. 033, 2014. 248

[481] M. Cicoli, J. P. Conlon, M. C. D. Marsh, and M. Rummel, "3.55 keV photon line and its morphology from a 3.55 keV axionlike particle line," *Phys. Rev.*, vol. D90, p. 023540, 2014. 248

[482] Y. Fukuda *et al.*, "Evidence for oscillation of atmospheric neutrinos," *Phys. Rev. Lett.*, vol. 81, pp. 1562–1567, 1998. 248

[483] Q. R. Ahmad *et al.*, "Direct evidence for neutrino flavor transformation from neutral current interactions in the Sudbury Neutrino Observatory," *Phys. Rev. Lett.*, vol. 89, p. 011301, 2002. 248

[484] T. Araki *et al.*, "Measurement of neutrino oscillation with KamLAND: Evidence of spectral distortion," *Phys. Rev. Lett.*, vol. 94, p. 081801, 2005. 248

[485] P. Adamson *et al.*, "Measurement of Neutrino Oscillations with the MINOS Detectors in the NuMI Beam," *Phys. Rev. Lett.*, vol. 101, p. 131802, 2008. 248

[486] J. Kubo, E. Ma, and D. Suematsu, "Cold Dark Matter, Radiative Neutrino Mass, $\mu \to e\gamma$, and Neutrinoless Double Beta Decay," *Phys. Lett.*, vol. B642, pp. 18–23, 2006. 249

[487] Y. Kajiyama, J. Kubo, and H. Okada, "D(6) Family Symmetry and Cold Dark Matter at LHC," *Phys. Rev.*, vol. D75, p. 033001, 2007. 249

[488] D. Suematsu, T. Toma, and T. Yoshida, "Reconciliation of CDM abundance and $\mu \to e\gamma$ in a radiative seesaw model," *Phys. Rev.*, vol. D79, p. 093004, 2009. 249, 252

[489] D. Suematsu, T. Toma, and T. Yoshida, "Enhancement of the annihilation of dark matter in a radiative seesaw model," *Phys. Rev.*, vol. D82, p. 013012, 2010. 249

[490] D. Aristizabal Sierra, J. Kubo, D. Restrepo, D. Suematsu, and O. Zapata, "Radiative seesaw: Warm dark matter, collider and lepton flavour violating signals," *Phys. Rev.*, vol. D79, p. 013011, 2009. 249

[491] Y. Kajiyama, H. Okada, and T. Toma, "Direct and Indirect Detection of Dark Matter in D6 Flavor Symmetric Model," *Eur. Phys. J.*, vol. C71, p. 1688, 2011. 249

[492] Y. Kajiyama, H. Okada, and T. Toma, "A Light Scalar Dark Matter for CoGeNT and DAMA in D6 Flavor Symmetric Model," 2011. 249

[493] T. Toma and A. Vicente, "Lepton Flavor Violation in the Scotogenic Model," *JHEP*, vol. 01, p. 160, 2014. 249, 252

[494] S.-Y. Ho and J. Tandean, "Probing Scotogenic Effects in Higgs Boson Decays," *Phys. Rev.*, vol. D87, p. 095015, 2013. 249, 252

[495] S.-Y. Ho and J. Tandean, "Probing Scotogenic Effects in e^+e^- Colliders," *Phys. Rev.*, vol. D89, p. 114025, 2014. 249, 252

[496] D. Schmidt, T. Schwetz, and T. Toma, "Direct Detection of Leptophilic Dark Matter in a Model with Radiative Neutrino Masses," *Phys. Rev.*, vol. D85, p. 073009, 2012. 249, 254, 255, 256

[497] K. Griest and D. Seckel, "Three exceptions in the calculation of relic abundances," *Phys. Rev.*, vol. D43, pp. 3191–3203, 1991. 253